11.0N

6G Near-field Technologies White Paper 2.0

6G Near-Field Technologies White Paper 2.0

Consultants

Tiejun Cui (tjcui@seu.edu.cn), Southeast University

Ping Zhang (pzhang@bupt.edu.cn), Beijing University of Posts and Telecommunications

Xiaohu You (xhyu@seu.edu.cn), Southeast University

Yonina Eldar (yonina.eldar@weizmann.ac.il), Weizmann Institute of Science

Jiangzhou Wang (j.z.wang@seu.edu.cn), Southeast University

Jiying Xiang (xiang.jiying@zte.com.cn), ZTE Corporation

Editors in Chief

Yajun Zhao (zhao.yajun1@zte.com.cn), ZTE Corporation

Linglong Dai (daill@tsinghua.edu.cn), Tsinghua University

Jianhua Zhang (jhzhang@bupt.edu.cn), Beijing University of Posts and Telecommunications

Long Li (lilong@mail.xidian.edu.cn), Xidian University

Chapter Editors

Chongwen Huang (chongwenhuang@zju.edu.cn), Zhejiang University

Yuanwei Liu (yuanwei@hku.hk), The University of Hong Kong

Yifei Yuan (yuanyifei@chinamobile.com), China Mobile

Shuang Zheng (zheng.shuang@zte.com.cn), ZTE Corporation

Contributors (*Order by the first letter of names.)

Ahmed Al Hammadi (ahmed.alhammadi@tii.ae), Technology Innovation Institute

Ahmed Elzanaty (a.elzanaty@surrey.ac.uk), University of Surrey

Ang Chen (chenang1122@mail.ustc.edu.cn), University of Science and Technology of China

Anton Tishchenko (a.tishchenko@surrey.ac.uk), 5G/6G Innovation Centre, University of Surrey

Ashwin Thelappilly Joy (qq566jd@surrey.ac.uk), 5G/6G Innovation Centre, University of Surrey

Beixiong Zheng(bxzheng@scut.edu.cn), South China University of Technology

Bo Ai (boai@bjtu.edu.cn), Beijing Jiaotong University

Bohao Wang (bohaowang@zju.edu.cn), Zhejiang University

Bokai Xu (20251197@bjtu.edu.cn), Beijing Jiaotong University

Boqun Zhao (boqun1@ualberta.ca), University of Alberta

Chan-Byoung Chae(cbchae@yonsei.ac.kr), Yonsei University

Changsheng You (youcs@sustech.edu.cn), Southern University of Science and Technology

Chao Feng (chao_feng@seu.edu.cn), Southeast University

Chao Zhou (zhouchao2024@mail.sustech.edu.cn), Southern University of Science and Technology

Chau Yuen (chau.yuen@ntu.edu.sg), Nanyang Technological University

Chen Sun (chen.sun@sony.com), SONY China Research Lab

Chen Yang (shijianyc@163.com), Beijing Institute of Technology (Zhuhai)

Chenhao Qi (qch@seu.edu.cn), Southeast University

Chenxi Zhu (zhucx1@lenovo.com), Lenovo Research

Chong Han (chong.han@sjtu.edu.cn), Shanghai Jiao Tong University

Chong Huang (chong.huang@ieee.org), Sun Yat-sen University

Chongjun Ouyang (c.ouyang@qmul.ac.uk), Queen Mary University of London

Chongwen Huang (chongwenhuang@zju.edu.cn), Zhejiang University

Cong Zhou (zhoucong@stu.hit.edu.cn), Harbin Institute of Technology / Southern University of Science and Technology

Cunhua Pan (cpan@seu.edu.cn), Southeast University

Dajie Jiang (jiangdajie@vivo.com), vivo Software Technology Co. Ltd.

Daniel Benevides da Costa (danielbcosta@ieee.org), King Fahd University of Petroleum & Minerals

Davide Dardari (davide.dardari@unibo.it), University of Bologna

Deyue Zou (zoudeyue@dlut.edu.cn), Dalian University of Technology

Di Zhang (dr.di.zhang@ieee.org), Zhengzhou University

Dongxuan He (dongxuan_he@bit.edu.cn), Beijing Institute of Technology

Du Pan (pandu@cmdi.chinamobile.com), China Mobile Group Design Institute Co., Ltd.

Ehsan Tohidi (tohidi@tu-berlin.de), Technische Universität Berlin

Emil Björnson(emilbjo@kth.se), KTH Royal Institute of Technology

Fambirai Takawira (Fambirai.takawira@wits.ac.za),

University of Witwatersrand

Fan Liu (fan.liu@seu.edu.cn), Southeast University

Fan Wang (wangf@docomolabs-beijing.com.cn), DOCOMO Beijing Communications Laboratories Co. Ltd.

Fan Zhang (zf22@mails.tsinghua.edu.cn), Tsinghua University

Fang Fang (fang.fang@uwo.ca), Western University

Fang Yang (fangyang@tsinghua.edu.cn), Tsinghua University

Faouzi Bader (carlos-faouzi.bader@tii.ae), Technology Innovation Institute

Feifei Gao (feifeigao@ieee.org), Tsinghua University

Feng Shu (shufeng0101@163.com), Hainan University

Gabriele Gradoni (g.gradoni@surrey.ac.uk), 5G/6G Innovation Centre, University of Surrey

Gang Yang (yanggang@uestc.edu.cn), University of Electronic Science and Technology of China

Gaojian Huang (g.huang@hpu.edu.cn), Henan Polytechnic University

Gaojie Chen (gaojie.chen@ieee.org), Sun Yat-sen University

Gaurav Bhargava (gauravbhargav87@gmail.com), National institute of Technology Meghalaya

Gong Tierui (tierui.gong@ntu.edu.sg), Nanyang Technological University

Guiping Lu (344088386@qq.com), Beijing Institute of Technology (Zhuhai)

Haifan Yin (yin@hust.edu.cn), Huazhong University of Science and Technology

Haiquan Lu (haiquanlu@seu.edu.cn), Southeast University

Haixia Liu (hxliu@xidian.edu.cn), Xidian University

Haiyang Miao (hymiao@bupt.edu.cn), Beijing University of Posts and Telecommunications

Haiyang Zhang (haiyang.zhang@njupt.edu.cn),Nanjing University of Posts and Telecommunications

Hamidreza Tagvahee (h.taghvaee@surrey.ac.uk), 5G/6G Innovation Centre, University of Surrey

Hao Jiang (jianghao@nuist.edu.cn), Nanjing University of Information Science and Technology.

Hao Lei (19211425@bjtu.edu.cn), Beijing Jiaotong University

Hao Qin (hao.qin@ucdconnect.ie), University College Dublin

Hao Xue(xuehao@xidian.edu.cn), Xidian University

Haodong Zhang (zhanghd2021@mail.sustech.edu.cn), Southern University of Science and Technology

Haris Pervaiz (haris.pervaiz@essex.ac.uk), University of Essex

Hong Ren (hrenw@seu.edu.cn), Southeast University

Hongbo Xing (hbxing@bupt.edu.cn), Beijing University of Posts and Telecommunications

Hongkang Yu (yu.hongkang@zte.com.cn), ZTE Corporation

Hongliang Luo (luohl23@mails.tsinghua.edu.cn), Tsinghua University

Hongqiang Cheng (chenghq2023@mail.sustech.edu.cn), Southern University of Science and Technology

Hongxia Miao (hongxia_miao@bupt.edu.cn), Beijing University of Posts and Telecommunications

Huizhi Wang (wanghuizhi@seu.edu.cn), Southeast University

Jalil Kazim(Jalil.Kazim@glasgow.ac.uk), University of Glasgow

Ji Wang (jiwang@ccnu.edu.cn), Central China Normal University

Jiachen Tian (tianjiachen@seu.edu.cn), Southeast University

Jian Song (jsong@tsinghua.edu.cn), Tsinghua University

Jianchi Zhu (zhujc@chinatelecom.cn), China Telecom Research Institute

Jiangzhou Wang (j.z.wang@seu.edu.cn), Southeast University

Jianhua Zhang (jhzhang@bupt.edu.cn), Beijing University of Posts and Telecommunications

Jianwu Dou (dou.jianwu@zte.com.cn), ZTE Corporation

Jiao Wu (jiao.wu@kaust.edu.sa), King Abdullah University of Science and Technology

Jiapeng Li (lijiapeng2023@mail.sustech.edu.cn), Southern University of Science and Technology

Jiaqi Han (jqhan@xidian.edu.cn), Xidian University

Jiaqi Xu (jiaqi.xu@qmul.ac.uk), Queen Mary University of London

Jiaxue Li (jiaxue_li@gs.zzu.edu.cn), Zhengzhou University/China

Jiayi Zhang (jiayizhang@bjtu.edu.cn), Beijing Jiaotong University

Jiayu Shen (shenjy@zju.edu.cn), Zhejiang University

Jie Hu (hujie@uestc.edu.cn), University of Electronic Science and Technology of China

Jie Feng(eejiefeng@mail.scut.edu.cn), South China University of Technology

Jiguang He (jiguang.he@tii.ae), Technology Innovation Institute

Jintao Wang (wangjintao@tsinghua.edu.cn), Tsinghua University

Jingqing Wang (jqwangxd@xidian.edu.cn), Xidian University

Josep Miquel Jornet (j.jornet@northeastern.edu), Northeastern

University

Jun Du (jundu@tsinghua.edu.cn), Tsinghua University

Jun Liu (cnliujun93@gmail.com),University of Electronic Science and Technology of China

Kai-Kit Wong (kai-kit.wong@ac.ucl.uk), University College London

Kangda Zhi (k.zhi@tu-berlin.de), Technische Universität Berlin

Kangjian Chen (kjchen@seu.edu.cn), Southeast University

Kun Yang (kun.yang.txyj@vivo.com), vivo Software Technology Co. Ltd.

Kun Yang(kunyang@nju.edu.cn), Nanjing University

Lexi Xu (xulx29@chinaunicom.cn), China Unicom & Beijing University of Posts and Telecommunications

Leyi Zhang (leyi.zhang@zte.com.cn), ZTE Corporation

Li Chen (chenli87@ustc.edu.cn), University of Science and Technology of China

Lijuan Dong (donglijuan_2012@163.com), Shanxi Datong University

Linglong Dai (daill@tsinghua.edu.cn), Tsinghua University

Lipeng Zhu (zhulp@nus.edu.sg), National University of Singapore

Liyang Lu (luliyang@mail.tsinghua.edu.cn), Tsinghua University

Long Li (lilong@mail.xidian.edu.cn), Xidian University

Long Zhang (lzhang1224@qq.com), Sun Yat-sen University

Lulu Song (lulu_song@gs.zzu.edu.cn), Zhengzhou University

Marco DI RENZO (marco.di-renzo@universite-paris-saclay.fr), Paris-Saclay University

Mengnan Jian (jian.mengnan@zte.com.cn), ZTE Corporation

Mérouane Debbah (merouane.debbah@ku.ac.ae), Khalifa University of Science and Technology & CentraleSupelec, University Paris-Saclay

Miaowen Wen (eemwwen@scut.edu.cn), South China University of Technology

Mingyao Cui (cuimy23@connect.hku.hk), The University of Hong Kong

Mingju Li (limingju@xiaomi.com), Xiaomi

Mingyao Cui (cui-my16@tsinghua.org.cn), Tsinghua University

Mohsen Khalily (m.khalily@surrey.ac.uk), 5G/6G Innovation Centre, University of Surrey

Muhammad Ali Imran (Muhammad.lmran@glasgow.ac.uk),

University of Glasgow

Nan Zhang (zhang.nan152@zte.com.cn), ZTE Corporation

Nan Zhao (zhaonan@dlut.edu.cn), Dalian University of Technology

Nanxi Li (linanxi@chinatelecom.cn), China Telecom

Navneet Agrawal (navneet.agrawal@tu-berlin.de), Technische Universität Berlin

Neel Kanth Kundu (neelkanth@iitd.ac.in), Indian Institute of Technology Delhi

Özlem Tugfe Demir (ozlemtd@kth.se), KTH Royal Institute of Technology

Pan Tang (tangpan27@bupt.edu.cn), Beijing University of Posts and Telecommunications

Pengfei Wang (wangpengfei1121@vivo.com), vivo Software Technology Co. Ltd.

Qammer H. Abbasi (Qammer.abbasi@glasgow.ac.uk), University of Glasgow

Qi Gu (guqi@chinamobile.com), China Mobile

Qi Zhang (zhang.qi33@zte.com.cn), ZTE Corporation

Qiang Feng (qfeng@xidian.edu.cn), Xidian University

Qingqing Wu (qingqingwu@sjtu.edu.cn), Shanghai Jiao Tong University

Qingxiao Huang (qxhuang@std.uestc.edu.cn), University of Electronic Science and Technology of China

Qiuyan Liu (liuqy95@chinaunicom.cn), China Unicom

Qu Luo (q.u.luo@surrey.ac.uk), University of Surrey

Qurrat-Ul-Ain Nadeem (qurrat.nadeem@nyu.edu), New York University (NYU) Abu Dhabi and NYU Tandon

Ran Ji (ranji@zju.edu.cn), Zhejiang University

Ritao Cheng (chengritao@cmdi.chinamobile.com), China Mobile Group Design Institute Co., Ltd.

Robert W. Heath Jr (rwheathjr@ucsd.edu), University of California, San Diego

Rui Zhang (rzhang@cuhk.edu.cn), The Chinese University of Hong Kong, Shenzhen / National University of Singapore

Ruiqi (Richie) Liu (richie.leo@zte.com.cn), ZTE Corporation

Ruirui Sun (sunrr@seu.edu.cn), Southeast University

Saber Hassouna (Saber.Hassouna@glasgow.ac.uk), University of Glasgow

Seungnyun Kim (snkim94@mit.edu), Massachusetts Institute of Technology

Shan Wang(wang.shan40@zte.com.cn), ZTE Corporation

Shaohua Yue (yueshaohua@pku.edu.cn), Peking University

Shengheng Liu (s.liu@seu.edu.cn), Southeast University

Shi Jin (jinshi@seu.edu.cn), Southeast University

Shicong Liu (sc.liu@my.cityu.edu.hk), City University of Hong Kong

Shihang Lu (lush2021@mail.sustech.edu.cn), Southern University of Science and Technology

Shiru Duan (duanshiru822@qq.com), Beijing Information Science and Technology University

Shuai S.A. Yuan (shuaiyuan1997@zju.edu.cn), Zhejiang University

Shuang Zheng (zheng.shuang@zte.com.cn), ZTE Corporation

Shubhankar Majumdar (shubuit@gmail.com), National institute of Technology Meghalaya

Shuhao Zeng (shuhao.zeng96@gmail.com), Princeton University

Shupei Zhang (zhangshupei@pku.edu.cn), Peking University

Sicong Liu (liusc@xmu.edu.cn), Xiamen University

Sławomir Stańczak (slawomir.stanczak@tu-berlin.de), Technische Universität Berlin

Songtao Gao (gaosongtao@cmdi.chinamobile.com), China Mobile Group Design Institute Co., Ltd.

Syed Tariq Shah (syed.shah@essex.ac.uk), University of Essex

Tahsin Akalin (Tahsin.Akalin@univ-lille.fr), University of Lille

Tianqi Mao (maotq@bit.edu.cn), Beijing Institute of Technology

Tiantian Ma(mitiantianma@mail.scut.edu.cn), South China University of Technology

Tianwei Hou (twhou@bjtu.edu.cn), Beijing Jiaotong University

Tianyu Liu (liuty2022@mail.sustech.edu.cn), Southern University of Science and Technology

Tingting Fan (Emme.Fan@sony.com), SONY China Research Lab

Victor Monzon Baeza (vmonzon@uoc.edu), Universitat Oberta de Catalunya

Wahab Almuhtadi (almuhtadi@ieee.org), Algonquin College

Wenchi Cheng (wccheng@xidian.edu.cn), Xidian University

Wang Liu (w_liu@seu.edu.cn), Southeast University Wanming Hao (iewmhao@zzu.edu.cn), Zhengzhou University Wei Ci (cw99@seu.edu.cn), Southeast University

Wei E.I. Sha (weisha@zju.edu.cn), Zhejiang University

Wei Li (l_wei@ntu.edu.sg), Nanyang Technological University

Wei Xi (xiwei@xiaomi.com), Xiaomi

Weidong Hu (hoowind@bit.edu.cn), Beijing Institute of Technology

Weidong Li (weidongli@hust.edu.cn), Huazhong University of Science and Technology

Weihua Yu (ywhbit@bit.edu.cn), Beijing Institute of Technology/BIT Chongqing Institute of Microelectronics and Microsystems

Wenhui Yi (23125012@bjtu.edu.cn), Beijing Jiaotong University

Wenjie Hou (byhhwj@163.com), Beijing Institute of Technology (Zhuhai)

Wenyan Ma (wenyan@u.nus.edu), National University of Singapore

Wentao Yu (wyuaq@connect.ust.hk), The Hong Kong University of Science and Technology

Wei Zhang (w.zhang@unsw.edu.au), University of New South Wales

Xiang Li (lix@docomolabs-beijing.com.cn), DOCOMO Beijing Labs

Xianghao Yu (alex.yu@cityu.edu.hk), City University of Hong Kong

Xianjun Yang (yangxianjun@cictmobile.com),CICT Mobile Communication Technology Co., Ltd.

Xiaolin Hou (hou@docomolabs-beijing.com.cn), DOCOMO Beijing Labs

Xiaowen Tian (xtian8@ncsu.edu), North Carolina State University

Xidong Mu (x.mu@qub.ac.uk), Queen's University Belfast Xin Su (suxin@chinamobile.com), China Mobile

Xin Su (suxin@cictmobile.com), CICT Mobile Communication Technology Co., Ltd.

Xin Wang (wangxin01@stu.xidian.edu.cn), Xidian University

Xing Zhang (xing_zhang@njupt.edu.cn), Nanjing University of Posts and Telecommunications

Xingqi Zhang (xingqi.zhang@ualberta.ca), University of Alberta

Xingwang Li (lixingwang@hpu.edu.cn), Henen Polytechnic University

Xinrui Li (xinrui_li@seu.edu.cn), Southeast University Xinwei Yue (xinwei.yue@bistu.edu.cn), Beijing Information Science and Technology University

Xinyu Xie (xinyuxie@sjtu.edu.cn), Shanghai Jiao Tong University

Xiyuan Liu (1910670@tongji.edu.cn), Tongji University

Xu Gan (gan_xu@zju.edu.cn), Zhejiang University

Xu Shi (shi-x19@mails.tsinghua.edu.cn), Tsinghua University

Xue Xiong(ftxuexiong@mail.scut.edu.cn), South China University of Technology

Xuehua Li (lixuehua@bistu.edu.cn), Beijing Information Science and Technology University

Xuesong Cai (xuesong.cai@pku.edu.cn), Peking University

Xusheng Zhu (xushengzhu@sjtu.edu.cn), Shanghai Jiao Tong University

Xiao Zheng (zheng_xiao@stu.xidian.edu.cn), Xidian University

Yajun Zhao (zhao.yajun1@zte.com.cn), ZTE Corporation

Yan Gao (3220221590@bit.edu.cn), Beijing Institute of Technology

Yan Shi (yanshi@mail.xidian.edu.cn), Xidian University

Yang Liu (yangliu_613@dlut.edu.cn), Dalian University of Technology

Yang Zhang (y_zhang@seu.edu.cn), Southeast University

Yanxia Cao (caoyx28@chinaunicom.cn), China Unicom

Yanze Zhu (yanzezhu@sjtu.edu.cn), Shanghai Jiao Tong University

Yasheng Jin (yashengjin@seu.edu.cn), Southeast University

Yifan Li (liyifan97@foxmail.com), Nanjing University of Science and Technology

Yifei Yuan (yuanyifei@chinamobile.com), China Mobile

Yiming Yu (yuyiming@cmdi.chinamobile.com), China Mobile Group Design Institute Co., Ltd.

Ying Gao (yinggao@sjtu.edu.cn), Shanghai Jiao Tong University

Yiwei Sun (sunyiweiyjy@chinamobile.com), China Mobile

Yizhe Zhao (yzzhao@uestc.edu.cn), University of Electronic Science and Technology of China

Yong Zeng (yong_zeng@seu.edu.cn), Southeast University, Purple Mountain Laboratory

Yongli Ren (renyongli@tsinghua.edu.cn) , Tsinghua University

Yongpeng Wu (yongpeng.wu@sjtu.edu.cn), Shanghai Jiao Tong University

Yonina Eldar (yonina.eldar@weizmann.ac.il), Weizmann Institute of Science

Yu Han (hanyu@seu.edu.cn), Southeast University

Yuan Xu (yuan_xu@zju.edu.cn), Zhejiang University

Yuanbin Chen (chen_yuanbin@163.com), Beijing University of Posts and Telecommunications

Yuanwei Liu (yuanwei@hku.hk), The University of Hong Kong

Yuexia Zhang (zhangyuexia@bistu.edu.cn), Beijing Information Science and Technology University

Yuhao Chen (yc3718@princeton.edu), Princeton University

Yuhua Jiang (jiangyh20@mails.tsinghua.edu.cn), Tsinghua University

Yuming Bai (bym@bit.edu.cn), Beijing Institute of Technology

Yunpu Zhang (yunpu.zhang@my.cityu.edu.hk), City University of Hong Kong / Southern University of Science and Technology

Yunqi Sun (sun.yunqi@zte.com.cn), ZTE Corporation

Yutong Zhang (yutongzhang@pku.edu.cn), Peking University

Yuxiao Wu (220240864@seu.edu.cn), Southeast University

Zhaohui Yang (yang_zhaohui@zju.edu.cn), Zhejiang University

Zhaolin Wang (zhaolin.wang@qmul.ac.uk), Queen Mary University of London

Zhaoyang Zhang (zhzy@zju.edu.cn), Zhejiang University

Zhe Wang (zhewang_77@bjtu.edu.cn), Beijing Jiaotong University

zhen chen (chenz.scut@gmail.com), University of Macau

Zhen Gao(gaozhen16@bit.edu.cn), Beijing Institute of Technology

Zheng Li (stones_li@outlook.com), Zhengzhou University

Zhengyu Zhu (iezyzhu@zzu.edu.cn), Zhengzhou University

Zhenjun Dong (zhenjun_dong@seu.edu.cn), Southeast University

Zhenqiao Cheng (chengzq@chinatelecom.cn), China Telecom

Zhenyu Zhang (zhangzhenyu3@xiaomi.com), Xiaomi

Zhiguo Ding (zhiguo.ding@ieee.org), Khalifa University

Zhiqiang Yuan (yuanzhiqiang@bupt.edu.cn), Beijing University of Posts and Telecommunications

Zhiwen Zhou (zhiwen_zhou@seu.edu.cn), Southeast University

Zhonglun Wang (wangzl256@163.com), University of Electronic Science and Technology of China

Zhuo Xu (xz23@mails.tsinghua.edu.cn), Tsinghua University

Chapter Contacts
Chapter 2: Xin Su (suxin@chinamobile.com), China Mobile

Chapter 3: Yuan Xu (yuan_xu@zju.edu.cn), Zhejiang University

Chapter 4: Haiyang Miao (hymiao@bupt.edu.cn), Beijing University of Posts and Telecommunications

Chapter 5: Zhuo Xu (xz23@mails.tsinghua.edu.cn), Tsinghua University

Chapter 6: Xidong Mu (x.mu@qub.ac.uk), Queen's University Belfast

Chapter 7: Shuang Zheng (zheng.shuang@zte.com.cn), ZTE Corporation

White Paper 2.0: Writing Instructions and Key Updates

1. Background and Motivation

Following the release of the initial version last year [R1], we are now embarking on the development of White Paper 2.0. This update is driven by the impending launch of the 6G study item by the Third Generation Partner Project (3GPP) in 2025. In anticipation of this significant milestone, it is imperative that we revise and enhance the existing white paper to align it with the evolving landscape of 6G technologies, particularly in the realm of near-field technology applications. The primary objectives of this update are to actively promote research and standardization efforts in near-field technologies, and to identify potential key scenarios and technologies for standardization, thereby providing crucial references for the 6G standardization process.

2. Key Updates and Enhancements in White Paper 2.0

Content Refinement and Update: White Paper 2.0 builds upon the foundation laid by its predecessor, refining and updating the content to reflect the latest advancements and insights in the field. Existing sections have been reviewed and revised to ensure accuracy, relevance, and comprehensiveness.

Addition of Engineering Implementation and Standardization: Recognizing the growing importance of practical implementation and standardization in the 6G era, White Paper 2.0 places special emphasis on these aspects. A dedicated chapter has been introduced to delve into the challenges and solutions of engineering implementation, as well as the standardization processes and frameworks relevant to near-field technologies.

[R1] Y. J. Zhao, L. L. Dai, J. H. Zhang, et al. "6G Near-field Technologies White Paper," FuTURE Forum, Nanjing, China, Apr 2024. doi: 10.12142/FuTURE.202404002.

Scan the QR code to download the latest
version of the white paper.

Abstract

In June 2025, Third Generation Partner Project (3GPP) is scheduled to officially launch its 6G research project, marking the global evolution of 6G from a visionary stage toward a new phase characterized by critical technological development, standardization, and practical applications. 6G networks leverage larger antenna apertures and higher frequency bands (e.g., mid-bands, millimeter waves, terahertz) to prioritize near-field characteristics. The integration of reconfigurable intelligent surfaces (RIS), extremely large aperture arrays (ELAA), movable antennas (MA), and cell-free architectures will expand near-field dominance, creating a quasi-ubiquitous near-field propagation environment.

From the perspective of spatial resource utilization, while conventional far-field systems can only separate signals in the angular domain, the transition toward near-field operation enhances the capacity to exploit the depth domain in future wireless systems. Near-field technology, equipped with numerous antennas, has attracted increasing attention in 6G networks for its potential to provide higher data rates through beam focusing, precise angular-depth localization and sensing, as well as efficient wireless power transfer. Near-field research reveals a paradigm shift in understanding propagation characteristics of electromagnetic waves. These waves can no longer be simply regarded as plane waves but should be accurately modeled as spherical waves. This revised modeling emphasizes the importance of previously overlooked electromagnetic phenomena in system modeling and design. These phenomena include spatial non-stationarity, finite-depth beam focusing, tri-polarization, and evanescent waves. Beyond conventional wave modeling, near-field research unlocks access to novel wavefronts, such as non-diffracting beams (including self-healing Bessel beams and curved Airy beams). Traditional communication algorithms, tailored for far-field conditions, may underperform in 6G near-field environments, and model-agnostic algorithms might not fully capitalize on these new characteristics.

This white paper reviews typical application scenarios for near-field technologies in future wireless networks. It then delves into the fundamental electromagnetic principles underlying near-field effects and their disruptive impact on communication systems, systematically elucidating the constraints and enablers imposed on system architecture design—with a focus on the core metrics of degrees of freedom and capacity. Recognizing that channel characterization is foundational to communication system design, the paper provides a detailed discussion of near-field channel research paradigms from both measurement and modeling perspectives, and further explores key technologies such as channel estimation, beamforming, and codebook design. It prospectively examines the collaborative innovation between near-field technologies and other fields, including integrated sensing and communication, wireless power transfer, and physical layer security. At the engineering practice level, the latest advances in 6G spectrum allocation, the implementation of near-field propagation techniques, and network deployment strategies are highlighted. Additionally, standardization impacts of near-field technologies for 6G are also provided. This white paper aims to establish a unified cognitive framework for near-field technologies, bridging theoretical advances with standardization efforts and engineering implementation.

Table of Contents

List of Figure

1 Introduction

As the commercialization of 5G wireless networks gains momentum, there is a growing emphasis on exploratory research into the upcoming 6G wireless networks. This era of technological advancement witnesses 6G networks being characterized by a more visionary and performance-driven ethos compared to their predecessors. In June 2025, 3GPP will officially launch its 6G research project, marking the global evolution of 6G from a visionary stage toward a new phase characterized by critical technological development, standardization, and practical applications.

Traditional wireless networks, spanning from 1G to 5G, predominantly operate within a spectrum below 6 GHz, often below 3 GHz. Due to the physical constraints on antenna arrays and the proportional relationship between element spacing and wavelength, these spectrum bands necessitate the use of relatively small numbers of antennas. Consequently, the combined effect of these lower-dimensional antenna arrays and lower frequency bands confines the range of wireless near-field communication (NFC) to mere meters or even centimeters, thereby shaping the design of these systems around far-field assumptions.

However, the transition to 6G networks is marked by the adoption of larger antenna apertures and higher frequency bands, such as new mid-frequency, millimeter-wave (mmWave), and terahertz bands, which accentuate near-field characteristics[1][2], as shown in Table 1.1. The integration of emerging technologies such as Reconfigurable Intelligent Surface (RIS)[1][3][4], extremely large aperture arrays (ELAA)[5], movable antenna (MA)[6], and cell-free networks[7] is expected to amplify the prevalence of the near-field scenario in future wireless networks. Consequently, this shift challenges traditional far-field plane wave assumptions and underscores the need to rethink strategies for spatial resource utilization[8]. While conventional systems have effectively exploited far-field spatial resources, the exploration and utilization of near-field spatial resources in 6G networks promise to introduce novel physical dimensions to wireless communication systems [9]. This shift towards near-field regions in 6G networks catalyzes a new wave of research in near-field technology paradigms.

Table 1.1 Near field range of typical scenarios (Rayleigh distance)

D f	2.6 GHz (low band)	7 GHz (Mid band)	28 GHz (mmWave band)	220 GHz (THz band)
0.5m	**4 m**	12 m	48	372
1.6m	60 m	**119 m**	476	/
3.0m	210 m	420 m	/	/

In the realm of near-field technology, the nuanced propagation behaviors of electromagnetic waves necessitate a departure from plane wave approximations to embrace spherical wave treatments. This paradigm shift brings forth a plethora of hitherto overlooked electromagnetic phenomena, including spatial non-stationarity, tri-polarization, evanescent waves, and the capacity for near-field focusing, all of which pose challenges to the efficacy of traditional communication algorithms within the context of 6G's near-field environment.

Harnessing near-field effects holds the promise of facilitating the realization of a broader spectrum of application scenarios and key performance indicators outlined in IMT-2030. This white paper explores potential application scenarios based on near-field technology, as shown in Fig. 1.1.
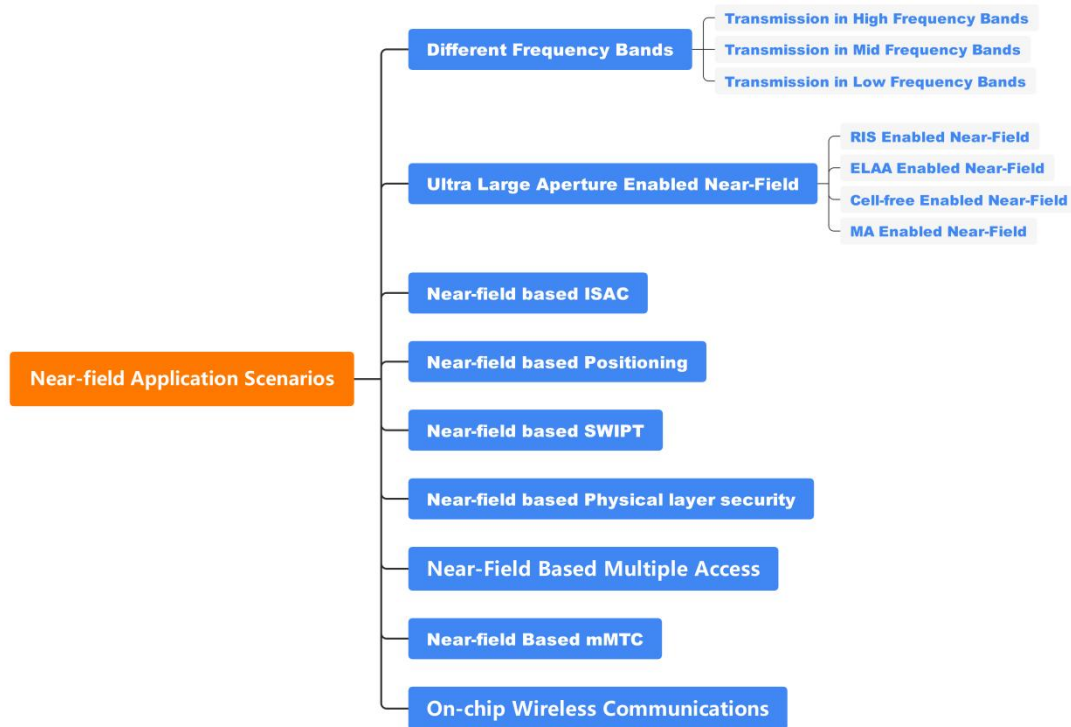
Fig. 1.1 Near-field Application Scenarios

Through meticulous examination of both theoretical foundations and technological advancements, we have crafted a preliminary framework for near-field technology, as illustrated in Fig. 1.2. Our discourse commences with an exploration of the definition of near-field in electromagnetic theory, tracing the origins of near-field electromagnetic effects and their ramifications on existing communication systems. Drawing upon an extensive body of literature, this article provides an encompassing synthesis of near-field effects on communication system design and performance, with particular emphasis on degrees of freedom and communication capacity.

A nuanced comprehension of near-field channel characteristics and models is pivotal for communication system design and evaluation. Thus, our article underscores the imperative for exhaustive channel measurements and precise channel characterization. Furthermore, we delve into near-field transmission technologies, encompassing facets such as channel estimation, beamforming, codebook design, beam training, multiple access technology, system architecture, deployment considerations, and implications for standardization. Then, we explore the convergence of near-field technology with other domains, including positioning, wireless power transfer (WPT), physical layer security, orbital angular momentum-based near-field, AI-driven communications, and near-field on-chip wireless communications. Additionally, we highlight progress in both engineering and standardization, covering the primary 6G spectrum allocation, enabling technologies for near-field propagation, and network deployment strategies.

Framework of Near-field Technology

- **Fundamental Theories**
  - Near-field Range Partitioning
    - Characterizing Near-Field and Far-Field Boundaries: Perspectives and Empirical Rules
    - A Method for Near-Field Classification
  - Near-field Electromagnetic Physical Effects
    - Near-field Electromagnetic Signal Model
    - Near-field Electromagnetic Effects
    - Near-field Beam Characteristics
  - Near-field Degree-of-freedom Theoretical Analysis
    - The number of degrees of freedom of the electromagnetic field
    - Degree of freedom and interference mitigation for Near-field sparse MIMO
  - Near-field Performance Analysis and Measurement
    - Near-field Performance Analysis
    - Electromagnetic Normalization of Near-Field Channel Matrix
    - Near-Field Measurement and Near-Field to Far-Field Transformation
- **Channel Measurement and Modeling**
  - Near-field Channel Measurement
  - Near-field Channel Simulation
  - Near-field Channel Modeling
  - Bridging the Gap between Near and Far-Field Models
- **Transmission Technologies**
  - Near-Field Channel Estimation
  - Near-Field Beamforming
  - Near-Field Codebook Design
  - Near-Field Beam Training
  - Near-Field Multiple Access
    - LDMA
    - NOMA
    - URA
  - Non-Coherent Communication Schemes
  - Deployment of Near-Field Communication System
- **Integration of Near-field Technology with Other Technologies**
  - Near-field Based Positioning
  - Near-Field Based ISAC
  - Near-Field Based SWIPT
  - Physical Layer Security in Near-Field
  - Near-Field Based OAM
  - Near-Field Based Intelligent Communication
  - Near-field On-chip Wireless Communications
  - Near-field and Material Sensing

Fig. 1.2 Framework of Near-field Technology

Despite notable advancements in the research on near-field propagation characteristics, a dearth of literature offers a systematic synthesis of near-field technology. Therefore, this article endeavors to bridge this gap by furnishing an all-encompassing summary of near-field technology's application scenarios, fundamental theories, channel measurement and modeling methodologies, transmission technologies, and integration with allied fields. This white paper aims to establish a unified cognitive framework for near-field technologies, bridging theoretical advances with standardization efforts and engineering implementation.

2 Near-field Application Scenarios

In November 2023, the International Telecommunication Union's 5D Working Group on Wireless Communications (ITU-R WP5D) released a framework and overall goal proposal for the development of IMT towards 2030 and beyond, proposing typical 6G scenarios and capability indicator systems, as shown in Fig. 2.1 [10][11]. 6G scenarios include immersive communication, ultra-large-scale connections, extremely high reliability and low latency, artificial intelligence and communication, integration of perception and communication, ubiquitous connections, etc. The key 6G capability indicators include 9 enhanced 5G capabilities and 6 new capability dimensions, including peak data rate, user experienced data rate, spectrum efficiency, regional traffic, connection density, mobility, latency, reliability, security privacy elasticity, coverage, sensing related indicators, AI-applicable indicators, sustainability and positioning [12]. 6G is expected to continue the efforts of 5G-Advanced in terms of continuously enhancing connection experiences for mobile users and enabling more vertical industries [13].
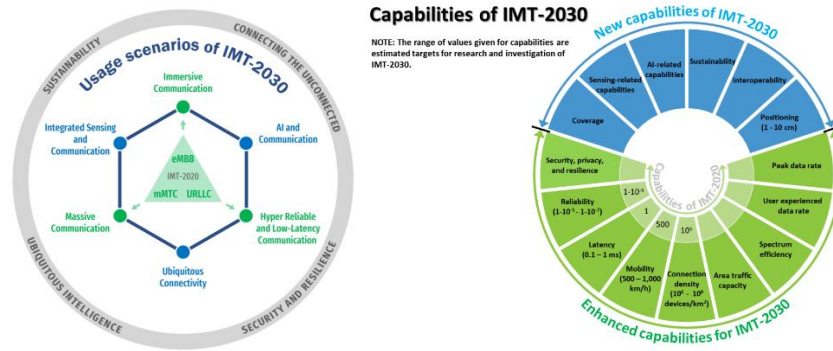
Fig. 2.1 IMT-2030 application scenarios and key capability indicators [10].

To meet the spectral efficiency requirements of IMT-2030, it is necessary to further explore the application potential of higher frequency bands and larger-scale arrays. Concurrently, the ultra large-scale-arrays in higher frequency bands will bring near-field effects. The so-called near-field effect refers to the situation where, under certain distance conditions, the assumption of electromagnetic waves as plane wavefront in the far-field no longer holds and needs to be modeled as spherical wavefront. The spherical wavefront carries not only angle information, but also depth information. Electromagnetic beam focusing occurs concurrently in both the angular and depth domains, forming near-field beam focusing [14]. By utilizing the near-field effect, more application scenarios and key performance indicators of IMT-2030 can be better achieved, such as integrated sensing and communication (ISAC), positioning, security, mobility, etc. This section will explain the application scenarios of near field based on the above analysis.

2.1 Near-field in Different Frequency Bands

The expansion of bandwidth and the increase of antennas will bring greater capacity and higher spectral efficiency to wireless communication systems. Typical 2G, 3G, 4G, and 5G communication systems use bandwidths of 0.2 MHz, 5 MHz, 20 MHz, and 100 MHz, respectively, and larger bandwidths will be required for 6G in the future.

In May 2023, China's Ministry of Industry and Information Technology (MIIT) issued a new version of the Regulations of the People's Republic of China on the Division of Radio Frequencies (MIIT Decree No. 62), which is the first in the world to use all or part of the bandwidth of the 6425-7125 MHz frequency band, totaling 700 MHz, for the 5G-A/6G system [15]. In December of the same year, the International Telecommunication Union (ITU) held the World Radiocommunication Conference 2023 (WRC-23) in Dubai, UAE, and completed a new round of revisions to the Radio Rules, newly dividing 6G spectrum resources in the mid-band of 6425-7125 MHz with a total of 700 MHz of bandwidth for most of the countries in the world [16]. In December 2023, the international standardization organization, 3GPP, held its Edinburgh, UK meeting, in which the first projects for Rel-19, the second version of the 5G-Advanced standard, including eight areas such as channel modeling studies for the new 7-24 GHz spectrum are established [17]. As reported in study of 6G mid band frequency by Nokia, a new spectrum ranges: 4.400–4.800 GHz, 7.125–8.400 GHz and 14.800–15.350 GHz are potentially available for 6G, subject to further study in the WRC-27 cycle [18]. The report also highlights about a US spectrum pipeline outside the WRC process concerning the lower 3 GHz band (3.100–3.450 GHz), which is being considered for shared use with military radar, and the 12.7 GHz band (12.700–13.250 GHz), which will be exclusively used for licensed mobile broadband.

Compared to the sub-6 GHz low-frequency band, which is widely used in 5G, and the high-frequency bands, such as millimeter wave and terahertz, which may be used in 6G in the future, the mid-frequency band, which combines the advantages of both coverage and capacity, is of great value for the wide-area high-capacity coverage of 6G, and it is expected to be one of the fundamental frequency bands for 6G, as shown in Fig. 2.2.
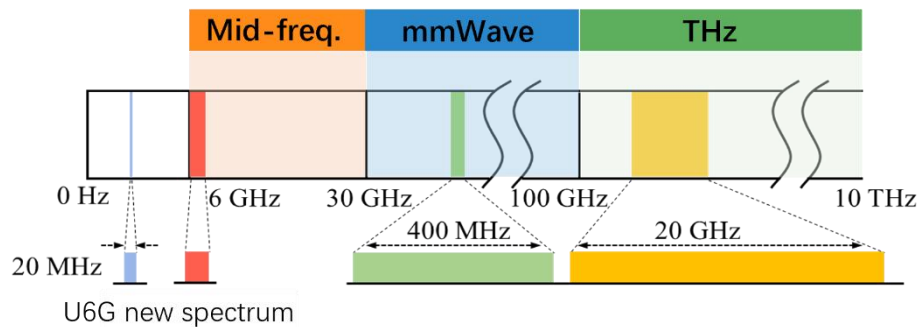
Fig. 2.2 Full spectrum of high, medium and low bands for the future 6G

In the future, 6G high, medium, and low frequency bands are likely to face near-field communication. 6G Technologies, a research report published by the 6G Alliance in June 2022, also clearly points out the necessity of researching near-field in 6G high, medium, and low frequency bands [18].

2.1.1 High Frequency Band Transmission

mmWave and terahertz (THz) wireless communication can utilize large available bandwidth to improve data transmission rates, making it one of the key technologies for the next generation of communication systems [19][20][21]. In order to compensate for the path loss of high-frequency transmission, base stations (BS) operating on these frequency bands will be equipped with large-scale antenna arrays. The application of large-scale antenna arrays will increase the possibility that the users in high-frequency communication falling into the near-field region, while traditional wireless systems typically operating in the far-field range. Under millimeter wave and terahertz conditions, the near-field

distance of relatively small antennas/surfaces can also reach several tens of meters. For example, the near-field distance of a uniform linear array with 128 antennas working at 300 GHz would be 65 meters, which covers a relatively large area. Namely, the far-field plane wave assumption on electromagnetic fields is no longer applicable at actual communications distances. Thus, a near-field model of spherical waves should be used. The management of spherical wavefront can be transformed into flexible beamforming ability. For example, utilizing the spherical wavefront can focus the electromagnetic waves into a spot rather than traditional beam steering under far-field condition, which is referred as the concept of beam focusing in recent literature[22]. Beam focusing can support multiple orthogonal links even at similar angles.

The ability to focus beams in large-scale multiple input multiple output (MIMO) systems largely depends on the signal processing capability of the antenna array, with different processing capabilities in different architectures. The most flexible solution for a given radiation element array is full-digital architecture, where each antenna element is connected to a dedicated radio frequency (RF) chain. Under this architecture, the transceiver can simultaneously control infinite beams in multiple directions, greatly improving spatial flexibility. However, when deploying large-scale arrays in 5G and more advanced communication systems, implementing full-digital architectures becomes extremely challenging due to increased costs and power consumption. To alleviate this, large-scale MIMO communications adopt a hybrid analog-digital architecture. This hybrid architecture combines low dimensional digital processing and high-dimensional analog precoding, typically achieved through phase shifter interconnections, resulting in fewer RF links than antenna components. Another emerging technology for effectively implementing large-scale arrays is dynamic meta-surface antennas, which can programmatically control the transmit/receive beam patterns, provide advanced analog signal processing capabilities, and naturally achieve frequency chain reduction without the use of dedicated analog circuits. This also densifies antenna components, thereby improving focusing performance. Reference[23] explores multi-user communications in near-field utilizing various antenna architectures, including all digital arrays, hybrid architectures based on phase shifters, and dynamic meta-surface antennas, as well as the impact on downlink multi-user systems when forming focused beams.
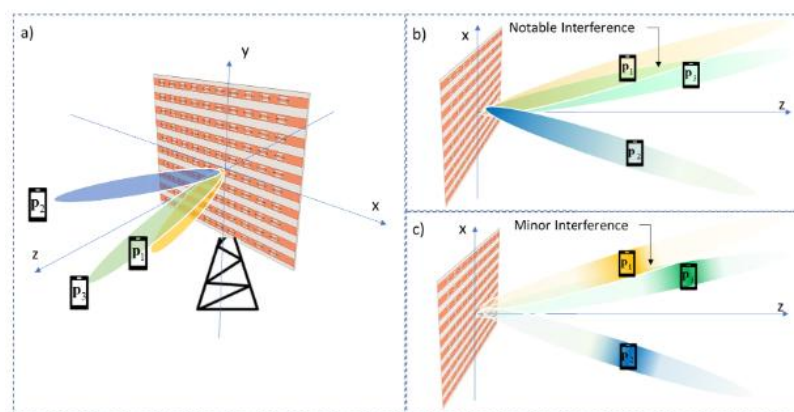
Fig. 2.3 Multi user near-field communication with beams pointing to each user
(a) towards each user in three-dimensional space; (b) beam steering in far-field, leads to interference between users at the same angle; (c) beam focusing in near-field, with minimal interference[23]

In addition, new types of wavefronts become available beyond spherical waves when operating in the near field[24]. By wavefront, we refer to the imaginary surface representing all points in a wave that are in the same phase at a given time. Among others, the use of Bessel beams has been recently

proposed[25][26]. Bessel beams are no-diverging beams that focus the signal along a line. To generate an ideal Bessel beam, one would need an infinite aperture (i.e., an infinite lens or antenna array or reflect-array). When using a finite aperture, the Bessel beam only exist until a maximum distance delimited in the near-field. Focusing the power along a line, instead than on a point, can drastically reduce the amount of channel state information (CSI) to ensure the reliable transmission of information. Moreover, Bessel beams are self-healing, i.e., even when they are partially blocked, the signal is regenerated to the original level after the obstacle [27][28]. This can be leveraged to overcome blockage, which is one of the main problems for high-frequency systems. Another type of non-conventional wavefronts that can be generated in the near field are Airy beams [29]. These are also non-diffracting beams that, in this case, focus along a curving line. This allows for example to circumvent obstacles (See Fig. 2.4).
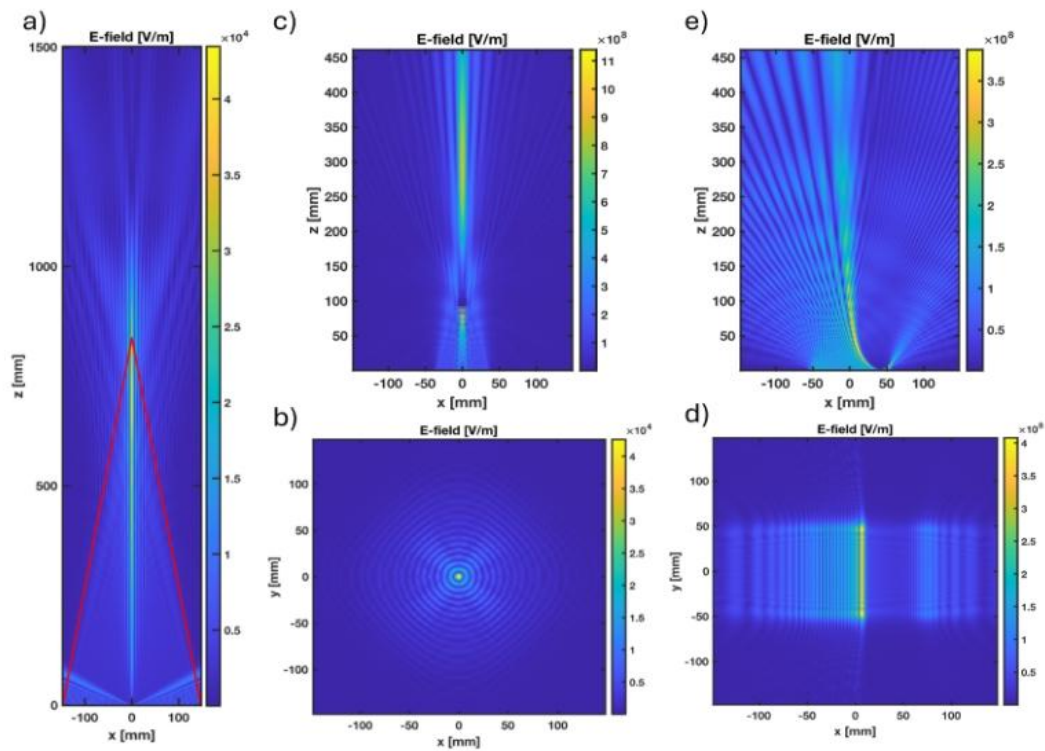
Fig. 2.4 Non-diffracting beams to circumvent obstacles
a) Illustration of a Bessel beam, focusing a long a line in the near field; b) Phase distribution of a Bessel beam; c) Bessel beam regeneration after an obstacle; d) Phase distribution of an Airy beam; e) A curving Airy beam.

Traditionally, Bessel beams and Airy beams have been generated at optical frequencies and utilizing different types of lenses. For example, axicons are utilized to generate Bessel beams. Nevertheless, these wavefronts can be generated utilizing arrays, reflect-arrays and meta-surfaces[30] with a large number of elements[31][32] at least phase control per element. Operating with new types of wavefronts drastically changes many well-known concepts [33], including the study of interference across different type of beams, CSI estimation, joint ultrabroadband waveform and wavefront design [31], and even physical layer security[34].

2.1.2 Mid Frequency Band Transmission

In September 2020, 3GPP completed the approval of the 6 GHz licensed frequency band, initiated the standardization of mid frequency band RF. Then, 3GPP successfully completed the standardization of the 6425-7125 MHz licensed frequency band in September 2022. Subsequently in December 2023, 3GPP further listed channel modeling in the 7-24 GHz mid frequency band as one of the earliest standard topics in the second standard version of 5G-Advance, continuing promoting the standardization process of the mid frequency band. At the same time, in May 2023, the Ministry of Industry and Information Technology of China issued a new version of the "Regulations on the Classification of Radio Frequency in the People's Republic of China", which clearly divides the 6 GHz mid frequency band for 5G/6G mobile communication systems. The 6 GHz frequency band has a continuous large bandwidth of 1200 MHz, which has lower propagation path loss and stronger coverage ability compared to the high-frequency band. It has both coverage and capacity advantages and can be used for wide area high-capacity coverage in 6G communication. Therefore, the mid frequency spectrum resources will become one of the important alternative frequency bands for 6G communication.

Compared to the sub-6 GHz frequency band of 5G communication, the increase in communication frequency leads to weaker coverage due to large propagation losses in materials and smaller antennas in mid frequency centimeter wave communication. In order to compensate for the high path loss during the propagation of intermediate frequency signals, the antenna size of intermediate frequency BSs needs to be further increased. With the increase of communication frequency band and BS antenna array aperture, the near-field range of intermediate frequency communication will also be significantly expanded. Taking the 7 GHz communication system and BS with 1.6-meter antenna array as an example, its near-field range exceeds 100 meters. In the formal project of the 3GPP intermediate frequency channel modeling standard, near-field characteristics and spatial non-stationary characteristics are considered as new characteristics of mid frequency channels, becoming important considerations for improving the 3GPP channel model [17]. Therefore, near-field spherical wave communication will become an important scenario for mid frequency transmission.

Due to the shorter wavelength of mid frequency centimeter waves and the further increase in antenna size, mid frequency system is more likely to form high-resolution narrow spatial beams, therefore achieving higher spatial degrees of freedom. Typical application scenarios for this band include single user multi-stream or higher-order multi-user multiplexing scenarios. The modeling and measurement of near-field spherical wave channels in the mid frequency range will provide a channel model foundation for mid frequency communication. The near-field spherical wave propagation model is expected to provide additional single user transmission spatial freedom. The focusing characteristics of near-field spherical waves can also be used for high-order multi-user multiplexing methods, further improving the throughput performance of 6G new mid frequency communication systems.
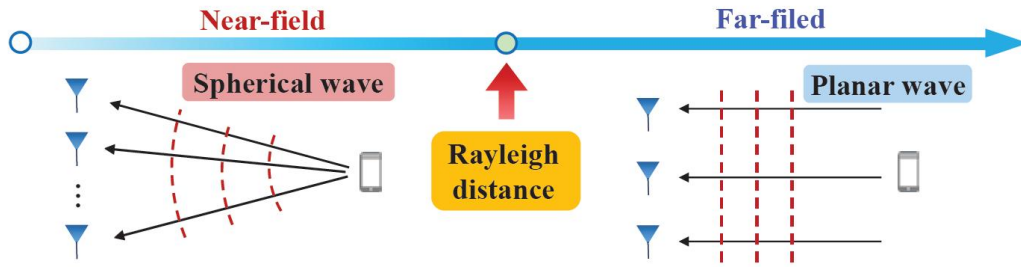
Fig. 2.5 An illustration for near field communication feature
For users located in the near field region, spherical wavefronts are utilized for communication
compared to plane wavefronts in the far field region.[35]

2.1.3 Low Frequency Band Transmission

The low frequency band (FR1, Sub-6GHz) defines the baseline coverage range of cellular networks. While expanding to higher frequency bands, 6G will also fully utilize the advantages of FR1 frequency band for wide coverage and deep penetration to improve spectrum efficiency and break through bandwidth bottlenecks. Large scale MIMO can be used in the low frequency range to improve the spectral and energy efficiency of 6G systems while ensuring wide coverage.

If traditional large-scale MIMO is deployed in the low frequency range, it will face limitations on antenna size due to tower or BS deployment. Modular or distributed large-scale MIMO, as well as meta-surface antennas, are expected to overcome size limitations and reduce the requirement of half wavelength distance between antenna units through compact antenna arrays. On the other hand, traditional cell-based deployment strategies pose challenges such as feasibility, processing, and architectural complexity. Therefore, large-scale MIMO in the low frequency range may adopt multi panel, multi transceiver nodes, non-cellular, and irregular large-scale distributed network deployment. In this scenario, further research is needed on distributed deployment strategies, the potential demand for new channel models from non-uniform antenna panels, large antenna arrays, and near-field effects when users may approach access points. Also, research that focuses on exploring efficient reference signal designs, channel acquisition frameworks for far-field and near-field channels, further evaluating the potential of artificial intelligence in channel acquisition would be valuable.

2.2 Ultra Large Aperture Enabled Near-field

2.2.1 RIS Enabled Near-field

RIS is considered as one of the key potential technologies in 6G, consisting of a large number of low-cost reconfigurable units [36]. Deploying RIS in wireless networks can effectively adjust the wireless channel between transmitters and receivers, thereby improving communication quality and coverage range, as already demonstrated by field trials [37]. One of the typical applications of RIS technology is to obtain sufficient beamforming gain through hundreds or even thousands of components for coverage blinding in millimeter wave and terahertz communications. The larger RIS array and higher operating frequency further expand the near-field area of RIS assisted communication links [38]. RIS is typically used to establish a direct connection channel between transmitters/receivers. In the far-field region, the rank of the channel is usually small, which restricts the spatial multiplexing gain of the channel. On the other hand, due to the nonlinear changes in signal amplitude and phase caused by spherical waves, near-field channels have better rank conditions, which can effectively

improve the multiplexing gain and spatial freedom of the system [39]. When users are located in the radiation near-field region, even if multiple users are at the same radiation angle, different near-field codebooks can be configured on the intelligent meta-surface to reduce co-channel interference through beam focusing, supporting multiple coexisting orthogonal links to achieve space division multiple access [40], as shown in Fig. 2.6. Similarly, the degrees of freedom provided by the spherical wavefront and the near-field radiation wave carrying both angle and distance information further enhances the accuracy of wireless positioning services and perception, as shown in Fig. 2.7 . On the other hand, this also means that the spatial non-stationarity of the channel is intensified, which will bring challenges to channel estimation, codebook design, beam training complexity, mobility management, signaling design, and other aspects.
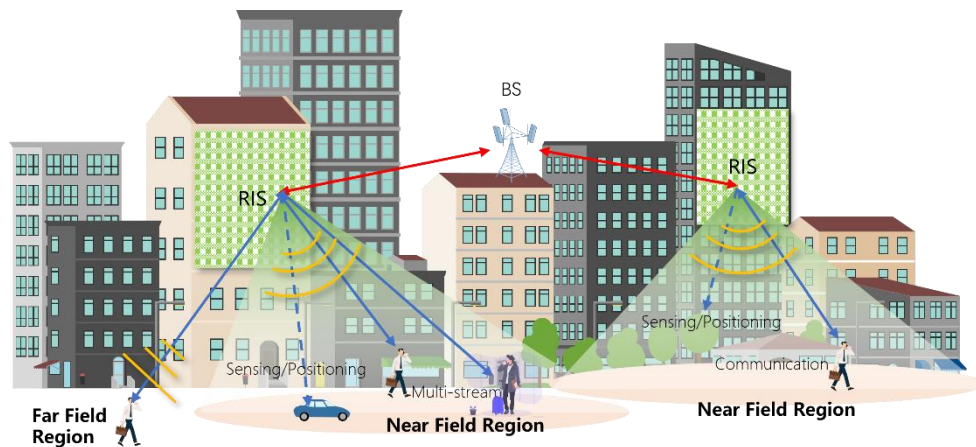
Fig. 2.6 RIS assisted near-field application scenarios.
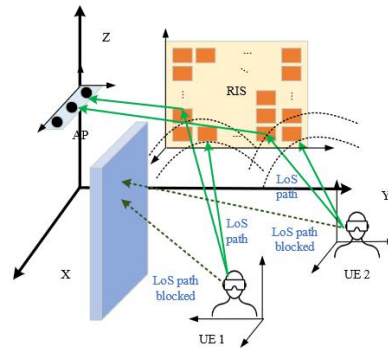
Fig. 2.7 Near field positioning model[41]

2.2.2 ELAA Enabled Near-field

ELAA is essential to the candidate technologies for 6G such as Extremely Large-Scale MIMO (XL-MIMO). Compared to 5G massive MIMO, ELAA for 6G not only means a sharp increase in the number of antennas but also results in a fundamental change of the electromagnetic (EM) characteristics. With the significant increase of the antenna number and carrier frequency in future 6G systems, the near-field region of ELAA will expand by orders of magnitude. The two commonly used ELAA architectures are co-located and distributed ELAAs, as shown in Fig. 2.8 (a) and (b). The antenna elements of co-located ELAA are typically separated by half wavelength, and its physical dimension is limited by the continuous platform [42]. By contrast, distributed ELAA is an architecture that antennas are widely distributed over a vast geographical region with multiple separated sites,

which are interconnected by the backhaul/fronthaul links, so as to perform joint signal processing. However, distributed ELAA, e.g., cell-free ELAA, usually requires the sophisticated site coordination and high backhaul/fronthaul capacity.

In order to complement for existing ELAA architectures, the works [43][44] propose a novel modular ELAA architecture. As illustrated in Fig. 2.8(c), the antenna elements of modular ELAA are regularly mounted on a shared platform in a modular manner. Each module is comprised of a moderate/flexible number of array antennas with the inter-element distance typically in the order of the signal wavelength, while different modules are separated by the relatively large inter-module distance, so as to enable conformal capability with the deployment structure in practice. For example, the modular ELAA with interlaced modules can be embedded into the discontinuous wall spaced by windows, like facade circumstances of shopping malls, factories or office buildings. Compared to co-located ELAA with the same number of antenna elements, modular ELAA not only has the characteristic of flexible deployment, but also a higher spatial resolution due to the larger physical dimension. However, since the inter-module distance is much larger than half wavelength, modular ELAA will lead to the undesired grating lobes. On the other hand, different from the distributed ELAA architecture, modular ELAA typically performs joint signal processing, without having to exchange or coordinate sophisticated inter-site information, which may ease the requirement of synchronization and reduce hardware cost associated with the backhaul/fronthaul links for distributed ELAA.

Uniform sparse ELAA is array architecture where the inter-element spacing is larger than half-wavelength, as illustrated in Fig. 2.8 (d), which is a special case of modular ELAA. In general, uniform sparse ELAA results in a narrower main lobe due to the higher spatial resolution, which can provide a significant interference suppression gain in scenarios with densely located users [45]. Similar to modular ELAA, uniform sparse ELAA gives rise to the undesired grating lobes, due to the inter-element spacing much larger than half wavelength.

It is worth mentioning that the above four array architectures are suitable for different application scenarios. For example, co-located, modular and uniform sparse ELAAs can all be used to support cellular hotspot communications, while modular and uniform sparse ELAAs achieve a higher transmission rate in scenarios with densely located users. Besides, distributed ELAA is able to provide a better communication service for geographically widely distributed users. Thus, the above four architectures complement each other, and the choice of appropriate ELAA architecture depends on the actual application scenario.
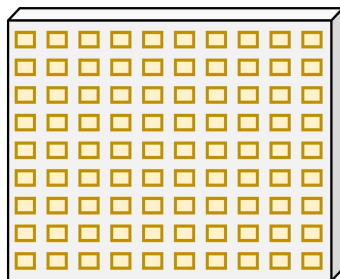
(a) co-located ELAA   (b) Distributed ELAA
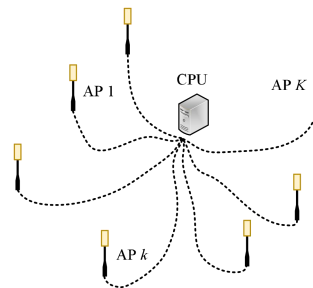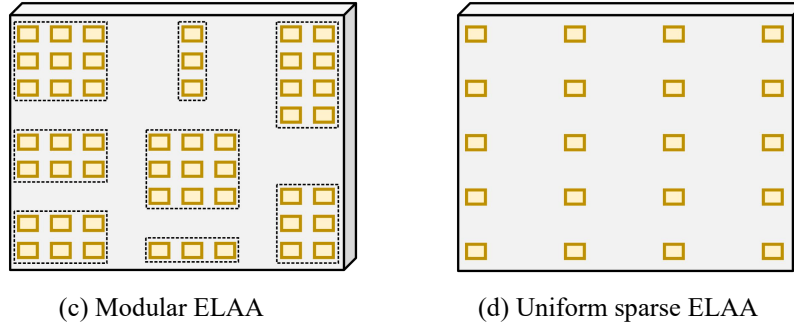
(c) Modular ELAA   (d) Uniform sparse ELAA
Fig. 2.8 Different architectures of ELAA [42]

2.2.3 Cell-Free Enabled Near-field

Unlike the classic cellular communication architecture, the Cell-Free communication architecture achieves a user centered communication paradigm by deploying a large number of access nodes in a distributed manner, effectively overcoming inter cell interference, avoiding communication interruptions, and further improving the performance of next-generation 6G mobile communication. Based on the Cell-Free communication architecture, the equivalent array aperture is significantly expanded due to the distributed deployment of multiple arrays, and the near-field spherical wave effect is more significant. Meanwhile, due to the denser distribution of access nodes and shorter communication distances, users will have a higher probability of being in the near-field range. In addition, due to the collaborative nature of non-cellular communication architectures, users may be served simultaneously by multiple access nodes with different antenna sizes and distances, which may be located in the far-field or near-field range of different nodes, facing more complex mixed far-field and near-field communication scenarios. Therefore, cellular free near-field communication will be one of the important application scenarios for future 6G.

The modeling of near-field spherical wave channels can provide a model foundation for cellular free communication systems. Due to its significant near-field spherical wave effect, considering the near-field spherical wave property can further improve the optimization accuracy of access nodes in cellular free architectures. At the same time, beamforming methods that are compatible with near-field spherical waves and far-field plane waves, efficient far-field cellular free communication channel estimation, and beam training schemes can better adapt to near-field communication scenarios, further improving the performance of cellular free communication systems.

2.2.4 MA Enabled Near-Field Communication and Sensing

Movable antenna (MA) technology has recently been introduced in wireless communication systems to control the movement of antennas at the Tx/Rx for improving wireless channel conditions and communication performance [6]. There are various practical methods that can be used to enable antenna movement, such as mechanical motors, microelectromechanical system (MEMS), liquid/fluid antennas, deployable structures, etc [46]. Due to their flexible movement capability, MAs can fully exploit the wireless channel spatial variation. For example, they can significantly enhance the spatial diversity performance, in terms of receiver signal power improvement and interference mitigation, as compared to conventional fixed antennas [47]-[49]. Besides, for multi-MA aided MIMO and/or multiuser communication systems, the channel matrices can be reshaped by antenna position optimization to increase the spatial multiplexing gain and thus the wireless channel capacity [50][51].

In addition, the exploiting of 3D position and 3D rotation can achieve the highest degrees of freedom (DoFs) in antenna movement for enhancing wireless communication performance, which renders the design of six-dimensional movable antenna (6DMA) systems [52]-[54]. Moreover, by integrating multiple MAs into an array, more flexible beamforming can be realized by jointly designing the array geometry and beamforming vector [55][56]. Since the effective array aperture scales with the size of the antenna moving region, enlarging the antenna moving region expands the near-field region of the Tx/Rx for communication as well as sensing [57]-[59], as shown in Fig. 2.9.
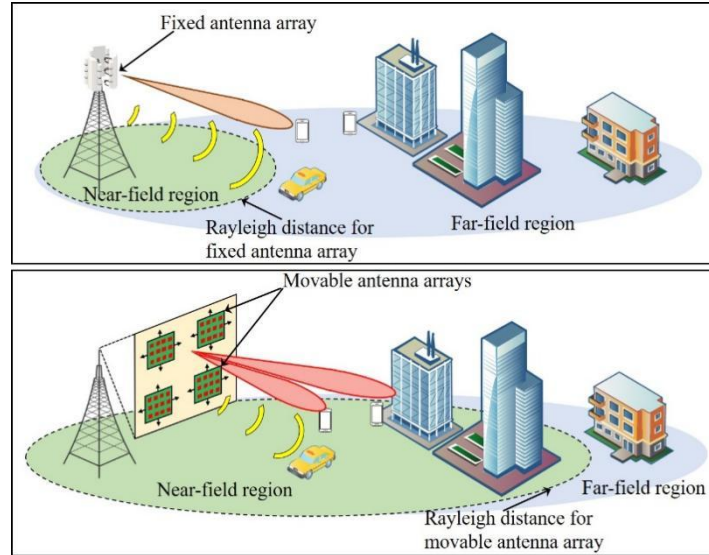
Fig. 2.9 MA for near-field communications and sensing

Different from the ELAA which requires an extremely large number of antenna elements and RF frontends, the number of MAs is moderate and can be kept constant even with the increasing moving region size. Thus, MAs can help reduce the hardware cost and RF power consumption as compared to ELAA. The performance advantages of MA systems, such as higher spatial diversity, enhanced multiplexing gain, and more flexible beamforming, become more appealing in 6G near-field communications because the spherical wave-based model renders more substantial channel variation in the spatial domain [57]-[59]. Furthermore, distributed MAs can be seamlessly integrated into cell-free communication systems, providing additional DoFs in antenna position and/or rotation for improving the performance of 6G networks. In wireless sensing and ISAC applications for 6G, the MA systems can effectively enlarge the antenna aperture such that the angular/ranging accuracy is increased manifoldly. For sufficiently large antenna moving regions, the MA-aided systems can realize super-resolution for near-field sensing. In summary, MAs opened up a new direction for research and engineering practice in 6G near-field communication and/or sensing. More collective efforts in theoretical research, technical exploration, system design, experimental verification, and standardization activities are required to unleash the full potential of MAs in future 6G networks.

2.3 Integrated Sensing and Communication

In addition to high-capacity communication, the next generation of wireless networks also has the potential to achieve high-precision perception. Therefore, the ISAC technology has also attracted widespread research interest in academia and industry [60]. Compared with traditional wireless positioning and channel estimation, wireless perception relies on the echo signal reflected by passive

targets, rather than the pilot signal sent by active devices. Currently, many existing modulation waveforms have been proven to be applicable to wireless sensing, such as orthogonal frequency division multiplexing (OFDM) and orthogonal time frequency space (OTFS), indicating that sensing functions can be seamlessly integrated into existing wireless communication networks [61][62]. Besides, novel dual-functional waveform design strategies have been developed to balance the communication and sensing performances under different application scenarios, e.g., ISAC at mmWave/THz frequencies or communication/sensing-centric ISAC services.

In far-field sensing, increasing the size of the antenna array often only improves the resolution of angle estimation, while the resolution of distance and velocity mainly depends on signal bandwidth and perception duration. However, in the near-field region, the propagation of spherical waves allows large-scale antenna arrays able to estimate the distance and movement speed between objects. On the one hand, even within a limited bandwidth, near-field channels can still effectively contain distance information, improving the resolution of distance estimation in narrowband systems. On the other hand, the estimation of target velocity depends on the estimation of Doppler frequency. Compared with far-field sensing, near-field sensing may have significantly different Doppler frequencies when observing two antennas in a large-scale antenna array from different directions, which can enhance the estimation of object movement speed [40][63], as shown in Fig. 2.10 Based on the above discussion, near-field effects have the potential to promote high-precision perception in situations where time-frequency resources are limited. Therefore, near-field synesthesia integration is a highly promising technology. A recent survey on the opportunities and challenges of ISAC in the near field can be found in [64].
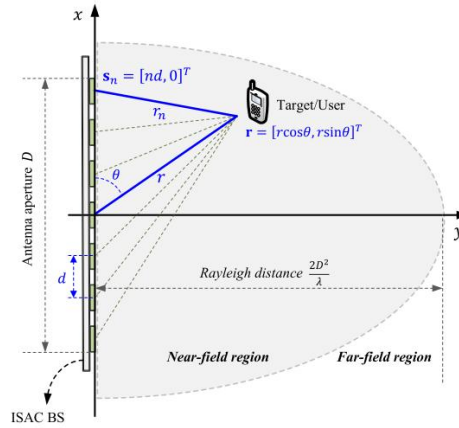
Fig. 2.10 Near field ISAC system[40]

2.4 Wireless Positioning

In traditional far-field communication systems, the angle and distance information of the target relative to the receiving point is mainly obtained by estimating the arrival angle and time of the signal at the target based on the assumption of plane waves [65]. The far-field communication system needs to deploy multiple receiving points as positioning anchors to estimate the three-dimensional coordinates of the target based on the angle and distance information of multiple anchors. In order to obtain more accurate angle and distance information, far-field communication systems usually need to configure measurement signals with larger bandwidth. In addition to the use of distance and angle, the

use of the characteristics of the received signal as a fingerprint for localization is also a common method of localization and has been studied in far-field communications [66]. In the near field, based on the spherical wave model, the arrival angles of signals from antenna units in different regions of the antenna array at the target are different. By utilizing the signal transmission characteristics of beam convergence, near-field communication systems locate targets through the differences in channel angles in different areas of the antenna array, thereby reducing the demand for measurement signal bandwidth [66]. Meanwhile, the deployment of large-scale antenna arrays is beneficial for further enhancing angular resolution and providing additional distance resolution in the near-field region, which is conducive to achieving high-precision positioning in 6G mobile communication [67].
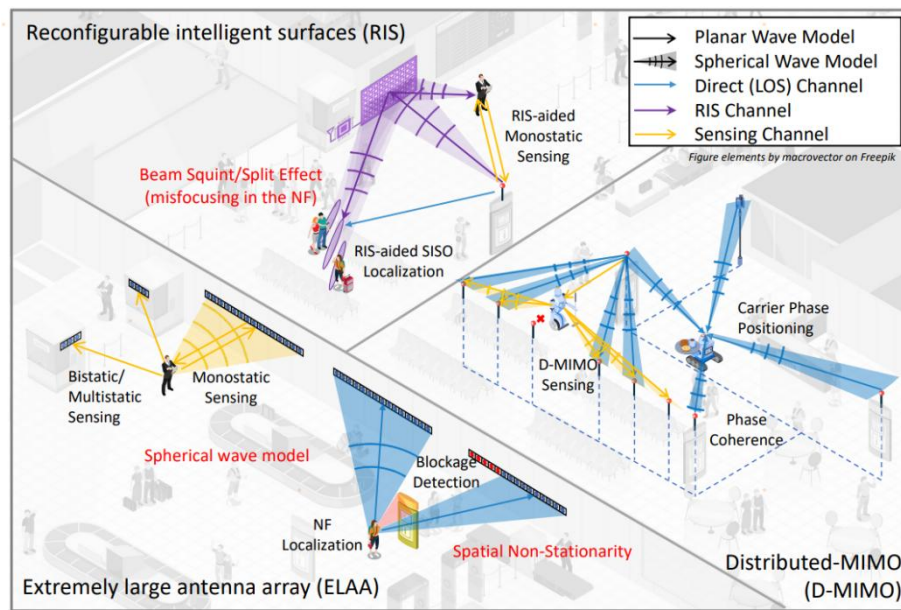
Fig. 2.11 High precision positioning based on near-field effects
High precision positioning services can be provided in the near-field through various forms such as ELAA, RIS, and distributed MIMO (D-MIMO).

The positioning process of near-field communication systems is different from traditional far-field communication systems in terms of signal system, channel model, and positioning principle. The two belong to heterogeneous positioning networks. Therefore, heterogeneous positioning network fusion algorithms are needed between far-field and near-field communication systems to ensure seamless positioning services [69][70]. The fusion of heterogeneous positioning networks relies on the implementation of positioning accuracy estimation algorithms [71][72]. For regional positioning systems, including near-field communication systems, positioning accuracy algorithms can evolve into availability estimation [73] to support two different modes of interoperability between heterogeneous positioning systems: "soft fusion" and "hard switching" [74].
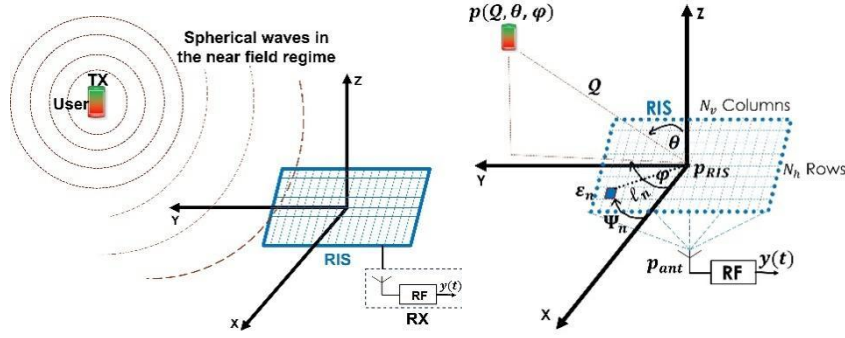
Fig. 2.12 RIS enabled near-field localization: (a). System Setup (b). Coordinate System

In the field of wireless communication networks, radiolocation technology, as a viable alternative to obtain user location data in environments where GPS signals are unavailable, not only improves the communication speed, but also enhances the positioning accuracy with each generation of mobile communication technology. In 4G systems, the user estimates the distance to each BS from the time-of-arrival (ToA), and the location is determined by using at least four Line-of-Sight (LoS) BSs of the TDoA measurements to determine the 3D position. In 5G systems, both the BS and the user device are equipped with multiple antennas that can simultaneously take into account the delay and angle of the signal propagation, improving the positioning accuracy and making it possible to efficiently locate the device using only one BS.

With the growth of applications such as smart factories, autonomous driving, and augmented reality, there is an increasing demand for higher positioning accuracy in 5G and 6G networks. 5G's wide bandwidth and large antenna arrays further enhance positioning accuracy. However, when 5G and 6G systems operate in the high frequency mmWave and THz bands, the connections between devices are susceptible to obstacles propagation is critical for accurate position estimation, and existing positioning methods will generate significant estimation errors if the LoS link is obstructed.

RIS provides reliable and highly accurate location estimation capability at low cost and with high energy efficiency[75]-[77]. When the LoS link is obstructed, the RIS can establish a virtual LoS link and perform accurate delay measurements using broadband signals[78]. Unlike non-reconfigurable scatterers in conventional environments, RIS can adjust the phase offset of its reflective units, resulting in significant beamforming gains. In addition, RIS has many elements that contribute to the resolution during positioning, enhancing the AoA for uplink or AoD positioning resolution for downlink[79].

For communication and positioning applications involving RIS, accurate and well-defined RIS phase control is essential. This requires the development of appropriate RIS phase control models that consider multiple factors such as mutual coupling[80][81], calibration[82], quantization and power loss per element[83]. Most of the existing studies have focused on ideal phase shifters, ignoring the effects, which are crucial for the effectiveness and reliability of RIS-based positioning methods[84][85].

There are two main modes of RIS-based localization techniques: receiving mode [85] and reflecting mode[86][87]. In the receiving mode, a large smart surface is used to determine the position of the user in front of it for both near-field and far-field scenarios. In reflection mode, the received signal strength (RSS) at different points is enhanced by adjusting the RIS reflection coefficients to improve the positioning accuracy[86]. However, these models may not be accurate enough when dealing with large surfaces and arrays, especially when the mobile device is in the Fresnel region instead of the Fraunhofer region. In the Fresnel region, the wavefront curvature is significant and

cannot be approximated as a plane wave, and ignoring the spherical wavefront misses critical information about the position and orientation of the mobile device.

Under the spherical wavefront channel model, [87] investigated 3D localization using a simplified RIS lens design to solve the RIS-assisted geometric near-field localization problem in the presence of LoS blocking and presented a Fisher information analysis and a closed form expression for the Fisher information matrix (FIM), showing the dependence of the position error bound (PEB) on the RIS phase profile. Three RIS phase profiles (random, directional and positional configurations) are used to demonstrate the role of RIS in near-field regional localization and communication. These profiles consider the magnitude and phase response of the RIS, using a realistic phase-dependent magnitude model. The random profiles provide a uniform signal-to-noise ratio (SNR) over the deployment area, while the directional and positional profiles increase the SNR near the user's location.

2.5 Simultaneous Wireless Information and Power Transfer

In near-field communication, a highly directional point beam can be achieved, which concentrates the target area of the beam near the target device, thereby concentrating the energy of the RF signal to the energy collection node of the Internet of Thing (IoT) devices. By utilizing the large number of antennas and high-precision position information, the efficiency of wireless energy transmission can be significantly improved, reducing energy waste during the transmission process. The near-field beam focusing characteristics limit the spread of energy to undesired location, but does not affect the efficiency on its own. In indoor scenarios or scenarios where the size of BS antennas is limited, wireless communication systems can use intelligent meta-surfaces to construct near-field channels and gather signal energy from home BSs to energy harvesting nodes. In addition, in the near-field communication system, the super large antenna array can obtain higher spatial resolution in the near-field range based on the wireless channel of spherical wave model, so that the BS can support higher density simultaneous wireless information and power transfer (SWIPT) terminals. SWIPT allows devices to harvest energy from RF waves and convert it to electrical energy, storing that energy into the device's battery, maximizing the device's lifespan and representing a new solution to limited energy[88][89].
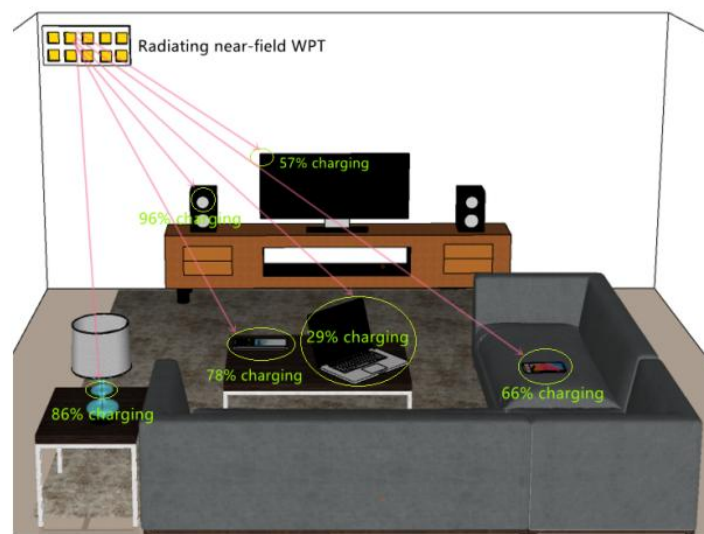
Fig. 2.13 Schematic diagram of near-field wireless energy transmission

2.6 Physical Layer Security

Due to the natural broadcasting and mobile characteristics of wireless communication, the communication of legitimate users in the network is easily eavesdropped and attacked by illegal users, and secure transmission has always been an important issue in wireless communication. In far-field communication, if the eavesdropper is in the same direction as the legitimate user, especially when the eavesdropper is closer to the BS, secure transmission will be difficult to achieve. Unlike the directional focusing of beamforming in far-field communication, in near-field communication assisted by ultra large arrays, the beams formed by BSs have strong positional focusing [90]. This property allows the energy of the transmitted signal to concentrate at the location of legitimate users rather than just in their direction, effectively reducing information leakage at the location of eavesdropping users and improving the system's secure channel capacity. By optimizing the beam focusing design of the BS, the potential of near-field communication in enhancing physical layer security can be fully explored.
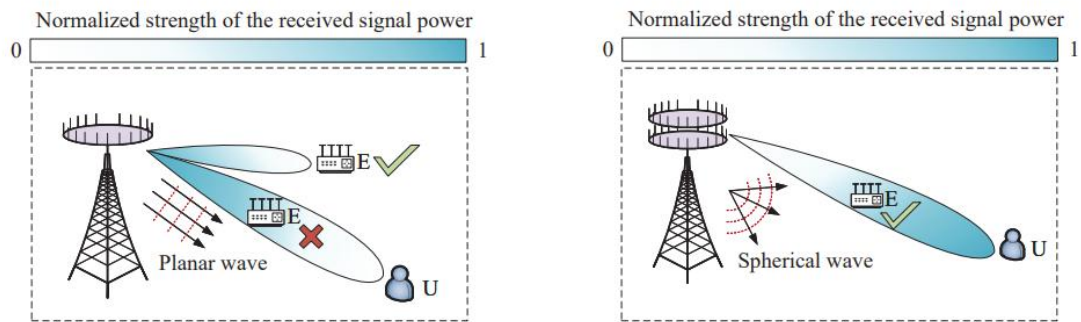
Fig. 2.14 Left: Far field secure communication using beam steering. Right: Near field secure communication using beam focusing.

2.7 Multiple Access

Multiple access technologies leverage time, frequency, code, and space domains in order to achieve the efficient utilization of transmission resources, which is the key to improving the transmission rate of the next-generation wireless network. In the current 5G massive MIMO system, spatial division multiple access (SDMA) utilizes orthogonal resources in the angular domain to distinguish different users; non-orthogonal multiple access (NOMA) further allows multiple users to reuse the same resource block and mitigate the inter-user interference through the power or code domain; unsourced random access introduces a competition mechanism of access resources (such as codewords), which saves the resource overhead intended for random access with short data packages in the scenario of massive machine-type communications (mMTC).

Compared with the far-field transmission model applied in multiple access technologies such as SDMA, the near-field transmission model reveals the two-dimensional beam focusing characteristics in the angle-distance domain and yields a larger spatial degree of freedom (DoF), indicating a great increase in available spatial resources. Therefore, integrating near-field characteristics into the design of multi-access technologies would be more conducive to serving the access requirements of massive users and further improving the system spectrum efficiency.
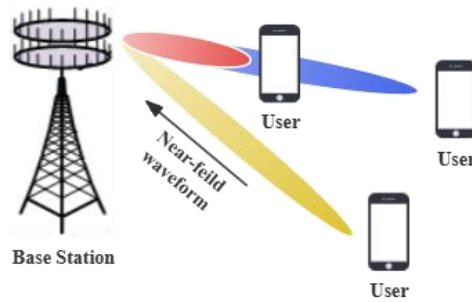
Fig. 2.15 Schematic diagram of near-field multiple access

2.8　Massive IoT Communications

Massive IoT communications refer to the networking infrastructure and protocols required to support the connectivity needs of a large number of IoT devices. These devices typically generate and transmit small amounts of data intermittently, often with low power consumption requirements. In such a scenario, massive control type interactions are the dominant communication scenario. These control type communications are mostly with short packet that is even shorter than the signaling data length, but of a massive number. The communication infrastructure must be capable of supporting a massive number of IoT devices, potentially numbering in the millions or even billions. This requires scalable network architectures, protocols, and management systems that can efficiently handle the increased traffic and device density. On the other hand, some high concurrent communications might happen with even faster transmission speed requirements, for instance, while working together to deliver a real-time industrial situation awareness to the control center in the industrial IoT applications. By addressing these requirements, communication infrastructure needs to effectively support the connectivity needs of massive IoT deployments, enabling a wide range of applications and unlocking the full potential of IoT technology.

ELAA-based Near-field technology is a potential player for massive IoT communications in 6G, especially for the massive connectivity and high-speed concurrent communication requirements. By incorporating the ELAA, the BS can connect more IoT devices within the range of the Rayleigh distance. Moreover, the ELAA system working on the near-field range will be an ideal solution to the high-speed concurrent communications. According to a prior study [91], arbitrary signal to noise ratio (SNR) can be achieved simply by increasing the transceiver number, which yields faster transmission speed while deployed.

2.9　On-chip Wireless Communications

On-chip Wireless Communications refers to the utilization of on-chip antennas or near-field coupling, among other wireless interconnect methods, to facilitate data exchange and wireless communication between different modules within or among chips. The transmission distance of on-chip wireless communication typically falls below 1cm, offering advantages such as low loss, high transmission rates, and high integration. The applications of on-chip communication are widespread, notably in the IoT domain, enabling seamless interconnection among smart chips, devices, and wearables, thereby significantly enhancing communication efficiency and reducing wiring complexity.

However, this technology faces limitations including increased chip area costs, security and privacy concerns, and increased power consumption. Nevertheless, as the operating frequency rises to the mmWave/THz frequency bands, the size of on-chip antennas significantly reduces, leading to a substantial decrease in chip area [92][93] Moreover, the proximity between transceiver chips reduces, thereby relaxing the signal power requirements for wireless communication. Additionally, the high frequency signals exhibit good directionality, enhancing the security and reliability of information transmission. These factors substantially alleviate the design complexity of on-chip wireless communication systems[94].

Simultaneously, compared to traditional wired communication method between chips, utilizing wireless communication can avoid the drawbacks introduced by transmission lines, such as high latency, high crosstalk, limited bandwidth, and parasitic effects. As illustrated in Fig. 2.16, by integrating on-chip antennas into the chip, the signal transmission mode shifts from traditional wired transmission to on-chip and inter-chip wireless communication, forming a flexible architecture of on-chip networks, thereby avoiding the limitations of wired interconnection layouts[95].
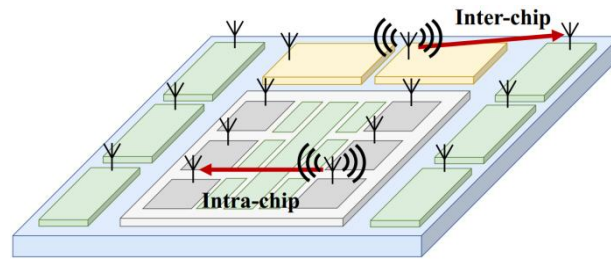
Fig. 2.16 Utilizing on-chip and inter-chip communication with antennas

Additionally, on-chip wireless communication plays a significant role in signal transmission between different system-level chiplets. As illustrated in Fig. 2.17, when forming a System-on-a-Chip (SoC) through heterogeneous integration, the difficulty of high-frequency interconnection between chiplets arises due to different structures and semiconductor materials. Traditional wire bonding methods severely degrade signal integrity. By utilizing on-chip wireless communication, high-speed, high-bandwidth heterogeneous integration between chiplets can be achieved, effectively enhancing the versatility of large-scale heterogeneous systems[96].
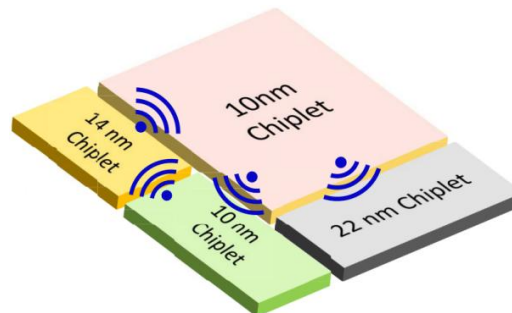
Fig. 2.17 Wireless interconnection between chips with different semiconductor materials

Furthermore, as on-chip wireless communication exploits the radiation effects of on-chip antennas or near-field coupling, it is no longer constrained by the one-to-one data transmission mode of traditional wired interconnection. In terms of data transmission, it offers higher flexibility and adaptability, enabling one-to-many transmission to support high-density device connections and data

exchanges among massive devices, thus providing more feasibility for the design of single-chip multi-core processors, as illustrated in Fig. 2.18 [97].
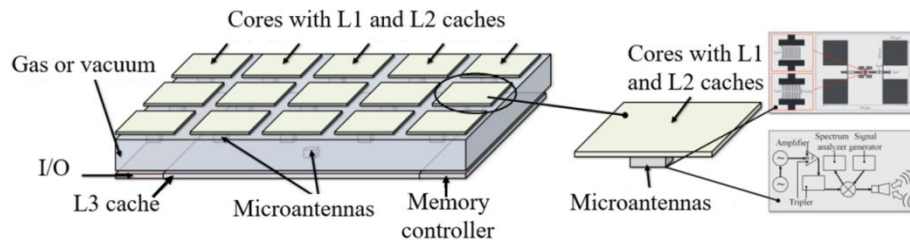
Fig. 2.18 Single-chip multi-core processors utilizing on-chip wireless communication technology

In conclusion, on-chip wireless communication can be widely applied in various mobile devices and embedded systems, such as smartphones, tablets, smartwatches, IoT devices, etc., to enhance the performance of communication devices. The application of on-chip wireless communication in 6G can reduce communication latency, provide faster data transmission capabilities, and enhance the real-time performance and energy efficiency of communication systems. High-speed and efficient on-chip communication provide feasible solutions for future 6G wireless communication systems, terahertz integrated circuits, and chip-to-chip communication interconnections.

3 Fundamental Theories of Near-field

With the technological evolution from 5G to 6G communication, in order to further improve beamforming performance and communication rates, larger antenna array apertures and higher communication frequencies are being employed. However, larger arrays also bring many traditionally far-field communication scenarios into the electromagnetically-defined near-field communication range. In near-field communication, the electromagnetic waves used for information transmission can only be regarded as spherical waves instead of plane waves. This emerging physical characteristic is inevitable and gives rise to many new electromagnetic effects, such as spatial non-stationarity, polarization, and evanescent waves. As a result, many traditional communication algorithms that were explicitly designed for far-field operation suffer from severe performance degradation or fail to leverage the new features for optimal performance in 6G near-field scenarios[1][2]. In this chapter, starting from the definition of near-field provided by electromagnetic theory, we analyze the near-field electromagnetic effects, explaining their sources and impacts on existing systems. Furthermore, based on the existing literature on near-field communication, we summarize the changes in communication system design and performance caused by the emergence of near-field effects, focusing primarily on communication DoFs and communication capacity.

The foundational theory of near-field comprises four main parts: electromagnetic near-field definition, near-field electromagnetic properties and physical effects, theoretical analysis of near-field communication DoFs and near-field performance analysis.

3.1 Near-field Range Partitioning

In this section, we first introduce the differences between far-field and near-field communications. Then, we establish principles for determining the boundaries of far-field and near-field regions in several typical application scenarios.

As shown in Fig. 3.1, based on electromagnetic theory and antenna theory, the fields around a transmitter can be divided into the near-field and far-field regions, with the near-field further classified into the reactive near-field region and the radiative near-field region [98]. The reactive near-field region is limited to the space close to the antenna (within the Fresnel distance), where evanescent waves dominate, and the electromagnetic field does not propagate from the antenna in the form of radiative waves. The radiative near-field region extends several wavelengths away from the antenna (between the Fresnel distance and the Rayleigh distance). The Rayleigh distance is also known as Fraunhofer distance. In this region, the amplitude differences between electromagnetic waves on different antennas within the array are not significant, but the phase changes exponentially with the index of the antennas. The signal propagation model in this region must be modeled using a spherical wave model. The far-field region surrounds the radiative near-field region, and in the far-field, electromagnetic waves can be approximated as plane waves. Since the reactive near-field region is usually small and evanescent waves decay exponentially with distance, practical near-field communication systems primarily focus on wireless communication within the radiative near-field region, where "near-field" generally refers to the radiative near-field region.

3.1.1 Characterizing Near-Field and Far-Field Boundaries: Perspectives and Empirical Rules

In existing research, there are multiple perspectives and empirical rules to characterize the boundaries between the near-field and far-field regions, mainly including phase difference, power difference, channel capacity, and localization error.

(1) Phase difference perspective

From the perspective of phase difference, the classic boundary between near-field and far-field is referred to as the Fraunhofer distance or Rayleigh distance [99] (considering a maximum phase difference between spherical wave and plane wave model not exceeding $\frac{\pi}{8}$), expressed as $\frac{2D^2}{\lambda}$, where D represents the maximum aperture of the antenna, and λ represents the wavelength of the carrier. If the distance between the user and the BS is greater than the Rayleigh distance, the user can be considered to be in the far-field region. In this region, the signal propagation can be approximated as plane waves. On the other hand, if the distance between the user and the BS is smaller than the Rayleigh distance, the user can be considered to be in the near-field region.
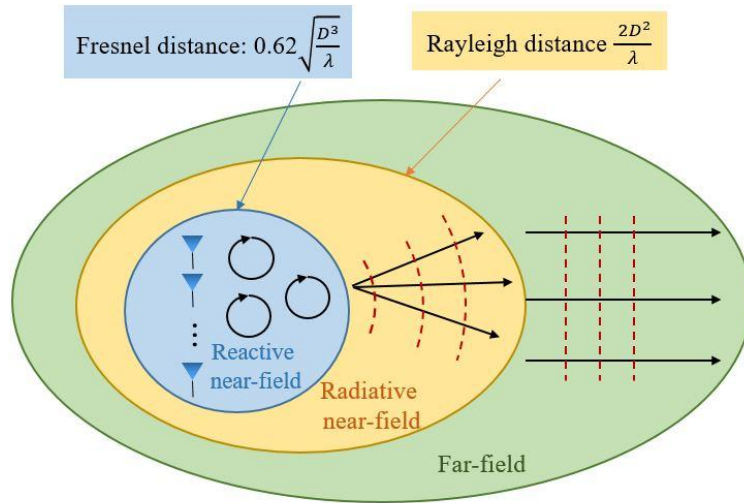
Fig. 3.1 Far-field plane wavefront and near-field spherical wavefront and corresponding physical space normalized received energy

Plane waves differ from spherical waves in their ability to adjust to radiant energy from space. More precisely, plane waves are far-field approximations of spherical waves. In the far-field region, the phase of an electromagnetic wave can be approximated by a Taylor expansion in terms of a linear function of the antenna exponent. This clean linear phase forms a plane wavefront that is only related to the angle of incidence. Thus, using the plane wavefront, far-field beamforming can steer the beam energy to specific angles at different distances, which is also known as beam steering. Unfortunately, this clean linear phase does not completely reveal information about the spherical wave. In the near-field region, the phase of a spherical wave should be derived accurately based on the physical geometry, which is a nonlinear function of the antenna index. The information on the angle of incidence and the distance for each path between the BS and the user equipment (UE) is contained in this nonlinear phase. By utilizing the additional distance information of the spherical wavefront, near-field beamforming can focus the beam energy at a specific location and achieve energy focusing

in both the angle and distance domains. Based on this property, near-field beamforming is also known as beam focusing.

The primary concept behind the derivation of the Rayleigh distance is as follows [98]. The true phase of an electromagnetic wave must be calculated based on an accurate spherical wavefront model and the BS antenna position. In the far-field case, this phase is usually approximated by a first-order Taylor expansion based on a planar wavefront model. This approximation results in a phase difference which increases with decreasing distance. The distance between the center of the BS array and the center of the UE array is defined as the Rayleigh distance when the maximum phase difference between all BS and UE antennas reaches $\pi/8$. Therefore, if the communication distance is shorter than the Rayleigh distance, the maximum phase difference will be greater than $\pi/8$. In this case, the far-field approximation becomes inaccurate, so it is necessary to utilize the near-field propagation model.

Based on this definition, the near-field ranges of single-input-multiple-output (SIMO), multiple-input-single-output (MISO), and multiple-input-multiple-output (MIMO) communication systems can be obtained. As shown in Fig. 3.2, the near-field range for SIMO/MISO scenarios is accurately determined by the classical Rayleigh distance, which is proportional to the square of the aperture of the BS array. For the MIMO scenario, both the BS array aperture and the UE array aperture contribute to the Rayleigh distance since ELAA is employed on both sides of the BS-UE link; i.e., the near-field range is proportional to the square of the sum of the BS array aperture and the UE array aperture. For RIS systems, the cascaded BS-RIS-UE channel consists of BS-RIS and RIS-UE links. Therefore, the $\pi/8$ maximum phase difference needs to be calculated by summing the BS-RIS distances and the RIS-UE distances when calculating the phase difference, and the near-field range of the RIS system is determined by the harmonic mean of the BS-RIS distances and the RIS-UE distances, as shown in Fig. 2. It can be further seen from Fig. 3.2 that RIS-assisted communication operates in the near-field region as long as either of these two distances is shorter than the Rayleigh distance. Therefore, near-field propagation is more likely to occur in RIS systems [35].
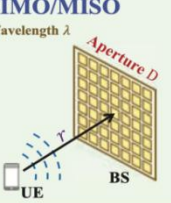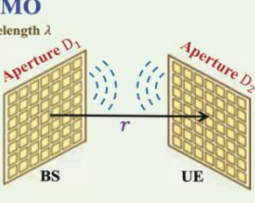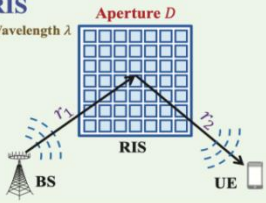
Fig. 3.2 Near-field range for typical communication scenarios

(2) Power difference perspective

When using the optimal Maximum Ratio Combining (MRC), signals from different antenna elements can be completely aligned in phase, thus eliminating the impact of phase differences on received power. However, the MRC combining weights derived from classical far-field planar wavefront cannot perfectly compensate for the phase differences of near-field spherical wavefront, leading to severe power losses. Based on this observation, reference [100] quantatively analyzes the relationship between the focal point of incident spherical wavefront and the induced power loss. Then, an effective Rayleigh distance is proposed to capture the physical region where the power loss is

greater than a threshold. This new metric allows a much more accurate characterization of the boundary of near-field region than the traditonal Rayleigh distance.

After eliminating the effect of signal phase on received power through MRC, the received power is only determined by the amplitude response differences of the antenna elements at the receiver. Considering the amplitude response differences of different antenna elements on the same transmitter antenna array, the *Critical Distance* and *Uniform Energy Distance* is proposed [101][102], which characterize the near-field range from the perspective of power differences between different antenna elements. That is, the power ratio between the weakest and strongest antenna elements detected at the receiver exceeds a specified threshold beyond this distance. The *Critical Distance* is determined by the antenna aperture, primarily characterizing the boundary of the field near the antenna aperture axis. The *Uniform Energy Distance* further considers factors such as array structure and the projected aperture of the antenna array, providing a more accurate description of the near-field boundary in off-axis regions.

Looking at the differences in received power between the plane wave channel model and the spherical wave channel model from another perspective, reference [103] has derived the equal-power lines and equal-power surface for the near-field region based on the uniform linear array (ULA) and the uniform circular planar array (UCPA) structures respectively, characterizing the near-field range.

(3) Capacity perspective:

From the perspective of capacity, the near-field range can be described by combining the channel capacity [104], eigenvalues [105], rank [103], multi-stream transmission characteristics [106], or effective DoFs [107], to evaluate the applicable area of far-field plane waves and near-field spherical waves. Reference [103] proposes the boundary of the near-field region through equip-rank surface. It shows that the near-field range increases with the number of scatterers in both LoS and non-line-of-sight (NLoS) environments, with is more apparent in the NLoS environment. Considering spatial reuse, reference [106] introduces the effective reuse distance metric $D_{max}^{(m)}$, representing the maximum distance at which the channel can efficiently accommodate m independent spatial streams at a specific signal-to-noise ratio (SNR). The near-field boundary from the perspective of multi-stream transmission is discussed by combining the channel's effective DoFs [107], which demonstrates that the near-field range is not only related to the antenna array aperture but also influenced by the number of antenna elements.

(4) Localization error perspective

The Fraunhofer distance serves merely as a rough estimate to delineate between the far-field and near-field regions. However, for localization applications, it is not an appropriate boundary between near and far fields, as it does not consider several essential parameters for localization, such as AoA, beam squint, or transmit power. In fact, it has been shown in [108] that this distance is insufficient to suggest when the mismatched far-field model can be used in practice, instead of the more accurate near-field, without significant performance degradation due to the model mismatch. Therefore, a metric based on the mismatched Cramer-Rao lower bound is proposed, such that the boundary between the far-field and the near-field is the -3 dB contour of the model mismatch positioning error between the two regimes.

(5) Mathematical model perspective

Existing literatures on near-field communications usually assume that the antenna elements are either isotropic or simply characterized by the projected aperture. In practice, individual antenna

element is also directional in general, i.e., the signal power of each antenna element depends on its locally observed angle of arrival/departure (AoA/AoD), which may render commonly used methods unjustified. Therefore, reference [109] introduces the normalized difference between the near-field NUSW model and far-field UPW model considering the directivity of each array element, which accounts for both the phase and amplitude simultaneously. Based on such metric, closed-form expressions of the near-field and far-field boundary are obtained by using the commonly used cosine-based directional gain pattern in antenna theory.

(6) Polarization perspective

To fully exploit polarization dimensions, dual-polarized XL-MIMO, which deploys dual-polarized antennas at both the BS and the UEs, serves as a promising solution. Unlike conventional single-polarized systems, a new parameter named cross-polarization discrimination is a unique parameter for dual-polarized XL-MIMO channels. It is defined as the ratio between co-polarized power and cross-polarized power, which quantifies how much power remains in the same polarization as the transmit signal when propagating through wireless channels. For dual-polarized XL-MIMO systems, the XPD varies across BS antennas due to enlarged radiation aperture of the antenna array, which, however, has not been considered in current boundary definitions. Neglecting these variations could lead to inaccurate channel characterizations, thus negatively impacting transmit covariance optimization performance.

Addressing this gap, we proposes a novel distance criterion termed the non-uniform XPD distance, specifically tailored to dual-polarized XL-MIMO, which can be utilized to optimize the transmit covariance and improve the ergodic capacity of the considered system. Specifically, as shown in Fig. 3.3, there are two main factors that can result in the discrepancies in XPDs across BS antenna elements: propagation distances and angles of departure. Due to the enlarged aperture size of the BS antenna array, the discrepancies in distances from different BS antenna elements to the UE cannot be neglected. Further, the AoDs of various BS antennas relative to clusters in wireless propagation environments also differ, leading to the variation of XPD with different BS antenna elements [110].
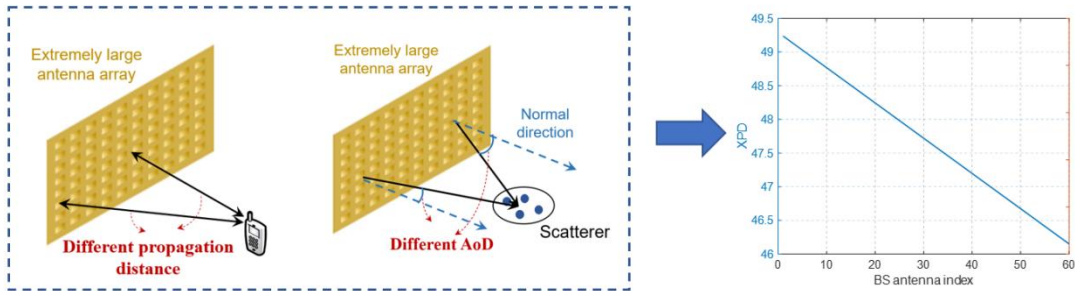
Fig. 3.3 Illustration of the main factors leading to variant XPD over BS antennas

By considering such XPD variances over different BS antennas, we propose Non-uniform XPD distances to complement existing near-far field boundary. The Non-uniform XPD distance is defined as a threshold for the BS-UE distance, within which the discrepancy in XPD across different BS antennas cannot be neglected [111], as shown in Fig. 3.4.
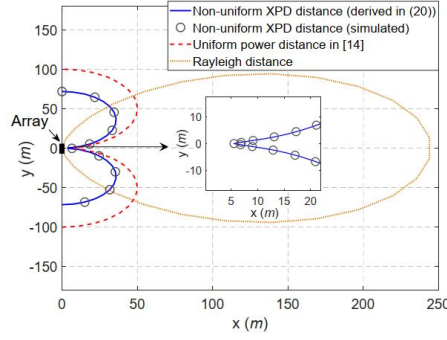
Fig. 3.4 Comparison of non-uniform XPD distances with direction-dependent Rayleigh distances.

Further, non-uniform power distances are also considered, characterizing the maximum BS-user distance within which the difference in pathloss (and thus received power) across antenna elements cannot be neglected.

3.1.2 A Method for Near-Field Classification

For a MIMO scenario with K single antenna users at the transmitter and N antennas at the receiver, the signal sent by the k-th user to the n-th antenna is [112][113]:

$$y_{k,n} = \frac{1}{4\pi \| \boldsymbol{p}_k - \boldsymbol{p}_n \|} e^{-j\frac{2\pi}{\lambda}\|\boldsymbol{p}_k - \boldsymbol{p}_n\|} + n_\sigma, \tag{3.1}$$

where λ is the wavelength of the signal, $\boldsymbol{p}_k$ and $\boldsymbol{p}_n$ are the position coordinates of the user and the n-th antenna, respectively. According to Fig. 3.1, whether the user is in the far field or near field depends on the value of $\frac{2\pi}{\lambda} \| \boldsymbol{p}_k - \boldsymbol{p}_n \|$ [99]. According to Fig. 3.1 and the causes of the near field, we can divide the near field into the following three cases:

● Near-field of short distance communication: The reason for the near-field phenomenon is that $\|\boldsymbol{p}_k\|$ is relatively small. In this case, the distance between the user and the array is relatively short, resulting in a large curvature of the wavefront, so the curvature cannot be ignored as 0. Therefore, spherical wave and near-field model are needed. This case often occurs in the indoor communication scene, where the scattering environment is rich and the multipath effect is obvious. However, due to the slow movement of indoor users, the Doppler effect is not obvious. The main difficulty of beamforming design and user location estimation in this case is the processing of multi-paths.

● Near-field of large size array: The reason for the near-field phenomenon is that $\|\boldsymbol{p}_N - \boldsymbol{p}_0\|$ is large, where $\boldsymbol{p}_0$ is the coordinate of the reference antenna. In this case, even if the curvature of the incoming wave is small, since the radian of the wave front is large, the plane wave far-field model cannot be used for modeling. In this case, the main difficulty of beamforming design is the estimation of the curvature of the incoming wave.

● Near-field of high frequency: The reason for the near-field phenomenon is that λ is small. In this case, electromagnetic waves have high spatial resolution, so even if the radian and curvature of the wavefront are relatively small, the plane wave model cannot be used. Due to the sparse nature of high-frequency channels, the location algorithms usually need to be done where there are few anchor

points. In addition, due to the high spatial resolution of high-frequency beams, higher accuracy is required for channel parameters estimation and user location estimation process.

It should be pointed out that since $||\boldsymbol{p}_k||$, $||\boldsymbol{p}_N - \boldsymbol{p}_0||$, and λ are three independent variables, these three cases are not mutually exclusive. Therefore, we need to study the changes that these three cases will bring to beamforming design and etc. Table 3.1 analyzes the main differences among these three scenarios.

Table 3.1 Classification of near-field

	Short distance	Large size array	High frequency
Difference from far-field	Short distance	Large size	High frequency
Reasons for using spherical wave model	Large curvature	Large radian	High spatial resolution
The main reason for high channel rank	Rich scattering environment	Non stationary of spatial channels	Nonlinear signal space
Signal amplitude fading	Cannot be considered equal	Cannot be considered equal	Generally can be considered equal
Multi-path effects	Significant	Significant	Not significant
Doppler effect	Generally not obvious	Uncertain	Obvious
Main difficulties in algorithm design	How to deal with and utilize rich scattering environments	How to deal with the non-stationary spatial characteristics of channels	How to implement high-precision algorithms

It should be emphasized that although all three scenarios may occur in practical applications, the main motivation for near-field research at present is to serve high-frequency communication. In high-frequency scenarios, due to the increase in Rayleigh distance, a large number of users are in the near-field area, making near-field communication a research focus. So in the process of studying near-field, we should pay more attention to the characteristics of high-frequency near-field channels, rather than treating the three types of near-field as one to study.

3.2 Near-field Electromagnetic Physical Effects

In the near-field region, the electromagnetic physical effects of wireless signals will become non-negligible. Specifically, electromagnetic physical effects include tri-polarization effects, energy mapping effects, etc. Next, we will start with Maxwell's equations to establish electromagnetic near-field channels and reveal these electromagnetic near-field effects.

3.2.1 Near-field Electromagnetic Signal Model
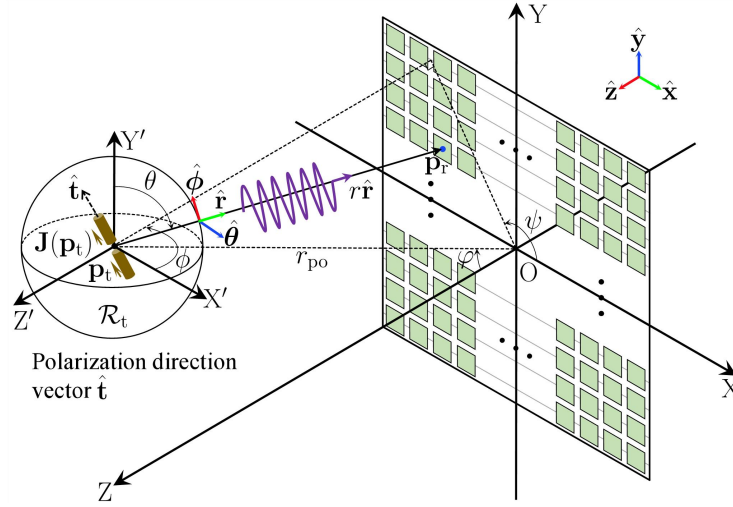
Fig. 3.5 Near-field electromagnetic radiation system diagram

As shown in Fig. 3.5, in the Cartesian coordinate system $OXYZ$, we consider that the transmitter is located at point $\mathbf{p}_t = (x_t, y_t, z_t)$ inside the source region $\mathsf{R}_t \subseteq \mathsf{R}^3$ and equipped with a current density $\mathbf{J}(\mathbf{p}_t)$. The transmitter is a common low-cost single-polarized antenna with a normalized polarization direction vector $\hat{\mathbf{t}} = t_x\hat{\mathbf{x}} + t_y\hat{\mathbf{y}} + t_z\hat{\mathbf{z}}$ ($\hat{\mathbf{x}}$、 $\hat{\mathbf{y}}$、 $\hat{\mathbf{z}}$ are three basis vectors). The coordinates of each point on the receiving array are $\mathbf{p}_r = (x_r, y_r, 0)$.

Further, we consider the scalar electric field defined from the power point of view. Specifically, we exploit the scalar electric field that is a component of the *Poynting vector* perpendicular to the *observation region:* $\mathrm{E}_s(\mathbf{r}) = |\mathrm{E}_s(\mathbf{r})|\exp(\mathrm{j}k_0 r)$, where

$$
\begin{aligned}
|\mathrm{E}_s(\mathbf{r})|^2 &= \overbrace{\|\mathrm{E}(\mathbf{r})\|^2}^{\text{Transmitting energy}} \overbrace{\left(-\frac{\mathbf{p}_r - \mathbf{p}_t}{\|\mathbf{p}_r - \mathbf{p}_t\|}\cdot\hat{\mathbf{z}}\right)}^{\substack{\text{Energy mapping effects}\\\text{along the } Z\text{-direction}}} \\
&= \mathrm{E}_{\text{in}}^2 \underbrace{\frac{1}{4\pi r^2}}_{\substack{\text{Free space}\\\text{attenuation}}} \underbrace{\frac{z_t}{r}}_{\substack{\text{Energy}\\\text{mapping}\\\text{factor}}} \underbrace{\frac{1}{r^2}\left[\left(t_y x_{r,t} - t_x y_{r,t}\right)^2 + \sum_{(\alpha,\beta)\in\mathsf{M}}\left(t_\alpha \ell_\beta + t_\beta \ell_\alpha\right)^2\right]}_{\text{General polarization loss}},
\end{aligned}
\tag{3.2}
$$

where $\mathsf{M} = \{(z,x),(z,y)\}$, $\ell_x = x_{r,t}$, $\ell_y = y_{r,t}$, $\ell_z = z_t$, $x_{r,t} = x_r - x_t$, $y_{r,t} = y_r - y_t$.

$\mathrm{E}_{\text{in}} = \dfrac{\eta_0 I_{\text{in}}}{2}$ is the initial electric intensity measured in volts.

In particular, when the transmitter is polarized toward the positive Y axis, i.e., $\hat{\mathbf{t}} = \hat{\mathbf{y}}$. (3.2) can be simplified to

$$\left|\mathrm{E}_{\mathrm{s,Y}}(\mathbf{r})\right|^2 = \mathrm{E}_{\mathrm{in}}^2 \frac{1}{4\pi r^2} \frac{z_{\mathrm{t}}}{r} \frac{x_{\mathrm{r,t}}^2 + z_{\mathrm{t}}^2}{r^2}. \tag{3.3}$$

When the signal is incident perpendicularly to the receiving surface, i.e., $x_{\mathrm{t}} = y_{\mathrm{t}} = 0$ and

$\dfrac{z_{\mathrm{t}}}{r} = 1$. (3.3) can be simplified to

$$\left|\mathrm{E}_{\mathrm{s,Y,v}}(\mathbf{r})\right|^2 = \mathrm{E}_{\mathrm{in}}^2 \frac{1}{4\pi r^2} \frac{x_{\mathrm{r,t}}^2 + z_{\mathrm{t}}^2}{r^2}. \tag{3.4}$$

When $y_{\mathrm{t}} = y_{\mathrm{r}}$, i.e., $\dfrac{x_{\mathrm{r,t}}^2 + z_{\mathrm{t}}^2}{r^2} = 1$, there is no polarization loss, and (3.4) is simplified to

$$\left|\mathrm{E}_{\mathrm{s,Y,v}}(\mathbf{r})\right|^2 = \mathrm{E}_{\mathrm{in}}^2 \frac{1}{4\pi r^2}. \tag{3.5}$$

(3.5) is the classic Friis formula.

Next, we give the classic far-field signal formula:

$$\mathrm{E}_{far}(\mathbf{r}) = \frac{\mathrm{E}_{\mathrm{in}}}{2\sqrt{\pi} r_{\mathrm{po}}} \exp\left[\mathrm{j} k_0 \left(r_{\mathrm{po}} - \frac{x_{\mathrm{r}} x_{\mathrm{t}} + y_{\mathrm{r}} y_{\mathrm{t}}}{r_{\mathrm{po}}} \right) \right], \tag{3.6}$$

where $r_{\mathrm{po}} = \sqrt{x_{\mathrm{t}}^2 + y_{\mathrm{t}}^2 + z_{\mathrm{t}}^2}$, and the phase term uses a second-order Taylor expansion. Further, (3.6) can be simplified to

$$\mathrm{E}_{far}(\mathbf{r}) = \frac{\mathrm{E}_{\mathrm{in}}}{2\sqrt{\pi} r_{\mathrm{po}}} \exp\left(\mathrm{j} k_0 r_{\mathrm{po}} \right) 。 \tag{3.7}$$

From the near-field signal models (3.2) - (3.5) and far-field signal models (3.6) and (3.7), we can see:

● For a near-field signal model, the amplitude term will include the polarization loss of the antenna, the energy mapping coefficient, and the point-to-point free space loss factor, and the phase term will be determined by the exact point-to-point distance.

● The far-field signal model is an approximation of the near-field signal model. For the far-field signal model, the amplitude term only has a fixed free space loss factor, and the distance of the phase term is also a fixed distance from the transmitter to the receiver reference point.

3.2.2 Near-field Electromagnetic Effects

Tri-polarization effect arises naturally for near field communication since the solution to the Maxwell's equation for a dipole antenna has a rapid-decaying radial component. Considering the tri-polarization effect, in [114] the authors considered both the near-field spherical wave channel and the multi-polarization effect using a vector Green's function, and based on this the multi-polarized

near-field spherical wave channel as well as the proposed polarization and channel oriented dual precoding are considered, and the considered systematic diagram is shown as follows.
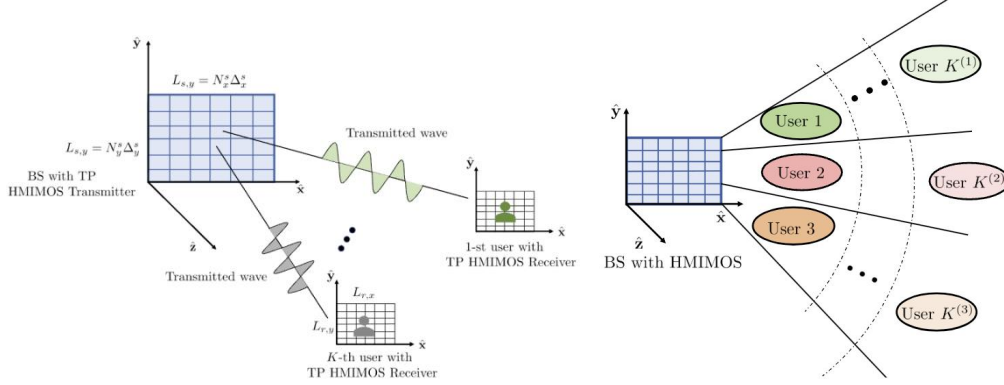
Fig. 3.6 Near-field multi-polarized spherical waves model

Simulation results demonstrate that the multi-polarization effect in near-field communication can significantly increase the system capacity in a specific range.

(b) Channel capacity v.s. distance z (a) Channel capacity v.s. SNR
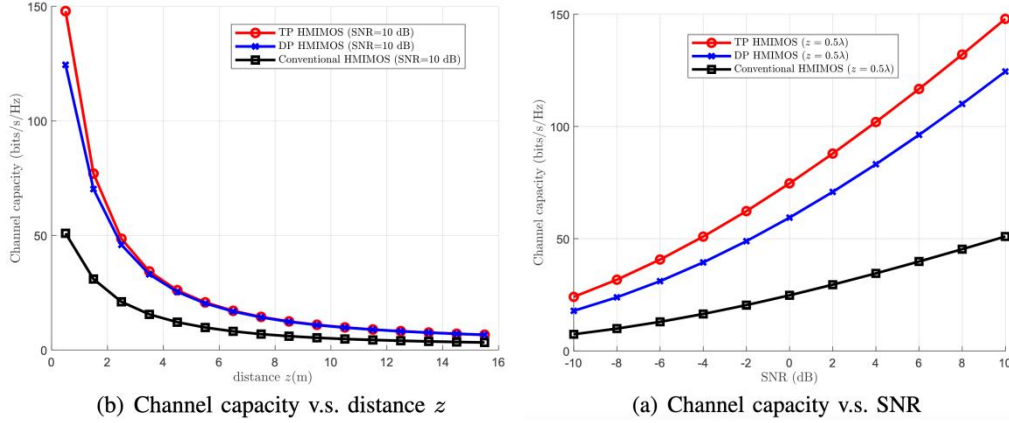
Fig. 3.7 Near-field tri-polarized channel capacity

The near-field evanescent wave effect mainly affects the communication DoFs and capacity of the reactive near-field, which we will describe in the next subsection. For the near-field beam splitting effect, in a near-field RIS, a phase shifter-based beamformer can produce a focused beam aligned to a specific location, thus providing beam focusing gain. Such beamformers work well in narrowband systems. However, for broadband systems, due to the use of an almost frequency-independent phase shifter, spherical beams of different frequencies are focused at different physical locations, which is known as the near-field beam splitting effect. This effect can lead to severe array gain loss because beams of different frequencies cannot be aligned with the target user at a specific location, which needs to be carefully considered in the design of broadband systems.

Although the beam splitting effect makes it more difficult to align the energy of a broadband system to the user, resulting in a degradation of the beam focusing performance, it has a corresponding benefit: since the same guiding frequency corresponds to the generation of spatially multiple beams, it is possible to control the angular range of the beam coverage at different frequencies by designing the system parameters. With this benefit, very fast CSI acquisition can be realized in the far-field for fast beam training or beam tracking. The research on this problem in traditional far-field communication is mainly divided into two types of work: the first type of technique hopes to mitigate the array gain loss

caused by far-field beam splitting, and introduces time-delay circuits in the beamforming structure to mitigate the far-field beam-splitting effect; the second type of technique realizes the fast acquisition of far-field CSI in a large-scale multiple-input-multiple-output system by controlling the time-delay parameter and the multiple beams.

The effect of near-field beam splitting effect is shown in Fig. 3.8, where it can be seen that there are multiple energy focusing points spatially during near-field broadband communication.
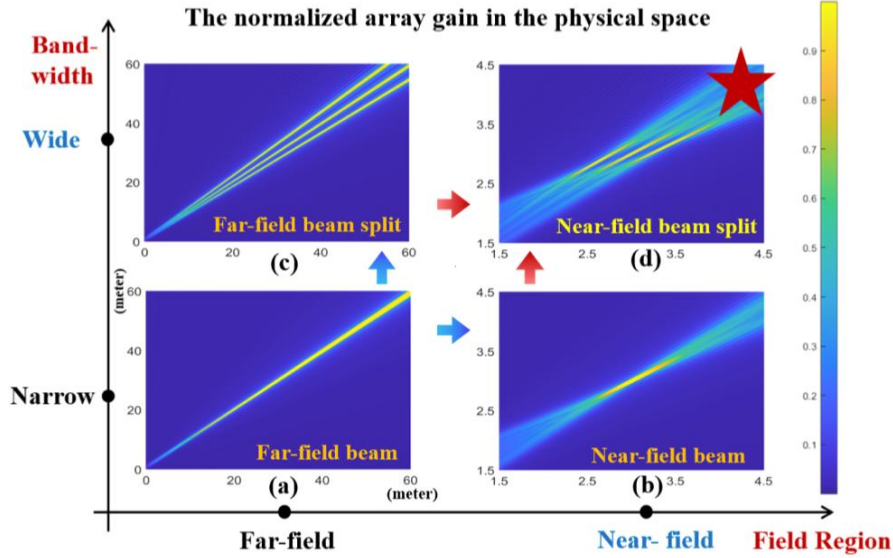
Fig. 3.8 Near-field beam splitting effect schematic

The near-field beam splitting effect is defined and analyzed in the paper [115], and a time delay (TD) based beamformer is utilized to overcome this effect. We propose to divide the whole array into subarrays and then assume that the user is located in the near-field range of the whole array but in the far-field range of each subarray. On this basis, delay circuits can also be utilized to compensate for the group delay between different subarrays caused by the near-field spherical wavefront. As a result, the beam over the entire bandwidth can be focused at the desired spatial angle and distance, and the near-field beam splitting effect is mitigated accordingly.

3.2.3 Near-field Beam Characteristics

After studying the near-field characteristics, the properties of the near-field beam can be analysed and summarized in the following three points: near-field distance-domain focusing, distance-domain asymptotic orthogonality, and distance-domain focusing properties of rectangular and circular array.

First, for the near-field distance-domain focusing characteristics, the depth-of-focus (DF) was calculated in [116] When a transmitter with distance F is focused using matched filtering, the DF is:

$$z \in \left[\frac{d_{FA}F}{d_{FA}+10F}, \frac{d_{FA}F}{d_{FA}-10F} \right] \tag{3.8}$$

where d_{FA} is the array Rayleigh distance, and the depth of the beam depends on where the matched filter is focused as shown in Fig. 3.9. When the focus is less than $d_{FA}/10$, the depth of the near-field beam assignment is finite.
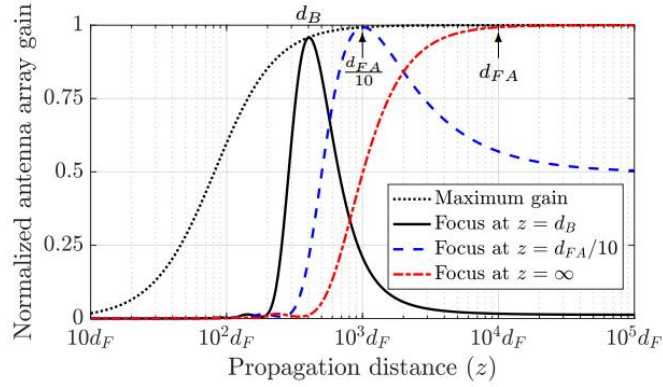
Fig. 3.9 Trend of beam gain with distance

Near-field beam focusing concentrates the beam energy at a specific location determined by angle and distance. In order to utilize the additional spatial distance domain resources to improve the spectral efficiency, researchers in [117] demonstrated the asymptotic orthogonality of the near-field array response vectors, and the channel correlation can be expressed as:

$$f^{near} \approx \left| \frac{C(\beta) + jS(\beta)}{\beta} \right| \tag{3.9}$$

where $\beta = \sqrt{\frac{N^2 d^2 (1-\theta^2)}{2\lambda} \left| \frac{1}{r} - \frac{1}{\bar{r}} \right|}$. This means that as the number of array antennas N tends to infinity, β also tends to infinity and f^{near} tends to 0. As shown in Fig. 3.10, as the number of antennas increases, the correlation between two array response vectors at different distances at the same angle tends to 0.
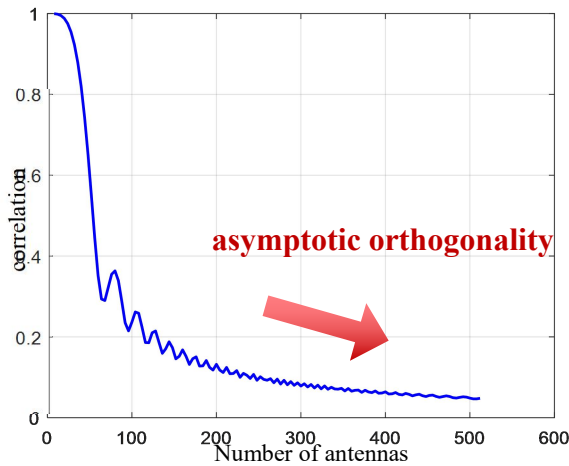
Fig. 3.10 Channel correlation versus antenna curve

The above two beam characteristics are for the Uniform planar array (UPA) and ULA scenario, respectively. Moreover, the distance-domain focusing characteristics are elaborated next for the uniform circular array (UCA) [118]. The beam focusing gain in the UCA scenario is approximated as a zeroth-order first-type Bessel function. From Fig. 3.11, it can be seen that the ULA beam focusing gain decreases smoothly with decreasing distance, while the beam focusing gain of UCA decreases faster, which indicates that UCA is able to focus the signal power in a smaller range and mitigate the power leakage.
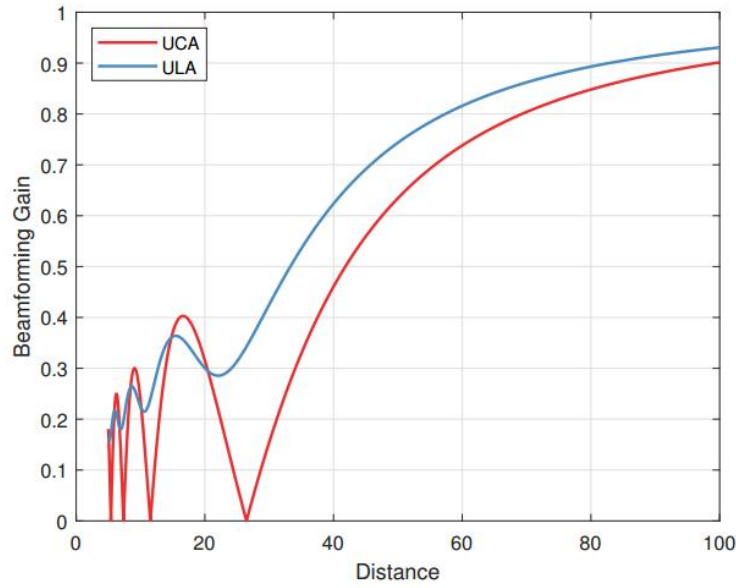
Fig. 3.11 Comparison of beamforming gain between UCA and ULA
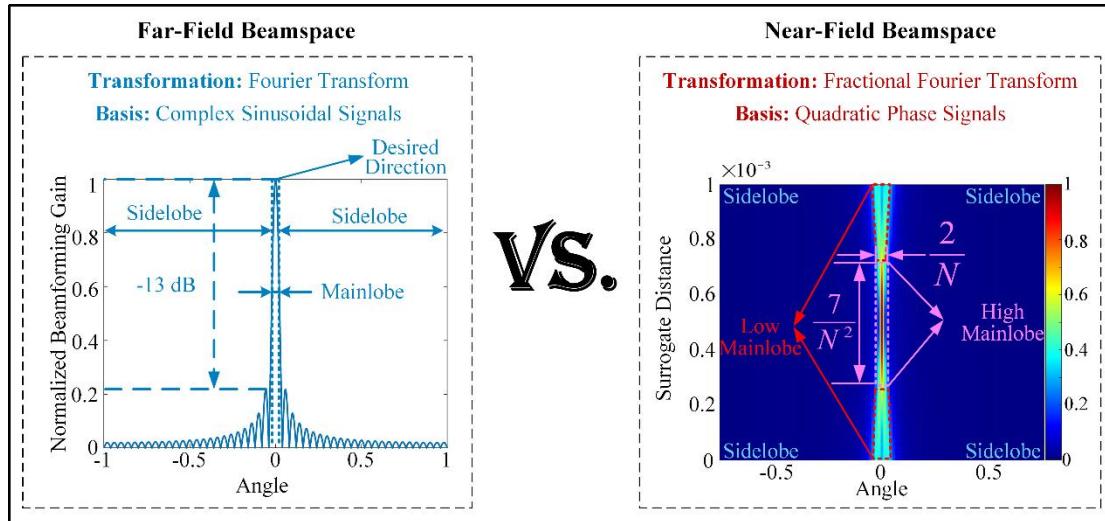
Fig. 3.12 Comparisons of far-field and near-field beamspaces.

In addition, the properties of the near-field beam can also be analyzed from the perspective of beamspace [119]. Different from the far field that connects the antenna space and the beamspace by the Fourier transform, the antenna space is mapped to the near-field beamspace with the fractional Fourier transform. As shown in Fig. 3.12, the near-field beamspace is divided into three parts, including high mainlobe, low mainlobe, and sidelobe. The analysis of the high mainlobe reveals that its 3 dB beamwidth and beam depth are given by $2/N$ and $7/N^2$, respectively. The analysis of the low mainlobe reveals that its beamwidth increases linearly with the increase of the surrogate distance deviation, while the square of its average beamforming gain increases inversely with the increase of the surrogate distance deviation. Moreover, leveraging the properties of the fractional Fourier transform, it is demonstrated that the near-field beamspace satisfies Parseval's relation, maintains translation invariance, and enables efficient computation via a fast fractional Fourier transform algorithm.

3.3 Near-field Degree-of-freedom Theoretical Analysis

3.3.1 The number of degrees of freedom of the electromagnetic field

As previously mentioned, (radiating) near field propagation condition takes place when exploiting very large antennas and high frequency bands. From Fig. 3.13, reporting the Fraunhofer distance below that the system works in the near field, it is evident that the wireless system is likely to operate in the near-field region at practical distances when considering mm-wave and beyond frequency bands even with relatively large antennas.
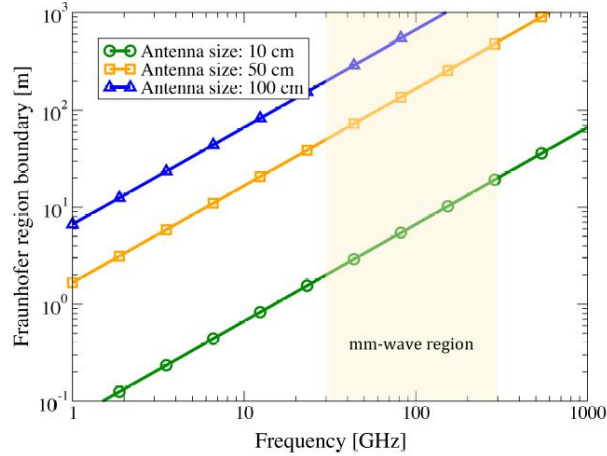
Fig. 3.13 Fraunhofer boundary as a function of the frequency and antenna size [121].

In the near-field condition, while classical communication models fail because based on the plane wave assumption, new opportunities emerge as the waveform may contain richer information. Therefore, new design paradigms and technologies requiring a tighter interaction between EM theory and information theory (IT) are needed. The main question that might arise is *what are the ultimate performance limits of communication when operating in the near field*?

To answer this question, fundamental limits must be technology agnostic and based on IT/EM arguments. Regarding the technology neutrality, in order to abstract from the specific implementation of the antenna, it is convenient to model the antenna surface as a continuous array of an infinite number of infinitesimal antennas in which any surface current can be generated. The wireless communication exploiting an uncountable infinite number of antennas in a finite space has been recently defined as holographic MIMO. In this manner, implementation-related aspects concerning the mutual coupling among the antenna elements are not involved in the discussion. The optimal communication between antenna surfaces, considering a continuum of infinitesimal antennas and the continuous wireless channel, can be modeled as the problem of communicating between a couple a spatial regions [120]. This enables moving away from the classical MIMO model of point-defined antennas, which can be considered as a particular case of this general formulation.
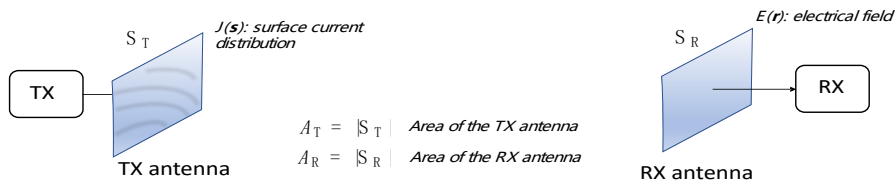
Fig. 3.14 Technology-agnostic reference TX and RX antenna surfaces.

Regarding EM arguments and with reference to Fig. 3.14 , consider a transmit antenna with surface S_T of area A_T containing infinitesimal source currents $J(s)$. Any point source in S_T generates the (outgoing) wave given by the tensor Green's function $G(r)$ [120]. By adding all the waves from the sources in S_T, the resulting electric field $E(r)$. at the generic location r in free-space is given by

$$E(\boldsymbol{r}) = \int_{S_T} G(\boldsymbol{r} - \boldsymbol{s})\, J(\boldsymbol{s})\, d\boldsymbol{s} \tag{3.10}$$

The goal is to determine how many orthogonal communication channels, namely *communication modes*, with as large coupling intensities as possible can be activated between the two surfaces. Due to the finite size of the surfaces, only a limited number N of communication modes are dominant (DoFs). The generic communication mode corresponds to a couple of source current and electrical field spatial distributions $\phi_n(s)$ and $\psi_n(s)$, respectively associated with the coupling intensity ξ_n.
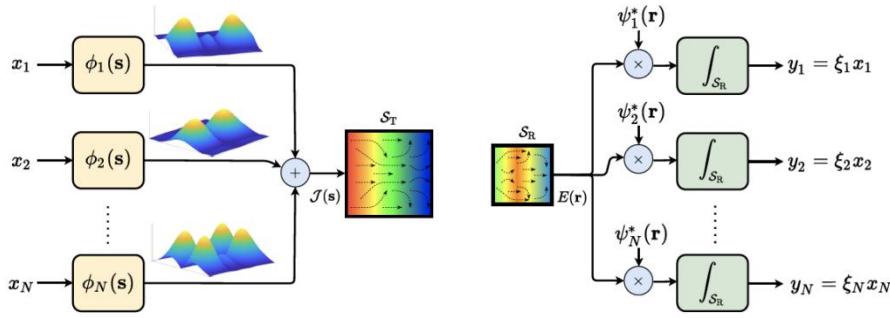
Fig. 3.15 Information-theoretical optimal communication system [121].

Solving this problem as done in [120] leads to the information-theoretical optimal communication system depicted in Fig. 3.15. Since the DoF N along with the modes intensity are the parameters that determine the maximum possible capacity of the system, it is of interest evaluating N. This analysis has been carried out in [120] where it has been shown that N depends only on the geometry of the system relative to the wavelength λ. For instance, in case of two antenna surfaces located at distance d in a paraxial configuration of area A_T and size $S_x \, x \, S_y$, respectively, the DoF is given by

$$N = \frac{2A_T}{\lambda^2} \left(\frac{S_x \, tan^{-1}\left(\frac{S_y}{\sqrt{4d^2+S_x^2}} \right)}{\sqrt{4d^2+S_x^2}} + \frac{S_y \, tan^{-1}\left(\frac{S_x}{\sqrt{4d^2+S_y^2}} \right)}{\sqrt{4d^2+S_y^2}} \right) \tag{3.11}$$

It is interesting to evaluate the behaviour of this formula for large distances $d \gg S_x, S_y$

$$N^{(large)} = \frac{2A_T A_R}{\lambda^2 \, d^2} \tag{3.12}$$

and the asymptotic behaviour for very large RX antenna surfaces, that is

$$N^{(asympt)} = \frac{\pi A_T}{\lambda^2} \tag{3.13}$$

The previous equation indicates that in this case the DoF depend only on the area of the transmit surface (normalized to the square half-wavelength), i.e., the area of the smallest of the 2 antennas, and it represents the ultimate DoF limit which is independent of the distance.
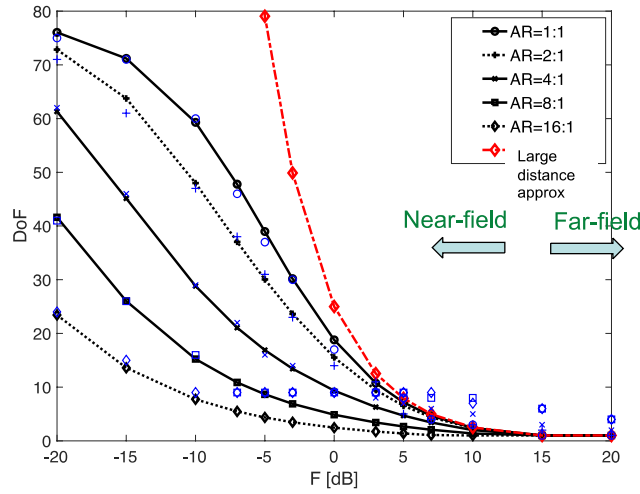
Fig. 3.16 DoF as a function of $F = d^2/A_R$ Dotted curves refer to simulation [120].

In Fig. 3.16, the DoF as a function of $F = d^2/A_R$ and the aspect ratio $AR = S_x/S_Y$ is shown by considering a small TX surface with size of 5cm at 28 GHz. For low F (very large RX surface), the DoF saturates to the limit value predicted by the theory, in this case equal to 78. It is interesting to note that when approaching the near-field region, several orthogonal channels, i.e., DoF, can be activated even when one of the two antennas is relatively small. As far as the Fraunhofer far-field regime is approached (large F), the DoF tends to one, as in conventional MIMO systems in free space condition where only the beamforming gain is present.

(a) $n = 1$

(b) $n = 2$

(c) $n = 3$

(d) $n = 4$
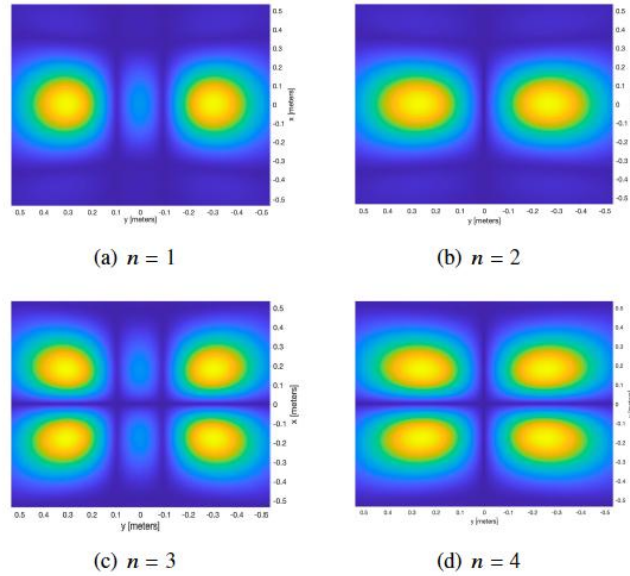
Fig. 3.17 Electric field distribution corresponding to the 4 strongest communication modes.

To get a qualitative idea about the shape of the corresponding communication modes, in Fig. 3.17 the amplitude of the spatial distribution of the electric field $\psi_n(s)$ observed at the receive antenna surface as response to the exciting current distributions $\phi_n(s)$, for $n=1,2, 3$ and 4, are reported under the same parameters used for the results in Fig. 3.16. From these figures one can notice that orthogonality does not involve in general non-overlapped waves. This means that classical beamforming or focusing schemes aiming at obtaining spatially non-overlapped waves are not in

general optimal. However, in [122] it has been shown that almost-optimal communication modes can be designed starting from focusing functions, thus avoiding numerical evaluations and the implementation of complex amplitude/phase antenna profiles.

Based on the Fourier plane wave unfolding channel modelling, the authors in [123] conducted detailed research on the wave number domain modelling of near-field large-scale antenna arrays, especially investigating the DoF and the communication capacity gain that can be brought about by the evanescent wave effect in the near-field communication, of which the DoF gain is shown as follows, and there can be a gain of 30% in the typical reactive near-field region. In the left side figure of Fig. 3.18, the white wave number points correspond to the plane waves available for far-field communication, the green wave number points correspond to the additional evanescent wave numbers available for near-field communication, and the red points are the evanescent wave numbers that are not available because of too much attenuation. Since 6G systems will mostly operate in the radiative near-field, we cannot expect to get more wave number points (spatial DoFs), but we can still make use of them for beamforming in both angle and depth, which was previously not possible.
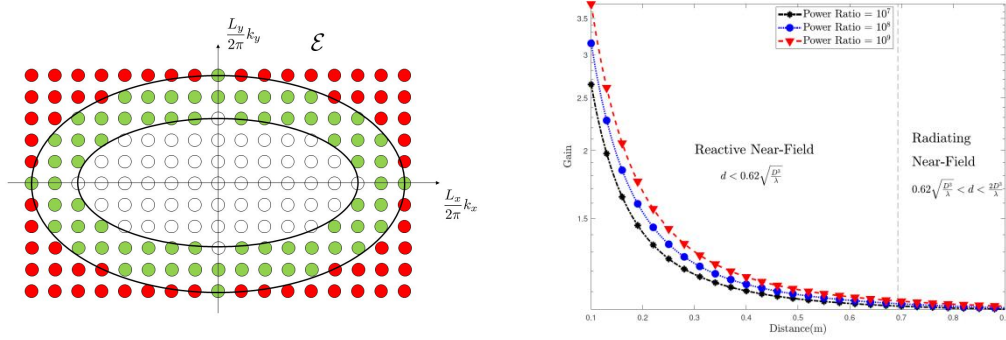
Fig. 3.18 Extra DoFs in the reactive near-field

Reference [124] proposed a signal space approach to study the number of DoFs of the electromagnetic field under arbitrary scattering conditions from the point of view of Nyquist sampling. It considers antenna elements in space as spatial sampling points and uses the sampling points required to recover the electromagnetic field as communication DoFs. Under isotropic propagation conditions, sampling per square meter is reduced by 13% compared to classical half-wavelength sampling. This gap increases as the angular selectivity of the scattering increases, resulting in a significant reduction in spatial sampling complexity.

(a) Circle packing in the wavenumber domain.   (b) Hexagonal sampling in the spatial domain.
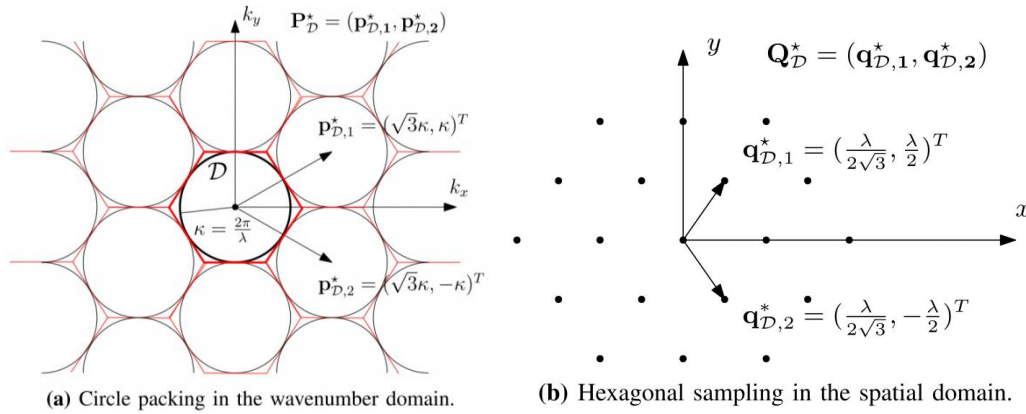
Fig. 3.19 Nyquist sampling under isotropic scattering conditions

In the context of spatially discrete (SPD)-MIMO, the comprehensive channel response in the narrowband case is represented as a matrix H. In this case, the number of DoFs of the channel is determined by the number of positive singular values of H or the rank of the correlation matrix HH^H. In a far-field MIMO LoS channel, the presence of only a single incident angle at all points across the array corresponds to plane-wave propagation. In such cases, the channel has a rank of 1, corresponding to only a single DoF. In contrast, within the near-field region, spherical waves manifest non-linearly varying phase shifts and power levels for each link. This inherent diversity increases the rank of the channel matrix. This implies that, by reducing the antenna spacing within a fixed aperture, the number of spatial DoFs can be significantly increased [125].

However, it is essential to note that when two antennas are in close proximity to each other, the waves they generate at the receiver become nearly indistinguishable. This limitation should be considered, as it could potentially restrict the achievable increase in channel capacity when incorporating a large number of antennas within a fixed aperture. For a given aperture, the singular values of matrix H presents a two-slope property. We denote the ordered positive singular values of matrix H as $\sigma_1 \geq \sigma_2 \geq \cdots \sigma_N$. Extensive simulations and measurements have consistently shown that, for small values of n, the σ_n values exhibit a slow decay until they reach a critical threshold, beyond which rapid decay occurs. This critical threshold is termed the number of effective DoFs (EDoFs), and is illustrated in Fig. 3.20 [125]. This phenomenon becomes more pronounced as the number of transceiver antennas increase. By assuming that $\sigma_1 \approx \sigma_2 \approx \cdots \approx \sigma_e \gg \sigma_{e+1} \approx \cdots \sigma_N \approx 0$, we approximate the number of EDoFs as $e \approx \mathrm{tr}^2(HH^H)/\|HH^H\|_F^2$ [126]. Besides, we note that the number of EDoFs of near-field channels decreases with the propagation distance. We note that $\mathrm{tr}^2(HH^H)/\|HH^H\|_F^2$ was originally introduced by Verdú to evaluate the slope of the capacity curve in the low bit SNR regime [127]. In recent years, some researchers have noticed that this expression can be also used to approximate the number of EDoFs of near-field channels.

Next, we examine the scenario where both transceivers are equipped with continuous-aperture (CAP) arrays, denoted as CAP-MIMO. In contrast to an SPD antenna array, which provides finite-dimensional signal vectors, the CAP array supports a continuous distribution of source currents within the transmit aperture. In this context, CAP-MIMO can be regarded as a limiting case of SPD-MIMO with an infinite number of antennas in a fixed aperture area, but this is achieved through spatial oversampling, so the number of EDoFs remains the same. For example, the singular values of the CAP-MIMO channel exhibit a "two-slope" trend, as depicted in Fig. 3.20 [128]. Therefore, for the near-field CAP-MIMO channel, the performance is still limited by the number of EDoFs. Unlike SPD-MIMO, CAP-MIMO channels cannot be characterized by a finite-dimensional matrix. Typically, it is necessary to use Green's functions to characterize the electromagnetic propagation environment between any two points on the transceiver apertures. Obtaining parallel subchannels requires performing eigenvalue decomposition on the kernel function of Green's functions, resulting in high computational complexity [128]. To estimate the number of EDoFs of near-field CAP-MIMO, one can replace the channel matrix H in the formula $e \approx \mathrm{tr}^2(HH^H)/\|HH^H\|_F^2$ with Green's functions [126]. Additionally, based on existing simulation results, the following conclusion can be drawn: the number of near-field EDoFs is proportional to the product of the transmitter-receiver aperture area and inversely proportional to the transmission distance between the transmitter and receiver [125].
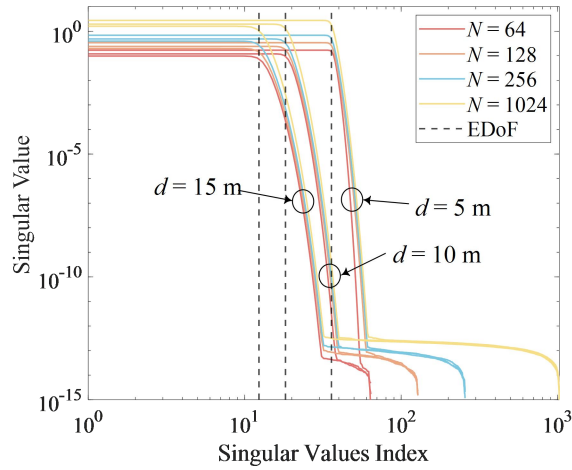
Fig. 3.20 Singular Values of Near-Field SPD-MIMO. D denotes the transmission distance and N is the number of transmit and receive antennas.

3.3.2 Degree of freedom and interference mitigation for Near-field sparse MIMO

For typical MIMO communication systems, antenna array elements are usually separated by half of the carrier wavelength. In order to achieve higher communication rate, as well as super resolution sensing, sparse MIMO with more than half wavelength element spacing become promising for future communication and sensing. On one hand, sparse MIMO possess a larger physical aperture, which can achieve narrower main lobe beams that make it easier to resolve densely located users. On the other hand, increased array aperture also enlarges the near-field communication region, which can enhance the spatial multiplexing gain, thanks to the spherical wavefront. However, sparse MIMO may suffer from severe inter-user interference due to multiple grating lobes, which also needs to be taken into consideration.

For single-user sparse MIMO communication, reference [134] studied the near-field multiplexing gain by deriving the closed-form expression of the near-field EDoFs as

$$
\varepsilon(\eta) \approx
\begin{cases}
1, & \eta < \dfrac{4l}{\lambda \bar{N}(\underline{N}-1)\cos\nu} \\[4mm]
\dfrac{\underline{N}^2}{-\left\lfloor \dfrac{4\alpha l}{\lambda \bar{N}\eta \cos\nu} \right\rfloor^2 + (2\underline{N}-1)\left\lfloor \dfrac{4\alpha l}{\lambda \bar{N}\eta \cos\nu} \right\rfloor + \underline{N}}, & \dfrac{4l}{\lambda \bar{N}(\underline{N}-1)\cos\nu} \leq \eta < \dfrac{4d}{\lambda \bar{N}\cos\nu} \\[4mm]
\underline{N}, & \eta \geq \dfrac{4\alpha l}{\lambda \bar{N}\cos\nu}
\end{cases}
\tag{3.14}
$$

where η denotes the sparsity of antenna array, and l is the distance between transmitter and receiver. $\bar{N}$ and N denote the maximum and minimum value of the number of transmit antenna and the receive antenna, respectively. Fig. 3.21 shows that the EDoF increases with the array sparsity for sparse MIMO before reaching its upper bound, which provides a theoretical threshold of antenna sparsity when the EDoF can achieve its maxima.
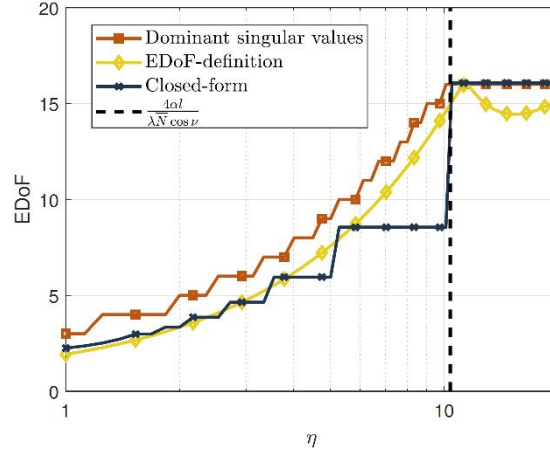
Fig. 3.21 EDoF versus array sparsity for sparse MIMO near-field communication

For multi-user sparse MIMO communication, reference [135] investigated the far-field communication based on uniform sparse antenna arrays. By leveraging the non-uniform spatial angle differences, it is demonstrated that sparse antenna arrays may offer superior interference suppression and enhanced spatial localization capabilities. For near-field sparse MIMO communication, reference [134] plotted the sum rate versus the receive SNR for different antenna sparsity at the BS, as shown in Fig. 3.22. It can be observed that for all the four considered cases, the sum rates increase as the receive SNR grows. Furthermore, for a given SNR, the sum rates tend to increase drastically with larger array sparsity, indicating the benefit of using sparse array at the BS.
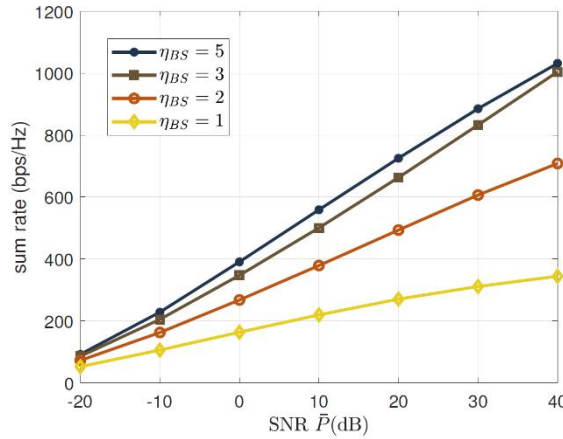
Fig. 3.22 Near-field sum rate versus receive SNR

3.4 Near-field Performance Analysis and Measurement

3.4.1 Near-field Performance Analysis

The evolution from 5G massive MIMO communication to 6G ultra-massive MIMO communication involves more than just a simple increase in the number of antennas or array size. It fundamentally changes the channel characteristics, such as transitioning from the traditional far-field uniform plane waves to near-field non-uniform spherical waves and from spatial stationarity to spatial non-stationarity [102][129][130]. As a result, most performance analyses based on the traditional far-field uniform plane wave model, such as asymptotic channel gains, need to be re-evaluated within the context of the new near-field models. Moreover, the authors in [131] investigated a cooperative

relaying Near-Field Communications (NFC) and Far-Field Communications (FFC) coexisting system with extremely large-scale array (XL-array), raising an interest question: does the capacity improvement from NFC compensate the performance loss suffered from more time slots? To provide the solution to this question, [131] analyzed the achievable capacity for the proposed NFC schemes compared with FFC, confirming that the capacity improvement from NFC compensates the performance loss from the half-duplex principle.

In the traditional far-field model, the equivalent channel gain of a uniform planar array increases linearly/quadratically (squared) with the array size until it approaches infinity. This conclusion clearly contradicts the laws of physics. To obtain more general conclusions, references [102][129][130] and references [132][133] have proposed new near-field spherical wave propagation models for massive MIMO active arrays and massive MIMO passive arrays, respectively. These models consider the asymptotic performance when the size of the active/passive array tends to infinity. In the spherical wave model based on near-field communications, the equivalent channel gain exhibits nonlinear growth with an increasing number of active antennas/passive elements, governed by the new parameter of angular span [134]. As the number of active antennas/passive elements tends to infinity, the equivalent channel gain converges to a constant value [102][129]-[133].

Compared to co-located massive MIMO arrays, sparse massive antenna arrays have a larger physical aperture, making their near-field characteristics more prominent. [135] studies the performance of uniform sparse antenna array. By exploiting the non-uniform distribution of the spatial angle difference, it is shown that sparse antenna arrays may achieve better interference suppression and super-resolution spatial localization capabilities. Fig. 3.23 shows the cumulative distribution function of communication rates for co-located and uniform sparse antenna arrays, and sparse array can achieve more than four-times data rate than co-located ULA.
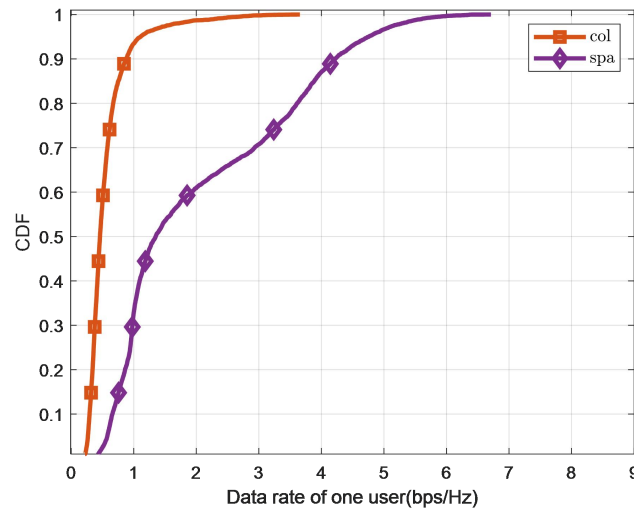
Fig. 3.23 CDF of data rate for co-located and sparse array[135]

Furthermore, [136]-[139] studied a novel modular array architecture to accommodate extremely large arrays, termed modular XL-array. All array elements in modular XL-array are regularly deployed in a modular manner on a common platform. Each module is comprised of a moderate/flexible number of array antennas with the inter-element spacing typically in order of half-wavelength, while different modules are separated by the relatively large inter-module spacing, so as to enable conformal capability

with the deployment environment in practice. [136][137] proposed the near-field non-uniform spherical wave (NUSW) model for modular XL-array. Under this model, the authors derived the closed-form expression for near-field SNR, which reveals the SNR scaling law and asymptotic performance, as well as the difference from the conventional far-field uniform plane wave (UPW) model. Fig. 3.24 shows that the SNR result under UPW model grows linearly unboundedly, while the SNR result under NUSW model approaches to a constant value. According to the characteristics of modular array architecture, [138] proposed sub-array based uniform spherical wave (USW) models under different angles/common angle, and analysed its near-field beam focusing patterns. It can be seen from Fig. 3.25 that compared to co-located counterpart with the same number of antennas, modular XL-array can significantly enhance spatial resolution from angular and distance dimensions, while at the cost of more severe grating lobes. To further alleviate the issue of grating lobes, [139] proposed a user grouping strategy based on greedy algorithm for the multi-user modular XL-MIMO communication system. As a result, users located within the grating lobes of each other are not allocated to the same time-frequency resource block (RB), which greatly mitigates inter-user interference (IUI) in multi-user scenarios. As can be seen in Fig. 3.26, in contrast to co-located counterpart, modular XL-MIMO can significantly enhance the communication performance.
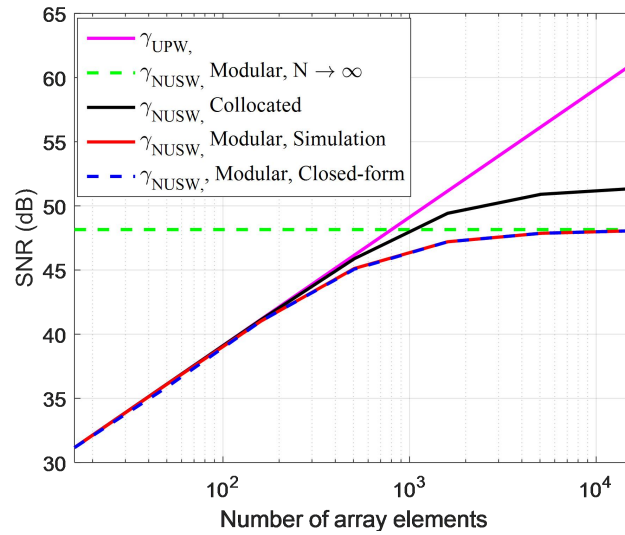
Fig. 3.24 SNRs versus the number of array elements for different models[136].
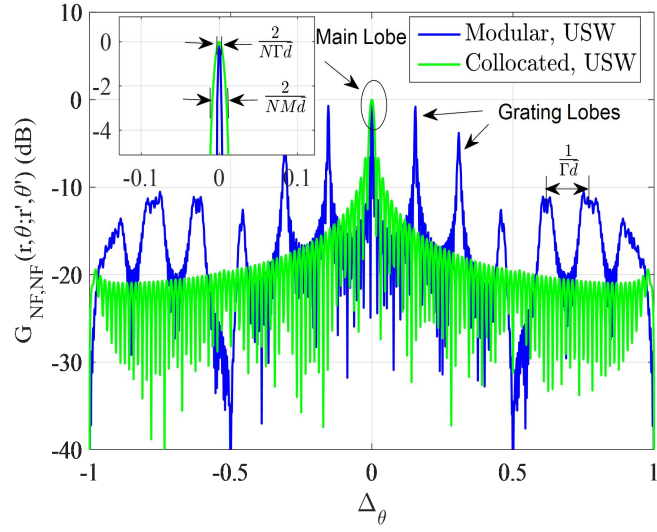
(a) Near-field beam focusing patterns versus spatial frequency differences.
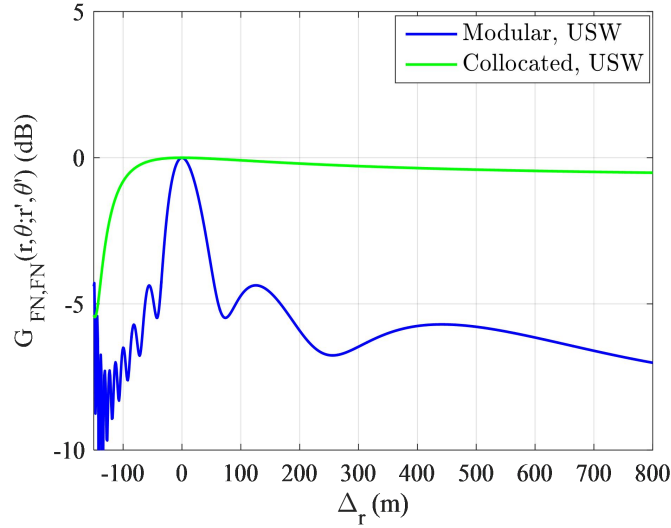
(b) Near-field beam focusing patterns versus distance differences.
Fig. 3.25 Near-field beam focusing patterns under different array architectures[138][139].
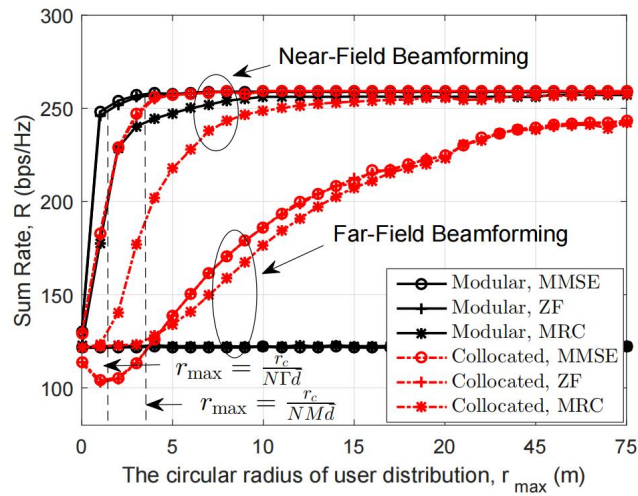
Fig. 3.26 Achievable sum rates for modular and co-located arrays versus
the circular radius of user distribution, under far-field and near-field linear beamforming [139].

Compared to large-scale active antenna arrays, the passive RIS is more likely to achieve extremely large-scale configurations in practice due to its appealing advantages, such as low cost and low energy consumption. In communication systems where an extremely large-scale RIS (XL-RIS) is deployed near the BS side, as illustrated in Fig. 3.27, the distances from users to the RIS and the BS are nearly the same. Moreover, when the RIS is sufficiently large, the effective propagation path loss of the reflected link is comparable to that of the direct link. Due to the half-space reflection nature of the RIS, a BS equipped with omnidirectional antennas will have at most half of its transmitted power reflected by the RIS. Therefore, a desired transmit diversity gain can be further achieved through deliberate design of the reflected link[132][133].

If we consider passive beamforming design with intelligent reflective surfaces, the beamforming gain of massive intelligent reflector arrays in the near-field model no longer strictly follows the traditional "square-law growth"[140]. Instead, it converges to a constant value as the number of reflective units tends to infinity [133][141][142].
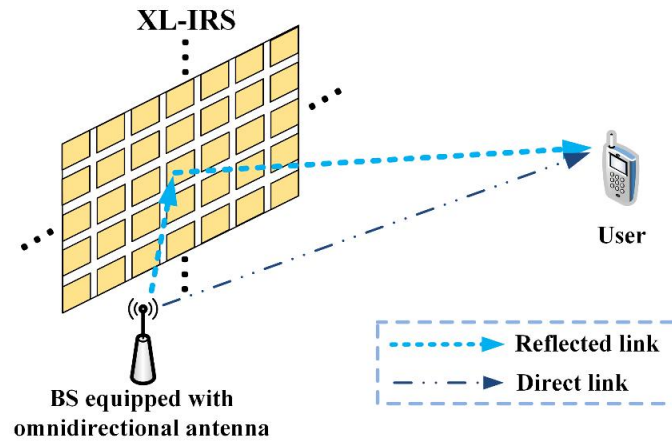
Fig. 3.27 XL-RIS aided communication system

Generally, the path loss increases with distance following a minimum loss exponent α of 2 (i.e., free-space loss model). In other words, the path loss exhibits a square decay with respect to the distance. However, reference [133] first unveiled that under near-field conditions, when the size of RIS goes infinity, the equivalent path loss of the reflected link with passive beamforming only decays with the absolute value of the distance, i.e., the equivalent minimum loss exponent α is 1 (the simulation results in Fig. 3.28 verified this conclusion).

For multi-path XL-MIMO communications, the spatial correlation is of paramount importance for the second-order statistical channel characterization. The far-field uniform plane wave (UPW) based spatial correlation only depends on the power angular spectrum (PAS), which exhibits spatial wide-sense stationarity (SWSS). By contrast, the near-field non-uniform spherical wave based spatial correlation depends on both the scatterers' angles and distances, i.e., power location spectrum (PLS), and SWSS is no longer valid [143][144].
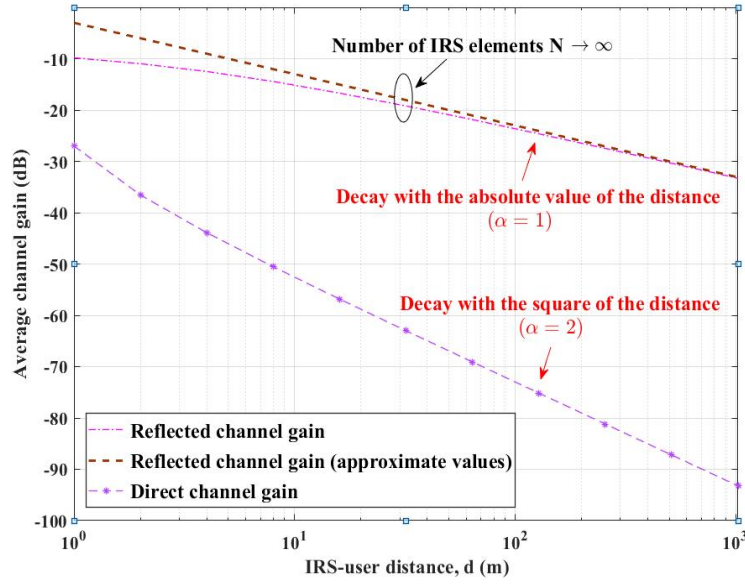
Fig. 3.28 Channel power gain versus the RIS-user distance

The investigation and derivation of fundamental bounds pertaining to near-field RIS-aided MIMO systems are presented in reference [143]. This work focuses on analyzing the spatial multiplexing gain in near-field LOS and low-scattering MIMO channels. More specifically, it establishes that the channel capacity can be achieved by diagonalizing the transmitter-RIS-receiver channel and applying water-filling power allocation to the ordered product of the singular values of the transmitter-RIS and RIS-receiver channels.

More in detail, consider the communication system sketched in Fig. 3.29, where a MIMO transmitter, e.g., a BS, communicates with a MIMO receiver, e.g., a UE, with the aid of an RIS. The transmitter and the receiver are equipped with N_F and N_B antennas, respectively.
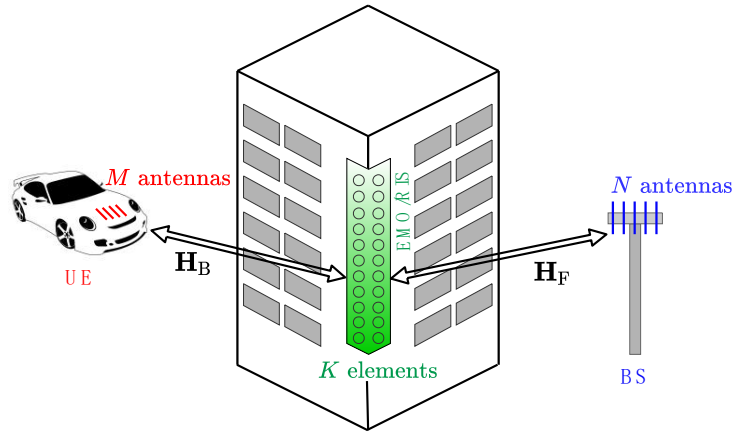
Fig. 3.29 A MIMO transmitter (a BS) communicates with a MIMO receiver (a UE) with the aid of an RIS [145].

The RIS is modeled as a MIMO array compromising K reconfigurable scattering elements. The channel matrix between the transmitter and the RIS is denoted by H_F (forward channel), and the channel matrix between the RIS and the receiver is denoted by H_B (backward or scattered channel). The end-to-end (transmitter-RIS-receiver) MIMO channel can be formulated as

$$H = H_B \, \Phi \, H_F \tag{3.15}$$

where Φ denotes the $K \times K$ matrix of reflection coefficients of the RIS. Typical designs for RIS assume that the matrix of reflection coefficients Φ is diagonal with unit modulus entries. This design eases the implementation complexity of RIS, but may not necessarily be optimal from the point of view of the power efficiency, performance, or may not consider the impact of mutual coupling in sub-wavelength (with inter-distances less than half-wavelength) implementations. Collectively, these designs fall within the umbrella of non-diagonal RIS [144]. To shed light on the optimal design of RIS from an information-theoretic standpoint, the authors in [143] depart by considering an arbitrary structure for the matrix Φ, which is not necessarily diagonal. The only imposed constraint for Φ is to be a unitary matrix, i.e., the RIS does not amplify the incident signals. They proved that the end-to-end channel capacity of the RIS-assisted MIMO communication is

$$C = \sum_{i=1}^{min(N_F, N_B)} log \left(1 + \sigma_{Fi}^2 \sigma_{Bi}^2 \frac{P_i}{\sigma_n^2} \right) \tag{3.16}$$

where σ_n^2 is the noise power, $\sigma_{Fi}^2 \, and \, \sigma_{Bi}^2$ are, respectively, the singular values of the forward and backward channels, and the power allocation $\{P_i\}$ is obtained through water-filling according to the ordered product of the singular values. The capacity is attained by designing the RIS reflection matrix as

$$\Phi = V_B \, U_F^H \tag{3.17}$$

where V_B and U_F are the right eigenvector matrix and the left eigenvector matrix of the backward and forward channels, respectively. In addition, the covariance matrix of the transmitted signal must be

$$Q = V_F \, diag(P_1, P_2, \ldots \ldots) V_F^H \tag{3.18}$$

The previous result unveils that the optimal design for RIS with a unitary matrix of reflection coefficients is non-diagonal. Non-diagonal RISs have attracted recent interest in the literature, and, supported by the previous result, they usually outperform diagonal RIS [144]. However, their practical implementation is more difficult, especially due to the complex configuration network to realize non-diagonal matrices.

Based on the optimal design for unitary RIS as above, it is, however, possible to investigate approximated diagonal (hence unitary by definition) designs for RIS that provide a rate close to the end-to-end channel capacity, as done in [143].

In addition to near-field communication, the extremely large-scale multiple-input-multiple-output (XL-MIMO) also provides new opportunities for high-precision sensing due to its ultra-high spatial resolution. In this context, the near-field sensing exhibits more practical scaling laws compared to far-field models [147]. Moreover, when the number of antennas in the XL-array goes infinity, the Cramer-Rao Bounds (CRBs) for angle estimations in XL-MIMO radar no longer decrease without limit, but converge to a constant value [148]. To investigate the fundamental limit of the proposed system's positioning accuracy, the authors in [149] obtained the FIM and CRLB while considering the antenna radiation pattern. The analysis results indicate that the Fisher Information Matrix grows quadratically with the size of the RIS (see Fig. 3.30).
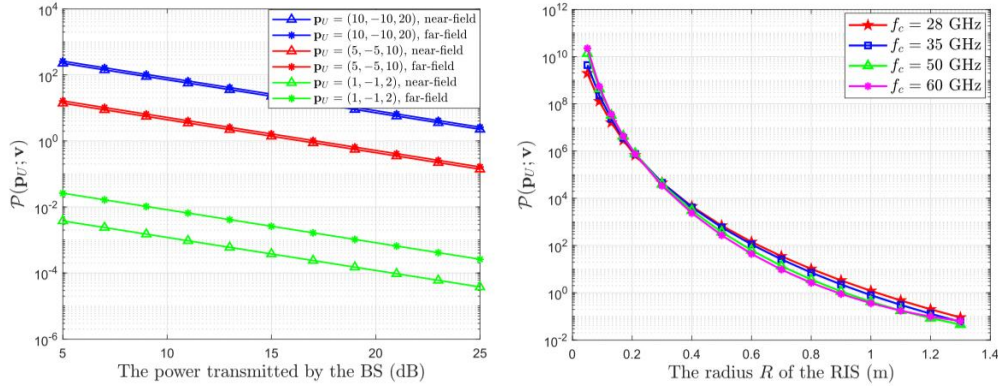
Fig. 3.30 RIS-assisted Localization Performance

Pizzo, Marzetta and other scholars have proposed to model the communication channel corresponding to a near-field massive antenna array in the wave number domain in the papers[150]-[152]. The main idea is to reconstruct the holographic MIMO (HMIMO) channel based on Fourier expansion using a finite number of sampling points of the channel in the wave number domain, as shown in Fig. 3.31. Similar to the Fourier transform between the time and frequency domains, the relationship between the spatial and wave number domains is also described by the Fourier transform, and the spatial domain channel can be characterized by the Fourier transform of the wave number domain channel, which is denoted by:

$$h(\boldsymbol{r}, \boldsymbol{s}) = \frac{1}{(2\pi)^2} \iiiint a_r(\boldsymbol{k}, \boldsymbol{r}) H_a(k_x, k_y, \kappa_x, \kappa_y) a_s(\kappa, \boldsymbol{s}) dk_x \, dk_y d\kappa_x d\kappa_y \quad (3.19)$$

where $H_a(k_x, k_y, \kappa_x, \kappa_y)$ denotes the wave number domain channel, $a_r(k, r)$ denotes the received wave vector, $a_s(\kappa, s)$ denotes the transmitted wave vector and $h(r, s)$ is the spatial domain channel. From the above equation, it can be seen that the channel model consists of three main components, i.e., the transmit and receive wave vectors and the wave number domain channel. Therefore, the modeling of the spatial domain channel can be equated to the alternative modeling of the wave number domain channel, which is given by the following equation:

$$H_a(k_x, k_y, \kappa_x, \kappa_y) = S^{\frac{1}{2}}(k_x, k_y, \kappa_x, \kappa_y) W(k_x, k_y, \kappa_x, \kappa_y) \quad (3.20)$$

where the wave number domain channel can be expressed in terms of the channel spectral density $S(k_x, k_y, \kappa_x, \kappa_y)$ related to the scattering environment and antenna arrangement. $W(k_x, k_y, \kappa_x, \kappa_y)$ relates to the stochastic properties of the channel. Wave number domain channels generally have a sparse structure, i.e., they are dominated by a finite number of nonzero coefficients. Based on sampling theory, the wavelength domain channel can be approximated by uniformly sampling a finite integral region. The accuracy of the channel approximation depends on the number of points of the region being sampled. As the computational complexity increases, one can obtain a more accurate representation of the channel by generating more samples.
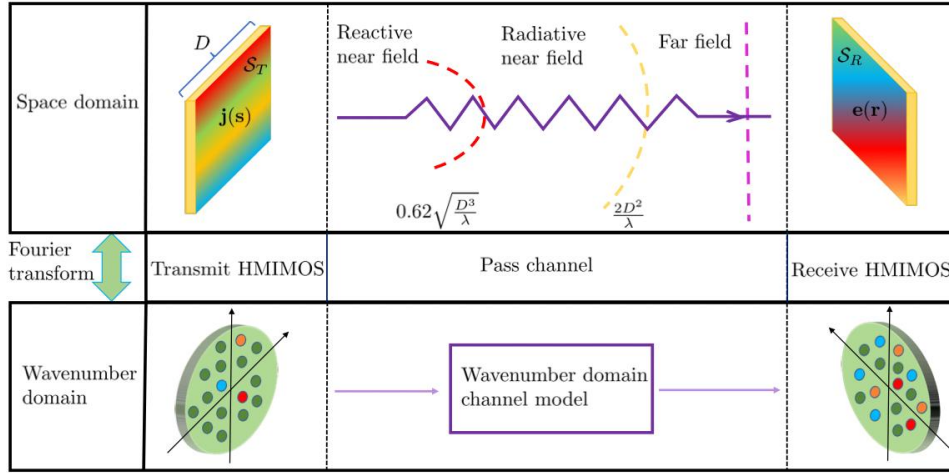
Fig. 3.31 Fourier plane wave expansion channel model

The simulation results corresponding to the spherical wave channel modelling are shown in Fig. 3.32, and it can be seen that the far-field Rayleigh fading model is no longer applicable at this point, while the modelled channel model coincides with the physical Clarke model.
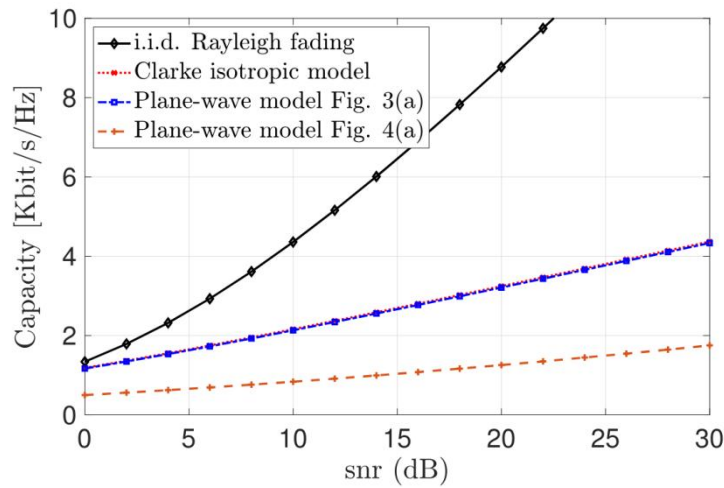
Fig. 3.32 Fourier plane wave expansion channel capacity simulation

The contribution [154] characterized the theoretical capacity limits of near-field communications based on electromagnetic propagation channels in Fig. 3.33. From the Maxwell's equations and the Helmholtz wave equation which describe the electromagnetic wave propagation properties, [154] used the Green's function to establish an electromagnetic near-field channel model for extremely large-scale discrete array with single-polarized antennas. Then, for the single-user scenario, the authors derived the closed-form capacity limit when the array has an extremely large aperture. They also revealed the impact of antenna polarization mismatch and discrete aperture on the system performance in the near field. Additionally, based on the proposed channel model, the authors proposed a more general expression for near-field Rayleigh distance, depicting the influence of signal incident angles and non-stationary array power on the field boundaries. Furthermore, for the multi-user scenario, the authors exploited the non-stationary features extracted from the single-user scenario to propose two low-complexity linear precoding schemes based on the concept of visibility regions and utilizing the

method from graph theory. These algorithms effectively addressed the high computational complexity challenges associated with extremely large-scale antenna arrays.
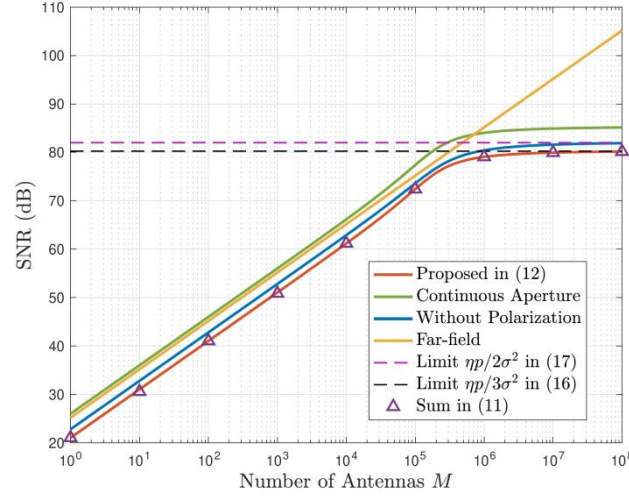
Fig. 3.33 Near-field electromagnetic channel capacity limit

The reference [155] provides a comprehensive summary overview of the current principles and technologies of HMIMO array near-field communication at the software and hardware levels, which is conducive to a full understanding of the principles, technological evolution, and development direction of HMIMO near-field communication (in Fig. 3.34).

Fig. 3.34 HMIMO Communication Application Scenarios

3.4.2 Electromagnetic Normalization of Near-Field Channel Matrix

Compared to traditional MIMO technology, HMIMO employs densely packed or even three-dimensional antenna arrays to achieve finer control over the spatial characteristics of electromagnetic waves, as illustrated in Fig. 3.35. In near-field HMIMO systems, the normalization method of the channel matrix plays a crucial role in evaluating channel capacity. Traditional approaches often assume that the average gain of subchannel is 1. However, this assumption fails to accurately capture the electromagnetic characteristics of different array topologies (e.g., three-dimensional arrays), potentially leading to capacity estimates that deviate from physical reality [156].
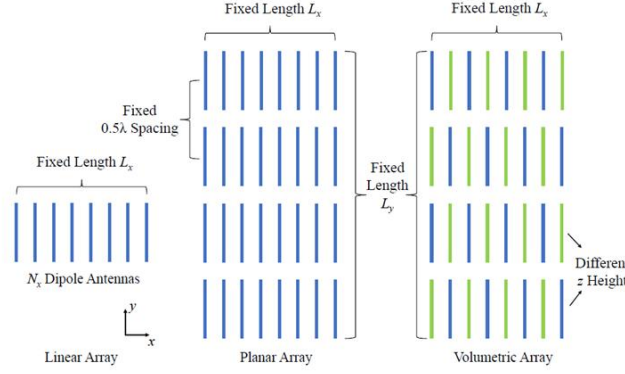
Fig. 3.35 Three types of near-field holographic array topologies

An electromagnetic normalization method for the HMIMO channel matrix is introduced here, accounting for array gain, antenna coupling, and near-field/far-field effects. By incorporating these physical factors, the normalization method provides a more accurate representation of the channel matrix, improving the precision of capacity evaluation. The traditional channel matrix normalization method assumes that the square of the Frobenius norm of channel matrix equals the product of the number of transmit and receive antennas

$$||\mathbf{H}||_F^2 = N_t N_r \tag{3.21}$$

where $\mathbf{H}$ represents the channel matrix, N_t and N_r denote the number of transmit and receive antennas, respectively. Under this assumption, the average subchannel gain is 1, and the normalization of the channel matrix depends solely on the number of antennas. However, this method overlooks the electromagnetic characteristics of the antenna array, leading to errors when dealing with complex dense or three-dimensional arrays. Electromagnetic-based channel matrix normalization, in contrast, accounts for array gain. In Tx non-coherent and Rx coherent scenario, the channel matrix should be normalized as

$$||\mathbf{H}||_F^2 = N_t G_r \tag{3.22}$$

While in Tx coherent and Rx coherent scenario, the channel matrix should be normalized as

$$||\mathbf{H}||_F^2 = G_t G_r \tag{3.23}$$

where G_t and G_r represent the average far-field (realized) gains of the Tx and Rx antenna array in the target directions (or angular range). This gain depends on the array topology, beamforming direction, and mutual coupling between antennas. The introduced normalization method effectively captures all electromagnetic characteristics of the antenna array. For near-field HMIMO communications, based on the dyadic Green's function [156], the channel matrix normalization can be formulated in a manner similar to the far-field case as

$$||\mathbf{H}^{pq}||_F^2 = G_t^{pq} G_r^{pq} \tag{3.24}$$

where G_t^{pq} and G_r^{pq} denote the near-field gains of the Tx and Rx array, p and q represent the polarizations of field and source, respectively.

Channel matrix normalization requires computing the array gain in the target direction. The far-field gain of an antenna array with an arbitrary topology can be evaluated using full-wave simulation, analytical method, or physical method. Full-wave simulations, performed using commercial software such as CST and HFSS, can directly compute the gain but are time-consuming and require significant computational resources. Alternatively, analytical methods provide a more efficient approach by integrating the radiation intensity U to compute the gain, expressed as

$$G(\theta,\phi) = \frac{U(\theta,\phi)}{\frac{1}{4\pi}\int_0^{2\pi}\int_0^{\pi} U(\theta,\phi)\sin\theta\, d\theta d\phi} \tag{3.25}$$

In the numerator, the double integral of the radiation intensity represents the total radiated energy, which has a closed-form solution. The detailed derivation can be found in[156]. The physical method relies on the effective aperture of the antenna array

$$G = 4\pi A_e/\lambda^2 \tag{3.26}$$

The effective aperture A_e of the array depends on the projected area of the array in the target direction. Specifically, the effective aperture for planar array is $L_x L_y \cos\theta$, and the effective aperture for volumetric array is $L_x L_y \cos\theta + L_x L_z \sin\theta \sin\phi + L_y L_z \sin\theta \cos\phi$, where L_x, L_y, and L_z denote the size of the array along three dimensions. The embedded radiation efficiencies of the array elements can also be approximately estimated based on an extension of Hannan's limit [156]. Based on the three methods described above, we can calculate the far-field average (realized) gain of the array in the target directions and use it to normalize the channel matrix accordingly.

In near-field communication scenarios, we can adopt the conceptual approach used for defining far-field gain, and compute near-field radiation intensity and total radiated energy based on the dyadic Green's function. Unlike in the far field, the relationship between the electric and magnetic fields in the near-field region is more complex, as they are no longer simply related by a wave impedance. Therefore, the calculation of near-field gain should rely on the Poynting vector to accurately characterize the radiation intensity, formulated as

$$S_p = \frac{1}{2} Re\left[\mathcal{E}_p(\mathbf{r}) \times \mathcal{H}_p^*(\mathbf{r})\right] \tag{3.27}$$

The vector electric field $\mathcal{E}_p(\mathbf{r})$ and magnetic field $\mathcal{H}_p^*(\mathbf{r})$ can be computed using the electric dyadic Green's function and the magnetic dyadic Green's function, respectively. Based on these field components, the radiation intensity for the target polarization can be further determined as

$$U_{pq}(\theta,\phi,R) = r^2 S_{pq}(\theta,\phi,R) \tag{3.28}$$

where r is the reference distance between Tx and Rx, and $R = |\mathbf{r} - \mathbf{r}'|$. Then we can obtain the near-field gain following the similar definition of gain in the far field. This method provides an accurate characterization of near-field properties, including cross-polarization and beamforming effects. Additionally, it enables the modeling of various gain losses specific to the near-field environment, as illustrated in Fig. 3.36.
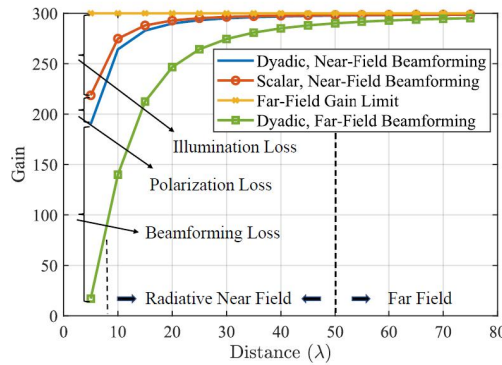

Fig. 3.36 Possible gain losses in near-field MIMO communications

These gain losses can typically be effectively compensated using signal processing techniques, while the gain values used in the normalization process should be flexibly chosen based on the

specific scenario. Additionally, corresponding empirical physical formulas are also proposed [156], which simplify the computational complexity in practical applications.

For far-field communication scenarios, based on the Kronecker model in rich multipath environments, we compared the channel capacities of planar arrays under different normalization methods. For near-field communication scenarios, we analyzed the variation of channel capacity with respect to the transmit-receive distance under different near-field loss conditions. The results are shown in Fig. 3.37. From the results, it is evident that traditional normalization methods introduce significant errors in capacity evaluation, especially when dealing with dense and volumetric arrays, where their limitations become more pronounced. These methods fail to accurately characterize the gain limits of antenna arrays, and do not account for efficiency losses caused by mutual coupling effects between antennas. As a result, the capacity evaluation deviates from the actual physical scenario. Particularly, in near-field communication, these gain losses are primarily concentrated in the reactive near-field region. Within this range, the characteristics of the electromagnetic field differ significantly from those in the far field. If conventional far-field beamforming methods are directly applied, severe performance degradation may occur.
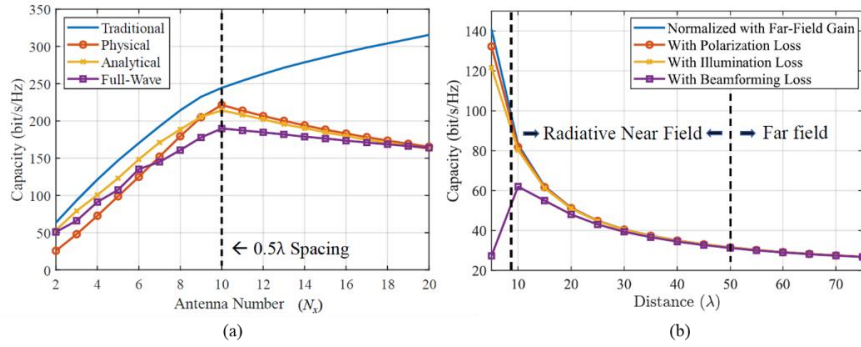
Fig. 3.37 Far-field and near-field capacities of planar arrays using different normalization methods. (a) Far-field analysis. (b) Near-field analysis.

3.4.3 Near-Field Measurement and Near-Field to Far-Field Transformation

Electromagnetic scattering characteristics refer to the various information contained in the scattered waves formed by the radiation of induced currents on the surface of an object when electromagnetic waves are irradiated. Measurement of electromagnetic scattering characteristics refers to obtaining information such as the radar cross section (RCS) and its statistical characteristics, angular scintillation and its statistical characteristics, polarization scattering matrix, and distribution of multiple scattering centers of a target through experimental instruments or professional testing equipment [157][158]. According to different testing distances, it can be classified as far-field measurement, compact-field measurement, and near-field measurement.

Far-field measurement requires a testing distance of $R \geq 2d^2/\lambda$, where d is the maximum size of the target and λ is the testing wavelength. Therefore, a larger space is required. Outdoor far-field testing sites require a large amount of land resources, and the site is also affected by natural meteorological environments such as precipitation, light, temperature, humidity, and wind speed. Although indoor far-field measurement avoids interference from the testing environment, it still requires the construction of large-scale darkroom buildings and the extensive installation of absorbing materials, which makes its construction and maintenance costs high.

Compact-field measurements occupy less space than far-field measurements. However, the contraction field requires high technical requirements and limited static area, making conducting full-scale testing for large targets impossible. Meanwhile, its higher cost makes it not an optimal choice.

Indoor near-field testing is a testing method that has developed in recent decades. Near field refers to testing distances less than the classical far-field conditions ($R<2d^2/\lambda$). Indoor near-field testing does not meet far-field conditions, and the measured data differs from the physical definition of scattering cross-sectional area, which cannot directly reflect the scattering characteristics of the target. The near-field scattering characteristics test results must be transformed into the target scattering cross-section obtained under far-field conditions through near-field and far-field transformation techniques. Therefore, high transformation accuracy, fast speed, and near-field and far-field transformation technology are the most critical factors determining the performance of indoor near-field testing fields. Indoor near-field testing can be divided into planar near-field scanning, cylindrical near-field scanning, and spherical near-field scanning according to the scanning method, and each scanning method requires corresponding near-field and far-field transformation algorithms. In recent years, near-field and far-field transformation technology has become a focus of research for scholars in target characteristic testing both domestically and internationally. The near-field and far-field transformation algorithm based on synthetic aperture imaging, studied by LaHaier, a scholar from General Dynamics in the United States, has become a hot topic of industry experts due to its simple implementation, high transformation accuracy, and good denoising function.

Early methods for measuring target characteristics were limited by testing equipment or locations and were often tested through narrowband and angle scanning. Even today, the ground plane field, which is most widely used in field testing, is more suitable for narrowband testing of targets [159]. The commonly used methods for near-far field transformation in narrowband measurements include Merlin filtering [160], equivalent aperture secondary radiation method [161], Hankel extrapolation method [162][163], etc.

Narrowband measurement conditions limit the near-field to far-field transformation technology in narrowband measurement. Traditional algorithms use certain approximations in the derivation process, which limits their applicability. Broadband measurement of targets can obtain electromagnetic scattering characteristics at multiple frequency points, and the measurement results contain more dimensional scattering information, which can improve the accuracy of single station near-field and far-field transformation[162]. Spherical near-field to Far-Field Transformation (CNFFFT) is commonly used in broadband measurements for near-field and far-field transformation. The CNFFFT algorithm, proposed by the LaHaie team [163]-[167], is a highly accurate and widely used near-field and far-field transformation algorithm in engineering applications.

4 Channel Measurement and Modeling of Near-field

In the era of 5th generation (5G), 3D MIMO is considered to be an important practical technology that enhances the performance of communication systems [168]. When the communication distance between BSs and users is greater than the Rayleigh distance, users are located in the far-field region of the BS. At this point, the electromagnetic waves reaching the BS array can be approximated as plane waves. Conversely, electromagnetic waves reaching the BS array need to be modeled as spherical waves when the communication distance is less than the Rayleigh distance [35]. At present, the new mid-band has attracted extensive attention from industry and academia[169]. In December 2023, the 3GPP, the leading standardization organization driving the development of the global mobile communications industry, identified the first 16 RAN proposals for Rel-19, including the 7-24 GHz channel model research section, which includes near-field and spatially non-stationary channel measurement and modeling. Currently, the research project is in the middle stage and will be completed by mid-2025 [170]. In the next generation communication systems, the array size and frequency will continue to increase, and the near-field range of ELAA systems can reach several tens of meters or even hundreds of meters. In typical deployment scenarios, it is necessary to consider near-field communication[171]-[174]. Understanding channel characteristics and models is a prerequisite for the design and technical evaluation of communication systems. Therefore, comprehensive channel measurements and accurate channel characterization are needed. Companies around the world have proposed various implementations of 3GPP channel models in the FR3 band, including near-field propagation and Spatial non-Stationary (SnS) characteristics.

This section will introduce near-field channel research from the dimensions of channel measurement and channel modeling, including channel measurement, statistical models, deterministic models, near-field channel spatial non-stationary characteristics, continuous element channel models, discrete element channel models, etc.

4.1 Near-field Channel Measurement

Channel measurement equipment is used to obtain the Channel Impulse Response (CIR) of the antennas at the transmission and reception ends of the link. As shown in Fig. 4.1, there are mainly two types of channel measurement platforms: time-domain channel measurement based on correlation and frequency-domain channel measurement. Correlation-based channel measurement platforms have the advantages of short sampling time and flexible operation at the transmission and reception ends. However, the disadvantages include limited operating bandwidth, limited system dynamic range, and complex synchronization between the transmission and reception ends [175]-[177]. Channel measurement platforms based on Vector Network Analyzers (VNAs) belong to the frequency-domain channel detection system. The advantages of this type of system include scalable working frequencies and bandwidth, high dynamic range, and ease of calibration. However, the frequency scanning time for such detection systems is typically long [178][179]. Therefore, VNA-based channel measurement platforms are usually limited to static scenarios. For the measurement of near-field MIMO channels, greater attention should be paid to the measurement capabilities in the spatial domain, as effectively utilizing the spatial dimension is a key task in near-field MIMO technology.

To achieve the measurement of near-field channels, there are currently several approaches for capturing the spatial distribution characteristics of the channels, including real antenna arrays, switchable antenna arrays, phased arrays, and virtual antenna arrays. However, when it comes to near-field channel measurements involving hundreds of antenna elements, most of these approaches face challenges. For real antenna arrays, switchable arrays, and phased arrays, the hardware cost and calibration complexity become very high due to the need for large arrays with physical dimensions.

Virtual antenna arrays are formed by mechanically moving a single antenna unit (or multiple antenna elements in the case of small antenna arrays) to create a large antenna array [168][180]-[182]. This method allows for convenient implementation of scalable array configurations and is the most commonly used in large-scale MIMO channel measurements. However, due to the slow mechanical movement, the measurement scenarios of virtual antenna arrays are limited to quasi-static environments.
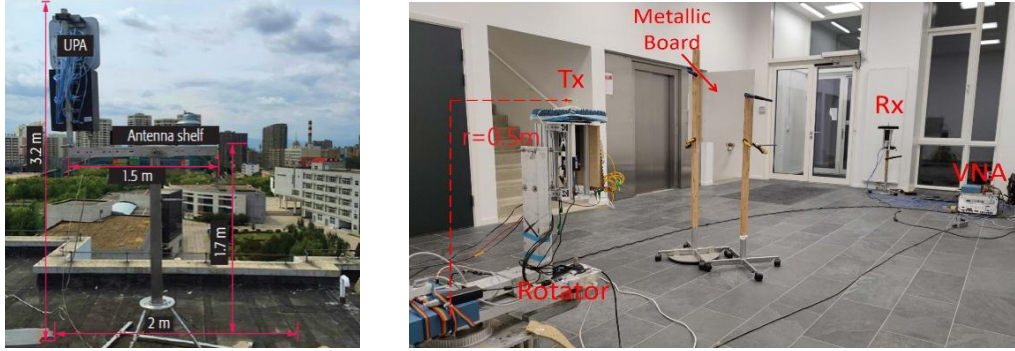

(a) Time domain   (b) Frequency domain

Fig. 4.1 Channel measurement platforms in time and frequency domains[168][182]

As shown in Fig. 4.2, near-field channel measurements based on a virtual array with a VNA. A rotator is used to achieve a uniformly circular array with different radii. For each element, the VNA performs frequency sweeping to collect the channel impulse response. In the current measurement setup, both the transmitter and receiver are equipped with omnidirectional antennas, and the line-of-sight distance is 6.5 meters. A metal plate is placed between the transmitting and receiving antennas as an obstacle. The Rx antenna forms a virtual circular array with a radius of 0.5 meters by mechanically rotating from 0° to 360° using a turntable, with a rotation step of 0.15°, forming 2400 antenna elements. The measurement frequency range is from 95 GHz to 105 GHz. From the results, several "S"-shaped curves can be observed, identified as multipath components with different delays on different array elements. This is a result of the significant variation in the propagation distance of multipath due to the near-field spherical wavefront effect. Additionally, in this scenario, most of the multipath measurements appear as incomplete "S"-shaped curves distributed across some elements, indicating the spatial non-stationarity of the channel. Partial obscuration occurs because some physically limited objects in the scene prevent the complete capture of multipath across the entire large array. The results suggest the presence of near-field and spatially non-stationary characteristics in ultra-large-scale MIMO channels. In reference[183], based on a time-domain channel measurement platform, virtual array measurements with 256 elements were conducted in the 3.5 GHz frequency band under LOS and NLOS conditions. Changes in cluster appearance and disappearance were observed, and corresponding models were established based on birth-death processes.
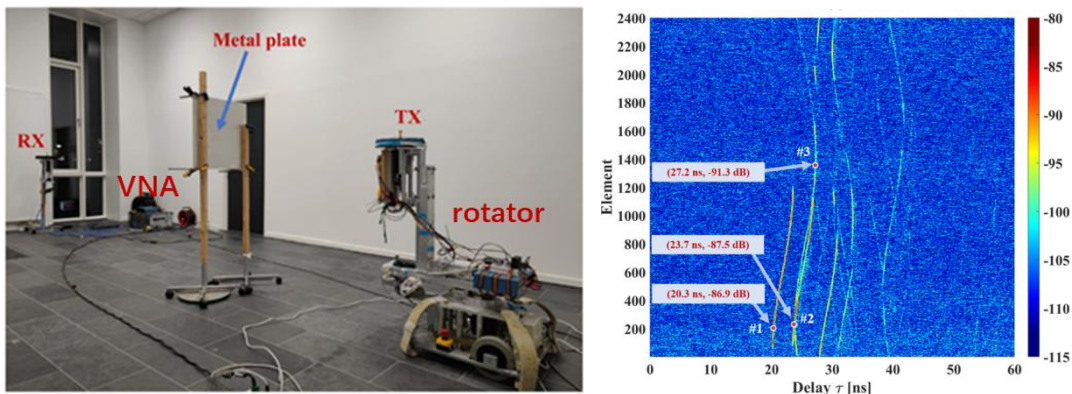
Fig. 4.2 (a) Near-field channel measurements with a virtual array based on VNA. (b) Channel impulse response on the array elements[183]

The measurement is conducted at the Shahe Campus of the Beijing University of Posts and Telecommunications, a typical Urban Macro (UMa) scenario. The transmitter is located on the roof of the teaching and experimental building, about 27.8 meters high, and the receiver is located on the ground, about 1.7 meters high. The measurement diagram is shown in Fig. 4.3. Trees and other things on the road can cause scattering of the signal.

(a) Scenario of XL-MIMO channel measurement   (b) Layout of XL-MIMO channel measurement
Fig. 4.3 XL-MIMO channel measurement [184].

As the antenna array aperture increases, the distance from the BS to the mobile terminal may change from the far field range to the near field range. Currently, the plane wave propagation based on the far field assumption is no longer applicable and is replaced by spherical wave propagation. Therefore, the angle, phase, and delay of different array areas of the BS reaching the mobile terminal will change accordingly.

The result at the Rx1 is shown in Fig. 4.4. Since the multipath angle distribution is relatively concentrated, only the results of the LoS path and one NLoS path are taken for observation. It can be seen that with the change of the subarray position, the AoD of the LoS and NLoS paths have shifted. These obvious angle shifts prove the existence of the spherical wavefront at Rx1.
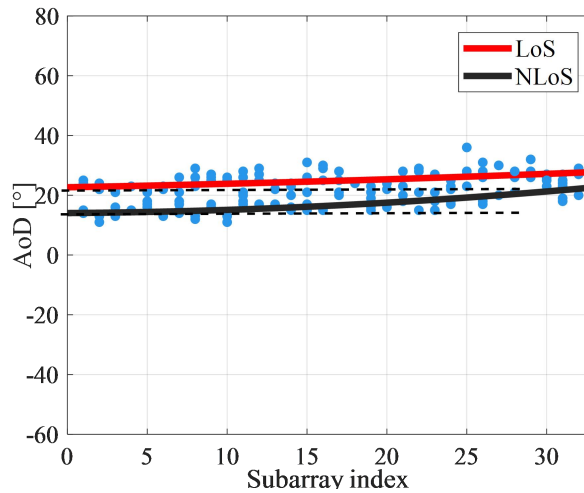
Fig. 4.4 Distribution of AoD in the array domain at Rx1

4.2 Near-field Channel Simulation

Near-field is a concept with relativity, for large-scale antenna array, based on the distance to the center of the antenna from near to far, there are three zones that can be classified, respectively: reactance near-field zone, radiation near-field zone (Fresnel zone) as well as the radiation far-field zone

(Fraunhofer zone). In the reactance near-field zone, the radiation pattern is similar to flat ripples with non-significant amplitude variations; In the radiation near-field zone, the antenna pattern is smoother with a tendency to beam forming; In the radiation far-field zone, the main lobe as well as the side lobe have been completed forming. The boundary distance between the radiated near field and the radiated far field is called the Rayleigh distance. In this scenario, the far-field condition is still satisfied between the transmitting antenna element and the receiving antenna element.

For the case where the distance between the transceiver antenna elements is also near-field, the simulation results are shown as in Fig. 4.5.
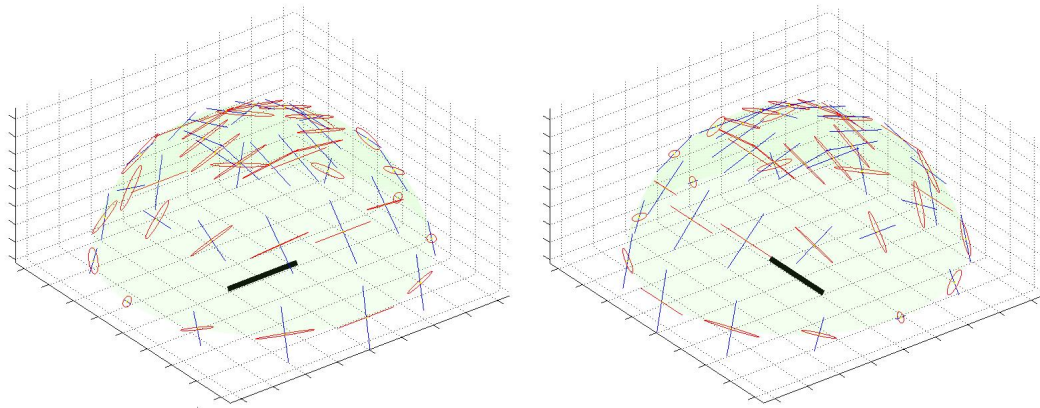
(1) The near field electromagnetic field distribution for horizontal polarization electric dipole (left).
(2) The near field electromagnetic field distribution for vertical polarization electric dipole (right).
Fig. 4.5 Near field simulation in element level

As shown in Fig. 4.5, the electric and magnetic field are demonstrated corresponding to horizontally and vertically polarized current sources in the near-field, respectively. The black line at the center of the hemisphere indicates the direction of the current source, the red line indicates the trace formed by the end of the electric field strength vector, and the blue line indicates the trace formed by the end of the electric field strength vector. It can be observed that the electric field strength vector exhibits elliptical polarization in the near field, and the axial ratio, major axis inclination angle, and ellipticity angle of the electric field strength at the near field points with different orientation angles are different, while the magnetic field strength exhibits stable linear polarization characteristics, which means that Poynting vector is a time-varying vector in the near field, which is a major difference between the element-level near field and the panel-level near field.

From point of view of engineering commercialization, the assumption of far-field between the transmitting element and the receiving element is generally still satisfied even for large-scale antenna arrays.

For the case where the transceiver antenna is in the near-field and the LOS/NLOS states between the elements are consistent, the channel states between the other element of the transceiver antenna need to be estimated based on the channel states of the Tx/Rx antenna's anchor elements, and the channel states between other elements of the Tx/Rx antennas can be derived based on the dual-mobility spatial consistency model when it is assumed that the NLOS paths of the wireless channel between the anchor elements are dominated by the specular reflections, assuming there are no spatial non-stationarity between any two pairs of elements of Tx and Rx antennas, such as channel birth and death etc.

To configure the antenna array as depicted in Fig. 4.6, operating at 6 GHz. The simulation results of spatial consistency for the intra-element in BS antenna are shown Fig. 4.8 - Fig. 4.10 in near field with a frequency of 6 GHz and 1024 elements (assuming the scenario that the terminal antenna is a single element).
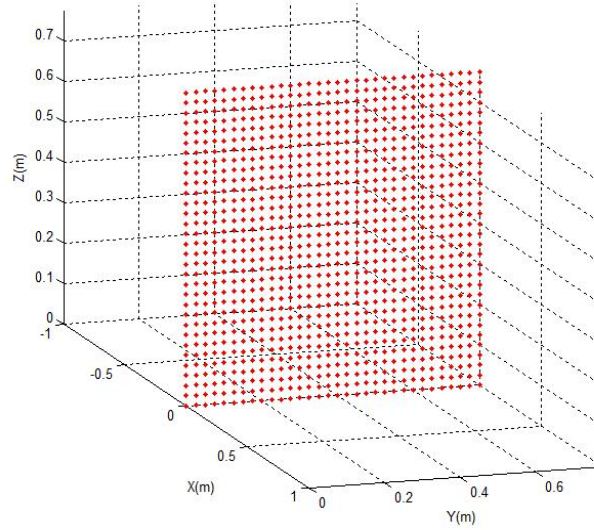
Fig. 4.6 The deployment of large antenna array (6GHz, 1024elements)
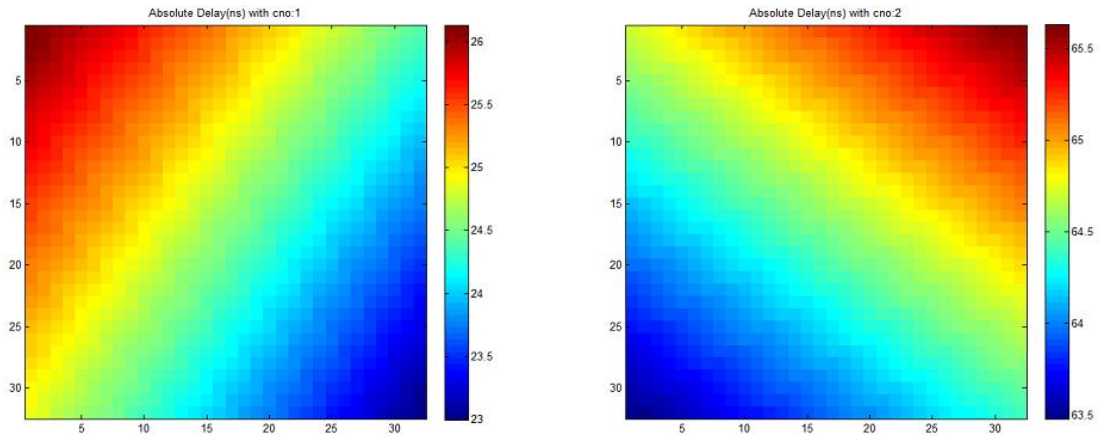
(1) Absolute delay of the 1st ray per element in BS antenna (left).
(2) Absolute delay of the 2nd ray per element in BS antenna (right).
Fig. 4.7 Absolute delay of a ray per element in BS antenna
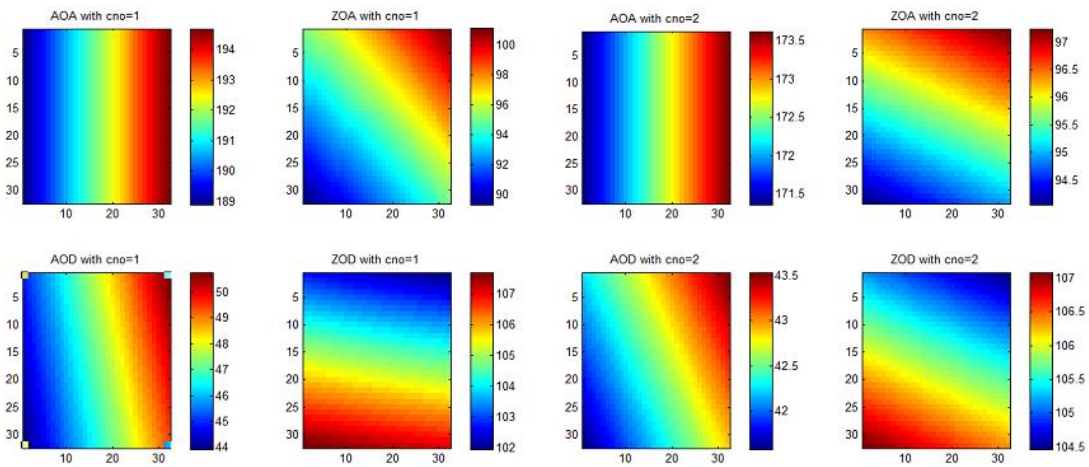
(1) AoA/AoD/ZoA/ZoD of the 1st ray per element in BS antenna (cno=1)
(2) AoA/AoD/ZoA/ZoD of the 2nd ray per element in BS antenna (cno=2)
Fig. 4.8 AoA/AoD/ZoA/ZoD of a ray per element in BS antenna
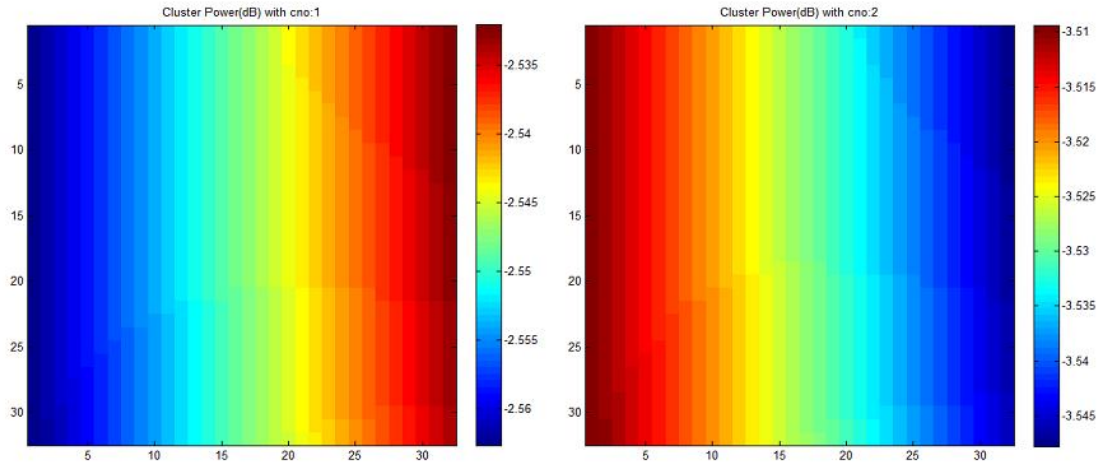
(1) Power gain of the 1st ray per element in BS antenna (cno=1)
(2) Power gain of the 2nd ray per element in BS antenna (cno=2)
Fig. 4.9 Power gain of a ray per element in BS antenna
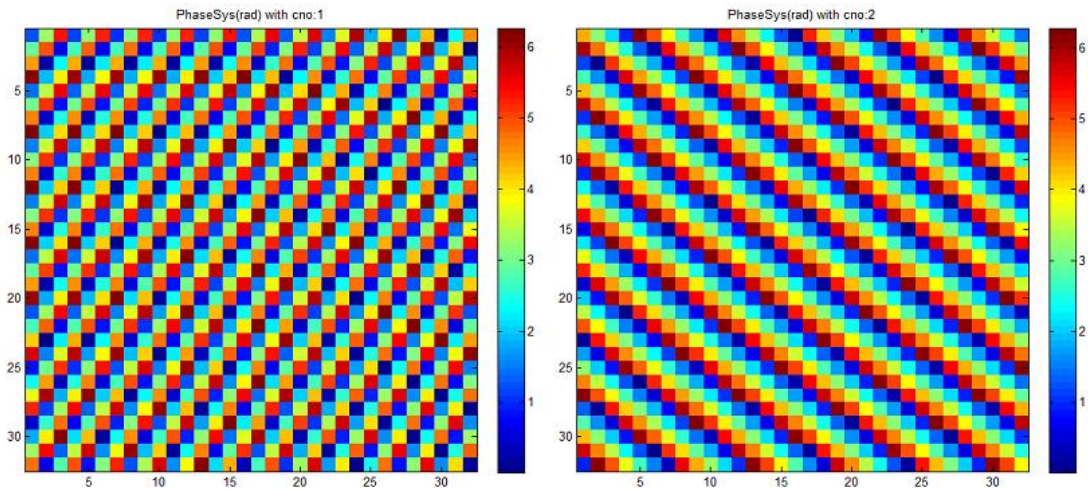
(1) Phase of the 1st ray per element in BS antenna (cno=1)
(2) Phase of the 2nd ray per element in BS antenna (cno=2)
Fig. 4.10 Phase of a ray per element in BS antenna

In the case of the presence of scatterers in the near-field of antenna arrays, it is necessary to study the correlation characteristics of the wireless channel among the elements in large antenna arrays based on the near-field scattering model (electromagnetic equations, high-frequency solution, or full-wave numerical solution).

As shown in Fig. 4.11, for an perfect electric conductor (PEC) conductor sphere near the large-scale array, the incident wave vector of the the plane wave is shown as the blue line, and the black points in the antenna array indicate the region of the incident wave vector that is blocked by the scatterer, and the red points indicate the region that is not blocked. The simulation results of the magnitude and absolute phase are shown in Fig. 4.12 to Fig. 4.13 per element after blocking , reflection and diffraction by scatter.
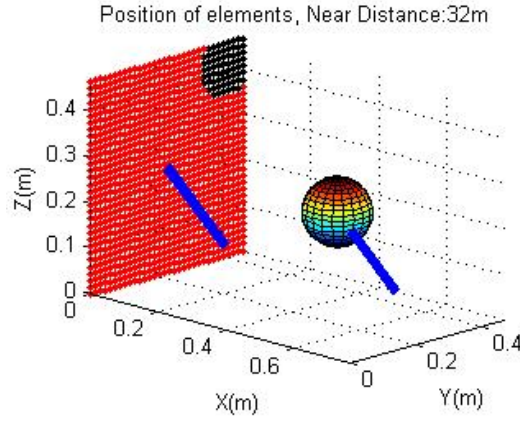
Fig. 4.11 The position of antenna array and PEC sphere as well as the incident wave vector

Signal Strength Gain(dB)
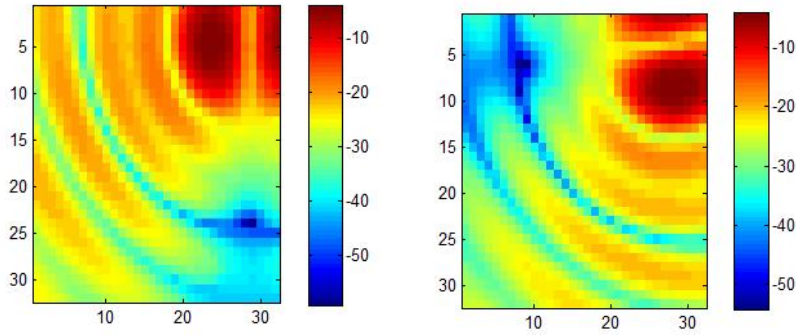
Fig. 4.12 The distribution of signal strength gain in antenna array due to H-pol and V-pol incident

Phase (rad)
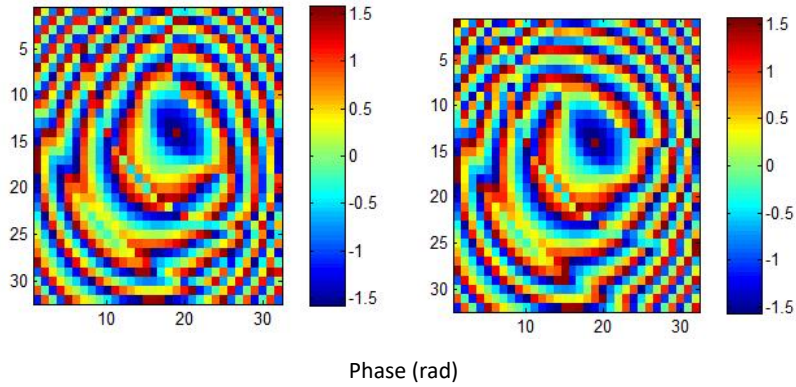
Fig. 4.13 The distribution of phase in antenna array due to H-pol and V-pol incident

As shown in Fig. 4.14, for a random scatter near the large-scale array, the incident wave vector of the plane wave is shown as the blue line, and the black points in the antenna array indicate the region of the incident wave vector that is blocked by the scatterer, and the red points indicate the region that is not blocked. The simulation results of the magnitude and absolute phase are shown in Fig. 4.15 to Fig. 4.16 per element after blocking, reflection and diffraction by scatter.
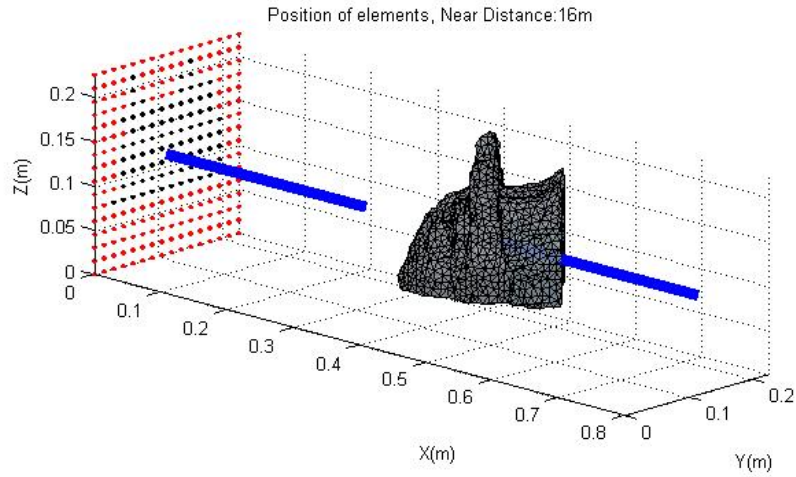
Fig. 4.14 The position of antenna array and random scatter as well as the incident wave vector
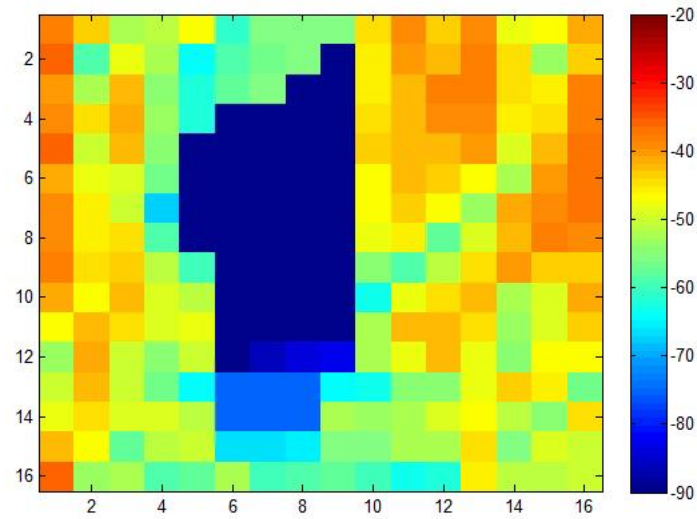
Signal Strength Gain(dB)

Fig. 4.15 The distribution of signal strength gain in antenna array due to V-pol incident
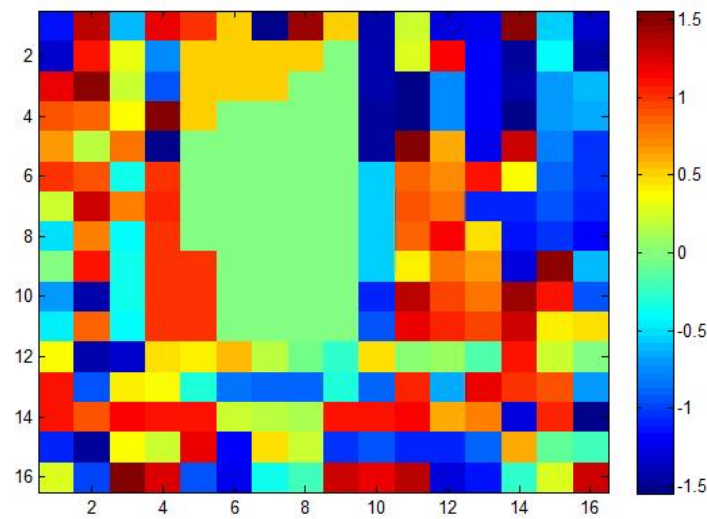
Phase (rad)

Fig. 4.16 The distribution of phase in antenna array due V-pol incident

4.3 Near-field Channel Modeling

There is a lot of work in the literature on massive MIMO channel modeling that considers near-field effects. For deterministic channel modeling, the Mobile and wireless communications Enablers for the Twenty-twenty Information Society (METIS) project [185] proposed a massive MIMO channel model based on ray tracing, which can represent spatial non-stationary characteristics. However, the high computational complexity and lack of detailed digital maps and material databases make this deterministic modeling method less applicable in some scenarios with complex environments. In [186], the authors proposed a deterministic ray-tracing method for THz channel model, and showed that the ray-tracing channel model captured the propagation characteristics well. For statistical channel modeling, the COST 2100 model [187] proposed the concept of the visible region for the first time to represent the spatially non-stationary channels of MIMO antennas, confining the cluster of mobile terminals to a limited region. In [188], the concept of the visible region is further extended to massive MIMO antenna arrays. Specifically, only the array elements in the visible region can see the cluster, while the array elements outside the visible region cannot. Based on the concept of the visible region, the birth and death processes on the array axis were used in [189] for statistical characterization of spatial non-stationary properties. To verify the model, statistical properties such as correlation and average lifetime of clusters on the matrix are analyzed numerically. In [190], based on channel characteristics, a stationary interval partitioning method on XL-MIMO arrays is studied. In [191], an efficient channel simulation method applied to ray tracing was proposed to realize the simulation of near-field and spatially non-stationary channels under the deployment of very large-scale antennas with guaranteed accuracy.

In [192], a new massive MIMO channel model framework is proposed, which accounts for near-field and spatial non-stationarity properties. Massive MIMO channels with near-field and spatially non-stationary properties are captured by spherical wave propagation and physical multipath propagation mechanisms. The validation based on channel measurement and model proves its effectiveness, which is briefly described below.
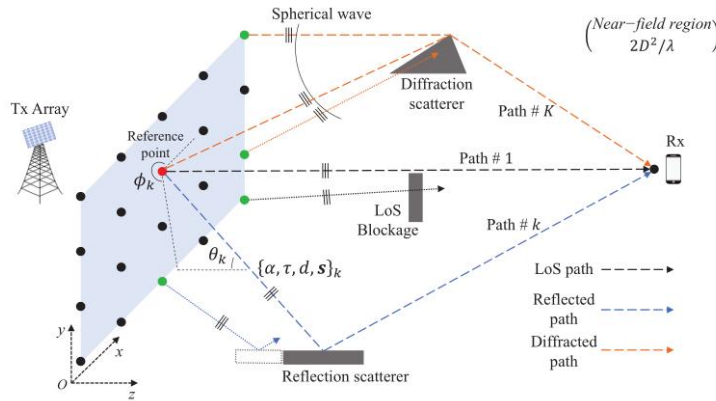
Fig. 4.17 Spherical propagation with the SnS characteristic

We assume there exist K SnS spherical-propagation paths between the Tx array and Rx. The massive MIMO channel at the frequency f can be modeled as a superposition of CFRs of the K paths on the array. It can be succinctly expressed as

$$\mathbf{H}^{sns}(f) = \mathbf{S} \odot \mathbf{A}(f) \cdot \mathbf{H}(f) \tag{4.1}$$

where $\mathbf{H}^{sns}(f)$ comprises M complex values, i.e., $\mathbf{H}^{sns}(f) \in C^{M \times 1}$, $f \in [f_L, f_U]$ denotes the frequency within the designed range, and represents elementwise product operation. A novel matrix $\mathbf{S}$ is introduced in the proposed modeling framework for the SnS property, which represents a

non-stationary parameter matrix reflecting the non-stationary characteristics of the channel. $\mathbf{H}(f) \in \mathbb{C}^{K \times 1}$ denote CFRs at f of the K paths at the reference point.

$$\mathbf{H}(f) = [a_1 e^{-j2\pi f \tau_1}, \cdots, a_k e^{-j2\pi f \tau_k}, \cdots, a_K e^{-j2\pi f \tau_K}]^T \tag{4.2}$$

where $\{\alpha_k, \tau_k\}$ represent the complex amplitude and propagation delay of the kth path, respectively. $(\cdot)^T$ denotes the transpose operation. $\mathbf{A}(f) \in \mathbb{C}^{M \times K}$ is the array manifold matrix. The manifold projected on the mth antenna element by the kth path, i.e., A's (m, k)th entry $a_{m,k}$, can be represented by the transfer difference of the mth element with respect to the reference point, i.e.,

$$a_{m,k}(f) = \frac{\|\mathbf{d}_k\|}{\|\mathbf{d}_{m,k}\|} e^{-j2\pi f \frac{\|d_{m,k}\| - \|d_k\|}{c}} \tag{4.3}$$

where c is the light speed and $\|\cdot\|$ represents the Euclidean norm of the argument. $\mathbf{d}_k$ denotes the vector pointing from the reference point to the first scattering source of the kth path propagation route. $\mathbf{d}_{m,k}$ denotes the vector pointing from the mth antenna element to the source point.
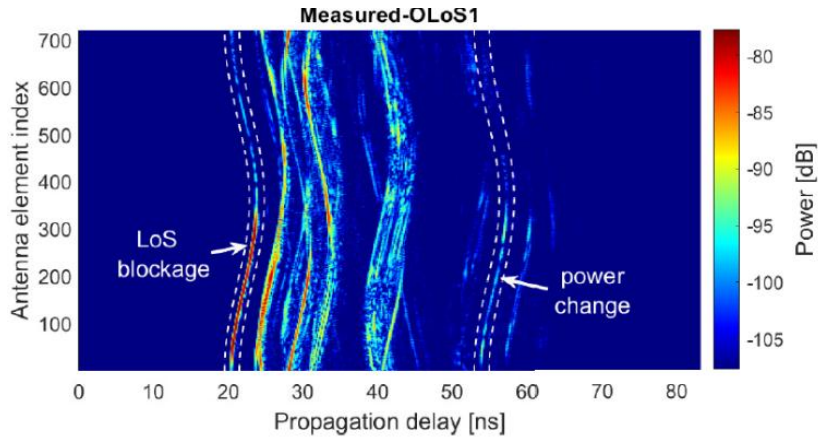

(a)
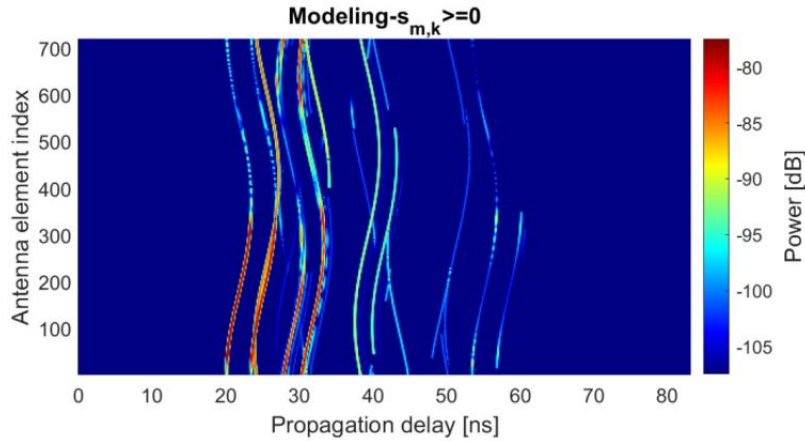
(b)

Fig. 4.18 (a) measurement result, (b) generation of channel model.

Fig. 4.18 shows the verification results. The generated channel by the model is shown in Fig. 3-4, where all SnS phenomena observed in the measurements are captured well. Besides the stationary paths, all SnS paths that have responses on the partial array with/without power change, are accurately generated.

Focusing on the modeling and simulation of ultra-large MIMO channels, [193] proposes an innovative simulation framework based on the 3GPP channel model, which adds support for the spatial non-stationary characteristics of massive MIMO channels and the simulation of near-field characteristics, and realizes the accurate generation of massive MIMO channel coefficients with near-field spatial non-stationary characteristics. The work on 6G channel emulator BUPTCMCCCMG - IMT2030 finish[1].

Because of the larger size of the XL-MIMO array, when the user approaches the array, the channel energy is only concentrated on part of the antennas, which is called the visibility region (VR) [194][195] of the user. In [196][197], VR is defined as the part of the array that occupies the majority of channel energy. In the actual scene with scatterers or obstacles, the scatterers are usually divided into multiple clusters. Thus, in [198]-[200], VR is cascaded by the visibility region Φ_{UC} between the user and the scatterer and the visibility region between the scatterer and the array, which represent the scatterers visible to the user and the array antennas visible to the scatterer, respectively, as shown in Fig. 4.19.
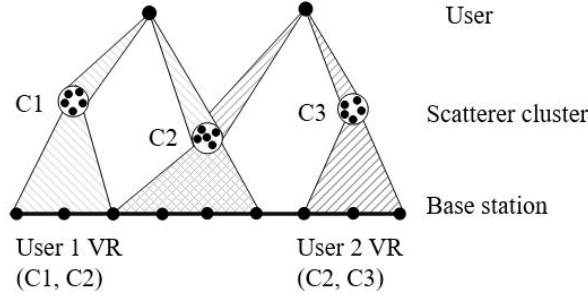

Fig. 4.19 Visibility region of the array and user

When the finite-path channel model is used, the occurrence of non-stationarity makes XL-MIMO channel model different from the traditional channel model, and the variance can be reflected by the steering vector. Firstly, in the vicinity of the array, since plane wave model is no longer accurate, the phase of each element in the steering vector should be described by the spherical wave model. Secondly, the amplitude of each element is no longer the same due to the uneven path loss across the array as well as the interaction caused by obstacles in the environment. Therefore, the spatially nonstationary finite-path channel model of user k is expressed by

$$\mathbf{h}_k = \sum_{c \in \Phi_{UC,k}} \sum_{s=1}^{S_c} \beta_{c,s} \mathbf{a}_{c,s} \tag{4.4}$$

where $\beta_{c,s}$ is the complex coefficient of the path generated by scatterer s in cluster c, which also represents the response of this path on the reference antenna, $\mathbf{a}_{c,s} \in \mathbb{C}^{N \times 1}$ is the steering vector of the path, and N is the number of antennas. By further considering VR, the finite-path channel model is transformed into

$$\mathbf{h}_k = \sum_{c \in \Phi_{UC,k}} \sum_{s=1}^{S_c} \beta_{c,s} \mathbf{a}_{c,s} \odot \mathbf{p}_c \tag{4.5}$$

$$\left[\mathbf{p}_c\right]_n = \begin{cases} 1, & \text{if } n \in \Phi_{CA,c} \\ 0, & \text{else} \end{cases} \tag{4.6}$$

---

[1] https://hpc.bupt.edu.cn/dataset-public/home-page

where $\odot$ takes Hadamard product, and $\mathbf{p}_c = \{0,1\}^{N \times 1}$ indicates the antennas visible from cluster c [200][201].

In addition, the XL-MIMO channel modeling can be based on the channel covariance matrix, which can also reflect VR. The channel covariance matrix illustrates the statistical covariance of the channel between different antennas and has been widely used in multi-antenna channel modeling. Let $\boldsymbol{R}_A \in \mathbb{C}^{N \times N}$ and $\boldsymbol{R}_s \in \mathbb{C}^{S \times S}$ denote the covariance matrices on the array side and the scatterer side, respectively, where S is the number of scatterers. In this case, the multi-antenna channel model based on channel covariance matrix is

$$\boldsymbol{h}_k = \boldsymbol{R}_A^{\frac{1}{2}} \boldsymbol{H}_w \boldsymbol{R}_s^{\frac{1}{2}} \boldsymbol{h}_w \tag{4.7}$$

where $\boldsymbol{H}_w \in \mathbb{C}^{N \times S}$ and $\boldsymbol{h}_w \in \mathbb{C}^{S \times 1}$ are small scale fading matrices. Since different clusters have different VRs, considering spatially non-stationary scenario, the channel between user k and the BS is represented as

$$\boldsymbol{h}_k = \left[\boldsymbol{G}_1, \ldots, \boldsymbol{G}_C \right] \boldsymbol{R}_s^{\frac{1}{2}} \boldsymbol{D}_{\mathrm{UC},k} \boldsymbol{h}_{w,k} \tag{4.8}$$

$$\boldsymbol{G}_c = \boldsymbol{D}_{\mathrm{CA},c} \boldsymbol{R}_{\mathrm{CA},c}^{\frac{1}{2}} \boldsymbol{H}_{w,c} \in \mathbb{C}^{N \times S_c} \tag{4.9}$$

where $\boldsymbol{G}_c$, C, and S_c represent the channel between the array and cluster c, the number of scatterer clusters and the number of scatterers in scatterer cluster c, respectively. S_c and C satisfy $\sum_{c=1}^{C} S_c = S$. $\boldsymbol{D}_{\mathrm{UC},k} = \{0,1\}^{S \times |\Phi_{\mathrm{UC},k}|}$ and $\boldsymbol{D}_{\mathrm{CA},c} = \{0,1\}^{N \times |\Phi_{\mathrm{CA},c}|}$ denote the cluster visible to user k and the antenna visible to cluster c, respectively. $\boldsymbol{R}_{\mathrm{CA},c} \in \mathbb{C}^{|\Phi_{\mathrm{CA},c}| \times |\Phi_{\mathrm{CA},c}|}$ is the covariance matrix across antennas within $\Phi_{\mathrm{CA},c}$, while $\boldsymbol{H}_w \in \mathbb{C}^{|\Phi_{\mathrm{CA},c}| \times S_c}$ and $\boldsymbol{h}_{w,k} \in \mathbb{C}^{|\Phi_{\mathrm{UC},k}| \times 1}$ are small scale fading matrices.

Based on the near-field NUSW and partial array visibility characteristics, the near-field spatial correlation function of multi-path XL-array communications with mixed LoS and NLoS links is developed [142][202], denoted by $\boldsymbol{\Theta} = \boldsymbol{\Theta}^{\mathrm{LoS}} + \boldsymbol{\Theta}^{\mathrm{NLoS}} \in \mathbb{C}^{N \times N}$, with $\boldsymbol{\Theta}^{\mathrm{LoS}} \in \mathbb{C}^{N \times N}$ and $\boldsymbol{\Theta}^{\mathrm{NLoS}} \in \mathbb{C}^{N \times N}$ being the near-field spatial correlation functions of LoS and NLoS components, respectively. For the LoS link, the element of the developed near-field spatial correlation is modeled as

$$\left[\boldsymbol{\Theta}^{\mathrm{LoS}} \right]_{n,m} = \frac{K}{K+1} \mathsf{E}\left[\xi_n^{\mathrm{LoS}} \xi_m^{\mathrm{LoS}} \right] \frac{d^2}{d_n d_m} e^{-j\frac{2\pi}{\lambda}(d_n - d_m)} \tag{4.10}$$

where K is the K-factor, $\xi_n^{\mathrm{LoS}} \in \{0,1\}$ is the random variable to model the (in)visibility of the nth antenna element to user for the LoS link, d_n is the distance between the nth antenna element and user, and d is the distance between the antenna element $n=0$ (the center element of the array) and user. The developed near-field spatial correlation of LoS component depends on the position of the UE, which is different from the far-field model only depending on the AoA of the UE. For the NLoS links, a novel near-field spatial correlation in integral form is modeled as

$$\left[\boldsymbol{\Theta}^{\mathrm{NLoS}}\right]_{n,m} = \frac{1}{K+1} \int_{s \in S} \mathsf{E}\left[\xi_n^{\mathrm{NLoS}}(s)\xi_m^{\mathrm{NLoS}}(s)\right] \frac{r^2}{r_n(s)r_m(s)} e^{-j\frac{2\pi}{\lambda}(r_n(s)-r_m(s))} f(s)d(s)$$

(4.11)

where s is the scatterer characterized by its AoA and distance to the center antenna element r, S is the support of random scatterers, $\xi_n^{\mathrm{NLoS}}(s) \in \{0,1\}$ is the random variable to model the (in)visibility of the nth antenna element to scatterer s for the NLoS link, $r_n(s)$ is the distance between scatterer s and the nth antenna element, and $f(s)$ represents the PDF of scatterer s's location. The scattering power distribution of the developed near-field spatial correlation of the NLoS component is characterized by the power location spectrum, rather than the power angle spectrum in traditional far-field models. The near-field spatial correlation no longer exhibits spatial wide-sense stationarity and is more generalized than the far-field model, as the proposed near-field spatial correlation model can degenerate to the far-field model when the user/scatterer is located in the far-field region of the XL-array array.

As shown in Fig. 4.20, for antenna arrays or RIS based on discrete elements, the resulting near-field channel can be modeled as the complex-valued sum of all far-field channels between each individual transmit antenna (TA) and the receive antennas (RA). This type of channel model is referred to as the Non-Uniform Spherical Wave (NUSW) model [203]. Consequently, the near-field channels between antenna arrays can be characterized by a channel matrix with dimensions corresponding to the numbers of receive and transmit antennas. The DoFs in the near-field channels are determined by the rank of this channel matrix, achieving full rank even in the absence of scatterers. Regarding CSI acquisition, near-field channels demand higher precision than far-field channels to effectively utilize their enhanced DoFs. For extremely large-scale MIMO systems, subarray-based estimation methods might be employed. For spatially discrete antennas, NUSW channel models strike an appropriate balance between accuracy and complexity in most scenarios.
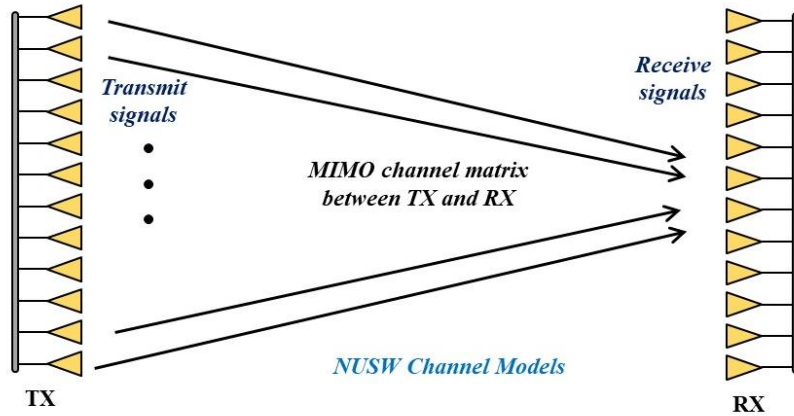

Fig. 4.20 NUSW channel model for spatially discrete antennas

In recent years, meta-materials have been used to realize (approximate) continuous transmit and receive apertures, thus facilitating holographic beamforming. Compared to traditional beamforming techniques, holographic beamforming achieved through continuous-aperture (CAP) antennas provides ultra-high spatial resolution [203]. In the case of continuous-aperture antennas, near-field channel modeling can rely on the Green's function method [204]. In this model, the Green's function can be regarded as the spatial impulse response function between the continuous-element transmitter and the

near-field receiver. As depicted in Fig. 4.21, employing the Green's function method allows for computing the electromagnetic field distribution in a given area for a specified transmitter current distribution. Consequently, based on the specific properties of the receiving antennas, the received field strength or induced current distribution can be obtained. This model yields an accurate volume-to-volume model (i.e., transmitter effective volume to receiver effective volume) compared to the traditional point-to-point model, enabling full utilization of the higher DoFs in the near-field channel. Similar to discrete antennas, continuous-element antennas also require more precise CSI due to their channel modeling reliance on Green's functions and spatial integration. CSI acquisition for continuous-element antennas remains a challenging subject for future research.
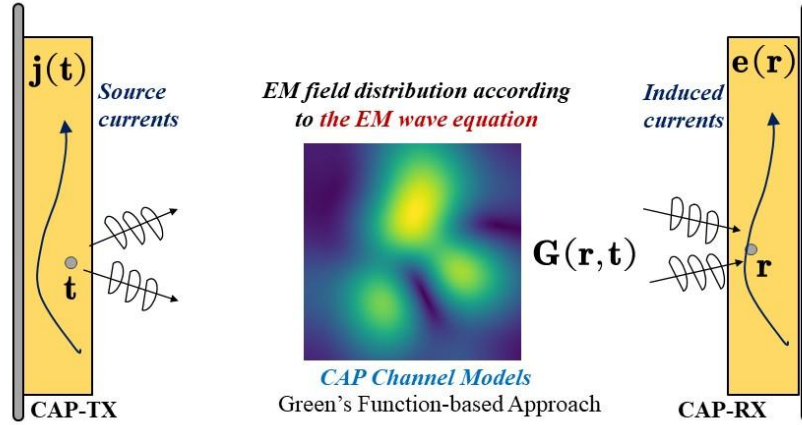

Fig. 4.21 Green's function-based channel model for CAP antennas

The aforementioned use of metamaterial-based aperture antennas, also referred to as HMIMO, enables breakthroughs in uncontrollable factors of traditional wireless channels, reshaping the wireless propagation environment and introducing new DoFs, particularly in near-field scenarios. Research has indicated that traditional channel modeling approaches are no longer applicable in near-field channel scenarios [205]. Currently, the most effective near-field modeling approaches are derived from electromagnetic field theory and utilize tools such as computational electromagnetics to characterize wave propagation channels. By combining the advantages of information theory, an electromagnetic field information theory mathematical analysis framework has been established, leading to the development of field propagation models for massive MIMO communications.

The multi-polarized free-space channel, as shown in Fig. 4.22, considers both the near-field spherical wave channel and the multi-polarization effects through the vectorial Green's function. Based on this, a model for the multi-polarized near-field spherical wave channel is established.
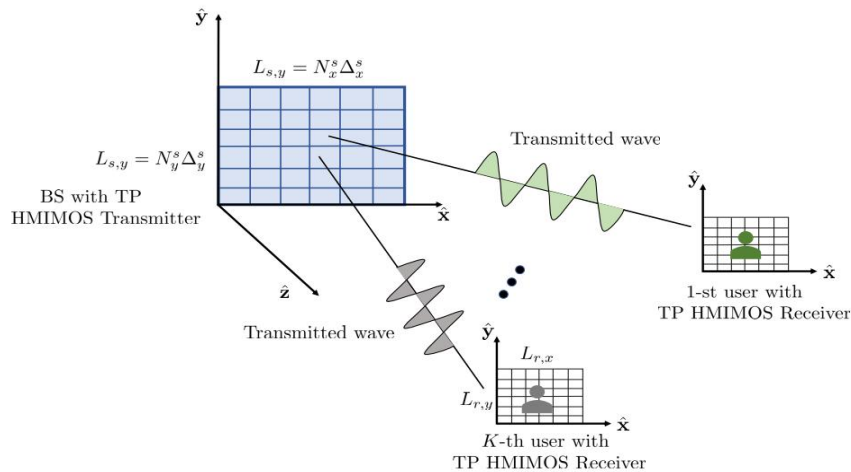
Fig. 4.22 Modeling of near-field multi-polarized spherical waves

The received electric field in the transmitting HMIMO system can be represented as:

$$\mathbf{E}(\mathbf{r}) = \sum_{n=1}^{N_s} \int_{\Delta^s} d\mathbf{r}'_n \bar{\mathbf{G}}\left(\mathbf{r}, \mathbf{r}'_n\right) \cdot \mathbf{J}\left(\mathbf{r}'_n\right) = \sum_{n=1}^{N_s} \int_{-\Delta^s_x/2}^{\Delta^s_x/2} \int_{-\Delta^s_y/2}^{\Delta^s_y/2} dx'_0 dy'_0 \left[\bar{\mathbf{I}} + \frac{\nabla\nabla}{k_0^2}\right] \frac{e^{ik_0 r_n}}{4\pi r_n} \mathbf{J}\left(\mathbf{r}'_n\right),$$

(4.12)

The channel from the n-th transmitting antenna of the HMIMO system to a specific receiving point can be represented as:

$$\mathbf{H}_n = \mathcal{E}(\tilde{R}_n)\mathbf{C}_n = \mathcal{E}(\tilde{R}_n)\left(c_1(\tilde{R}_n)\mathbf{I} + c_2(\tilde{R}_n)\vec{\mathbf{r}}_n\vec{\mathbf{r}}_n\right),$$

(4.13)

$$c_1(\tilde{R}_n) = \left(1 + \frac{i}{k_0\tilde{R}_n} - \frac{1}{k_0^2\tilde{R}_n^2}\right), c_2(\tilde{R}_n) = \left(\frac{3}{k_0^2\tilde{R}_n^2} - \frac{3i}{k_0\tilde{R}_n} - 1\right),$$

(4.14)

The size of the receiving HMIMO at the receiver end is typically smaller than that of the transmitting HMIMO at the sender end. Therefore, it is reasonable to assume that the power of each receiving HMIMO antenna is proportional to its size: $\Delta^r = \Delta^r_x \Delta^r_y$. Consequently, the channel between the n-th transmitting HMIMO antenna and the m-th receiving HMIMO antenna can be expressed as:

$$\mathbf{H}_{mn} = \Delta^s \Delta^r \frac{e^{(ik_0\tilde{R}_{mn})}}{4\pi\tilde{R}_{mn}} \operatorname{sinc} \frac{k_0(x_m - x'_n)\Delta^s_x}{2\tilde{R}_{mn}} \operatorname{sinc} \frac{k_0(y_m - y'_n)\Delta^s_y}{2\tilde{R}_{mn}} \mathbf{C}_{mn} = \begin{bmatrix} H^{xx}_{mn}, H^{xy}_{mn}, H^{xz}_{mn} \\ H^{yx}_{mn}, H^{yy}_{mn}, H^{yz}_{mn} \\ H^{zx}_{mn}, H^{zy}_{mn}, H^{zz}_{mn} \end{bmatrix},$$

(4.15)

where $\mathbf{C}_{mn} \triangleq c_1(\tilde{R}_{mn})\mathbf{I} + c_2(\tilde{R}_{mn})\vec{\mathbf{r}}_{mn}\vec{\mathbf{r}}_{mn} \in \mathbb{C}^{3\times3}$. Thus the entire channel matrix can be expressed as:

$$\mathbf{H} = \begin{bmatrix} \mathbf{H}_{xx} & \mathbf{H}_{xy} & \mathbf{H}_{xz} \\ \mathbf{H}_{yx} & \mathbf{H}_{yy} & \mathbf{H}_{yz} \\ \mathbf{H}_{zx} & \mathbf{H}_{zy} & \mathbf{H}_{zz} \end{bmatrix} \in \mathbb{C}^{3N_r \times 3N_s},$$

(4.16)

where the channel submatrix $\mathbf{H}_{pq} \in \mathbb{C}^{N_r \times N_s}, p, q \in \{x, y, z\}$ represents the channel between the transmitter component in the p-polarization direction to the receiver component in the q-polarization direction.

The channel capacity of tri-polarized HMIMO is higher compared to dual-polarized HMIMO and conventional unpolarized HMIMO as in Fig. 4.23 [206].
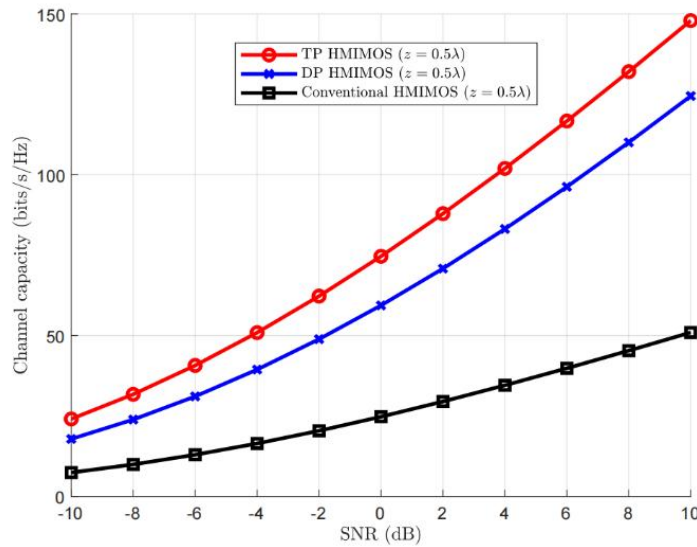

Fig. 4.23 Multi-polarized channel capacity

The existing channel models usually assume that the scattering clusters are located in the near field or the far field. However, in reality, there are mixed near and far fields in the medium and

ultra-massive MIMO systems, that is, some scattering clusters are located in the near field and some scattering clusters are located in the far field. In other words, very large MIMO channels usually consist of both far field and near field path components. The existing near-field or far-field channel models cannot match the characteristics of the hybrid near-field channel, so a channel model considering both the far field and the near field will be established next.

The boundary division between near field and far field has an impact on many aspects of wireless communication systems, such as array antenna characterization, propagation channel, perception, etc. [107]. In order to build a hybrid near and far field channel model, we first discuss the boundary division between far field and near field. According to whether the transceiver is configured with multiple antennas, the system can be divided into MISO/SIMO and MIMO. The far-field and near-field boundaries of these two types of systems are described below.

MISO/SIMO system: The classical antenna near and far field boundary is the Rayleigh distance, $2D^2/\lambda$,where D represents the array aperture and λ represents the carrier wavelength.

MIMO systems: For MIMO systems, an extended form of Rayleigh distance is widely accepted, i.e, $2(D_R + D_T)^2/\lambda$, where D_R, D_T represent the maximum array aperture of receiver and transmitter respectively.
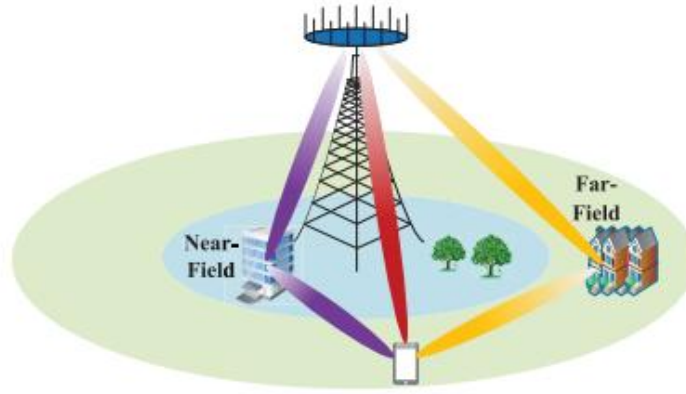

Fig. 4.24 XL-MIMO hybrid near and far field propagation environment

As shown in Fig. 4.24, there are two different scattering clusters in the ultra-large MIMO system. The cluster away from the BS is located in the far field region and generates the far field component, while the cluster near the BS is located in the near field region and generates the near field component. In this case, the BS serves a distant user. Although the direct connection path belongs to the far field component, the near field component generated by the near field cluster may also exist in the channel, so the mixed channel of the far field and the near field must be considered.

In order to describe the characteristics of the mixing of near and far fields in the channel, the formula of the mixed field channel model is as follows:

$$\mathbf{h}_{hybrid-field} = \sqrt{\frac{N}{L}} \left(\sum_{l_f=1}^{\gamma L} \alpha_{l_f} \mathbf{a}\left(\theta_{l_f}\right) + \sum_{l_n=1}^{(1-\gamma)L} \alpha_{l_n} \mathbf{b}\left(\theta_{l_n}, r_{l_n}\right) \right)$$

(4.17)

Where, L represents the number of paths, $\gamma \in [0,1]$ is an adjustable parameter, used to control the ratio of near field cluster and far field cluster, α_{l_f} and θ_{l_f} respectively represents the l_f path gain and arrival Angle of the first far field path, $\mathbf{a}(\theta_{l_f})$ and θ_{l_f} is related to the far field array guide vector, α_{l_n}, θ_{l_n} ,and r_{l_n} respectively represents the path gain, angle and distance of the first near field path, $b(\theta_{l_n}, r_{l_n})$ is θ_{l_n} and r_{l_n} related to the near field array guide vector. When $\gamma = 1$, the

mixed field model becomes a far field model, when $\gamma = 0$, the model becomes a near field model. Therefore, the mixed-field model is a more general channel model, and the existing near-field and far-field models can be regarded as its special cases.


Far-field   Near-field

$\frac{2D^2}{\lambda}$

planar wavefront   spherical wavefront
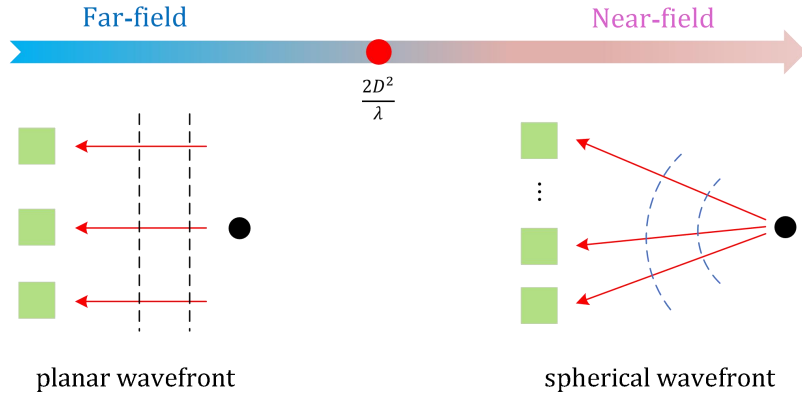
Fig. 4.25 Illustration of the planar and spherical wavefronts in the RIS-enabled channel model

Existing studies have shown that there are obvious differences in investigating RIS-enabled channel statistics based on the assumption that transmitter and receiver are in far-field regions of each other, compared to the assumption that the transceivers are in near-field regions[207][208]. Therefore, the Rayleigh distance criterion must be derived to determine the boundary of the far-field and near-field propagation scenarios for measuring the channel propagation statistics, as shown in Fig. 4.25. In the existing literature, the planar wavefront assumption has been adopted to simplify the channel modeling process in MIMO systems under far-field condition. In practice, the far-field condition is not always satisfied in RIS-assisted wireless communications. This is mainly because that the dimension of RIS becomes comparable to the propagation distance and no longer negligible when the RIS units number is large [209][210]. To address this issue, it is important to propose a sub-array partitioning scheme to divide the entire RIS array evenly into several smaller sub-arrays, where each sub-array consists of several RIS units. For each sub-array, the far-field condition holds, meaning that the dimension of each sub-array is much smaller and negligible as compared to the propagation distances. Consequently, we can apply planar wavefront assumption to each sub-array, as shown in Fig. 4.26. In each sub-array, once the distance/angle parameters of any one RIS unit are calculated, the distance/angle parameters of the remaining RIS units can be obtained accordingly. This significantly reduces the channel modeling complexity [211]. In the proposed dynamic sub-array partitioning scheme, the sub-array Rayleigh distances are adopted as the boundary of far-field and near-field to perform dynamic sub-array partition, which establishes a dynamic mapping relationship between sub-arrays and physical propagation environments.

Far-field planar model   Sub-array partition model
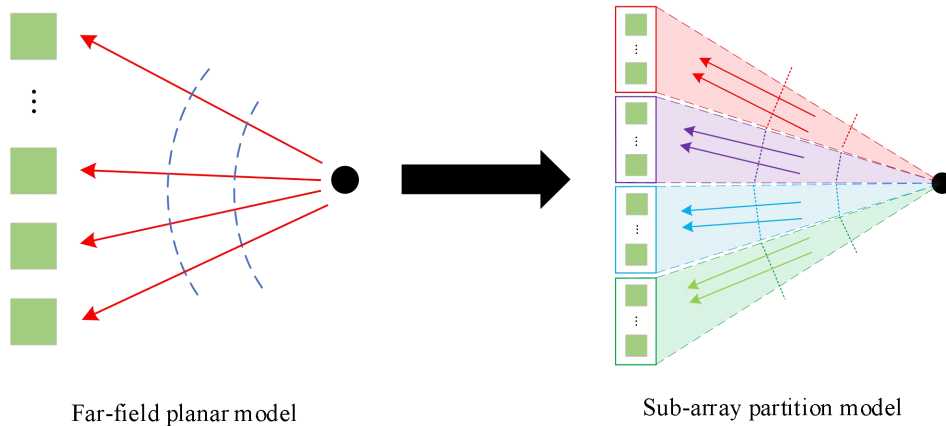
Fig. 4.26 Illustration of the sub-array partition model.

In RIS-enabled channel scenarios, the Fraunhofer distance, which distinguishes between the far-field and near-field ranges, can be expressed as

$$L_{\mathrm{RIS}} = \frac{2d_M^2\left((M_x-1)^2+(M_z-1)^2\right)}{\lambda}$$

(4.18)

with λ being the wavelength. Due to the dynamic features of the transceivers, the distance between the transceivers and the RIS continually vary in the real-time motion stage [212][213]. This will result in the alternating presence of near-field and far-field ranges, making the conventional methods that rely solely on spherical or planar-wave-based channel models inadequate for assessing the communication system performance for RIS-enabled scenarios [214]. To tackle this challenge, it is important to divide the entire RIS array into $M_x^{\mathrm{sub}}(t) \times M_z^{\mathrm{sub}}(t)$ sub-arrays in an evenly distributed manner. The largest sub-array contains $M_x^{\mathrm{sub}}(t) \times M_z^{\mathrm{sub}}(t)$ RIS reflecting elements. For the convenience of the subsequent derivations, assume that the largest sub-array is square under the premise of acceptable computational complexity, i.e., $M_{x,\max}^{\mathrm{sub}}(t) = M_{z,\max}^{\mathrm{sub}}(t)$. In order to ensure that the planar-wave model can be applied to each sub-array, the distances $\xi_{T,\mathrm{RIS}}(t)$ and $\xi_{R,\mathrm{RIS}}(t)$ are required to meet the following constraint condition:

$$\xi_{T,\mathrm{RIS}}(t) \geq \frac{2\left(P\delta_T + \sqrt{2}d_M(M_{x/z,\max}^{\mathrm{sub}}(t)-1)\right)^2}{\lambda}$$

(4.19)

$$\xi_{R,\mathrm{RIS}}(t) \geq \frac{2\left(Q\delta_R + \sqrt{2}d_M(M_{x/z,\max}^{\mathrm{sub}}(t)-1)\right)^2}{\lambda}$$

(4.20)

In light of this, we can obtain the constraint of the largest sub-array $M_{x/z,\max}^{\mathrm{sub}}(t)$ as follows:

$$M_{x/z,\max}^{\mathrm{sub}}(t) \leq min\left\{\underbrace{\frac{\sqrt{\lambda\xi_{T,\mathrm{RIS}}(t)}}{2d_M}-\frac{P\delta_T}{\sqrt{2}d_M}+1}_{g_1}, \underbrace{\frac{\sqrt{\lambda\xi_{R,\mathrm{RIS}}(t)}}{2d_M}-\frac{Q\delta_R}{\sqrt{2}d_M}+1}_{g_2}\right\}$$

(4.21)

In addition to the above constraint conditions, it is crucial to ensure that the dimension of the RIS panel in each sub-array remains smaller than that of the entire RIS array, that is, $M_{x/z,\max}^{\mathrm{sub}}(t) \leq M$. Therefore, the $M_{x/z,\max}^{\mathrm{sub}}(t)$ also needs to satisfy the following constraint:

$$M_{x/z,\max}^{\mathrm{sub}}(t) = \begin{cases} min\left\{\lfloor g_1 \rfloor, \lfloor g_2 \rfloor, M\right\}, & \text{if } min\left\{g_1, g_2\right\} > 1 \\ 1, & \text{if } min\left\{g_1, g_2\right\} \leq 1 \end{cases}$$

(4.22)

where $\lfloor x \rfloor$ denotes the operation of the largest integer not greater than x. Here, we have

$$M_{x/z}^{\mathrm{sub}}(t) = \begin{cases} \dfrac{M_{x/z} - \mathrm{mod}\left(M_{x/z}, M_{x/z,\max}^{\mathrm{sub}}(t)\right)}{M_{x/z,\max}^{\mathrm{sub}}(t)} + 1, \\ \qquad \text{if } \mathrm{mod}\left(M_{x/z}, M_{x/z,\max}^{\mathrm{sub}}(t)\right) \neq 0 \\ M_{x/z} / M_{x/z,\max}^{\mathrm{sub}}(t), \\ \qquad \text{if } \mathrm{mod}\left(M_{x/z}, M_{x/z,\max}^{\mathrm{sub}}(t)\right) = 0 \end{cases}$$

(4.23)

Consequently, for the $(m_x^{\mathrm{sub}}, m_z^{\mathrm{sub}})-\text{th}$ sub-array, i.e., $m_x^{\mathrm{sub}} = 1, 2, ..., M_x^{\mathrm{sub}}(t)$ and $m_z^{\mathrm{sub}} = 1, 2, ..., M_z^{\mathrm{sub}}(t)$, their numbers of RIS reflecting elements are represented by

$$M_{m_{x/z}^{\text{sub}}}(t) = \begin{cases} M_{x/z}^{\text{sub}}(t), & \text{if } 1 \le m_{x/z}^{\text{sub}} < M_{x/z}^{\text{sub}}(t) \\ M_{x/z} - \left(M_{x/z}^{\text{sub}}(t) - 1\right) M_{x/z}^{\text{sub}}(t), & \text{if } m_{x/z}^{\text{sub}} = M_{x/z}^{\text{sub}}(t) \end{cases}$$

(4.24)

For the convenience of subsequent expressions, define the $m_{x,z}^{\text{sub}}$ as the $(m_x^{\text{sub}}, m_z^{\text{sub}})$. It is worth noting that the proposed sub-array partitioning scheme is a software-level method, which implies that the sub-arrays can be repartitioned dynamically to accommodate the motion of the transmitter and receiver. Therefore, the proposed sub-array partitioning scheme can be extended to divide the large antenna arrays at the transmitter and receiver in ultra massive MIMO systems into small sub-arrays to reduce the modeling complexity.

As shown in Fig. 4.27, when the dimension of the RIS array is relatively small, which causes the propagation distance from the RIS to the transceivers to exceed the Rayleigh distance of the RIS-enabled channels; therefore, the planar wavefront assumption will hold for accurately characterizing the channel statistics in this context. The results in the RIS-enabled channel models based on the near-field scenarios provide the same performance as those based on the far-field scenarios. However, when the RIS array dimension continually increases, the length of the Rayleigh distance can be larger values. This results in the transmitter and receiver within the near-field scenarios of the RIS-enabled channels, which leads to different performance characteristics regarding modeling errors.
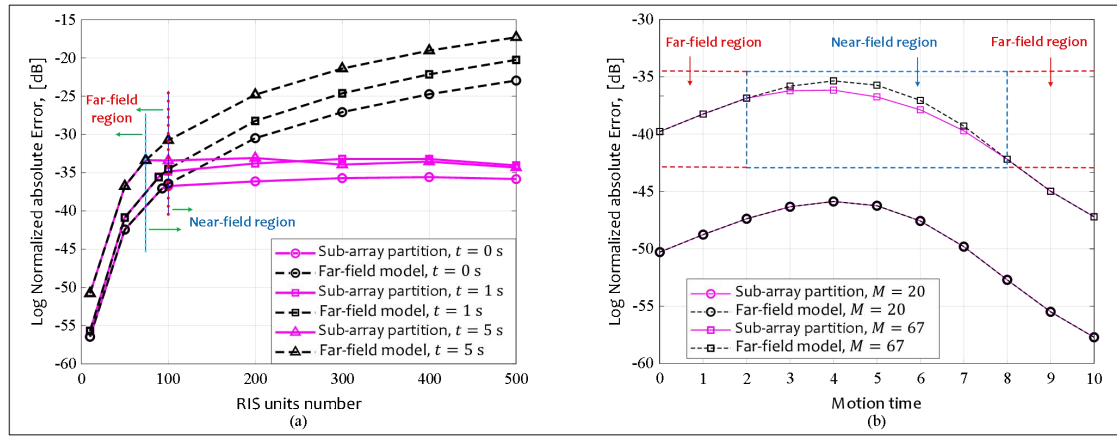

Fig. 4.27 Comparisons of the channel modeling accuracy based on the sub-array partition-based algorithm and that based on the far-field planar wavefront model under different motion time instants and different RIS units.

By performing a spatial Fourier transform on the received signals across the array, the angular domain representation of the channel can be obtained. Under far-field conditions, the angular domain channel exhibits sparsity. However, with the introduction of spherical wave characteristics in the near-field scenario, the near-field angular domain channel will manifest a power diffusion effect, which disrupts the sparsity property. Consequently, conventional angular domain sparsity-based algorithms for channel estimation, beamforming, and beam training become ineffective. Nevertheless, through quantitative analysis of the diffusion effect in the angular domain of near-field channels, it becomes feasible to enable angular domain-based algorithm design and characteristic analysis for near-field scenarios.

On the other hand, the angular domain channel obtained directly through Fourier transform is defined over a set of angular domain orthogonal bases, whose resolution is fundamentally constrained by the array aperture and operating wavelength. To address the resolution limitation inherent in the angular domain characterization, we propose a novel approach that directly models the near-field

diffusion effect in the wave-number domain [215]. The wave-number domain, which can be considered as the continuous counterpart of the angular domain, enables precise reconstruction of the wave-number domain channel from angular domain measurements through rigorous application of the Nyquist sampling theorem.
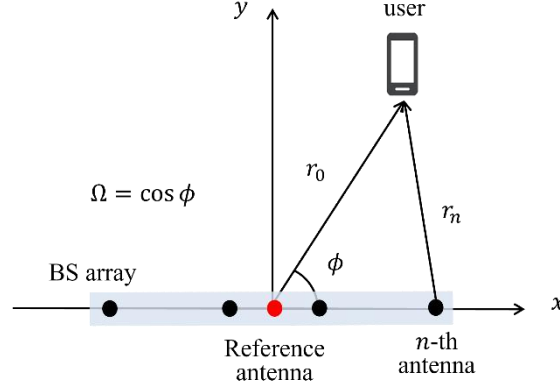

Fig. 4.28 System model

Fig. 4.28 illustrates a narrow-band XL-array system, operating at a carrier frequency of f_c, with the carrier wavelength denoted as $\lambda = c/f_c$. The antenna spacing in the ULA is represented by $d = \lambda/2$, resulting in the array aperture of $D = (N-1)d = (N-1)\lambda/2$. The reference antenna is positioned at the center of the array, with the origin of the coordinate system chosen at the location of the reference antenna, and the x-axis aligned along the array direction. The distance and angle of departure from the reference antenna to the user are denoted as r_0 and ϕ, respectively, and $\Omega = \cos\phi$. The near-field range of the array is characterized by the Rayleigh distance: $r_{ray} = 2D^2/\lambda$. When $r_0 < r_{ray}$, the user is within the near-field region of the BS, and the downlink channel can be modeled using the near-field steering vector as

$$\boldsymbol{h}_{near} = \sqrt{N}h_0\boldsymbol{b}(\Omega, r_0) \tag{4.25}$$

where $h_{near} \in \mathbb{C}^{N \times 1}$ is the channel vector and h_0 is the complex gain of the path at the reference antenna. Based on the spherical wavefront propagation model, considering both amplitude and phase variations, the near-field steering vector can be modeled as

$$\boldsymbol{b}(\Omega, r_0) = \frac{1}{\sqrt{N}}\left[\frac{r_0}{r_1}e^{-j\frac{2\pi}{\lambda}(r_1-r_0)}, ..., \frac{r_0}{r_N}e^{-j\frac{2\pi}{\lambda}(r_N-r_0)}\right]^T \tag{4.26}$$

where r_n denotes the distance from the n-th antenna of BS array to the user. The x-coordinate of the n-th antenna is $x_n = d(n - \frac{N+1}{2})$, where $n \in N = \{1, 2, ..., N\}$. Then r_n can be calculated as

$$r_n = \sqrt{r_0^2 + x_n^2 - 2r_0x_n\Omega}. \tag{4.27}$$

By applying the discrete Fourier transform (DFT) to the channel vector h_{near}, the virtual angular domain representation of the channel can be obtained as

$$\boldsymbol{H}_{near,A} = \boldsymbol{F}^H\boldsymbol{h}_{near} = \sum_{n=1}^{N}\boldsymbol{a}^H(\Omega_n) \cdot \boldsymbol{h}_{near} \tag{4.28}$$

where $F = [a(\Omega_1), .., a(\Omega_N)] \in \mathbb{C}^{N \times N}$ denotes the Fourier transform matrix. $a(\Omega_n) = \frac{1}{\sqrt{N}}\left[1, e^{j\pi\Omega_n}, ..., e^{j(N-1)\pi\Omega_n}\right]^T$ denotes the far-field steering vector and $\Omega_n = \frac{2n-N-1}{N}$, $n \in N$.

By extending x_n to a continuous variable x, the near-field channel (4.1) can be transformed into a univariate function defined on $x \in X = [-D/2, D/2]$ as follows:

$$h_{near}(x) = h_0 \frac{r_0}{\sqrt{r_0^2+x^2-2r_0x\Omega}} e^{-j\frac{2\pi}{\lambda}\left(\sqrt{r_0^2+x^2-2r_0x\Omega}-r_0\right)} \tag{4.29}$$

By applying the Fourier transform (FT) to (4.4) the near-field channel response can be expressed in the wave-number domain as $H_{near}(k_x)$, where the k_x denotes the wave-number of x-axis:

$$H_{near}(k_x) = \int_{-D/2}^{D/2} h_{near}(x) e^{-jk_x x} \, dx \tag{4.30}$$

The wave-number domain channel and angular domain channel are essentially the FT and DFT of the near-field channel response $h_{near}(x)$. Therefore, $H_{near,A}$ can be viewed as a wave-number domain sampling of $H_{near}(k_x)$, while h_{near} can be viewed as a spatial domain sampling of $h_{near}(x)$. The sampling interval in the spatial domain is d, and only the portion of the wave-number domain with $|kx| \le 2\pi/\lambda$ supports the transmission of communication power beyond the radiative near field[216]. Consequently, the wave-number domain bandwidth is denoted as $B_k = 2 \cdot 2\pi/\lambda$. Since $B_k \le 2\pi/d$, satisfying the Nyquist sampling theorem, $H_{near,A}$ can be used to reconstruct $H_{near}(k_x)$.

Specifically, comparing the kernel function of (4.5) with the exponential component of (4.3), the sampling positions in the wave-number domain can be determined as $k_{x,n} = \frac{2\pi}{\lambda} \frac{2n-N-1}{N}$, and the sampling interval in the wave-number domain is denoted as $\Delta(k_x) = \frac{4\pi}{\lambda N}$. Consequently, $H_{near}(k_x)$ can be interpolated as

$$H_{near}(k_x) = d \sum_{n=-\infty}^{+\infty} \widetilde{H}_{near,A}[n] \cdot \text{sinc}\left(\frac{k_x-k_{x,n}}{\Delta(k_x)}\right) \tag{4.31}$$

Where $\widetilde{H}_{near,A}[n]$ denotes the n-th element of $\widetilde{H}_{near,A}$ and $\widetilde{H}_{near,A}$ is the periodic extension of $H_{near,A}$, $\widetilde{H}_{near,A}[n] = H_{near,A}[\text{mod}(n, N)]$. $\text{sinc}(x) = \frac{\sin(\pi x)}{\pi x}$。 As established in the preceding analysis, the angular domain channel inherently contains complete information of its wave-number domain counterpart. Crucially, the wave-number domain provides more intuitive visualization of angular characteristics through its continuous spatial frequency representation. This fundamental relationship motivates our subsequent selection of the wave-number domain as the principal framework for channel modeling and analytical investigations

By substituting the near-field channel in spatial domain (4.4) into the Fourier transform in the wave-number domain (4.5), the precise expression for the near-field wave-number domain channel can be obtained as

$$H_{near}(k_x) = h_0 \int_{-D/2}^{D/2} \frac{r_0}{\sqrt{r_0^2+x^2-2r_0x\Omega}} e^{-j\left[\frac{2\pi}{\lambda}\left(\sqrt{r_0^2+x^2-2r_0x\Omega}-r_0\right)+k_x x\right]} \, dx \tag{4.32}$$

The integrals shaped like (4.7) are known as oscillatory integrals, i.e. $I = \int A(x) e^{j\psi(x)} dx$. Based on the Principle of Stationary Phase, if the phase function $\psi(x)$ exhibits a stationary point x_s within the integration interval, i.e. $\dot{\psi}(x_s) = 0$, the oscillatory integral can be approximate as $I \approx$

$\sqrt{\frac{2\pi}{|\ddot{\psi}(x_s)|}}A(x_s)e^{j\left\{\psi(x_s)+sgn[\ddot{\psi}(x_s)]\frac{\pi}{4}\right\}}$. If $\psi(x)$ has no stationary point within the integration domain, I can be

approximate as 0. Therefore, to rigorously investigate the spatial distribution characteristics of the diffusion region, it necessitates a systematic examination of the following critical condition: Under what parametric configurations does the phase function $\psi(x)$ develop stationary points within the integration interval.

As can be seen from (4.7), the expression of the phase function is $\psi(x) = -\frac{2\pi}{\lambda}\left(\sqrt{r_0^2 + x^2 - 2r_0x\Omega} - r_0\right) - k_xx$, and its first-order derivative function is $\dot{\psi}(x) = -\frac{2\pi}{\lambda}\frac{x - r_0\Omega}{\sqrt{r_0^2 + x^2 - 2r_0x\Omega}} - k_x$. So $\psi(x)$ have unique stationary point:

$$x_s = r_0\left[\Omega - \frac{k_x}{\sqrt{\left(\frac{2\pi}{\lambda}\right)^2 - k_x^2}}\sqrt{1 - \Omega^2}\right] \tag{4.33}$$

Notice that the integral range of (4.7) is $[-D/2, D/2]$, when $x_s \in [-D/2, D/2]$, k_x needs to be satisfied by

$$k_x \in \mathcal{X}_k = \left[\frac{2\pi}{\lambda}\frac{\Omega - \frac{D}{2r_0}}{\sqrt{1 + \left(\frac{D}{2r_0}\right)^2 - \frac{D}{r_0}\Omega}}, \frac{2\pi}{\lambda}\frac{\Omega + \frac{D}{2r_0}}{\sqrt{1 + \left(\frac{D}{2r_0}\right)^2 + \frac{D}{r_0}\Omega}}\right] \tag{4.34}$$

When the distance between the users and BS is generally not small enough to be on the order of the array aperture; hence, $r_0 \gg D$, by taking the Taylor series expansion as $D/r0 \ll 1$, and retaining the first-order term, $\mathcal{X}_k$ can be approximate as:

$$\mathcal{X}_{k,s} = \left[\frac{2\pi}{\lambda}\left(\Omega - \frac{D}{2r_0}(1 - \Omega^2)\right), \frac{2\pi}{\lambda}\left(\Omega + \frac{D}{2r_0}(1 - \Omega^2)\right)\right] \tag{4.35}$$

Fig. 4.29 illustrates the comparative simulation results of the wave-number domain channel response, angular-domain channel response, and the approximated wave-number domain channel model. The analysis demonstrates that: The wave-number domain constitutes a continuous superset of angular-domain characterization, and the proposed approximation model exhibits an approximately rectangular function profile. The approximately derived diffusion region demonstrates effective correspondence with the diffusion phenomenon observed in the wavenumber domain.
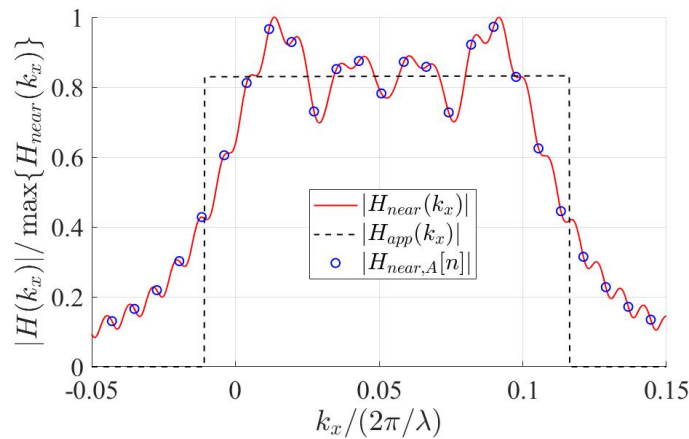
Fig. 4.29 Near-field angular domain channel, wave-number domain channel, and wave-number domain approximation results.

4.4 Bridging the Gap between Near and Far-Field Models

With the increasing importance of near-field considerations alongside the established significance of far-field characterizations, there is a growing necessity to bridge the gap between these two domains. Here, we summarize some recent findings by drawing parallels between conventional channel modeling methods and those based on the fundamental wave propagation modeling approach via Maxwell's equations (Green's function). Our objective is to offer engineers and researchers fresh perspectives, enabling them to leverage techniques developed for standard far-field models in the exploration of near-field scenarios. Specifically, we concentrate on environments devoid of scattering, where communication relies solely on the LoS link.

To elucidate the characteristics of near and far-field models, we examine a MISO system setup, focusing on beamforming applications at various distances from the transmitter [217]. This system comprises a rectangular grid of $N = N_x N_y$ small antenna elements, uniformly spaced at half of the wavelength at the transmitter. In our simulations, we utilize a carrier frequency of 30GHz corresponding to a wavelength of $\lambda = 0.01m$. The transmitter configuration comprises a rectangular grid of antenna elements, with $N_x = 20$ antennas along the X-axis and $N_y = 200$ antennas along the Y-axis. Each antenna element has a square shape with a side length $a = 0.5\lambda$.

In Fig. 4.30 (a), (b), and (c), we examine the performance of a matched filter beamformer designed to maximize the received power at the receiver positioned at $(0,0,\text{d})$ with $d = 10\lambda = 0.1m$, $d = 250\lambda = 2.5m$, and $d = 5000\lambda = 50m$, respectively. From plots (a) and (b), the discrepancy between the near and far-field models becomes evident. In the near-field scenario, the near-field model allows for power concentration at the specific receiver position, and for $d' = d \pm \delta,\ \delta > 0$, the power decreases. In contrast, in the far-field, the transmitter can only concentrate power towards an angular orientation of the receiver. As illustrated in Fig. 4.30 (c), when the distance between the transmitter and the receiver is sufficiently large, the near and far-field models almost coincide, indicating that the far-field model serves as an approximation of the near-field model. It is noteworthy that for the given transmitter antenna configuration, the Fraunhofer distance is approximately 200m. However, this distance provides a highly conservative estimate for the reliable employment of far-field models. This discussion underscores the accuracy of the near-field model in describing wireless propagation and highlights its utility in leveraging an additional DoF (the distance d) to enhance performance in various applications. Notably, in Fig. 4.30 (a) with d=0.1m, the far-field model tends to overestimate the received power. Further elaboration and analysis can be found in [217].
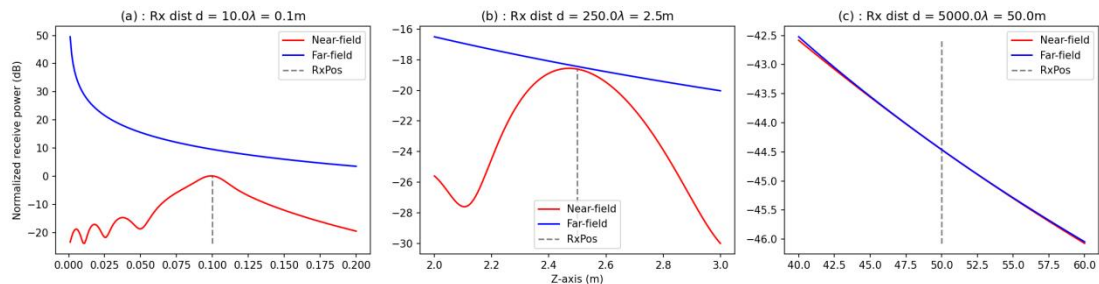

Fig. 4.30 Comparison of near and far-field models for different Tx-Rx distances [217].

5 Transmission Technologies of Near-field

Due to the mismatch between near-field propagation models and existing far-field communication technologies, existing far-field technologies will experience significant performance degradation in the near-field region. This chapter will introduce near-field communication technologies from the aspects of channel estimation, beamforming, codebook designing, beam training, multiple access technology, non-coherent detection, and deployment.

5.1 Near-Field Channel Estimation

Accurate CSI is fundamental for designing accurate beamforming in 6G communications, which is a key factor in achieving ultra-high-speed transmission. The Massive MIMO 5G technology was designed around the use of model-agnostic channel estimation, using uplink pilots, uplink-downlink duality, and the use of non-parametric channel estimation methods. These methods can be used for near-field estimation without any modifications. Nevertheless, there are good reasons for considering parametric estimation methods in 6G: the increased carrier frequency reduces the available pilot resources per coherence block and increased number of antennas calls for more pilot resources. This issue can be resolved by shifting to parametric methods, where channels are described with a number of parameters that is independent of the number of antennas. However, the new characteristics introduced by near-field communications pose challenges when applying such methods.

Previous parametric estimation methods designed for mmWave bands often utilize the sparsity of far-field channels in the angle domain and employ compressive sensing (CS) algorithms to recover sparse channels with low pilot overhead. To achieve this goal, the Fourier transformation is first performed in the antenna domain of the channel, converting it to the sparse angle domain. Then, the sparse signal reconstruction methods such as Orthogonal Matching Pursuit (OMP) are utilized to accurately reconstruct the sparse angular-domain channel. The far-field channel estimation scheme heavily relies on the sparsity of the angular-domain channel, which originates from the far-field planar-wave model. Due to the fact that the near-field channel of ELAA is composed of spherical waves, the propagation characteristics of near-field spherical waves will lead to energy spread effects in the near-field angular-domain channel, where the energy of each near-field path spread to multiple angles in the angle domain. The energy spread effect disrupts the sparsity of near-field channels in the angle domain (ref. Fig. 5.1). Therefore, existing channel estimation schemes will suffer from a serious performance decrease in near-field communications.
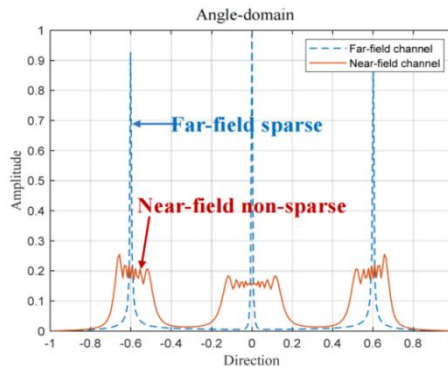

Fig. 5.1 The energy spread effect in the angle-domain

To overcome the energy spread problem in near-field communications, a near-field codebook dictionary matrix can be constructed based on the characteristics of near-field spherical waves, where the sparsity of near-field codebooks can be restored and thereby compressive sensing methods could be leveraged in near-field communications. Specifically, the existing angular-domain dictionary matrix of far-field Fourier transformation is a uniform sampling of spatial angles, ensuring the sparsity of far-field channels in the angle domain. To adapt to the propagation characteristics of spherical waves, an additional non-uniform sampling of spatial distance can be added on the basis of uniformly sampled spatial angles, while ensuring that the coherence of codewords is as small as possible in the distance domain dimension for the ULA. This allows for the simultaneous extraction of channel information in the two dimensions, i.e. "angular-distance" (polar) domain with the near-field polar domain codebooks. Based on the Fresnel approximation, it can be proven that the proposed polar domain representation method can adapt to the near-field propagation environment, ensuring the sparsity of the near-field channel in the polar domain [218]. By transforming the channel from the spatial domain to the polar domain and utilizing the sparsity of the near-field channel in the polar domain, compressive sensing could be utilized to achieve low-overhead channel estimation.
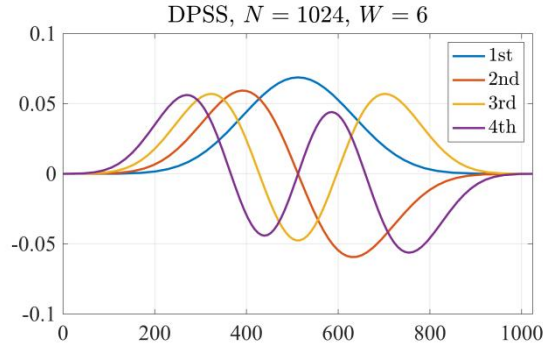
Fig. 5.2 Demonstration of DPSS codewords

The optimal sparse representation of the channel can be achieved with an orthogonal codebook, specifically the eigen-codebook, which is composed of eigenvectors of the channel matrix. Such design can be traced back to the spectral concentration problem, where the codewords correspond to the optimal sequences achieving energy spectral concentration in a double band-limited system. Eigen-codebook ensures perfect orthogonality and minimizes the codebook size while capturing the essential features of the channel. However, the design of eigen-codebooks lacks a unified and straightforward rule across diverse scenarios. Fortunately, in near-field ULA communication systems, it has been demonstrated that the optimal codebook aligns with the eigenvectors of a Sinc-Toeplitz matrix [219], known as discrete prolate spheroidal sequences (DPSSs), as shown in Fig. 5.2, The DPSS-based codebook not only achieves the optimal sparsification of the channel matrix but also minimizes coherence among codewords, making them highly effective for precise channel estimation and efficient recovery in compressive sensing frameworks.

In [220], by exploiting the fact that with given observations, the angle and distance are coupled, a distance-parameterized angular-domain sparse near-field channel representation dictionary is proposed, followed by joint dictionary learning and sparse recovery channel estimation algorithm. The proposed algorithm iteratively estimates the angle and distance parameters, which are then used for the reconstruction of the near-field channel. Specifically, the proposed near-field channel representation

dictionary takes the distance as an unknown parameter while only the sampling at the angle domain is performed, which well addresses the high storage and high coherence issues brought by the polar-domain method, as illustrated in Fig. 5.3. To reduce the dictionary construction difficulty of the polar-domain method, a model-based deep learning approach was proposed for the near-field channel estimation in [221]. In this work, a small-sized dictionary was learned from the received observations to represent the near-field channel, and the channel parameters are recovered by virtue of a learning-based iterative shrinkage thresholding algorithm.
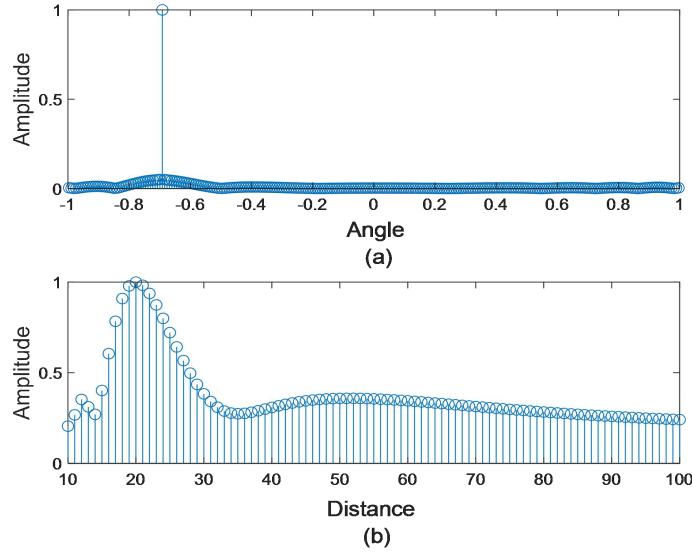
(a) The distance-parameterized angular-domain dictionary. (b) The Polar-domain dictionary.
Fig. 5.3 Dictionary coherence comparison

In addition to constructing codes in the near-field polar domain to ensure the sparsity of the near-field channel, in [222], a wavefront transformation-based matrix is constructed to transform the near-field channel into an approximation of the far-field channel, or even a far-field channel. Then, a DFT matrix is used to project the channel onto the angle domain, ensuring the sparsity of the channel. Unlike the structure of far-field channels, existing near-field channels include an additional distance matrix, which is the phase deviation of different antenna array units. To alleviate the impact of phase deviation, a row full rank matrix perpendicular to the space where the far-field steering vector matrix is located can be constructed based on the structural characteristics of the near-field channel and far-field channel. A full rank matrix can be obtained through matrix operation, and the diagonal elements of the full rank matrix can be extracted and normalized as the constructed wavefront transformation matrix. When the number of antennas is large enough, the wavefront transformation matrix is related to angles and distance, and the estimation error of the channel will approach zero [222].
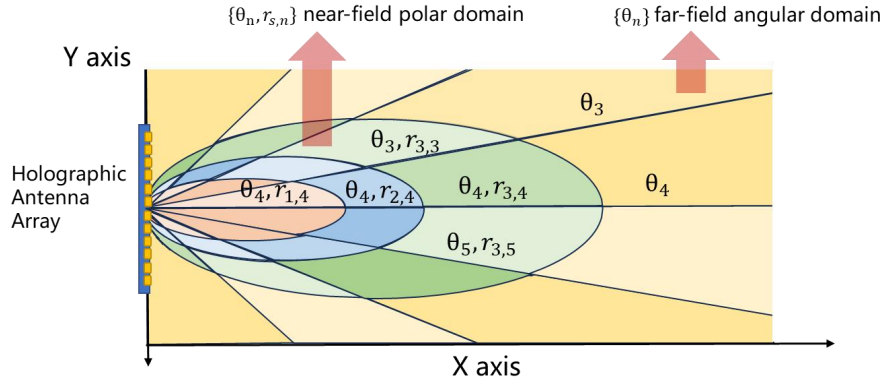
Fig. 5.4 Space Partition Based on Joint Angular-Polar Domain Transform

To mitigate the accuracy, decrease of far-field methods in near-field communications, [223] proposes a power-diffusion-aware orthogonal matching pursuit algorithm (PD-OMP) for hybrid-field channel estimation. Different from other hybrid-field channel estimation methods, PD-OMP transforms the spatial-domain channel to the joint angular-polar domain, where both the near-field and the far-field steering vectors are included in the compressed sensing dictionary. As shown in Fig. 5.4, the space covered by the holographic antenna array is divided into the near-field region and the far-field region. In the joint angular-polar domain, the near-field region is partitioned two-dimensionally in both direction and distance with near-field steering vectors, and the far-field region is partitioned one-dimensionally in direction with far-field steering vectors.

Based on the transform result in the joint angular-polar domain, PD-OMP estimates all path components of the hybrid-field channel in iteration. In each iteration, a peak representing a path is detected in the transform result and PD-OMP calculates this path's power diffusion range, which quantifies the range of power diffusion in the joint angular-polar domain. The power diffusion effect of this path is therefore identified and then eliminated so that the estimation of the remaining path components is not affected by the power diffusion effect. It is noticed that the amplitude of the highest peak, which represents the path with the strongest power gain, is larger than the interference of the power diffusion effect of the other paths. Therefore, in the first iteration, this peak can be detected and the corresponding power diffusion range can be identified, which ensures that each path component can be detected successfully in the following iteration.

Due to the energy spread effect, the near-field channel exhibits block structure in angular domain, i.e., the significant angle ingredients of the channel are continuous. Moreover, as polar-domain representation contains the angle ingredients, the near-field channel in the polar domain also exhibits block structure. The authors in [224] reformulated the near-field channel as a block-sparse model by exploiting this structural characteristic. They further proposed an enhanced compressed sensing technique, called block-dominant compressed sensing, to perform reliable near-field channel estimation in both angular and polar domain. Benefiting from the exploitation of the subspace information among various channel blocks, channel estimation by the way of block-dominant compressed sensing offers fertile advantages in terms of both accuracy and complexity.

By further considering the dual-band deployment of practical communication systems, [225] proposed various dual-band near-field channel estimation schemes based on the block-sparse model in [224]. The authors present several theoretical results, revealing that the reliability high-band channel

estimation with minimum estimation error can be guaranteed with the assistance of the low-band CSI. The single subcarrier and multiple subcarrier systems are analyzed separately to achieve the optimal solution of the corresponding system. Furthermore, both on- and off-grid scenarios are verified to substantiate the feasibility of the dual-band channel estimation schemes, which results in a significant reduction in pilot overhead.

Apart from the works on ULA, [226] and [227] propose parametric deconstruction techniques for a more general UPA scenario that incorporates both two-dimensional azimuth-elevation angles and distance parameters. In particular, these coupled geometry parameters, consisting of a pair of elevation-azimuth angles and the distance, are decomposed independently by employing a carefully designed mapping strategy from the original channel matrix to the three covariance matrices, each of which is associated exclusively with a single geometry parameter. This results in three independent one-dimensional (1D) parameter recovery problems that can be solved using compressive sensing techniques. Furthermore, benefiting from independent parametric estimates, the multiplicative complexity order can be relaxed to its additive counterpart. This implies that the proposed Triple Parametric Decomposition (TPD) enables practical implementation due to the beneficially reduced gridding and computational complexity as well as viable pilot overhead savings.

In [231], the authors proposed an adaptive and robust deep learning framework, called fixed point networks (FPNs), for iterative channel estimation in hybrid far-field and near-field THz ultra-massive MIMO systems. Each iteration consists of a closed-form linear estimator (LE) for decoupling the measurements, and a residual network-based non-linear estimator (NLE) for denoising the estimated hybrid-field channels. The authors prove that if the concatenation of the LE and NLE is a contractive operator, then FPNs will converge to a unique fixed point with linear convergence rate, providing an adaptive performance-complexity tradeoff. In combination with the orthogonal approximate message passing (OAMP) algorithm, the proposed FPN-OAMP can directly generalize to various mismatches in terms of channel distributions, noise conditions, and measurement matrices.

As an extension, in [232], an unsupervised Bayes-optimal channel estimator is proposed based on score matching for near-field holographic MIMO systems. The method only requires noisy received pilot signals for training, and can work in unknown environments. It demonstrates robustness, adaptability, and quasi-optimal performance for fully-digital and hybrid HMIMO systems without requiring prior channel knowledge. The performance of the learning-based estimator can be predicted based solely on received pilot signals [233], as verified by results in hybrid-field massive MIMO systems. In addition, the principles and techniques of deep learning-based near-field XL-MIMO systems, including channel estimation, are further summarized in [234], covering both iterative and non-iterative algorithm design.

By exploiting the near-field channel sparsity in the polar domain and the high-performance capabilities of deep learning (DL)-based algorithms in channel estimation (CE), the authors in [228] proposed two channel estimation schemes, i.e., the polar-domain multiple residual dense network (P-MRDN) and the polar-domain multi-scale residual dense network (P-MSRDN) based CE schemes. Moreover, the proposed schemes were compared with the polar-domain orthogonal matching pursuit (P-OMP) algorithm[218] to reveal the impact of channel sparsity on the performance of both traditional and DL-based algorithms.

To mitigate the influence of additional Tx/Rx-coupled LoS component in the double-sided near-field MIMO, which cannot be decomposed into the multiplication of transmitter-side and receiver-side array response vectors, the authors in [229] proposed a unified LoS/NLoS-mixed compressive-sensing-based estimation method. The Tx/Rx-coupled LoS component and Tx/Rx-decomposed NLoS paths, far-field and near-field cases, and near-field MIMO/MISO scenarios, are uniformly considered under this estimation scheme.
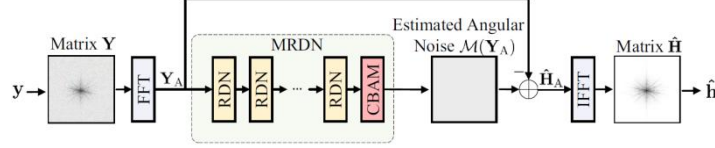

Fig. 5.5 MRDN-based channel estimation scheme
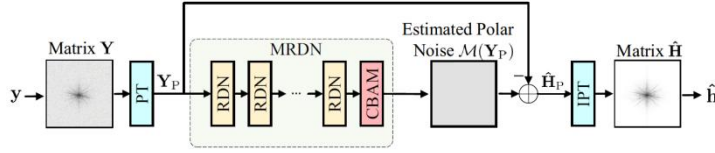
Fig. 5.6 P-MRDN-based channel estimation scheme

Fig. 5.5 illustrates the conventional MRDN-based channel estimation scheme [230]. The MRDN aims to transform the received signal into the angular domain using Fast Fourier Transform (FFT), thereby fully utilizing the sparsity of the channel in the angular domain. Subsequently, the MRDN is employed to recover the sparse far-field channel in the angular domain. However, the sparsity of the near-field channel in the angular domain is not significant. Instead, similar to the sparsity of the far-field channel in the angular domain, the radiation near-field channel exhibits certain sparsity in the polar domain.

As shown in Fig. 5.6, to leverage the polar-domain channel sparsity in near-field systems, the proposed P-MRDN-based channel estimation scheme adopts the polar-domain transform (PT) to transform the received signal into the polar domain counterpart, similar to the angular domain transformation. The key distinction between the MRDN and PMRDN lies in their approach to exploit the inherent channel sparsity. The MRDN-based CE scheme transforms the channel to the angular domain, exploiting the angular-domain sparsity in the far-field. In contrast, the P-MRDN-based CE scheme transforms the channel to the polar domain, leveraging the polar-domain sparsity in the near-field. To further improve the channel estimation accuracy, the authors in [230] define a parallel part of the atrous spatial pyramid pooling (ASPP) and residual dense network (RDN), named ASPP-RDN, as shown in Fig. 5.7. By incorporating the notion of ASPP into the proposed P-MRDN, the new CE scheme can achieve lower normalized mean-square error (NMSE) performance as the ASPP can integrate multi-scale features of its input.
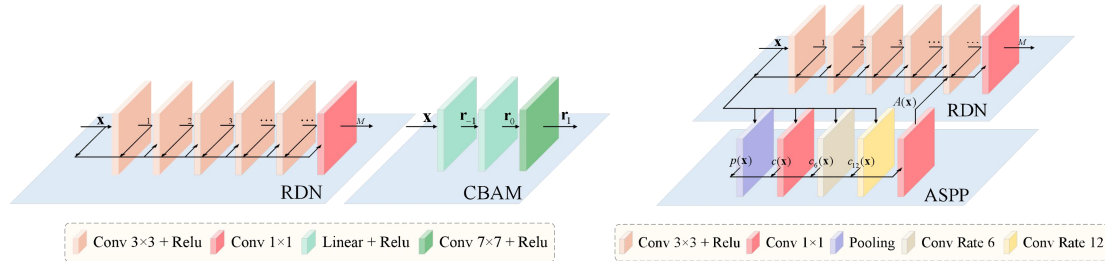
Fig. 5.7 RDN、CMAM and ASPP-RDN system models

To compensate for the product-distance path-loss in high frequency bands, one efficient approach is packing more and more reflecting elements, leading to the so-called extremely large-scale RIS (XL-RIS) [236]. Compared with the conventional RIS with a modest number of reflecting elements, XL-RIS introduces a fundamental change in the wireless channel modelling, shifting from the conventional far-field planar wavefronts to the new near-field spherical ones. In order to fully unleash the potential of XL-RIS in enhancing wireless communication performance, accurate CSI is indispensable yet challenging to acquire. There exist two key issues in XL-RIS channel estimation, when the XL-RIS has an extremely large aperture. First, different from the existing works that only considered the near-field RIS-user channel, both the BS and users may be located in the near-field region, thus rendering the cascaded channel modelling and channel estimation more complicated. Second, the spatial non-stationarity may concurrently exist in both the BS-RIS and RIS-user channels, termed as double-sided VRs, where only a portion of XL-RIS elements are visible to the BS and users.

Fig. 5.8 Illustration of XL-RIS aided wireless system.
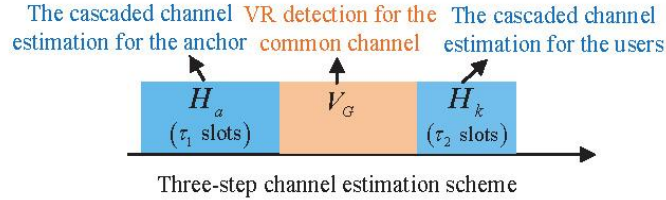
Fig. 5.9 Illustration of three-step channel estimation.

To address these issues, the authors in [237] studied efficient channel estimation design for XL-RIS assisted multi-user systems, where both the BS and users are located in the near-field region of the XL-RIS. As shown in Fig. 5.9, a three-step XL-RIS channel estimation scheme is proposed to effectively estimate the BS-RIS-user cascaded channels accounting for the non-uniform spherical wavefronts and double-sided VRs for the XL-RIS. Specifically, in the first step, an anchor node is delicately deployed to estimate the cascaded BS-RIS-anchor channel for decoupling the double-sided VRs. Then, the BS-sided VR information is accurately detected by an efficient VR detection method. As such, only the channels from the visible XL-RIS elements to the BS are estimated, thereby reducing the pilot overhead for estimating the cascaded BS-RIS-user channels. Finally, the common BS-RIS channel and BS-sided VR are utilized to consecutively estimate the cascaded BS-RIS-user channels with different user-sided VRs. Numerical results showcase the superior performance of our proposed XL-RIS channel estimation method as compared to various benchmark schemes.

In addition to the "angular-distance" (polar) domain, where the near-field channel model presents the sparsity, the fractional Fourier domain serves as another domain that represents the sparsity of the near-field channels. The main reason is that the received signal can be modeled as the superposition of several linear frequency modulation (LFM) components using Taylor expansion. Many LFM signal parameter estimation methods have been developed based on the fractional Fourier transform (FRFT) [238]. As analyzed in [239], the sparsity exhibited by near-field channels in the fractional Fourier domain is explained, and the orthogonality conditions are given for near-field codebook desig. The FRFT-based parameter estimation methods provide fundamental mechanisms for near-field channel estimation. The mechanism behind the sparsity of the near-field channel and the suitability of FRFT in estimating the near-field channel are explained in Fig. 5.10. Similar to the time-frequency distribution of a time-domain signal, the near-field channel model in a space-angle plane is illustrated in Fig. 5.10 (a), where the projection of the space-angle distribution in the angle domain corresponds to the red waveform in Fig. 5.1. The space-angle plane can be rotated via the FRFT, as shown in Fig. 5.10 (b). The projection of the space-fractional Fourier distribution in the fractional Fourier domain is a pulse, which aids near-field channel estimation, analogous to the role function of the blue pulses in Fig. 5.1. Therefore, the role of FRFT in near-field channel estimation is analogous to that of the Fourier transform in far-field channel estimation.
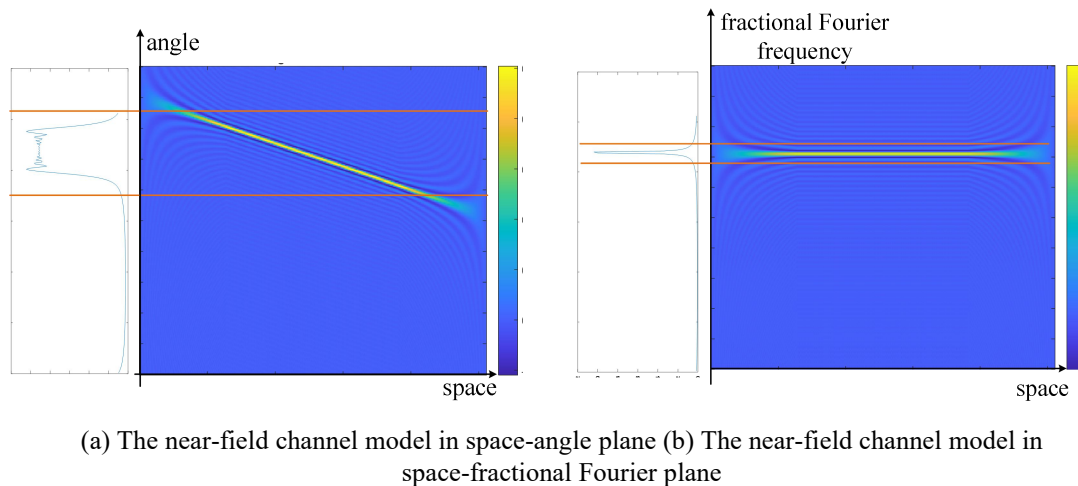
(a) The near-field channel model in space-angle plane (b) The near-field channel model in space-fractional Fourier plane
Fig. 5.10 Illustration of the FRFT in near-field channel estimation.

Different from most of the polar domain near-field channel estimation algorithms, which rely on the compressive sensing theory, the sparsity in the fractional Fourier domain enables low-complexity analytical near-field channel estimation methods. For example, [240] introduces the discrete FRFT-clean parameter estimation method for near-field channel estimation. However, this method is inherently an on-grid method, where the on-grid error becomes non-negligible. To address this problem, several two-step channel estimation methods have been proposed. For example, [241] combines the FRFT-based on-grid estimation with the Newton-based refinement to realize a gridless channel estimation approach, for which the Cramer-Rao lower bound and Ziv-Zakai bound are analyzed. [242] first demonstrates the sparsity of the hybrid near-field and far-field channel model in the fractional Fourier domain and then proposes a discrete FRFT-based Newton orthogonal matching pursuit algorithm without prior knowledge of the number of propagation paths.

Moreover, another key characteristic of the near-field channel is the spatial non-stationarity, i.e., different visibility regions (VRs) for different antenna subarrays. which hinders the application of traditional beamforming schemes. As indicated in [243], this phenomenon results in performance degradation for conventional beamforming schemes that neglect the non-stationarities. The formation of spatial non-stationary effects can be attributed to several factors, including unequal pathloss between the user and different array elements. As a consequence of extended array size, when the distance between users and the array is less than the Fresnel distance, the spherical wave propagation characteristics lead to weaker energy reception by antennas farther away from the user. From another perspective, the unequal channel power arises from the signal blockage caused by obstacles. Different from the far-field situation the total channel is more likely to be blocked, and the channel of a user in the near field or the Fresnel region may usually be obstructed partially, which leads to unequal distribution of channel power among the array elements. It can be anticipated that when users communicate with the BS equipped with an extra large-scale array, only partial array elements perceiving a favorable channel environment receive the majority of signal power. Conversely, a significant portion of array elements, owing to factors such as unideal distance and angle relative to the user, may only capture low signal power.

To obtain the CSI regarding the non-stationary and near-field characteristics, it is imperative to carry out VR identification from both the array side and the user side. When the fully-digital RF-front is equipped with the BS and a single-antenna user is served, the VR identification at the array side can be realized based on the uplink pilot [201][244]. However, the near-field and non-stationary characteristics are especially obvious for extra large-scale arrays with hybrid beamforming structures, the direct acquisition of received signal power corresponding to each antenna element poses significant challenges. Therefore, the authors in [245] consider the VR identification problem when a subarray-based hybrid beamforming structure is equipped with the BS. The near-field channel parameters are first extracted through the parameterized channel estimation schemes, afterwards the VR is identified by comparing the received signal and the reconstructed channel. Furthermore, the authors in [246] realize the VR identification with the fully connected hybrid beamforming structure. Inspired by the classical Alamouti code, the authors artificially create the time-domain relevance to enable the recognition of non-stationary effect in the space domain. The extra large-scale RIS also stands as one of the implementation approaches for extra large-scale MIMO systems, therefore the deployment of an extra large-scale RIS similarly introduces near-field and spatial non-stationary characteristics. Specifically, [247] considers the VR identification of extra large-scale RIS systems. The UE-RIS-BS cascaded channel is first estimated, and the VR is then identified by detecting the inequality power of the reconstructed channel. As for the VR identification at the UE side, the VR is defined as geometric areas associated with certain sets of antennas. That is, when a user is situated within the VR, the signal can be received by specific array elements. As the user transitions into another VR, the signal can be received by a different set of array elements. Based on this, authors in [248] further take the multipath in the UE-RIS channel and design a two-dimensional space-time-block-code based scheme to extract the signal for different VRs to realize accurate channel estimation. In [249], the VRs of some beacon users are assumed to be known as a priori, and then a neural network-based approach termed VR-Net is designed to detect the correspondence between the VRs and the sets of array elements, which realizes accurate VR identification with low complexity.
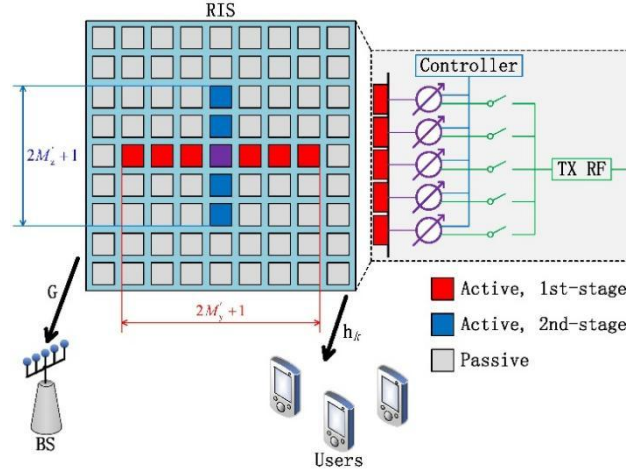
Fig. 5.11 RIS architecture transmitting pilots using one RF-chain.

Although various channel training schemes have been proposed in the existing literature, these existing methods are almost all cascaded-channel (CscdChn) type strategy. One limitation of CscdChn strategy lies in double-fading effect. That is, as unveiled in [250]-[252], the multiplicative fading coefficients of two-hop BS-RIS-user channel severely attenuate the receiving power of pilot signals. Since channel estimation (CE) accuracy is inversely proportional to signal-to-noise-ratio (SNR) of receiving pilots[253], it is indeed drastically degraded by the intrinsic double-fading effect of CscdChn type schemes. Based on the above inspections, alternative RIS CE schemes other than CscdChn are highly desirable to explore. Recently, the work [254] proposed a novel RIS transmitting (RIS-TX) training strategy via emitting pilots from RIS side using one TX RF-chain. This new strategy appropriately overcomes double-fading effect by directly measuring one-hop RIS channels while maintaining a high hardware efficiency. As reported in [254], applying linear estimators, RIS-TX scheme outperforms the CscdChn counterpart provided the number of RIS elements is modestly large (e.g., less than 10000). For RIS CE in the near-field (NF) environment, via leveraging NF channel models and applying spectral estimation with much less parameters than linear estimation in [254], RIS-TX training strategy can be further improved. Enlightened by this idea, we propose to accommodate RIS-TX training strategy [254] to NF channel models. Specifically, empowering by one TX RF-chain at UPA-shaped RIS (see Fig. 5.11), we let a sub-row and a sub-column of RIS elements transmit pilots during training process.We present a brand new RIS-TX channel training scheme suitable to NF channel models in a multi-user system by transmitting pilot signals to the BS and mobile users to perform CE with one TX RF-chain embedded in RIS device. This novel CE scheme can effectively overcome double-fading effect suffered by prevalent cascaded CE schemes. Based on the above RIS-TX strategy, we propose a two-stage training protocol with each stage emitting pilots from a sub-row and sub-column of RIS elements, respectively, which wisely decouples NF spectral parameters associated with the UPA-shaped RIS and hence efficiently conducts non-linear spectral estimation. For the typical NF propagation scenario where channel contains only LoS path, RIS channels can be estimated via sequential 1D-MUSIC searches. Our proposed training scheme yields mean-square-error (MSE) performance approaching Cramér-Rao lower bound (CRLB) and remarkably outperforms the linear estimation scheme [254] and the classical compressive-sensing (CS)-based method[255], which suffers from high CE error floor. Besides LoS-only scenarios, we further investigate the more generic case when all RIS channels contain multiple NLoS paths. In this case, one

major challenge lies in the low dimension of received signals at mobile users' side, due to the limited antenna size. To overcome this difficulty, we propose a two-step estimation procedure by first extracting dominant LoS path and then aggregating all users' data to retrieve NLoS parameters associated with commonly seen scatters. Our proposed training strategy appropriately decomposes high dimension spectral parameters, efficiently recovers NLoS parameters via sequential 1D-MUSIC search followed by handy matching process.

5.2 Near-Field Beamforming

Beamforming is a signal processing technique that uses antenna arrays to direct a wireless signal towards a specific receiver, rather than broadcasting it in all directions. It can be achieved by adjusting the weights and phases of the antenna elements to create constructive and destructive interference patterns in the desired directions or locations. Beamforming can improve the quality, capacity, and reliability of wireless communication by enhancing the desired signal and reducing interference. In the existing far-field wireless communication system, since the electromagnetic wave front is planar, beamforming can only control signal propagation in one dimension of angle. Unlike the far-field, in the near-field communications, the near-field beamforming (beam focusing) technique is able to focus the signal energy at a specific location by exploiting the propagation characteristics of spherical waves to achieve the control of signal propagation in both angular and distance domains [256][257]. Near-field beamforming (beamfocusing) provides a novel multi-user interference control mechanism.
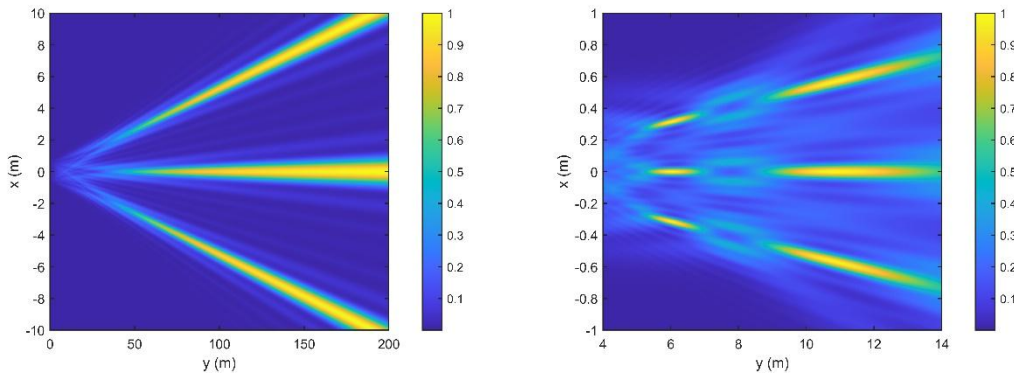
Fig. 5.12 Far-field beamforming and Near-field beamforming

With known CSI, the near-field beamforming design can still adopt the traditional MIMO beamforming design methods, such as Maximum Ratio, Zero-Forcing and Minimum-Mean Square Error, to achieve spatial multiplexing. Compared with far-field plane wave propagation, near-field spherical wave propagation can substantially enhance the spatial multiplexing capability. Specifically, as shown in Fig. 5.12, in far-field communications, the channels of different users converge to orthogonality only gradually in the angular domain as the antenna array size increases. This orthogonality is determined by the beam width. However, when the users are located in the near field, the asymptotic orthogonality of the user channels exists not only in the angular domain but also in the distance domain. This orthogonality is determined by both beam width and beam depth [258]. Therefore, in the near-field communications, beamforming is able to focus the beam on a specific angle and distance at the same time, achieving a higher DoFs of spatial multiplexing, effectively suppressing

inter-user interference, and facilitating multiple access. To exploit the multiple DoFs more effectively in near-field LoS MIMO channels with limited RF chain constraint, spatial path index modulation (SPIM) is also a promising beamforming architecture for higher energy efficiency in near-field communication [259].
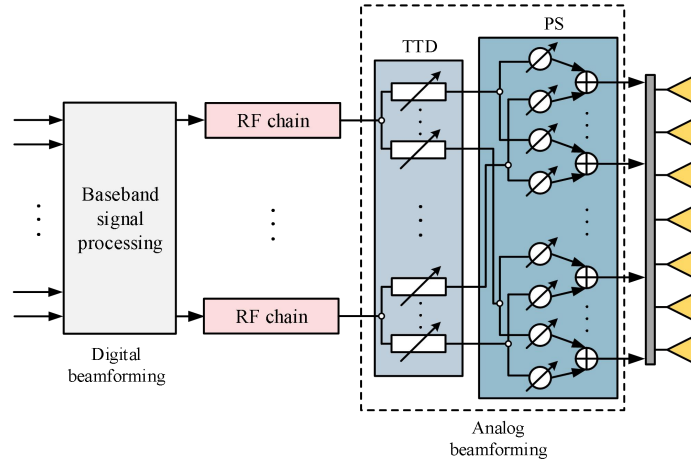
Fig. 5.13 Fully-Connected Delay-Phase Hybrid Beamforming
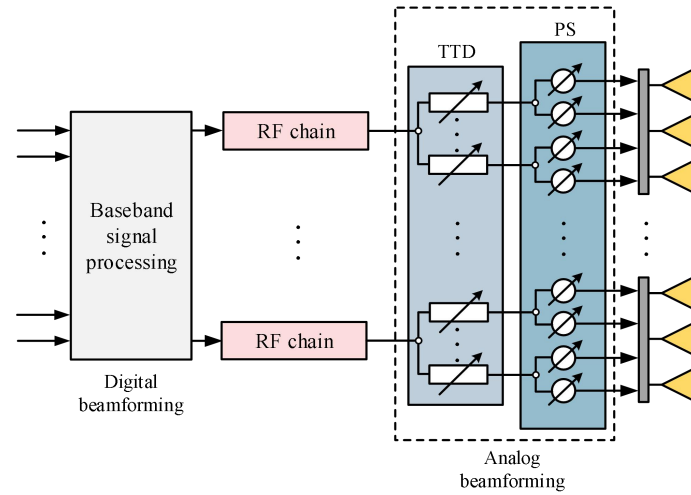
Fig. 5.14 Partially-Connected Delay-Phase Hybrid Beamforming
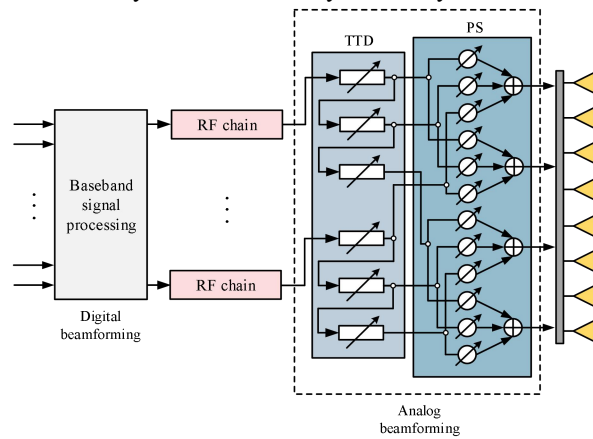
Fig. 5.15 Serially-Connected Delay-Phase Hybrid Beamforming

There is a dual wideband effect in multi-antenna wideband systems, namely a frequency wideband effect caused by multipath effects and a spatial wideband effect due to large antenna apertures. The

frequency wideband effect results in frequency selectivity of the near-field channel, causing serious inter-symbol interference (ISI) problems. Such challenges can be effectively addressed by various existing techniques, such as OFDM with cyclic prefixes. The spatial wideband effect allows different subcarriers to "see" the user position at different angles and distances. The problem of beam squinting or beam splitting can occur when transceivers use energy-efficient hybrid digital-analog beamforming architectures. Specifically, conventional analogue beamforming uses phase shifters (PSs) that are not frequency-selective to generate beams. PSs are unable to generate different beams for different subcarriers, and therefore are not able to accurately focus the beams at the user for different subcarriers. To cope with these challenges, [260] and [261] proposed a fully-connected delay-phase hybrid beamforming architecture, as shown in Fig. 5.13. This architecture effectively overcomes the beam squinting or beam splitting problems by introducing an appropriate amount of true time delayers (TTDs) to realize frequency-dependent analog beamforming.

However, in near-field communications, in order to ensure a certain scale of near-field range, antenna arrays are usually required to have a large aperture, which puts stringent requirements on the achievable maximum delay of individual TTDs. To address this issue, [262] and [265] proposed partially-connected and serially-connected delay-phase beamforming architectures (as shown in Fig. 5.14 and Fig. 5.15), respectively, in order to reduce the maximum delay requirement, and hence the hardware cost and complexity, as follows:

● Partially-Connected Delay-Phase Beamforming [262]: In this architecture, each RF chain is connected to an antenna subarray through TTDs and PSs. Therefore, each set of TTDs only needs to overcome the beam squinting or beam splitting issue of each subarray. Since each subarray has a smaller aperture, the maximum delay requirement of individual TTDs can be greatly reduced. However, there may be an unavoidable performance loss with this architecture as each RF chain cannot fully exploit the entire antenna array.

● Serially-Connected Delay-Phase Beamforming [265]: In this architecture, each RF chain is still connected to the entire antenna array. However, the TTDs no longer work independently in parallel, but are connected in serial. As a result, the architecture is able to utilize multiple short-range TTDs to accumulate a large delay and effectively overcome the beam squinting or beam splitting issue. However, the serial connection of TTDs introduces cumulative insertion loss at the same time, and therefore new TTDs with low insertion loss need to be designed.

The huge number of antennas in XL-arrays significantly increase the hardware cost and energy consumption, especially when the antennas employ high-resolution phase shifters (PSs). For example, in the mmWave bands, the power of a 4-bit PS is up to 45-108 mW, which is much larger than that of the low-resolution 1-bit PS with 5 mW only. Therefore, one practical and more energy-efficient design for XL-arrays is employing discrete PSs for analog beamforming. Nevertheless, this also introduces two new challenges. First, it is unclear whether discrete PSs will affect the beam-focusing effect, which is conventionally revealed under the assumption of continuous PSs. Second, the phase quantization under discrete PSs renders the existing beam pattern analysis method inapplicable, since there generally lacks a closed-form expression for the analog beamformer under discrete PSs.

The Fourier series expansion (FSE) method can be used to efficiently tackle the difficulty in characterizing the beam pattern properties under phase quantization, which decomposes the beam pattern function into a sum of various terms, each of which represents a dominant lobe. Then, through

analysis, we show that the main lobe still exhibits the beam-focusing effect, with its beam power increasing as the PS resolution improves, while its beam width and beam depth remain the same as in the continuous case. Moreover, discrete PSs also introduce additional grating lobes which can be classified into two types, featured by the beam-focusing and beam-steering effects, respectively. Note that the locations of grating lobes are dependent on the user location. For example, as shown Fig. 5.16, each dominant lobe does not overlap, which allows an effective representation of the beam pattern characteristics by the properties of the dominant lobe. It is observed that, in the case of 1-bit PSs, the main lobe focuses around the user's location, and the phenomena of grating lobes are obvious. The two types of grating lobes exhibit beam focusing and beam steering, respectively. However, when the XL-array has 2-bit PSs, the number of grating lobes and their powers are greatly reduced. In particular, Type-I grating lobes almost disappear in the pattern, while Type-II grating lobes still have mild powers.

| (1) Continuous PSs | (2) 1-bit PSs | (3) 2-bit PSs |
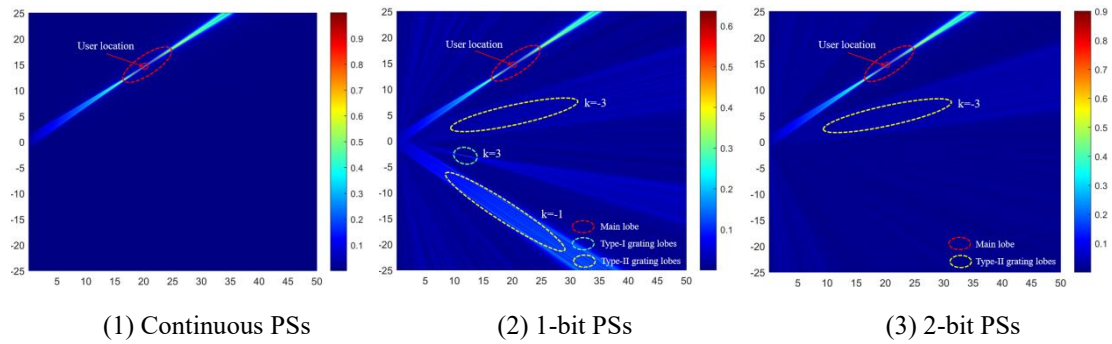
Fig. 5.16 The near-field beam patterns in different scenarios.

In addition, it is also shown that the PS resolution affects the beam power of both the main and grating lobes, while it has no influence on the beam-width and beam-depth. In general, the power loss in the main lobe due to discrete PSs decreases with PS resolution. In addition, the beam powers of grating lobes are suppressed more effectively when the PS resolution increases, which become negligible when the PS resolution is high enough, similar to the continuous PS case. In terms of the impact of discrete PSs on communication performance, it primarily arises from the main lobe power loss and the interference caused by grating lobes. Specifically, the main lobe power loss is solely dependent on the PS resolution, which can be mitigated by increasing. On the other hand, the interference from grating lobes is jointly determined by the user location, antenna number and PS resolution.

Apart from the favorable beam-focusing gain for near-field communications, the imperative CSI requirements for beamforming design pose challenges due to the informative near-field channel embedded with both the angle and distance information. Different from existing a clear linear relationship in the far-field channel, the near-field channel exhibits nonlinear variations among antennas, making it challenging to characterize the overall channel through several parameters. The aforementioned parametric CE schemes can effectively reduce the pilot overhand for one RIS-associated link. However, in multi-RIS-assisted scenarios, it still necessitates complex multi-stage design and large overhead to separately estimate the multiple RIS-associated links. For instance, to acquire RIS-associated CSI, the pilots allocated to different RISs should be orthogonal in multi-RIS-assisted systems, inevitably necessitating enormous CE overhead.
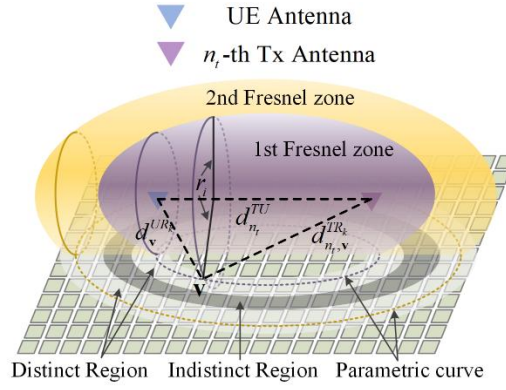
Fig. 5.17 The distributions of Fresnel zones.

To address such issue, as UE's location information is sharable for beamforming design among all RIS-associated links, the authors in [263] proposed a location-driven beamforming framework as opposed to existing CE-driven beamforming schemes. Therein, as shown in Fig. 5.17, by exploiting the Fresnel diffraction theory, the phase distributions of waves established by locations was revealed in the presence of 1-bit RIS element. The distributions of these ellipsoids depend on the distance of Tx-Rx link and operational frequency. Based on the known locations, simultaneous equations of the ellipsoids and the RIS plane are established and addressed by coordinate transformation [264].
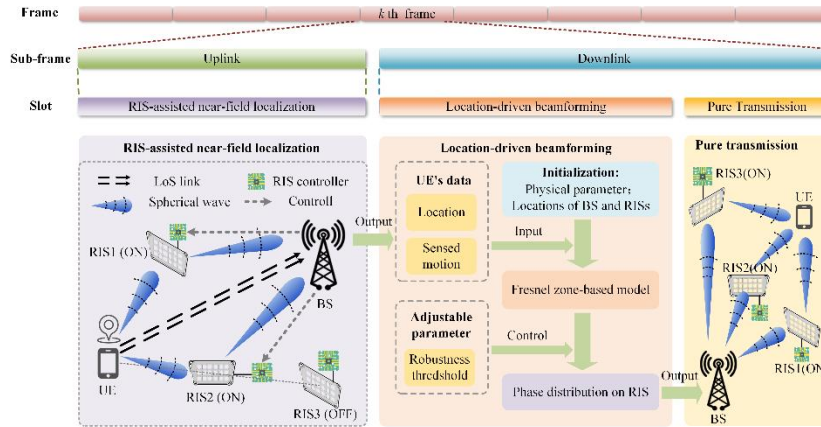
Fig. 5.18 The location-driven beamforming frame structure.

Then, by solving the formulated parametric equations of various Fresnel ellipsoids, a complete location-driven beamforming scheme and its corresponding frame structure was designed in Fig. 5.18, which also enabled the robust performance according to location deviation in practical scenario. The pilot overhead originates from the flexible selection capability in location-driven scheme and the sharing of UE's location for beamforming design. For example, the RISs with the similar direction relative to the UE cannot significantly improve the localization performance (RIS2 and RIS3 as shown in Fig. 5.18), and thus only enabling one of them helps to reduce the pilot overhead. Additionally, supported by enhanced localization precision in the near-field region, the location-driven beamforming scheme alternates as a potential solution for future RIS-assisted near-field communications, which can be further integrated with predictive beamforming by capturing UE's motion, exhibiting favorable expandability and compatibility with other technologies.

The existing works on near-field communications mainly focus on dense XL-arrays with half-wavelength inter-antenna spacing. This array configuration incurs high power consumption and hardware cost, due to the large number of antennas and phase shifters (PSs) required. For example,

considering a setup with 20 RF chains and 512 antennas with PSs fully-connected, the power consumption is up to 158.4 W, which is practically unaffordable.

To address this issue, the authors in [267] proposed to enable near-field communications by using sparse arrays (SAs), hence achieving higher spectrum efficiency and spatial resolution with a small number of antennas only. We first characterized the beam pattern of a sparse linear array and unveil the multiple beam focusing pattern, which motivates us to design a customized hybrid beamforming method to overcome the interference caused by grating lobes. Moreover, we proposed a novel array configuration, called extended coprime array (ECA), which effectively suppresses the interference power at grating-lobes [267].
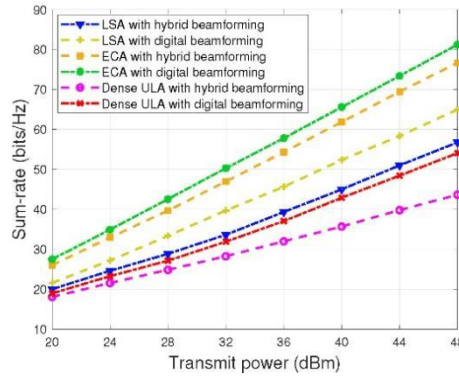
Fig. 5.19 Sum-rate versus BS transmit power
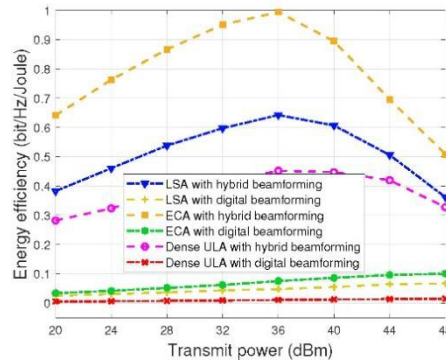
Fig. 5.20 Energy efficiency versus BS transmit power

The simulation results indicate that the proposed sparse arrays achieve higher energy and spectrum efficiency than dense arrays. In addition, the proposed hybrid beamforming design for ECAs achieves a higher sum-rate than that of the linear sparse array (LSA). This is intuitively expected, since the grating-lobes of LSAs have relatively high beam-power and thus incur high IUI when occurred.

In addition, under near-field non-stationary conditions, precoding can be designed using VR in the visible area of the antenna that dominates the user's received power. Considering that antenna VR has a significantly lower number of antennas compared to the entire ELAA, precoding based on VR design can significantly reduce the complexity of matrix inversion and other operations.

The authors of [154] proposes that the closed form expression for the received power of each sub-array can be calculated based on the near-field channel expression, in order to find the set of subarrays that play a dominant role in the signal reception process. Subsequently, based on the obtained VR information, the channels corresponding to each user in VR can be reconstructed to design low

complexity precoding based on VR. Meanwhile, due to the fact that array VR can receive the vast majority of signal energy, this algorithm can achieve performance similar to precoding based on full array received signals. Extremely large-scale antenna arrays have the ability to serve a large number of users, and considering the dispersed distribution of users in space, each user may have different antenna VR.

Therefore, based on the graph theory maximum independent set algorithm, users with similar VR can be divided into groups, and intra group interference can be eliminated using partial interference zero forcing algorithm. Compared to performing zero forcing interference cancellation on a large number of users, the partial interference zero forcing algorithm based on user grouping can further reduce the precoding complexity. Due to the small inter group interference between user groups with small VR overlap, the intra group interference cancellation algorithm can achieve system performance that is very close to full user interference cancellation [154].

Meanwhile, a beamforming design scheme was also proposed in [269], which utilizes the user visible area distribution information obtained through channel estimation from BSs for beamforming. As shown in Fig. 5.21, an extremely large-scale MIMO system with CPU and LPU collaborative processing is considered. By using distributed precoding based on subarrays at the BS, the non-stationary characteristics of the channel can be effectively utilized to achieve good spectral efficiency (SE), and low complexity receivers designed based on the randomized Kaczmarz (rKA) algorithm can achieve a balance between performance and complexity.
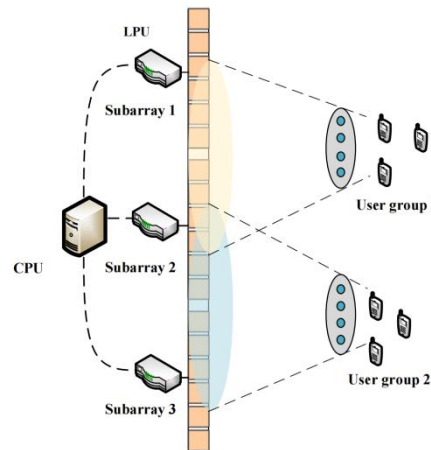
Fig. 5.21 Extremely large-scale MIMO system with CPU and LPU collaborative processing.

In [270], a dual beamforming scheme is designed based on a two-layer antenna architecture composed of an active layer of phased array antenna (PAA) and a passive layer of RIS, as illustrated in Fig. 5.22. The PAA acts as the feed antenna for the RIS, and the RIS forwards the incident signals to the UE equipped with conventional antenna arrays. Specifically, precoded signal streams are emitted by the PAA subarrays and beamformed towards the respective RIS subarrays. When the RIS size is sufficiently large, the incident power distribution on the RIS can be manipulated by steering the PAA beams so that a particular subset of RIS elements at desired locations can be illuminated. Next, the phases of the illuminated RIS elements are adjusted to steer the RIS beams towards the UE to achieve coherent transmission. The above system effectively realizes aperture adaptation with fixed physical antennas such that the effective LoS MIMO channel can be orthogonalized in order to achieve higher

spatial multiplexing gain. Furthermore, this scheme helps to reduce the cost and power consumption of the BS and is also able to simplify the baseband spatial processing of both BS and UE.
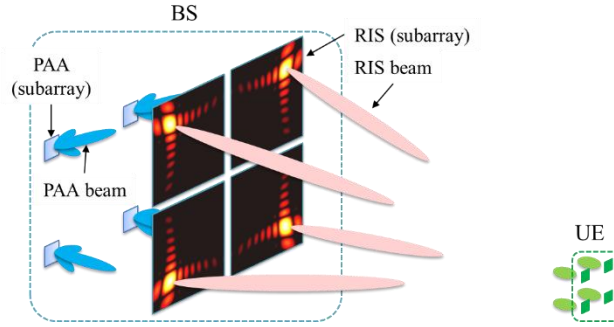
Fig. 5.22 PAA-RIS dual beamforming scheme

In addition to beam focusing that could result in a narrow beam given a large aperture and a high frequency, variable beamwidth near field beamforming is proposed to illuminate a larger region so that it's robust to user location errors. In [271], the authors used a technique that maps the RIS elements to a tunable spherical surface. By tuning the size and center of the surface, variable width beams and illuminated areas can be achieved. In addition, unlike the wider beam design in [272], the proposed spherical-mapping-based beamforming remains a good illumination shape when the BS and UE are far from the RIS boresight direction. The rate heatmap comparison using near field beam focusing, far field beamforming, and the proposed variable beamwidth design is provided in Fig. 5.23. The desired illumination region is marked in red. The system operates under 30 GHz and the number of RIS is 200×200. It can be seen that the proposed beamforming can illuminate the desired coverage region at the cost of decreased highest rate but a higher average rate.
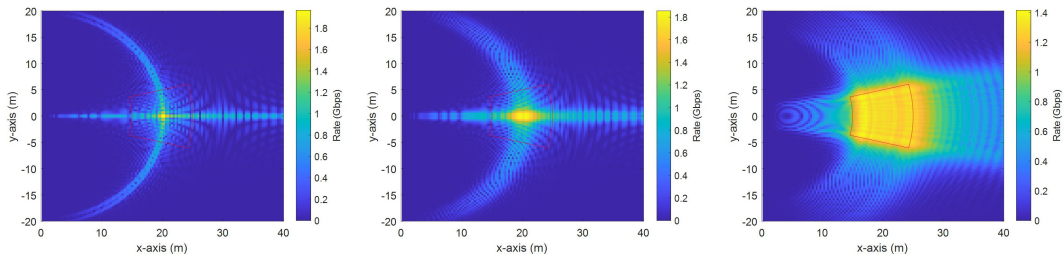
Fig. 5.23 Rate heatmap comparison
(From left to right: near field beam focusing, far field beamforming, the proposed variable beamwidth near field beamforming).

Compared to uniform arrays with half-wavelength spacing, sparse arrays can achieve larger aperture sizes, thereby fully exploiting the advantages of near-field communication. The beam gain characteristics of uniform sparse arrays in the hybrid field are analyzed in [273] to exhibit three key features including periodic beam gain, stronger beam focusing capability and higher spatial resolution compared to uniform arrays with half-wavelength spacing. However, due to the periodicity of the beam gain, uniform sparse arrays also suffer from grating lobes, causing severe multi-user interference. Therefore, an antenna position optimization algorithm based on successive convex approximation for non-uniform sparse arrays is proposed to reduce the impact of the grating lobes. As shown in Fig. 5.24, the non-uniform sparse array effectively suppresses the grating lobes compared to uniform sparse array.

a) Beam Pattern of Uniform Sparse Array
b) Beam Pattern of Non-Uniform Sparse Array
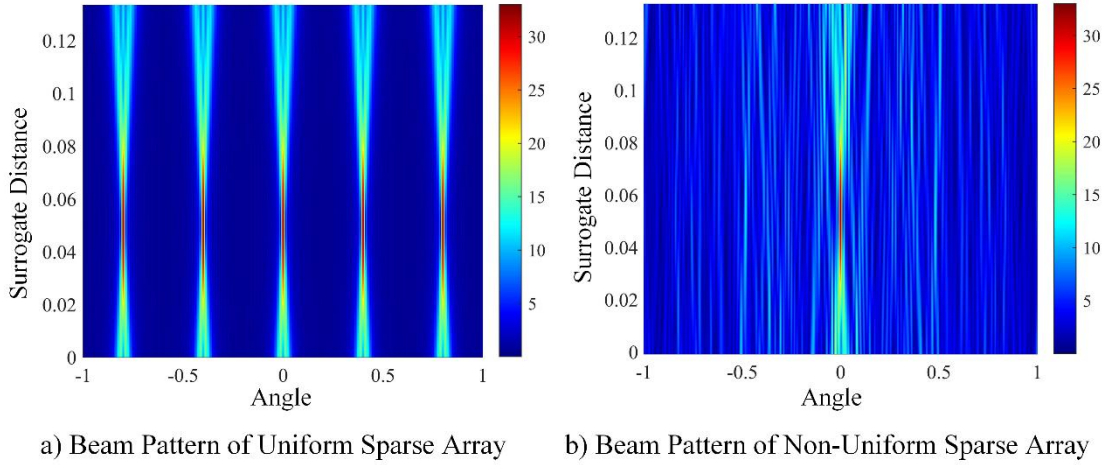
Fig. 5.24 Comparison of uniform and non-uniform sparse arrays in terms of the beam pattern

Moreover, it can be seen in Fig. 5.25 that the proposed non-uniform sparse array offers significant advantages in terms of supporting a higher number of users and improving data rate performance compared to existing uniform half-wavelength-spaced arrays and uniform circular arrays. Therefore, employing the beamforming scheme with non-uniform sparse arrays presents new possibilities for developing efficient near-field multi-user communication systems.
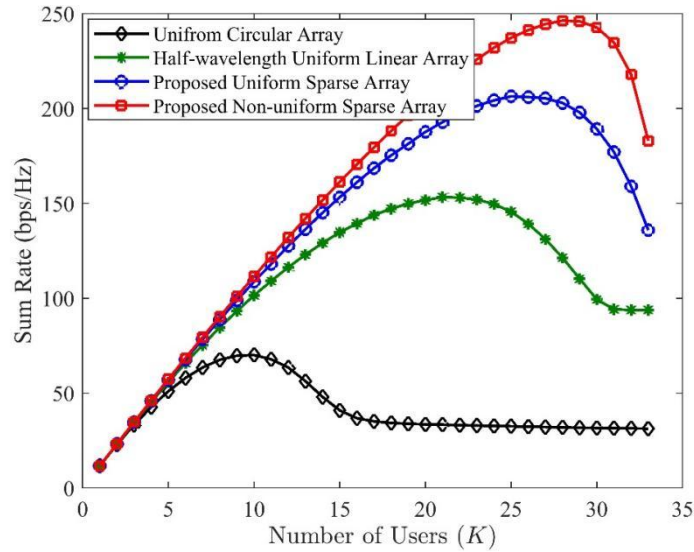
Fig. 5.25 Comparisons of different arrays in terms of sum-rate for different numbers of users.

There are two main types of electromagnetic wave convergence for near-field antennas. One is to converge the radiated electromagnetic wave energy at a focus point called near-field focusing. The other is to converge the radiated electromagnetic wave energy along a strip to maintain diffraction-free propagation called near-field beamforming, also known as non-diffraction beamforming [1]. Non-diffraction beamforming avoids the limited energy convergence area associated with near-field focusing, allowing the signal to be maintained over longer distances and effectively extending the transmission range. It also offers new features, such as self-healing, enabling transmission around obstacles, making it a promising technology for future 6G applications. In this section, we will analyze typical non-diffractive beams, including Bessel and Airy beams, and explore their propagation properties and advantageous use cases.

To accommodate the diverse application scenarios of 6G and meet their varying requirements, it is essential to design appropriate precoding strategies tailored to different transmission objectives. The near-field channel introduces new DoFs, making the need for flexible and adaptive precoding design more critical. Personalized and scenario-specific precoding designs will be key to realizing the wide-ranging functionalities of 6G networks.

In near-field focusing applications, the focal spot is typically small, resulting in a limited coverage area. This limitation becomes more pronounced as the array size increases, since it requires more precise alignment and tracking of the target user, significantly increasing the complexity of maintaining effective communication. Additionally, the small size of the focal spot presents challenges in supporting mobility. In scenarios where the target user or device is in continuous motion, the near-field focusing system must quickly and accurately adjust the focal point, demanding high tracking capability and processing speed, particularly in high-speed environments like communication for high-speed trains or cars.

Specifically, the radial coverage of a near-field focused beam is very limited. This limitation can lead to issues such as slower CSI updates, channel estimation errors, and delayed beam switching, all of which can significantly impact the quality of service for users. In high-speed mobility scenarios, for instance, the rapid changes in user position require higher tracking accuracy and faster response times to ensure the stability and reliability of the communication link. These challenges necessitate advanced technologies and algorithms to achieve precise positioning and rapid beam adjustment, thus meeting the high-performance demands of 6G networks across diverse scenarios.

To enhance the SNR of received signals, expand coverage, and better support user mobility, high-frequency near-field beamforming solutions offer significant potential. Among them, Bessel beams, stand out due to their unique non-diffractive properties and stable axial intensity distribution. The non-diffractive nature of Bessel beams allows them to maintain a stable intensity distribution during propagation, making them particularly effective in scenarios that require stable signal transmission.

Bessel beams can be viewed as a superposition of plane waves covering all azimuth angles from 0–360◦, forming a specific angle ϕ_c with the propagation axis, known as the convergence angle of the Bessel beam. The implementation of Bessel beams relies on LoS near-field channels, and the corresponding precoding must precisely match the characteristics of these channels to ensure the beam's formation and stable transmission. The precoding can be expressed as $\Phi_2(n,n) = \exp\left(jkl\sin\phi_c\right)$, where l represents the distance between the n-th element and the center of the transmitter. This beamforming precoding achieves a conical wavefront through phase compensation.

According to the characteristics of the zeroth-order Bessel beam, the depth of field—defined as the length of non-diffractive region—and the half-power bandwidth (HPBW) are

$$z_{\max} = \frac{D}{2\tan\phi_c(f)}, \tag{5.1}$$
$$HPBW = \frac{2.235\lambda}{2\pi\sin\phi_c(f)}.$$

In practical applications, increasing the convergence angle enhances the beam's focusing ability

but limits capacity to maintain focus over longer distances, which can be problematic for scenarios requiring long-distance stable transmission. Conversely, decreasing the convergence angle extends the non-diffractive region, allowing the beam to remain stable over greater distances, but this also increases cross-polarization components, thereby affecting signal purity and transmission quality. Therefore, in designing non-diffractive beams, it is essential to balance the convergence angle, DF, and cross-polarization effects to meet the requirements of various application scenarios.

Fig. 5.26 shows the intensity distribution of a Bessel beam generated under a transmission frequency of 30 GHz, using a transmitter with 60×60 units, and a convergence angle $\phi_c = 8 \arcsin(\lambda/4D)$. In the figure, λ represents the wavelength, and D represents the transmitter aperture. There is a significant deviation between the beam obtained with 1-bit quantization and the target beam. However, simulation comparisons reveal that the beam shape is significantly optimized when using 2-bit quantization.
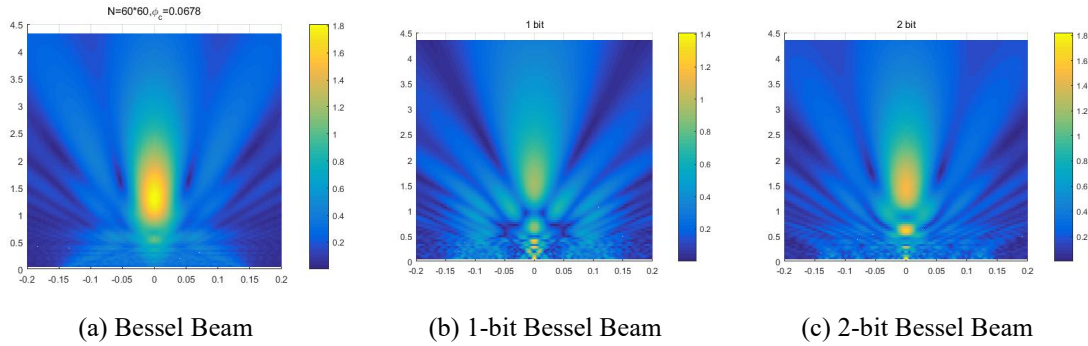
(a) Bessel Beam   (b) 1-bit Bessel Beam   (c) 2-bit Bessel Beam
Fig. 5.26 Bessel beam intensity distribution and the impact of quantization.

In the direction of signal propagation, Bessel beams generated through conical wavefront phase design exhibit excellent non-diffractive characteristics. Within the designated propagation range, these beamforming techniques achieve a uniform energy distribution, offering a more consistent energy distribution compared to near-field focusing beams. This feature of Bessel beams ensures high signal stability and continuous coverage, even in scenarios involving user mobility. The stable, non-diffractive nature of these beams is particularly crucial for wireless communication systems in dynamic environments. In high-frequency near-field communication applications, such as those found in 5G and 6G networks, Bessel beams effectively address signal instability caused by high-speed movement, providing a robust solution for maintaining communication continuity and reliability. As a result, Bessel beams hold significant potential for future high-speed wireless communication technologies, especially in scenarios demanding high stability and continuous coverage.

For high-order Bessel beams, in addition to their non-diffractive properties, they also possess the characteristics of non-diffractive vortex waves. In addition, other non-diffractive beams, such as Airy and Pearcy beams, can be combined with vortex waves to exploit the orthogonality and diversity of OAM modes, offering richer functionality (Further details are provided in Section 6.5.). In near-field scenarios, the research and application of vortex waves are more feasible than in far-field scenarios. Bessel beams, with their non-diffraction characteristics, maintain a stable energy distribution during propagation. Even when partially obstructed, the central portion of the beam remains strong, ensuring signal integrity. This makes Bessel beams particularly suitable for high-density urban environments and industrial IoT scenarios, where they can effectively handle signal interruptions caused by small

obstacles, ensuring stable communication links.

5.3 Near-Field Codebook Design

At present, the design of near-field codebooks mainly faces three major challenges. The first is that in practical applications, near-field phenomena often occur with extremely large-scale antenna arrays. The extremely large-scale antenna array has a higher spatial resolution, resulting in the need for more codewords to cover the entire near-field space. This makes the near-field codebook design bulky and time-consuming for beam training. The second issue is that near-field codebooks need to distinguish space from direction and distance variables, resulting in multiplicative time complexity and further expanding the volume of near-field codebooks. The third issue is that near-field space is difficult to orthogonally decompose. Due to the irregular shape of the near-field beam, the designed codebook may be unable to cover the entire near-field space, leading to near-field blind spots. In addition, if the orthogonality between codewords is not satisfied, it will cause some space to be covered by multiple codewords, resulting in redundancy in the codebook.

In the existing 5G NR standard, the precoding matrix indicator (PMI) codebook used to indicate CSI information uses DFT vectors as the basic unit of constructing codewords, which can be regarded as uniform quantization of the angle domain. When considering the scenario where the user is located in the near field, the fractional Fourier Transform (FRFT) vectors can be used as the basic codeword construction unit [274]. Specifically, as shown in Fig. 5.27 in the ULA scenario, the codewords are the FRFT vectors obtained by sampling the $\left(\sin\theta, \cos^2\theta/r\right)$ domains; while the UPA scenario corresponds to the sampling of the $\left(\sin\theta\cos\phi, \sin\theta\sin\phi, 1/r\right)$ domain. When the transformed distance domain information feedback value is 0, the FRFT codeword degenerates into a DFT codeword, maintaining compatibility with the existing PMI codebook scheme.

By analyzing the correlation between the near-field steering vector and the codeword, it can be found that the uniform sampling of the transform domain at equal intervals ensures the uniform, symmetrical, and monotonic characteristics of the correlation function distribution. From this, the maximum quantization error of the mixed field including near field and far field can be obtained. At the same time, the correlation function can be expressed by a quadratic polynomial, that is, the correlation contour is an ellipse. Based on this, the optimal sampling interval of the transform domain can be obtained analytically. Theoretical analysis shows that when the codebook size is limited, the angle domain should be quantized first. The distance domain introduced by the near field only requires a small number of samples, adding an additional 1 to 3 bits of feedback overhead[274]. In addition to sampling at equal intervals in the transform domain to obtain the near-field codebook, "angle-displaced" sampling can also be performed in the distance domain as shown in Fig. 5.28. Theoretical analysis shows that this new codebook design method can ensure the same quantization performance as uniform sampling, but the codebook size is only 77% of the comparison scheme.
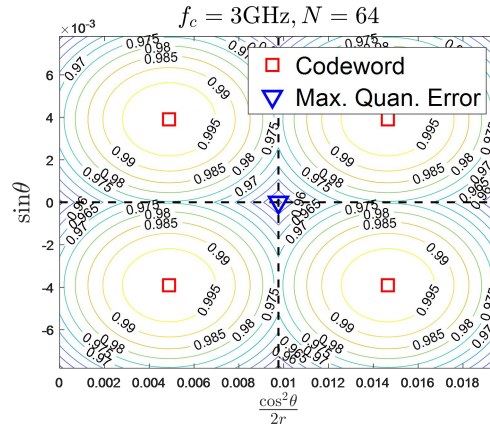
Fig. 5.27 Illustration of FRFT codeword quantization performance
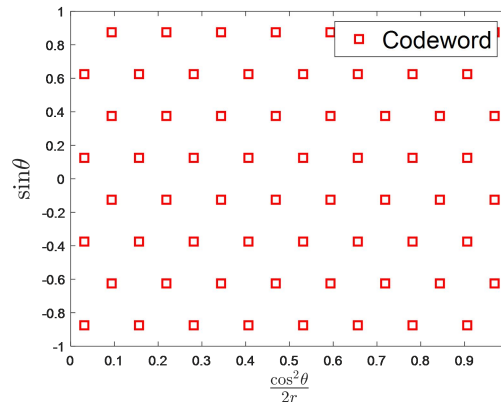
Fig. 5.28 Angle-displaced near-field codebook design method

The codebooks in 5G NR are based on DFT vectors, as shown in Fig. 5.29(a). But reusing DFT-codebooks for near-field beamforming causes severe SNR loss due to mismatch with the near-field channel. In contrast, beamfocusing based on the spherical wavefront assumption forms the optimum coherent beamformer for the near-field channel, as shown in Fig. 5.29 (d). However, ideal beamfocusing codewords are difficult to be expressed parametrically, and cannot be decomposed with Kronecker product for widely used uniform rectangular antenna arrays. Therefore, near-field codebooks shall be considered for large aperture MIMO antenna arrays.
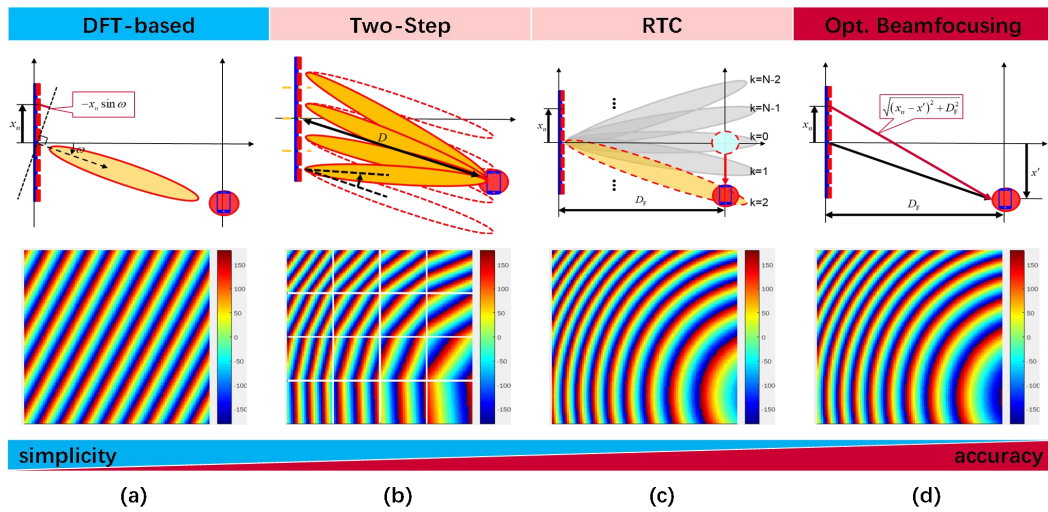
Fig. 5.29 Principle and phase distribution of far- and near-field codebooks

Two near-field codebooks are proposed by industry. One is referred to as two-step beamforming [275]. The idea is to divide a large aperture MIMO antenna array into multiple smaller subarrays such that the user is located in the far-field of each individual subarray and, thus, DFT-beams can be employed. The codewords are constructed as follows. In the first step, choose the DFT-beam pointing in the user direction for the entire array. In the second step, let the sub-beam of each subarray be steered by a small angle according to the relative position of the respective subarray w.r.t. the reference point of the entire array, and configure an initial phase for the subarray to compensate for the phase shift caused by the spherical wavefront. This codebook can be easily implemented accommodating the multi-panel antenna architecture. The other is referred to as ring-type codebook (RTC) [276]. The RTC is composed of two layers of codewords corresponding to the distance and the direction information of the user, respectively. The first layer of RTC is designed based on the Fresnel principle to form a focal point in the axial direction such that the user is located within the focal plane. The second layer is compatible with DFT-codebooks and meant to steer the focused beam generated by the first layer into the user direction. As compared to the two-step beamforming, the RTC is more accurate. Furthermore, the RTC still performs well with coarse phase quantization.

The near-field codebooks mentioned above can generate high-gain focused beams directed at specific UE locations. However, the beamwidth of focused beams is narrow, making it difficult to broadcast control channels/signals for a certain area. To address this issue, the above mentioned near-field codebooks are tailored in [277] to enable flexible beamwidth control. Specifically, the focal lengths are shortened to enlarge the beam footprint and, thus, to improve the coverage for an intended area, as shown in Fig. 5.30. The generated wide beams can be used to cell-specific channels/signals transmission, ensuring effective coverage of specific areas, while narrow beams are used for UE-specific channel/signal transmission to meet the high SNR requirements for data transmission.
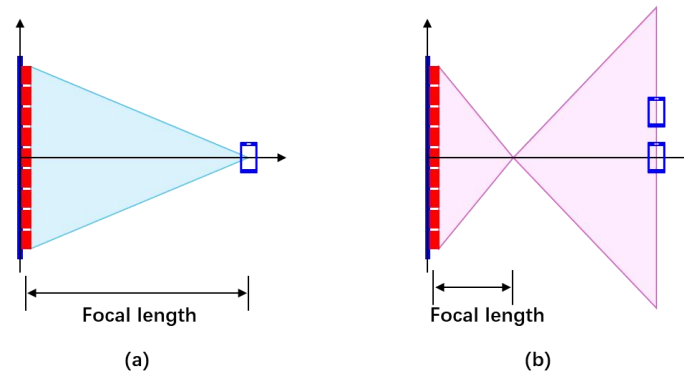
Fig. 5.30 Principle of the proposed flexible beamwidth control scheme.

Traditional codebooks are usually designed only for far-field areas. However, the enlargement in the physical dimension of antenna array causes the expansion of the near--field region, resulting in users being distributed across both near- and far-field regions [278]. Due to the different propagation characteristics of electromagnetic wave in different regions, traditional pure near- or far-field codebooks are no longer applicable to such a near-far field communication [279]. By combining propagation characteristics of the spherical wave for near field and plane wave for far field, a near-far codebook is constructed to perform beamforming without prior knowledge of user distribution [280].

1) **Codeword coverage discretization:** As shown in Fig. 5.31, the coverage of the transmitter is divided into the near- and far-field regions according to the radiation characteristics of electromagnetic

waves, and then further discretized into P areas corresponding to P codewords.

2) **Equivalent channel modeling:** Given the codeword coverage discretization, the equivalent channel from the transmitter to each area is constructed according to the electromagnetic wave propagation characteristics of each area.

3) **Codeword design:** The codeword design principle is that users receive no signal if they are outside the coverage area of the codeword, otherwise the received power is a constant C. Based on this principle and the equivalent channel models, each codeword design problem can be modeled as a quadratic problem and solved by a closed-form solution.
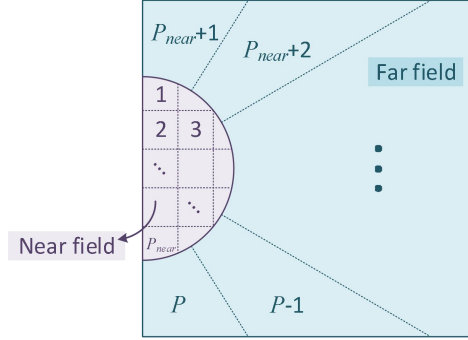
Fig. 5.31 Codeword coverage discretization in the near-far field codebook

In 5G NR, the candidate precoders of the Type I codebook as well as the orthogonal basis vectors of the Type II codebook are DFT vectors. However, in near field spherical wavefront, the phase difference between neighboring antenna elements is no longer equal. A novel codebook design for the near-field region with spherical wavefront should be studied. As illustrated in Fig. 5.32, consider an XL-MIMO system with a single polarization uniform line array, the distance difference between the ray of UE-antenna n and the ray of UE-reference antenna can thus be approximately calculated as $-nd\cos\theta + \frac{n^2 d^2 \sin^2\theta}{2r}$ by performing Taylor expansion.
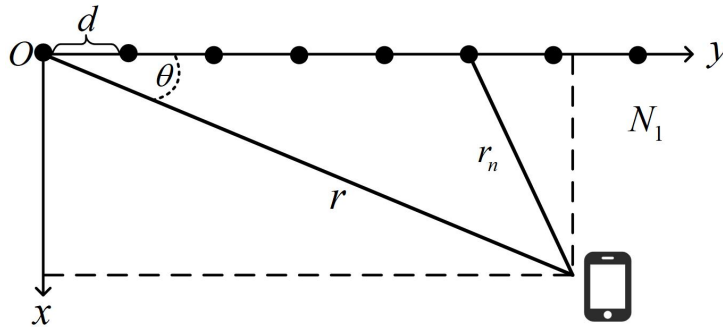
Fig. 5.32 Illustration of XL-MIMO system with single polarization ULA

Based on the distance of each antenna element in the antenna array from the UE, an element of the constant mode near-field precoder corresponding to antenna n can be represented as $w_n = \frac{1}{\sqrt{N_1}} exp\left(-j\frac{2\pi}{\lambda}\left(nd\cos\theta - \frac{n^2 d^2 \sin^2\theta}{2r}\right)\right)$. To reduce the feedback overhead of the codebook, quantization in the angle and distance domains is considered. Angle domain quantization: uniformly quantization of $\cos\theta$. Let $\cos\theta = \frac{2l}{N_1 O_1} - 1$ due to $-1 \leq \cos\theta \leq 1$, where O_1 denotes the oversampling factor of the angle domain quantization, and $l = 0,1,\cdots,N_1 O_1 - 1$ denotes the angle domain quantization index,

respectively. Distance domain quantization: uniformly quantization $\frac{1}{r}$. Let $\frac{1}{r} = \frac{o}{N_3 O_3 - 1}\left(\frac{1}{r_{min}} - \frac{1}{r_{max}}\right) +$

$\frac{1}{r_{max}}$ due to $r_{min} \leq r \leq r_{max}$, where N_3 represents the sampling point number of distance domain quantization, O_3 represents the distance domain quantization oversampling factor, $o = 0,1,\cdots,N_3 O_3 - 1$ represents the distance domain quantization index, r_{min} represents the minimum values of the distance, and r_{max} denotes the maximum values of the distance, respectively.

To determine whether the UE is located in the far-field region or near-field region of the antenna array, the following near-field identification scheme is considered. In the downlink transmission, the BS transmits reference signal (e.g., CSI-RS) and the UE performs channel estimation based on the reference signal and calculates the statistical covariance matrix of the channel matrix $\mathbf{C} = \mathbb{E}[\mathbf{H}^H\mathbf{H}]$. The UE performs an eigenvalue decomposition $\mathbf{C} = \mathbf{U}\mathbf{\Lambda}\mathbf{U}^H$ on the statistical covariance matrix $\mathbf{\Lambda}$, which is denoted as $\mathbf{\Lambda} = \mathrm{diag}(\lambda_1, \lambda_2, ...)$ and $\lambda_1 \geq \lambda_2 \geq ...$ with λ_1 being the largest eigenvalue and λ_2 being the second largest eigenvalue. The UE calculates the near-field indicator parameter $\omega = \left|\frac{\lambda_2}{\lambda_1}\right|$ and reports it to the BS. Generally, the near-field indicator parameter ω decreases with the increase of distance, it can thus be adopted as a criterion for determining the UE region. The BS determines that the UE is located in the near-field region or far-field region of the antenna array based on the threshold ω_0.

In order to obtain the performance of the near-field codebook, the proposed near-field codebook is evaluated compared with the existing 3GPP Type I codebook. The XL-MIMO system with single polarization uniform line array with $N_1 = 256$ antennas is considered, the antenna spacing is $d = \frac{\lambda}{2}$, the carrier frequency is 30 GHz, the number of transmission layers is fixed to 1, the free-space channel model is adopted, the number of sampling points in the angle and distance domains are 256 and 4, respectively.

The performance comparison of the near-field and far-field codebooks is depicted in Fig. 5.33. As can be observed from this figure, for the same angle quantization overhead, there are four highlighted regions due to the introduction of distance quantization, where the proposed near-field codebook has a significant gain over the existing far-field codebook.
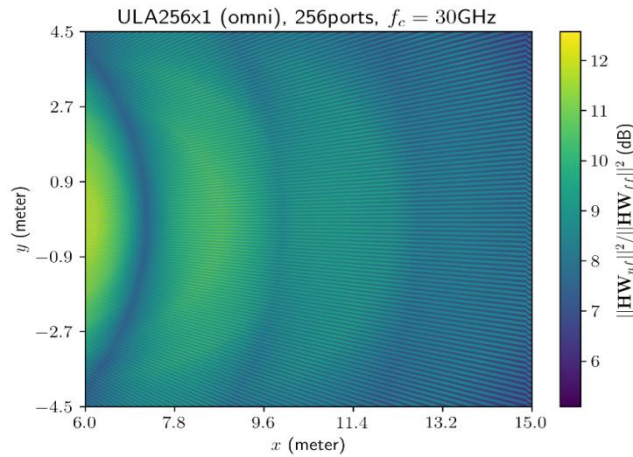
Fig. 5.33 Performance gain of near-field codebook over far-field codebook.

Fig. 5.34 provides the distribution of the near-field indicator parameter ω. From this figure it can be observed that when the UE is located at the boresight of the antenna array, the near-field indicator parameter keeps increasing as the distance between the UE and the antenna array decreases.
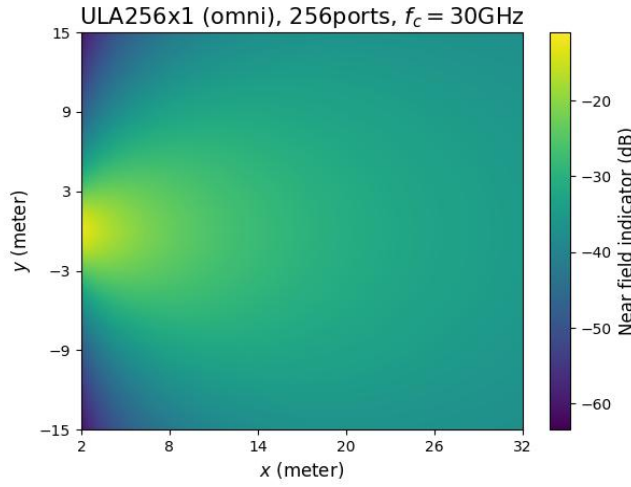
Fig. 5.34 Distribution of near-field indicator.

Fig. 5.35 illustrates the tradeoff between codebook performance and feedback overhead. The average loss represents the performance loss when the UE is using near-field codebook in the near-field range and the UE is using far-field codebook in the far-field range, compared to the case that the UE is using near-field codebook all the time. The average overhead represents the average value of the bit for required signaling overhead when the UE is in the near-field region using the near-field codebook and the UE is in the far-field region using the far-field codebook. When the near-field indicator parameter threshold is set to the minimum value, the BS determines all UEs as the near-field UEs, in which case near-field codebook is used without performance loss, corresponding to 10 bits feedback overhead. When the near-field indicator parameter threshold is set to the maximum value, the BS determines all UEs as far-field UEs, in this case far-field codebook is used with about 5 dB performance loss, corresponding to 8 bits feedback overhead. However, it is difficult to calculate the near-field indicator parameter threshold by closed-form solution, and a feasible way is to choose the empirical value.
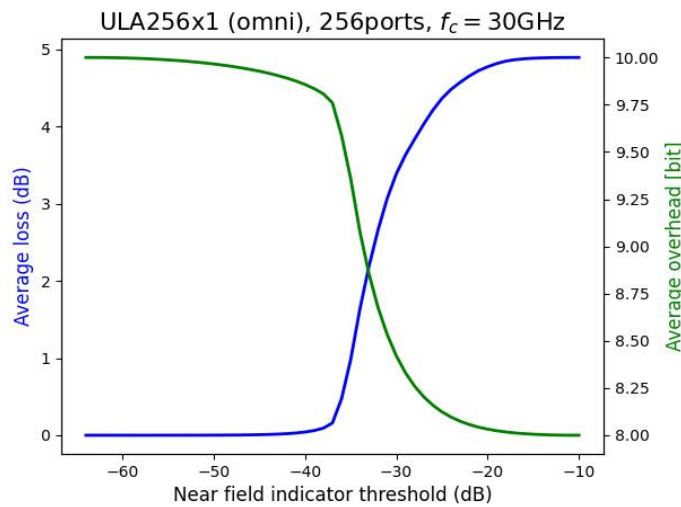
Fig. 5.35 Trade-off between performance and overhead.

Fig. 5.36 illustrates the performance gain of the near-field UE using near-field codebook and the far-field UE using far-field codebook compared to choosing far-field codebook all the time when the near-field indicator parameter threshold is set to -34dB. As can be observed from the figure, due to the introduction of distance domain quantization in the design of the near-field codebook, there are multiple "highlight" regions in the figure, where the proposed near-field codebook has a significant gain compared to the existing far-field codebook.
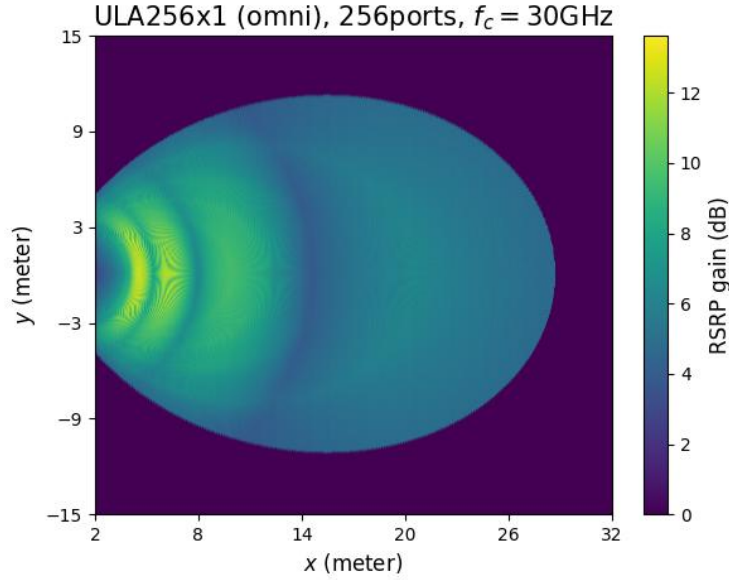
Fig. 5.36 Performance gain of near-field codebook over far-field codebook with near field identification.

In the future, near-field characteristics can be analyzed from two perspectives: signal processing and matrix theory, and near-field characteristics can be used to remodel near-field channels and codebook design rules. The near-field problem essentially belongs to the spatial filtering problem of non-stationary spatial signals. Its characteristics are similar to the frequency domain filtering problem of non-stationary time signals. By comparing the two, the near-field problem can be modeled as a spatial Doppler problem. The traditional estimation algorithm for Doppler frequency shift can be transferred to the near-field problem to estimate the directional shift of the near-field channel seen by antennas at different positions, thereby further deriving key near-field parameters such as user distance and direction. The future near-field codebook design can capture the non-stationary characteristics of near-field signals for design.

From the perspective of matrix theory, codebook design is based on the principle of compressive sensing. However, the signal space in the near-field is significantly different from that in the far-field. The far-field signal space exhibits linear characteristics, that is, the signal space is a low dimensional hyperplane; The near-field signal space is nonlinear and low dimensional. In addition, in multipath scenarios, the straight lines in far-field signal space have an orthogonal relationship, while the curves in near-field signal space do not have an orthogonal relationship. However, the near-field signal space is not any form of low dimensional manifold, and it has shape invariance. Cut two sub arrays of any size on the array, with the same spatial shape of the signals on them. If a codebook is designed based on this characteristic to estimate the spatial shape of the near-field signal, and then the low dimensional trend

未来移动通信论坛
FuTURE MOBILE COMMUNICATION FORUM

is projected onto a hyperplane, the problem of determining the near-field signal space will degenerate into a far-field problem.

Based on the above analysis, future near-field codebook design can be developed from the following ideas:

● No longer confined to the codebook design concept of cross-correlation forms. The traditional codebook design framework uses the designed and channel for cross-correlation, and then selects the codeword with the highest cross-correlation value as the final configuration of the array. However, the cross-correlation function is only applicable for estimating the direction of the wavefront and not for estimating the curvature of the wavefront. Due to the spherical wave characteristics of near-field electromagnetic waves, codebook design work needs to consider both the direction and curvature of the electromagnetic waves. Therefore, a single cross-correlation method can no longer perfectly meet the requirements. Autocorrelation methods and other methods can be used to assist in forming near-field codebooks.

● A "layered" codebook can be designed based on the principle of electromagnetic radiation. On a half wavelength antenna array, the near-field beam shape is mainly influenced by three factors. The first factor is the interference phenomenon caused by different antenna phases; The second is the diffraction phenomenon caused by the limited space of the array; The third one is the influence of the geometric relationship formed between the position and size of the array and the user's position. The coupling of these three factors leads to the irregular characteristics of near-field beams. Therefore, when designing codebooks, the three factors can be decoupled and considered separately, rather than directly designing near-field codebooks based on the results of the coupling of the three factors.

● Codebook design can be based on the analysis of the wave source position, without being limited to Fourier angle spectrum theory. The Fourier angle spectrum theory decomposes any form of wavefront into the sum of plane waves. The near-field wavefront is a spherical wave, so using angular spectrum theory for analysis and codebook design may introduce additional issues. Based on the analysis of the solution to the Helmholtz equation, we know that the solution of the angular spectrum theory is equivalent to the solution in the form of the Green's function, which is based on the analysis of the wave source position and is in the form of spherical waves. Using a solution in the form of spherical waves to represent near-field spherical waves is more concise and clearer than using the angular spectrum theory in the form of plane waves to represent near-field spherical waves. Therefore, designing near-field codebooks based on models such as Green's function is one of the future entry points.

5.4 Near-Field Beam Training

For XL-MIMO array communications in high-frequency bands with hybrid precoding architectures, near-field beam training becomes particularly important. The near-field beam training, can establish an initial high SNR link between the BS and the user before channel estimation and data transmission. Moreover, the XL-MIMO near-field wireless communication system has larger beam gain, narrower beam width, and stronger directivity regardless of whether one operates in the far-field or near-field, but it also poses new challenges to beam training. Existing research shows that directly using DFT-based far-field codebooks for near-field beam training will greatly reduce its achievable rate performance. It is because that the energy of a far-field directional beam aimed at a specific direction

will be spread to multiple angles, and the true user angle cannot be found through the maximum received signal power. Different from far-field beam training, XL-MIMO near-field beam training requires beam search in two dimensions in the angle and distance domains.

In [218], the authors proposed a new polar-domain codebook, in which each beam codeword points to a specific position with a target angle and distance. In terms of angle and distance sampling, this work suggests a strategy of uniform sampling of angles and non-uniform sampling of distances. Moreover, the sampling density of distance should decrease as the distance increases, so as to minimize the column coherence of adjacent codewords. Based on the near-field polar-domain codebook, a straightforward beam training method is to conduct a two-dimensional exhaustive search of all possible beam codewords.

However, this method leads to excessive beam training overhead. In order to reduce the training pilot overhead of exhaustive search, the authors in [281] proposed an effective two-phase fast near-field beam training method. Specifically, when far-field DFT beam codebook scanning is used, users can receive relatively high beam power within a certain angle domain (called the dominant angle region). This work revealed that the user's true angle is approximately in the middle of this dominant angle region. Therefore, by leveraging this important phenomenon, this method first estimates the user angle using angle domain DFT codebook scanning, and then use the polar-domain codebook to further estimate the user distance. The total beam training pilot overhead of this scheme is significantly lower than that of the two-dimensional exhaustive search scheme. A joint angle and distance estimation-based beam training scheme with DFT codebook was innovatively proposed in [282] The traditional beam training method determines the user angle based on the user's maximum received power. However, this does not make full use of the power pattern received at the user. The innovation of this scheme is to revisit the near-field beam training design based on the DFT codebook scanning. For the first time, this work proposes a new effective scheme to jointly estimate user angle and range. Specifically, this work first analyzes the received beam pattern at the user when far-field beamforming vectors are used for beam scanning. It shows an interesting observation that the received beam pattern contains useful user angle and range information. Then, based on this observation, two effective schemes are proposed to jointly estimate user angle and range. This scheme reduces near-field training pilot overhead while obtaining more accurate user distance information, which is useful for applications such as near-field user positioning.

By leveraging the characteristics of subarrays in partially connected structures，a unified beam training scheme, which exploits the fact that the near field of a full array may correspond to the far field of a subarray, is proposed for both near-field and far-filed scenarios [283]. Specifically, for each codeword of the pre-defined codebook in the hybrid field, a dedicated digital beamforming vector, which combines the gain of multiple subarrays, is designed to fully exploit the digital resources, enabling parallel digital combining to enhance the beam training efficiency. Finally, the codeword with the highest power after digital combining in the pre-defined hybrid field codebook is selected as the optimal codeword. The proposed scheme significantly reduces the overhead of beam training with negligible performance loss.

A three-stage hybrid field beam training scheme is proposed to reduce the training overhead and improve the beam training performance [284]. Specifically, in the first stage, the codebook is designed by analyzing the hybrid-field beam gain of the channel steering vector, with the codeword having the

highest received power selected as the optimal codeword of the first-stage beam training. In the second stage, several codewords, which cover the region of the channel path determined by the first-stage beam training, are combined to establish a new codebook for the second stage. Then, based on the measurements of the codewords, both the maximum likelihood and principle of stationary phase are proposed to refine the estimated channel parameters. In the third stage, the region of the channel path is further refined through a neighborhood search of the estimated channel parameters from the second stage. Then, a two-dimensional Gaussian function is proposed to approximate the beam gain in the surrogate distance-angle domain of the hybrid field. By using the Gaussian approximation and a small number of channel measurements, a least-squares estimator is developed to achieve high-precision estimates of the channel parameters.

In order to design an efficient beam training scheme from the perspective of hierarchical beam training, the authors in [286] proposed a near-field two-dimensional (2D) hierarchical beam training scheme. This scheme involves the design of a multi-resolution codebook that takes inspiration from hierarchical beam training methods used in far-field scenarios. Contrary to the far-field case, the optimal beam pattern for a near-field codeword should not only span a specific range of angles but also encompass a specific range of distances. It employs a full-digital framework to design the theoretical near-field codewords. Subsequently, based on these codewords, a practical codeword problem was formulated taking into account practical constraints such as digital-analog hybrid structure and quantized phase shift. Inspired by the Gerchberg-Saxton (GS) algorithm for digital holographic imaging phase recovery problems, the authors propose a full-digital architecture theoretical codeword design algorithm based on GS. Since a high-energy full-digital architecture is not achievable in an actual XL-MIMO system, practical codewords are designed using a digital-analog hybrid architecture. Finally, the authors develop a multi-resolution codebook using practical codewords, and proposed a near-field two-dimensional hierarchical beam training scheme. In addition, the authors in [285]. proposed an efficient near-field hierarchical beam training scheme. Specifically, in the first stage, the central sub-array of the XL-array is used to search the coarse user direction in the angular domain through a traditional far-field hierarchical codebook. Then, in the second stage, given a coarse user direction, a specially designed near-field codebook is used to progressively search for fine-grained user direction and distance in the polar-domain. The total beam training pilot overhead of this scheme is proportional to the number of antennas N, which further reduces the beam training pilot overhead. To adapt to the property near-field beams, the authors in [287] proposed the spatial-chirp codebook-based hierarchical near-field beam training method. All near-field beams are unified with the same beam pattern based on spatial-chirp codebook. It provided the hierarchical codeword update policy for angular and surrogate distance joint binary searching, and manifold-optimization-based training codebook enhancement was further designed. The scheme requires only on RF chain with analog structure, and can be simply extended to the multi-RF digital-analog hybrid structure. Most overheads can be reduced with comparable beam training accuracy to exhaustive searching. Additionally, authors in [288] utilized the near-field beam split to retrieve multiple beam training results simultaneously, increasing the beam training speed and reducing significantly the beam training overhead. The near-field beam split has different structures for different array structures. Authors in [300] analyzed the near-field beam split effect for the UCA and designed the frequency-dependent focusing based beam training to search multiple distances simultaneously to reduce the beam training overhead.

Benefiting from the powerful nonlinear relationship learning capability of neural networks, deep learning has received widespread attention as a branch of machine learning, and studies have shown that deep learning methods applied to near-field beam training can significantly reduce the pilot overhead [289][290]. The received signals corresponding to the far-field wide beam are used to estimate the optimal near-field beam, and two training schemes are specifically proposed, i.e., the original scheme and the improved scheme. The original scheme estimates the optimal near-field codeword directly from the output of the neural network. In contrast, the improved scheme performs additional beam testing, which can significantly improve the performance of beam training. The structure of the neural network proposed by this method for beam training is shown in Fig. 5.37.
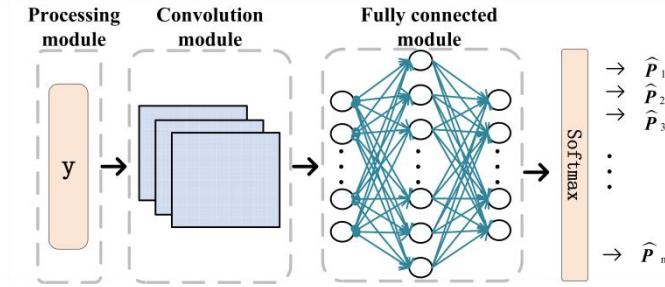
Fig. 5.37 Neural network structure for near-field beam training

A near-filed beam training scheme is proposed based on an angularly displaced codebook and deep learning techniques[291]. Specifically, the codewords, used to train a deep neural network, are uniformly selected with angular displacement from a two-dimensional distance-angle domain near-field codebook. Then, the optimal angle and distance that match the near-field channel path are determined from the output probability vector of the network. To further enhance the performance of beam training, several codewords, besides of the initially selected codewords, corresponding to the highest values in the probability vector are chosen for additional beam training. Finally, the optimal beam training codeword is determined based on the energy of the received signals.

In addition to performing near-field beam training in angle domain and distance domain, the location information of UEs can be used to further reduce the complexity of near-field beam training: divide the coverage area of BS into several initial grids, where the size of each grid is about equal to the coverage area of one near-field beam focus. In order to avoid the performance deterioration at the grid edge, the initial grid is shifted so that the terminal at the edge of the grid is in the center of the shifted grid. Based on whether UE is in the center or the edge of the initial grid, UE can determine to use the initial set of grids or one set of the shifted grids. Then, based on the specific grid in the selected set of grids, UE can determine the specific transmitting and receiving beam pair.

The authors in [292] investigated the near-field codebook-based beam training for multi-user modular XL-MIMO communications, where a novel near-field optimization-based codebook design is proposed by minimizing the levels of side lobes while maintaining the main lobe beamforming gain, and based on this, an efficient multi-beam training scheme enabled by grating lobes is devised to reduce beam training overhead [292] Numerical results verified the effectiveness of the proposed near-field beam optimization-based codebook in mitigating IUI for ultra-dense users, as well as the efficiency of the multi-beam training scheme [292].

An alternative fast beam training method is to leverage the multi-beam training scheme. However, the array-division-based multi-beam training method, which is widely used in far-field communications,

cannot be directly applied in the near-field scenario, since different sub-arrays may observe different user angles and there exist coverage holes in the angular domain. To address this issue, the authors in [293] first proposed to enable near-field communications by using sparse arrays (SAs), hence achieving higher spectrum efficiency and spatial resolution with a small number of antennas only. We first devise a new near-field multi-beam codebook by sparsely activating a portion of antennas to form an effective sparse linear array (SLA), hence generating multiple beams simultaneously by exploiting the near-field grating lobes [293]. In the first stage, several candidate user locations are identified based on multi-beam sweeping over time, followed by the second stage to determine the true user location with a small number of pilots for single-beam sweeping. Moreover, to further reduce beam training overhead, we design a sparse DFT codebook and a three-phase beam training method, which leverages the periodic beam split effect to estimate the user angle [294]. In particular, in the first phase, we utilize the sparse DFT codebook for beam sweeping in an angular subspace and estimate candidate user angles according to the received beam pattern. Then, a central subarray is activated to scan specific candidate angles for resolving the issue of angular ambiguity for identifying the user angle. In the third phase, the polar-domain codebook is applied in the estimated angle to search the best effective user range.The simulation results indicate that the proposed two beam training methods exhibit low-overhead characteristic than benchmark schemes and achieve nearly the same achievable-rate performance as the exhaustive-search beam training method (upper bound for on-grid beam training schemes).
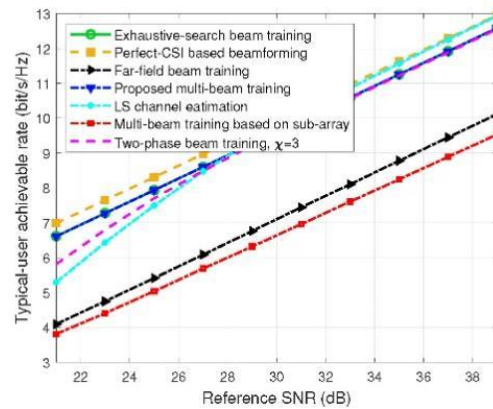
Fig. 5.38 Sum-rate versus SNR for multi-beam scheme.
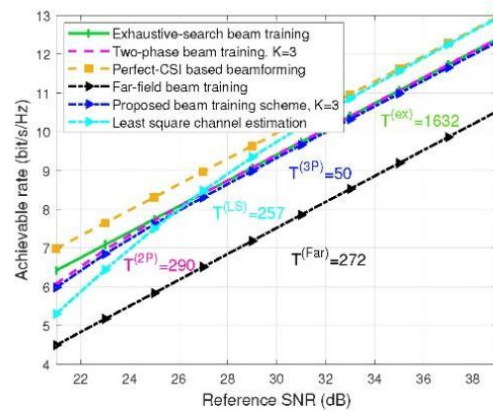
Fig. 5.39 Sum-rate versus SNR for DFT codebook scheme.

The introduction of ultra-massive arrays in 6G communication systems fundamentally changes channel characteristics, such as transitioning from far-field uniform planar waves to near-field

non-uniform spherical waves and transitioning of channel from spatial stationarity to spatial non-stationarity. Specifically, the channel spatial non-stationarity is prominent for XL-arrays, where different portions of the XL-array are visible to users at various locations, referred to as visibility regions (VRs). The existence of spatial non-stationarity has been validated by experimental measurements in [293]. Given this transition in channel systems, it is essential to propose new channel models and consider their statistical characteristics to assist in performance analysis. To address this issue, authors in [294] statistically characterize spatial non-stationarity utilizing a stochastic geometry approach based on the birth-death process along the array axis. Although conventional analytical methods, such as stochastic geometry, can also be used to characterize the VR ratio, they generally result in much more complicated forms that provide limited insights into the impact of system parameters on the visibility regions.

To address this issue, we first characterized the impact of system parameters on the visibility region based on the simulation results from Monte Carlo experiments, revealing the exponentially decreasing relationship between the average VR ratio—defined as the ratio of the average number of visible antennas to the total number of antennas—and the distance between the user and antenna array, as shown in Fig. 5.40. Based on this exponential relationship, we propose a new average VR ratio model by using the data regression method. Then, we analytically characterize the network ergodic capacity with random user locations. Furthermore, the results obtained for the XL-array with finite number of antennas are extended to the asymptotic case with an infinite number of antennas by using an efficient array partition method.

The simulation results indicate that the proposed model accurately characterizes the impact of user distance on the VR ratio and system performance. Additionally, a comparison with the performance of system designs that do not consider VR demonstrates the importance of incorporating VR in communication system design.
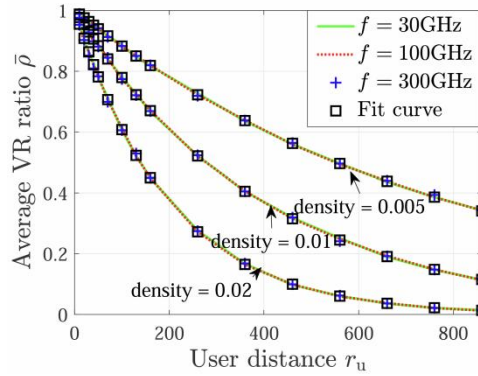
Fig. 5.40 Average VR ratio versus user distance.
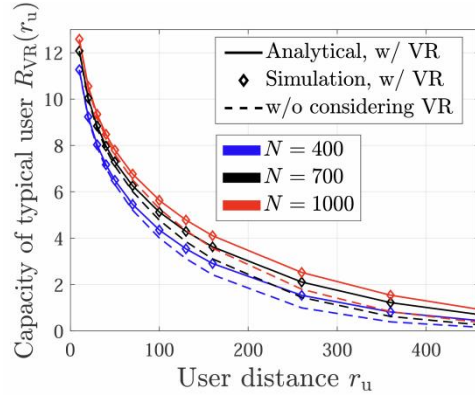
Fig. 5.41 Capacity versus user distance.

In high-speed railway (HSR) scenarios, the rapid movement of trains over short time intervals results in quickly changing channels, rendering the outcome of a single near-field beam training insufficient to support communication needs over extended periods. However, frequent beam training incurs substantial overhead. To address this issue, a Mobility-oriented Near-field Beam Training (MNBT) scheme is proposed, tailored for the downlink XL-MIMO HSR communication system in OFDM [297].

First, a three-dimensional (3D) XL-MIMO-OFDM channel model is constructed based on the scalar Green's function, as illustrated in Fig. 5.42[298]. Next, channel state parameters are obtained using a hierarchical near-field beam training algorithm [299]. Considering the regularity of HSR motion and the stability of speed and trajectory, train operation parameters are calculated with minimal beam training, aiming to predict the train's position at each subsequent time point. An inter-carrier interference (ICI) mitigation matrix is then constructed based on the predicted speed to counter the effects of Doppler frequency offset (DFO). To reduce the impact of parameter calculation errors on beam training effectiveness, an error real-time monitoring module is designed based on the convexity of the received signal function to correct prediction errors. Finally, simulation experiments confirm that the proposed MNBT method achieves significant beam focusing enhancement during train operation while greatly reducing training overhead. The overall algorithmic process is shown in Fig. 5.43.
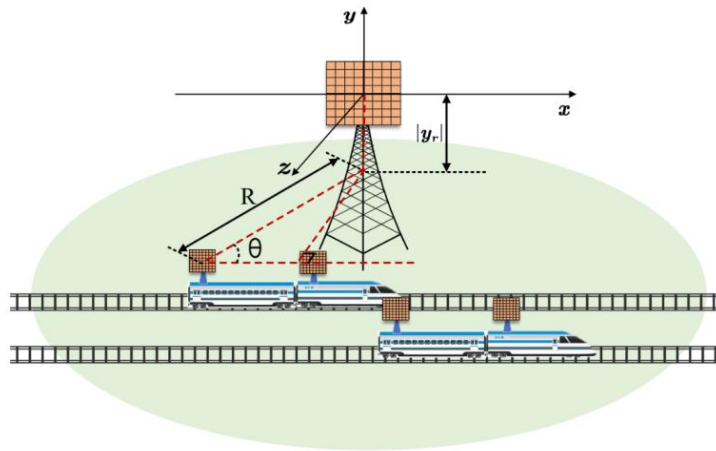
Fig. 5.42 XL-MIMO-enabled HSR communication systems.
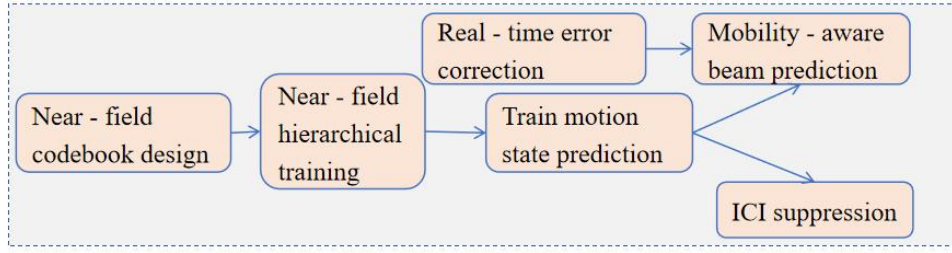
Fig. 5.43 The proposed MNBT scheme
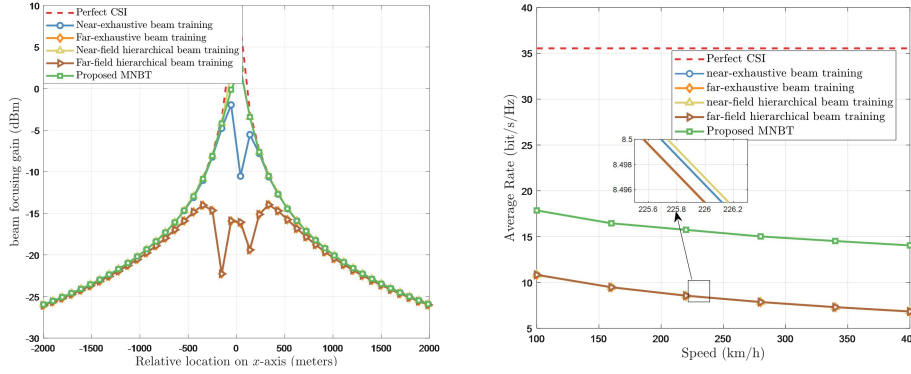
Fig. 5.44 Performance comparison between the MNBT-based scheme and traditional beam training scheme

In Fig. 5.44, we analyze and compare the performance of the proposed beam training scheme with existing beam training schemes applied in HSR communication systems. As the train moves past the BS, the proposed MNBT scheme achieves the same beam focusing performance as traditional near-field hierarchical beam training while significantly reducing training frequency and overhead. Additionally, increased train speeds raise DFO, which in turn intensifies ICI, causing a decline in system performance. However, the proposed MNBT scheme generates an interference suppression matrix, effectively enhancing the system's average transmission rate. Consequently, the MNBT scheme is more suitable to HSR communication scenarios than traditional beam training schemes.

In the current 5G NR network topology, the terminal is located in the far-field region of the BS antenna array, and the CSI-RS resource for beam management with only one or two ports in 3GPP TS 38.214 is sufficient, i.e., the measurement results of one port can be used directly for other ports. However, with the significant increase in the number of antenna array elements and the carrier frequency, the UE located in the far-field region of the BS antenna array becomes the UE in the near-field region. And the beam measurement results for one port can't be used for other ports directly.

In this paper, we consider an XL-MIMO system with a single polarization uniform line array with N antenna array elements and d_H as the antenna array element spacing. The N antenna array elements are divided into N_{grp} antenna sub-array and each antenna sub-array comprises $N_e = N/N_{grp}$ antenna array elements. With the hybrid beamforming structure, the signal of the RF chain is fed into the antenna array element in the corresponding antenna subarray through the phase shifter to form a beam.

For each transmit beam at the BS, the terminal in the near-field region needs to measure the Layer 1 Reference Signal Receiving Power (L1-RSRP) corresponding to each antenna sub-array, and select the best transmit beam corresponding to each antenna sub-array.

We evaluated the proposed near-field beam management scheme based on the main simulation parameter assumptions, i.e., carrier frequency as 30GHz, BS antenna configuration as (M, N, P, Mg, Ng) = (1, 200, 2, 1, 1) with 20 TxRUs, UE antenna configurations as (M, N, P, Mg, Ng) = (1, 1, 2, 1, 1), BS Tx beam pattern as $\phi_i = \left[-\frac{10\pi}{32}, -\frac{9\pi}{32}, -\frac{8\pi}{32}, \cdots, \frac{9\pi}{32}, \frac{10\pi}{32} \right]$ with 21 Tx beams.

Considering each antenna subarray as a beamformer, for the above evaluation assumptions of transmission beams, each sub-array will generate 21 horizontal beams and have the corresponding RSRP. Then for the antenna array composed of 10 sub-array, 210 beams and the corresponding RSRP can be obtained.

Based on the UE distribution Option 1 and Option 2 in the evaluation assumptions, UE distribution can be shown in Fig. 5.45.
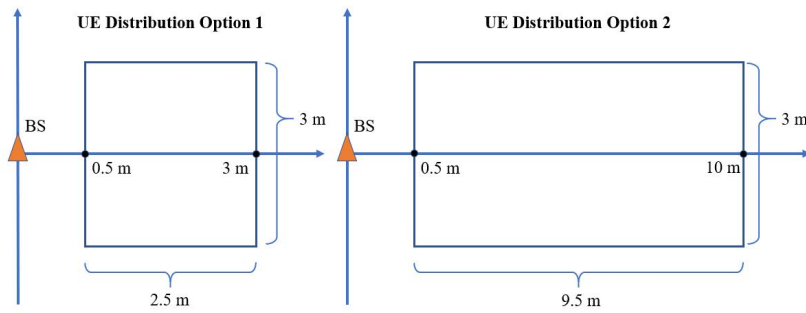
Fig. 5.45 UE distribution

The evaluation metrics include L1-RSRP values, where the L1-RSRP values include near-field L1-RSRP values, far-field L1-RSRP values, and the difference between the near-field L1-RSRP and the far-field L1-RSRP.

● Near-field L1-RSRP means the average L1-RSRP of 10 antenna sub-arrays when each antenna sub-array selects the best transmission beam independently.

● Far-field L1-RSRP means the average L1-RSRP of 10 antenna sub-arrays when all antenna sub-arrays select the same best transmission beam jointly.

● L1-RSRP difference means the difference between near-field L1-RSRP and far-field L1-RSRP.

For the case of UE distribution Option 1, the L1-RSRP difference between near-field L1-RSRP and far-field L1-RSRP can be seen in Fig. 5.46.
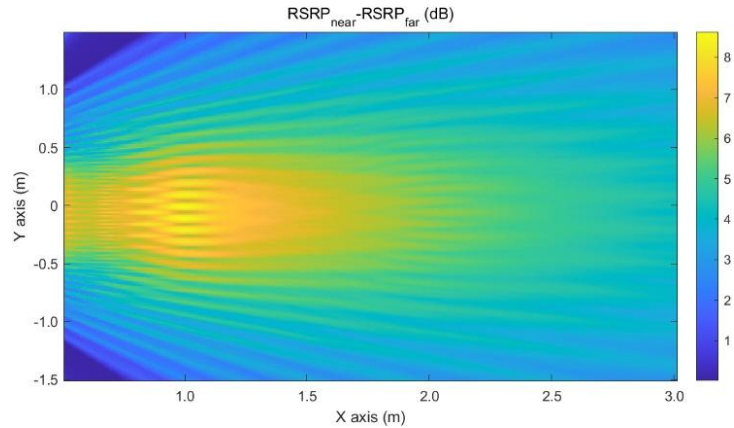
Fig. 5.46 L1-RSRP difference between near-field and far-field L1-RSRP (UE distribution Option 1)

For the case of UE distribution Option 2, the L1-RSRP difference between near-field L1-RSRP and far-field L1-RSRP can be seen in Fig. 5.47.
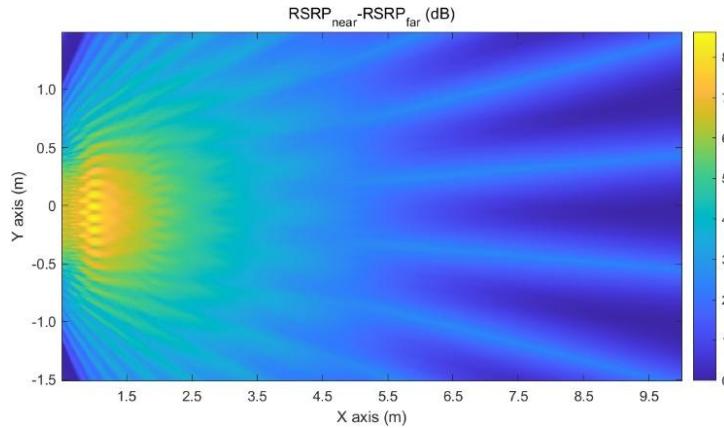
Fig. 5.47 L1-RSRP difference between near-field and far-field L1-RSRP (UE distribution Option 2)

5.5 Near-Field Multiple Access

5.5.1 LDMA

One of the main goals of wireless communication system design is to continuously improve transmission rates. Under certain bandwidth resource conditions, the improvement of transmission rate mainly depends on a significant increase in spectral efficiency. The improvement of spectral efficiency in 5G massive MIMO systems is mainly achieved through spatial division multiple access (SDMA) technology, which excavates spatial resources beyond the time and frequency domains, and utilizes different spatial beams to simultaneously serve multiple users on the same frequency. To achieve SDMA in pure LoS scenarios, existing 5G massive MIMO systems mainly generate high gain directional beams through large-scale array antennas. By using directional beams, wireless signals can be converged at specific angles. Different users are divided according to their angles, and different beams cover users at different angles. While improving the signal-to-noise ratio at the receiving end, the asymptotic orthogonality of different beams in the angle domain is utilized to effectively suppress inter user interference, thus achieving a multiplier increase in spectral efficiency.

By utilizing the new feature of the two-dimensional angle-distance focusing ability of near-field beams, SDMA turns into a location division multiple access (LDMA) technology with angle distance two-dimensional orthogonal resources, providing a new technological path for improving spectral efficiency [301]. Specifically, as shown in Fig. 5.48, unlike far-field beams that only have one-dimensional convergence characteristics in the angle domain, near-field beams have two-dimensional focusing characteristics in the "angular-distance" domain, that is, near-field beams can focus wireless signals at specific angles and distances (i.e., a certain position). Based on the two-dimensional focusing characteristics of near-field beams, similar to the angle domain asymptotic orthogonality of far-field beams, [301] first prove the distance domain asymptotic orthogonality of near-field beams, that is, as the antenna size expands, near-field beams focused at the same angle but different distances will tend to be orthogonal. Based on this, in 6G the MIMO technology can achieve a leap from distinguishing multiple users in the angle domain to distinguishing multiple users in the angle distance domain. By mining and utilizing undeveloped orthogonal resources in the distance

domain, near-field MIMO provides a new technological approach to improve the spectrum efficiency of wireless communication systems.
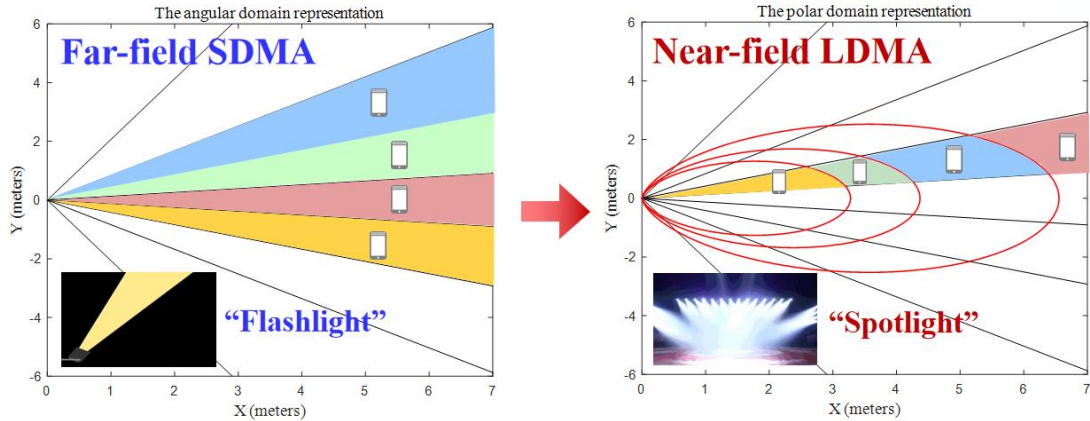
Fig. 5.48 Comparison between far-field SDMA and near-field LDMA

In numerous scenarios involving multiple-access systems, a primary goal is to concurrently serve numerous users while ensuring that the signals they receive adhere to a minimum signal-to-interference ratio (SIR) criterion. When users are roughly aligned at similar angles relative to the transmitter, their simultaneous service feasibility depends on both their distances from the transmitter and their inter-user separations. Consequently, the task evolves into identifying the subset of users for whom reliable simultaneous service is feasible. Because the selection of users is interdependent based on each other's SIR, solving the problem necessitates a joint approach encompassing all users. A graph-theoretic method utilizing the near-field channel model is outlined in [302], where the problem is cast as the maximum clique problem in an undirected graph and tackled using a heuristic algorithm. Fig. 5.49 illustrates the outcome of applying this algorithm to the system delineated in Section 4.3. From a pool of 100 users oriented similarly relative to the transmitter, five users are chosen, each requiring a minimum SIR of 18 dB. The graph demonstrates that closer to the transmitter, more users can be accommodated, while as the receiver moves farther away, concentrating the signal at a specific location becomes more challenging.
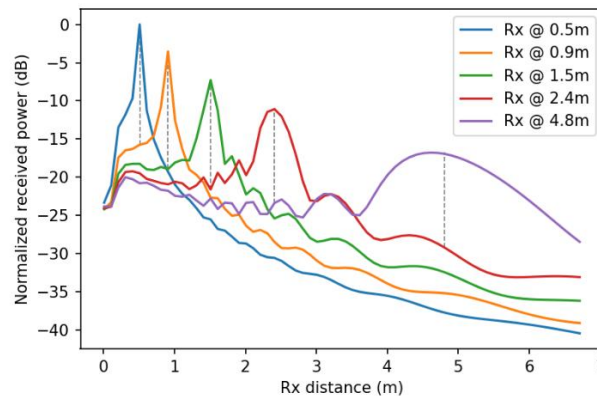
Fig. 5.49 Multiple-access in near-field for users with same angular orientation [302]

5.5.2 NOMA

Although near-field communications provide higher spatial resolution, it is still difficult to meet the demand for massive user access in wireless networks by only utilizing the DoFs in the direction of

range and angle. This is because, on the one hand, the resolution of beam focusing in near-field communication cannot achieve perfect accuracy except in the case where users are very close to the BS [303]; on the other hand, the large-scale antenna arrays at the BS normally employ hybrid analog-digital antenna structures in near-field communications. In this case, for Orthogonal Multiple Access (OMA) technology, the maximum number of connected users is limited by the number of RF chains. By contrast, Non-Orthogonal Multiple Access (NOMA) technology allows multiple users to be multiplexed over the same block of radio resources (e.g., time slots, subcarriers, spatial beams, etc.) and to be distinguished in the power domain or code domain, thus further enhancing the network spectral efficiency and user access capability. Therefore, near-field NOMA communications are conceived to be a promising solution. It is worth mentioning that the beam focusing capability of near-field communications also brings a series of new design opportunities for NOMA as shown in Fig. 5.50, which are discussed as follows:

● **"Far-to-Near" Successive Interference Cancellation (SIC):** Compared to far-field NOMA communications, the near-field beam focusing capability enables users far located from the BS (termed as far users) to achieve a higher equivalent channel gain than users close to the BS (termed as near users) with a single beam focused on the far users. Based on this feature, near-field NOMA enables a "far-to-near" SIC decoding operation [304]. The far user can act as a strong NOMA user to first decode and cancel the interference from the near user (weak NOMA user) before decoding its own signal. This is almost impossible to achieve in conventional far-field NOMA communications.

● **Range-domain NOMA User Clustering:** Compared to the angle-domain user clustering in conventional far-field NOMA, exploiting the range-domain DoFs provided by near-field beam focusing, users at the same angle can be further divided into several user clusters in near-field NOMA, which can significantly reduce inter-user interference [304].

● **Hybrid Near/Far NOMA Communication:** Due to the non-perfect accuracy of the near-field beam focusing, the signal strengths of the beams serving near-field users may be superimposed at the far field. Based on this property, additional far-field users can be served using NOMA technology without changing the legacy beamforming design of the near-field communications but further enhance the user access capability of the network [305].
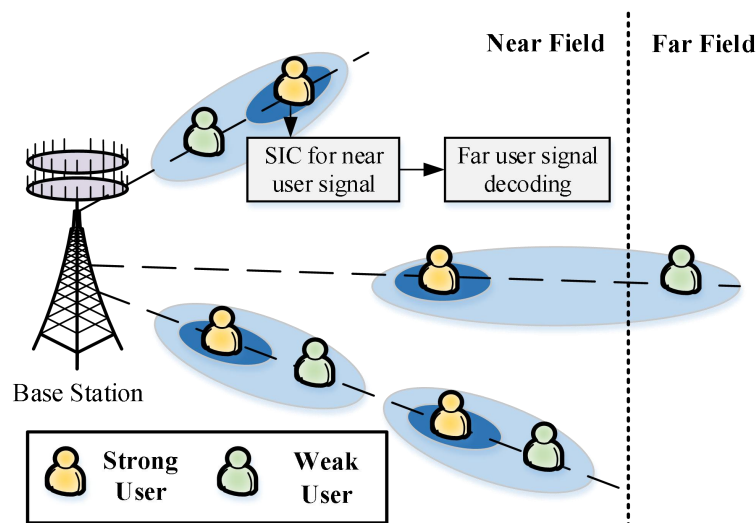
Fig. 5.50 Illustration of near-field NOMA designs

5.5.3 URA

In addition, next generation multiple access techniques aim to support the access of massive IoTs devices such as sensors. These users generally have a very low active probability and establish the uplink transmission via short packets. Unsourced random access (URA) is an efficient massive random-access scheme which assigns a common codebook for all potential users [306][307]. URA users select the transmitted codeword from the common codebook relying on their messages, with no obligation to identify themselves. Accordingly, the receiver reconstructs a list of messages without user identification. With the increasingly dense distribution of devices in the Internet of Things and the increase in the near-field distance caused by XL-MIMO deployments, a significant number of users are expected to locate in the near-field region. Therefore, URA schemes in the near-field condition are worthy of further exploration.

Considering that the number of codewords in the common codebook increases exponentially with the message length, multi-stage coding schemes are usually adopted for URA to reduce the system complexity. As the crucial step of decoding, the receiver requires to detect the transmitted codeword and reconstruct the corresponding channel. The near-field channel estimation technology provides a novel solution to this problem. First, codeword detection can be cast as a multiple measurement vector problem by capturing the coherent support structure of MIMO channel elements in the spatial domain, by which way the range of possible active codewords can be reduced. Then, the restricted common codebook along with the near-field channel codebook are employed to perform enhanced channel estimation in the polar domain. The above steps are performed alternately in a turbo manner to fully exploit the sparse structure of the near-field polar domain channel, which decreases the number of parameters required for reconstruction and reduces the codeword length.

On the other hand, the features of the near field channel in the dimensions of angle and distance can be regarded as the implicit "identity" of a specific user, which assist the codeword reorganization from multiple segments without the help of user identification [308]. The concatenation process can be performed by channel clustering without adding redundant check bits, which helps to improve the coding rate and the spectral efficiency.

5.6 Non-Coherent Communication Schemes

The challenges of channel estimation for near-field communications have been detailed in section 5.1. Given the difficulties in obtaining channel information, the use of non-coherent communication techniques is proposed where CSI is not required. Traditionally, non-coherent detection entailed a well-known 3dB loss in system performance compared to its coherent counterpart employing CSI. However, with the emergence of massive MIMO, this degradation has disappeared, equalizing both forms of transmission. Several proposed schemes for future communication systems, where non-coherent detection becomes relevant for near-field communications due to its properties, are presented in [309].

Non-coherent communications can offer several benefits and improvements to near-field communications (NFC) systems as follows:

● **Resilience to Multipath Fading**: In near-field environments, multipath fading can occur due to signal reflections from nearby objects. Non-coherent communication techniques using modulation schemes based on differential phase shift keying (DPSK) as presented in [309]-[311] are less

susceptible to multipath fading compared to coherent schemes. This resilience helps maintain communication integrity in NFC systems, especially in environments with complex signal propagation characteristics.

● **Robustness to Interference:** Non-coherent communication schemes are often more robust to interference and noise compared to coherent schemes. In near-field communication scenarios where there may be significant interference from surrounding electronic devices or environmental factors, non-coherent techniques can help maintain communication reliability.

● **Reduced Complexity**: Non-coherent communication schemes typically involve simpler modulation and demodulation processes compared to coherent schemes. This reduction in complexity can lead to lower-power and more cost-effective NFC transceivers, making them suitable for small, battery-powered devices like NFC-enabled smartphones, wearables, and IoT devices.

● **Simplicity:** Non-coherent communication techniques tend to be simpler to implement and require fewer resources compared to coherent schemes. This simplicity can be advantageous in NFC applications where low-power, low-cost, and efficient communication protocols are desirable.

● **Lower Complexity Transceivers:** Non-coherent communication systems typically require fewer complex transceivers compared to coherent systems. This can lead to smaller and more cost-effective NFC devices, making them more accessible for widespread deployment in various applications.

● **Improved Range:** Non-coherent techniques may offer improved range performance in certain near-field communication scenarios, especially when dealing with obstacles or attenuating materials. By optimizing the modulation and demodulation processes, non-coherent schemes can enhance communication range without significantly increasing power consumption.

● **Improved Signal Detection:** Non-coherent receivers do not require precise phase synchronization with the transmitted signal, making them more tolerant to timing offsets and phase distortions. As a result, non-coherent receivers can reliably detect signals even in the presence of frequency drift, phase noise, and other impairments commonly encountered in NFC environments.

● **Enhanced Security:** Non-coherent modulation techniques, such as frequency-shift keying (FSK), can provide inherent security benefits for NFC systems. By modulating the carrier frequency based on the data to be transmitted, FSK inherently spreads the signal energy across a wider frequency spectrum, making it less susceptible to interception or eavesdropping attacks.

● **Compatibility with Low-Cost Hardware:** Non-coherent communication techniques are well-suited for implementation on low-cost, low-power hardware platforms commonly used in NFC devices. By leveraging simple modulation schemes and efficient signal processing algorithms, non-coherent NFC transceivers can be deployed in a wide range of applications without significant hardware or computational overhead.

● **Adaptability to Dynamic Environments:** Non-coherent communication systems can adapt more effectively to dynamic NFC environments where signal conditions may vary rapidly. By employing adaptive modulation and error correction techniques, non-coherent NFC systems can maintain reliable communication links even in the presence of changing interference levels or channel conditions.

Overall, the use of non-coherent communication techniques in near-field communication systems offers a practical and efficient solution for achieving reliable, low-power, and cost-effective wireless connectivity in a variety of applications.

5.7 Deployment of Near-Field Communication System

According to **Chapter 3.1**, the classic criterion for distinguishing the near-field and far-field region is the Rayleigh/Fraunhofer distance, which increases with the physical size of the array and/or the carrier frequency. However, to attain significant performance enhancement in future 6G communication systems, promising technologies such as RIS, massive MIMO, and THz communication need to substantially increase the number of active antennas/passive elements, or mitigate the carrier frequency to higher bands. This thus leads to an increase in the originally negligible Rayleigh/Fraunhofer distance to tens or even hundreds of meters. Therefore, the traditional deployment strategies based on far-field models are no longer applicable to the XL-arrays for 6G, including both XL active arrays and XL passive arrays. Additionally, the deployment of XL active/passive arrays has a significant impact on key technologies for near-field communication, such as beamforming, channel estimation, WPT, and ISAC. These technologies exhibit distinct implementations and effects under various deployment strategies. In the following, we will introduce different deployment strategies from the perspectives of node placement, network deployment and optimization objectives.

(1) **Node placement:** The deployment scenarios of XL-arrays [312] can be classified into four main types: the BS side deployment [102], the relay side deployment [313], the user side deployment [314], and multiple sides deployment [315], as illustrated in Fig. 5.51. In practice, deploying XL-arrays at the BS or relay side is easier to implement. For the XL active arrays, deploying them directly at the BS/relay significantly enhances the capacity and coverage range of communication systems. However, this strategy faces challenges as some users are located in the near-field region of the BS/relay, necessitating the considerations of the mixed near- and far-field effects as well as the interference management between far-field and near-field users. For the XL passive arrays such as RISs, deploying them near the BS/relay not only improves the communication coverage but also substantially reduces the required number of (active) antennas at the BS/relay. Additionally, the multiplicative path loss induced by passive arrays decreases as the distance between the XL passive arrays and BS/relay reduces. In this context, besides the aforementioned mixed near- and far-field effects and interference issues among users, system design should also account for the near-field effects between the BS/relay and the XL passive arrays. Considering the device constraints in terms of the cost and energy consumption, it is impractical to deploy XL active arrays at the user side. On the contrary, with advantages of low cost and low power consumption, passive arrays (e.g., RISs) are more likely to be implemented in extremely large scale at the user side. Especially in scenarios involving a large number of randomly distributed users, XL passive arrays can be flexibly deployed as signal hotspots at the user side, significantly improving the probability of establishing virtual LoS links and enhancing user communication performance. In this context, the system design must also consider the near-field effects as the distance between the XL-arrays and users is within the Rayleigh/Fraunhofer distance.

(2) **Network deployment:** The deployment of XL-arrays (including XL active/passive arrays) can be classified into centralized deployment and distributed deployment. For a given number of active antennas/passive elements, these two deployment strategies exhibit distinct performance, as discussed

below. First, the centralized and distributed deployment have different equivalent channel states, leading to variations in communication rates and transmission delays. Second, for the distributed deployment, each served user can only benefit from the beamforming gain provided by its nearby array. In contrast, centralized deployment involves an array with a larger physical size, enabling multi-user sharing where all antennas/elements in the array can serve any user and thus achieving enhanced beamforming gains. Third, distributed deployment entails more nodes, thus requiring more round-trip links for information exchange compared to centralized deployment. The larger number of nodes renders higher network overhead and network complexity. Last, the flexibility of distributed deployment facilitates the establishment of virtual LoS links with users, thereby increasing the probability of establishing LoS links compared to centralized deployment.
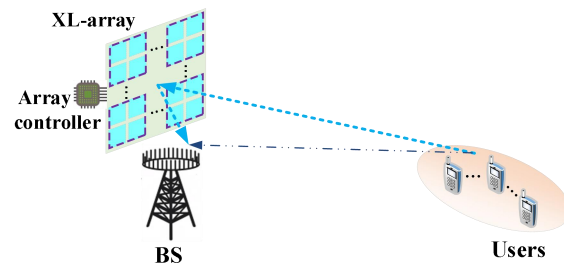
(1)Deployment at BS
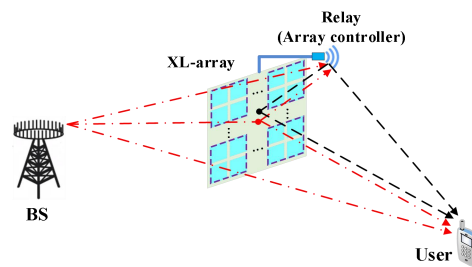
(2)Deployment at relay
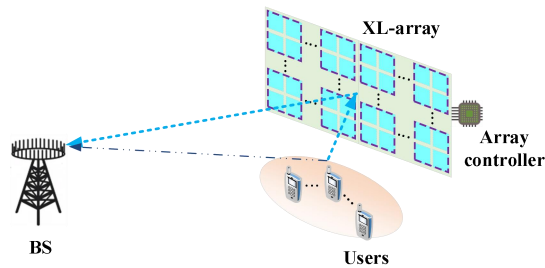
(3)Deployment at users
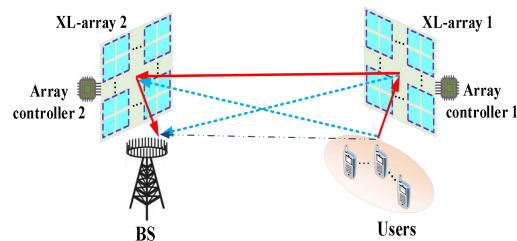
(4)Deployment at both BS and users

Fig. 5.51 Deployment scenarios of XL-arrays (taking RIS as an example)

(3) **Optimization objectives[316]**: For traditional far-field assumption-based cellular network deployment, the main optimization objective is the signal strength distribution of network coverage, also known as link budget. However, for near-field assumption-based network deployment, the optimization objective will not only include the signal strength distribution of coverage but also consider the changes in spatial freedom caused by near-field propagation characteristics. Therefore, when optimizing the deployment of near-field networks, factors such as near-field distance conditions, RIS size, deployment density, and angles relative to the coverage area must be considered.

Notably, most of the current research on near-field communication tends to study the performance of the near field and far field systems separately under the assumption that the propagation distance conforms to the constraints of near-field/far-field distances. Considering the distributed deployment of users and exploiting the characteristics of the near field, a hybrid communication architecture based on near-field relays can be envisioned, as depicted in Fig. 5.52. In this architecture, relays are deployed in proximity to the users, ensuring near-field communication conditions between the relays and users. Meanwhile, since the distances between the BS and relays are relatively remote, the communication between the BS and relays is considered as far-field communication. In the proposed hybrid communication architecture based on near-field relays, the deployment of relays and the corresponding strategies for different relays serving different groups of near-field users should be taken into account.
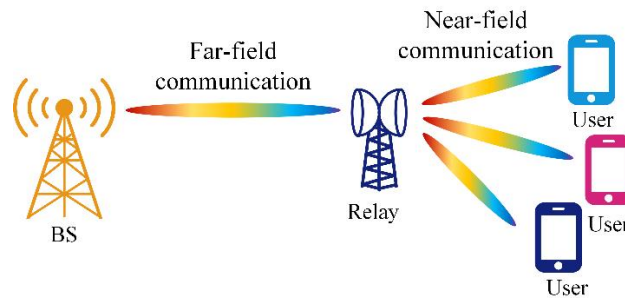
Fig. 5.52 A hybrid communication architecture based on near-field relays

6 Integration of Near-field Technology with Other Technologies

6.1 Near-field Based Positioning

In conventional far-field communications, the phase difference of the receiving antenna array is mainly determined by the AoA of the signal, so the process of channel localization can easily calculate the AoA of the signal to obtain the orientation information of the target. In contrast, efficient near-field communications require a more accurate modelling of the electromagnetic channel using a spherical wavefront [317]. In the spherical wavefront-based channel model, both distance and bearing information are included in the phase delay, which has the potential to accurately locate the target. Moreover, adopting the far-field model for near-field sources leads to a model mismatch problem that can deteriorate the positioning performance [321]. Therefore, along with the research and development of near-field communications, near-field positioning will be an important technology in the future 6G.

6.1.1 Near-Field and Positioning
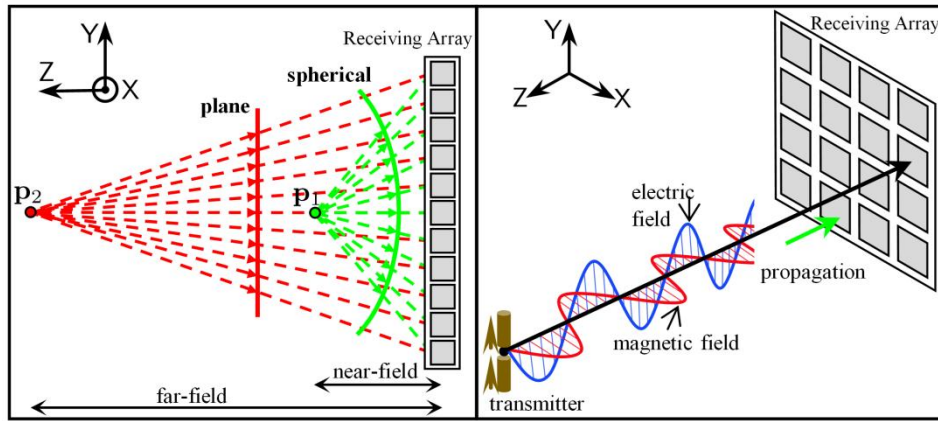
Fig. 6.1 Near-field signal model and far-field signal model.
(The transmitter P_2 is in the far field of the receiving array, and its signal model is represented by a plane wavefront. The transmitter P_1 is in the near field of the receiving array, and its signal model is represented by a spherical wavefront. The subfigure on the right gives a more accurate near-field signal model that considers the electromagnetic physical effects of the near field.)

Fig. 6.1 shows the near-field signal model and far-field signal model. From Fig. 6.1, we can explain the reasons why the spherical wavefront characteristics of near-field propagation are conducive to improving positioning accuracy:

(1) The plane wavefront modeling of the far-field signal causes the AoA obtained by different receiving antenna elements to be the same, so plane wavefront modeling in the far field can only estimate the AoA. To obtain the position parameter, one feasible approach is to deploy multiple spatially distributed arrays with known positions for the estimation of AoAs. Alternatively, the clock synchronization between the transmitter and the receiver can be employed to measure the time of arrival (ToA) provided wideband signals are used.

(2) However, the amplitude term and phase term of the near-field signal based on spherical wavefront modeling contain the precise distance from the transmitter to each receiving antenna. This

allows us to directly obtain the position information of the transmitter, thereby improving positioning accuracy.

In addition, the electromagnetic physical effects of near-field signals also make it possible to sense the attitude of the transmitter. From Fig. 6.2, the attitude of the transmitter is related to its physical shape. For a basic linear antenna, its attitude is represented by its orientation in three-dimensional space. Different spatial orientations will lead to different source current distributions, resulting in different excited electric fields. Therefore, the near-field electromagnetic signal and the attitude of the transmitter have a one-to-one mapping relationship, which allows us to estimate the attitude of the transmitter.
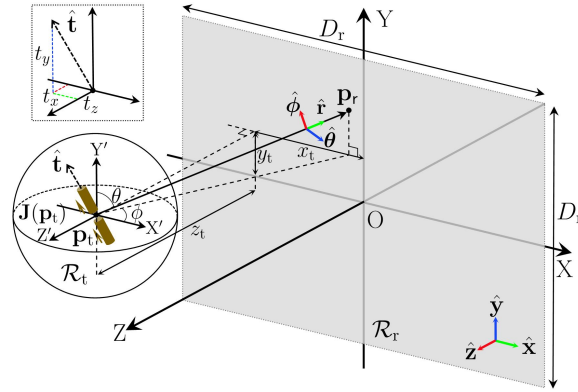
Fig. 6.2 Near-field positioning and attitude sensing.

In the literature [322], for the noise-free case, the author proposed the phase ambiguity distance and the spacing constraint distance to accurately divide the position domain of the transmitter. For each position domain, the author provided a feasible decoupling scheme and gave solutions to nonlinear electromagnetic equations.

Secondly, for the noisy case, joint positioning and attitude estimation needs to use signal estimation theory. Literature [323] pointed out that using the electromagnetic near-field model, in the millimeter wave frequency band or sub-THz frequency band and the size of the observation surface is at the meter level, the position estimation accuracy can reach the millimeter level. In [324], the authors developed Ziv-Zakai lower bounds for joint positioning and attitude estimation. Compared with the locally tight Cramér-Rao lower bound, the Ziv-Zakai lower bound can also provide accurate performance predictions in low signal-to-noise ratio regions. Through the Ziv-Zakai lower bound, the authors show that the attitude estimation can reach the 0.1 level (the estimation error range is ± 0.1).

It is noteworthy that source localization primarily estimates two positional parameters of the user: the angle and distance of the source relative to the BS. In far-field scenarios, source localization is usually a joint estimation problem: angle estimates are obtained through the AoA, and distance estimates are acquired through the ToA. However, this joint estimation requires precise synchronization and/or the participation of multiple access points, and its performance is usually suboptimal compared to direct positioning.

When wireless positioning shifts from far-field to near-field, the received signals exhibit a spherical wavefront rather than a planar wave. This enables the use of near-field spherical wave characteristics to enhance wireless positioning, achieving direct positioning. Specifically, the user's

location can be directly calculated based on the curvature of arrival (CoA) of the spherical wavefront, allowing a single array to determine both distance and direction simultaneously [324]. This contrasts with far-field methods, where complicated two-step AoA and ToA estimation is required. By leveraging these near-field techniques, positioning estimation accuracy is significantly improved while also substantially reducing implementation complexity [325]. However, when it comes to near-field sources, it's necessary to jointly search over both the angle and range due to the angle-range coupling inherent in the spherical wavefront. This may introduce some additional complexity. In this regard, some studies focus on proposing algorithms to decouple the angle and range, then divide the 2D search into two consecutive 1D searches over the range and angle, aiming to mitigate this complexity. In the presence of moving users, previous position estimates can be successfully exploited to improve the positioning accuracy at a certain time instant (tracking). Within this context, in [326]the performance bounds on tracking error have been investigated by considering the availability of prior statistical mobility models of the user.

In case antenna arrays are used at both the transmitter and receiver, i.e., in a MIMO configuration, working in the near field opens also the possibility to enable single-anchor 6D localization (position and orientation). The fundamental theoretical performance limits in positioning and orientation of near-field MIMO have been studied in [327] where the impact of the number of antenna elements as well as of the squinting effect have been investigated. It has been found that with a large number of antenna elements (massive MIMO), the effect of multipath on the localization and orientation error can be made as small as desired.

Another approach to positioning in the near field is to partition the large antenna array into multiple subarrays and approximate the signal received on each subarray as a planar wave, and combine the information from multiple subarrays to estimate the position of the user. By partitioning a large array of into N subarrays of equal size, the Rayleigh distance shrinks by $\frac{1}{N^2}$. This pushes a user close to the BS into the far field of the subarrays. This allows us to apply traditional array signal processing algorithms, such as Multiple Signal Classification (MUSIC) or Estimation of Signal Parameters via Rotational Invariance Technique (ESPRIT), to each subarray to find the individual AoA from the user. By combining the multiple estimated AoAs from the subarrays, one can estimate the position of the user $(\vec{r})$ with respect to the center of the array can be estimated as follows:

$$\vec{r} = argmin(\sum_{k=1}^{N} \gamma_k |(\vec{r} + \vec{r}_k) - \hat{a}_k((\vec{r} + \vec{r}_k) \cdot \hat{a}_k)|^2) \tag{6.1}$$

where $\hat{a}_k$ is the unit length direction vector at subarray k pointing towards the UE based on the estimated AoA, γ_k is the received SNR at subarray k, and $\vec{r}_k$ is the center of subarray k relative to the center of the entire array.
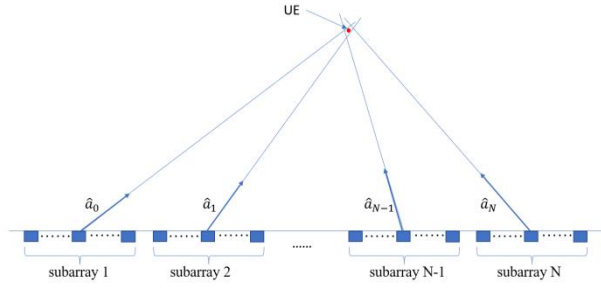
Fig. 6.3 User positioning with sub-arrays.

This approach is equivalent to approximate the nonlinear phase vector corresponding to spherical wave on a large array with *NK* elements with a set of *N* linear phase vectors of length *K*, each collected from a subarray of with *K* elements and corresponds to planar waves of slightly different AoAs. Fig. 6.4 shows this approximation works very well. The estimated user position $\vec{r}$ can be used to update the estimated AoAs ($\hat{a}_n$) for the sub-arrays, and further updates the channel estimation to the user. The estimated channel takes the form of a set of DFT-like vectors for the sub-arrays (and the phase offset between adjacent sub-arrays). By flipping the sign of the estimated phase, we have a beamforming vector closely approximating maximal ratio combining to focus the downlink signal to the user.
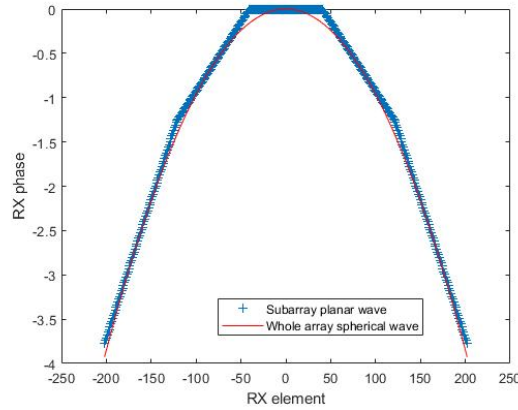
Fig. 6.4 The received phase of a spherical wave on a large array and its approximation with planar waves on 5 subarrays.

6.1.2 Near-Field Positioning Technology Based on RIS

In the presence of obstacles determining NLOS propagation conditions, localization might be challenging also considering that it typically requires the simultaneous connectivity with more reference BSs compared to those needed for communication. Adding more BSs could not represent a viable solution in many applications to due to the inherent increase of infrastructure cost. An interesting and potentially low-cost solution is given by the deployment of RISs that can be exploited as additional "virtual" reference nodes (see Fig. 6.5).
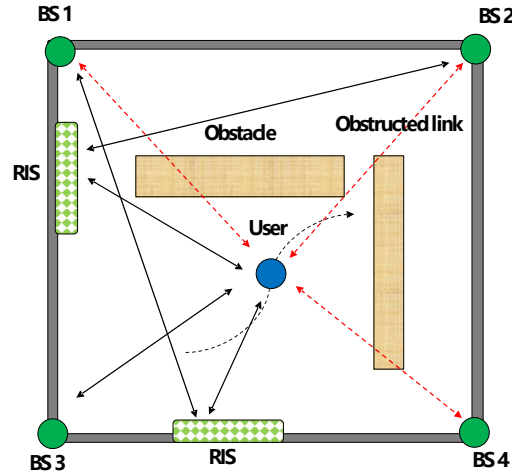
Fig. 6.5 RIS-aided localization: BS 2 and BS 4 can be seen by the user through the RIS thus ensuring at least 3 points of view as needed for 2D localization.

However, the optimization of the RIS' reflection characteristics poses several challenges because the position of the mobile user is not known beforehand and the RIS must be configured very often thus generating signaling overhead and implementation issues. Different approaches have been proposed in the literature. For instance, in [328] the fundamental theoretical limits in terms of position error bound (PEB) have been studied whereas in [329] an optimization algorithm is introduced in which, at each time step, the RIS is configured such that the PEB is minimized by starting from the previously estimated user position. Unfortunately, this algorithm does not solve the signaling overhead and it is not scalable with the number of users. To mitigate the signaling burden, in [331] a two-timescale joint precoding and RIS optimization algorithm is analyzed allowing a significant reduction of the RIS configuration rate by taking advantage of user statistical mobility models.

A different approach has been introduced in [330], where the reflection coefficient of each element of the RIS dynamically varies during the transmission of the reference OFDM signal emitted by the BS. This variation follows a predefined periodic pattern designed to enable the mobile user to estimate the delay of the signal component reflected by each visible element of the RIS provided that the system works in the near-field region of the RIS. Utilizing these BS-RIS-user delay measurements, the mobile user can then compute its own position without the need for signaling with the RIS then making the scheme scalable. Fig. 6.6   illustrates a practical example of NLOS localization facilitated by RIS using the above-described approach. In this scenario, a single-antenna user navigates within an indoor setting in the presence of several obstacles, with a BS emitting a reference OFDM signal. A long linear RIS is deployed (green patches in the figure), allowing the mobile user to determine its location by analyzing only the signals reflected by the RIS. Despite the presence of many obstacles that partially obstruct the RIS, the localization error along the mobile user trajectory remains limited to 20-30 cm, as seen from the inset plot. A narrowband version of the previous scheme exploiting the phase profile instead of time measurements is also investigated in [330]. RIS can also be exploited to solve near-field imaging problems utilizing XL-MIMO antennas as studied in [332], where the design of the optimal illumination waveform and RIS configuration is addressed.
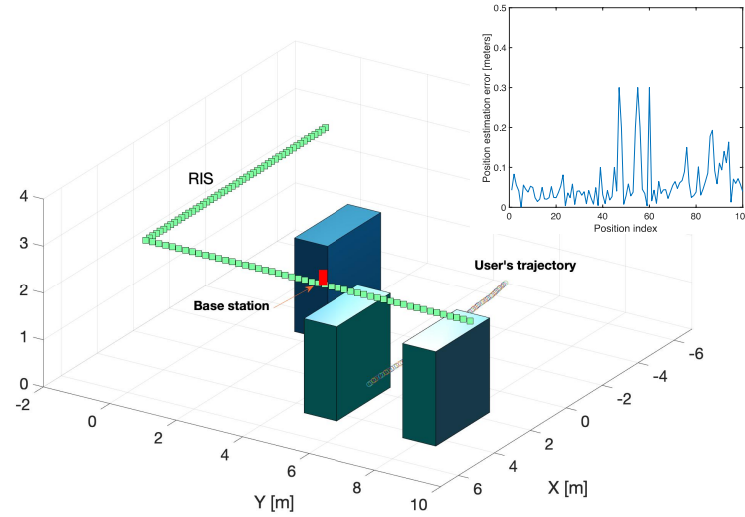
Fig. 6.6 RIS-assisted localization in a near-field NLOS scenario. 28 GHz system with 250 MHz bandwidth.

Near field communication and positioning based on massive MIMO technology require a large number of antenna elements and RF channels, including phase shifters, mixers, ADCs, etc., resulting in high hardware costs. In contrast, RIS-based near-field positioning can take full advantage of its flexible beam switching and channel reconstruction capabilities to achieve reliable communication and perception performance. Abundant time of flight (ToF) and spatial spectrum information can be obtained by a large number of period arrangement elements in the RIS array, which is expected to accurately estimate the source position. When the source incident on the RIS, the phase delay to different elements is a function of the distance d between the source and the center of the meta-surface and the orientation (θ, φ) of each element, which means that the source can be pinpointed effectively using spatial spectrum classification or maximum likelihood estimation [333][334].
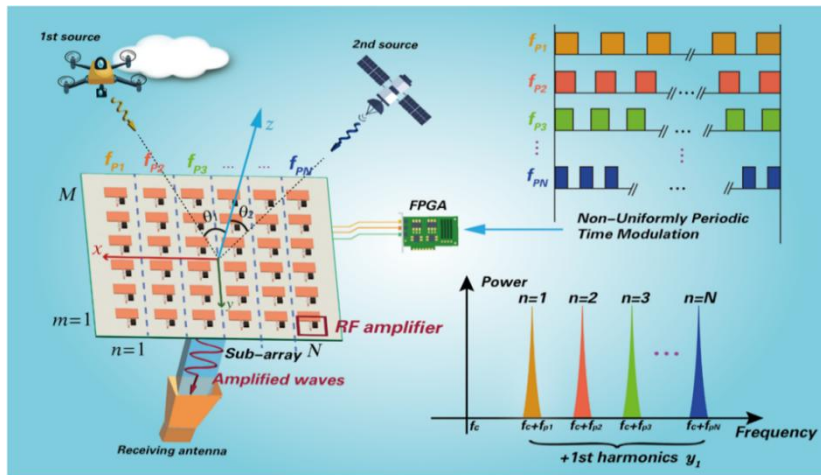
Fig. 6.7 Schematic diagram of two-dimensional DoA estimation based on RIS and non-uniform time modulation [335].

The basic theory and algorithms of information source's spatial positioning parameter estimation have been relatively mature, but many algorithms require multidimensional spatial spectrum search or high-complexity computations, which restricts the practical application because of hardware requirements, so there are still many problems to be solved. Therefore, based on the parameter estimation method of rank reduction or dimension reduction [336], the multi-dimensional spectral peak

search algorithm can be transformed into several one-dimensional searches, and the angle and distance parameter estimation can be matched automatically. However, the process of splitting the 2D search into two 1D searches is not straightforward. Initially, it requires the decoupling of bearing angles and distances or electrical angles. For example, by carefully selecting specific antenna elements to compute the channel covariance matrix, one of the electrical angles can be effectively eliminated from the problem, enabling 1D-compressive sensing for the AoA [337].

In addition, RIS-based positioning can significantly reduce hardware complexity, reducing DoA estimates that traditionally require multiple RF channels to just one. The spatial phase information can be stored in the spectrum through the space-time coding strategy, as shown in Fig. 6.7, which uses non-uniform time modulation to realize full-duplex multi-target positioning and adaptive beam scanning. The spatial spectrum information can also be contained in the received signal of multiple time slots by radiative multiple random beams, where holographic RIS and spherical wavefronts could be applicable[338][339].

In practical implementations, the metasurface array demonstrates remarkable operational flexibility through spatial resource partitioning. As illustrated in Fig. 6.8, edge elements of the metasurface can be selectively activated for near-field target localization while maintaining the remaining aperture for simultaneous beamforming control [340]. This architecture enables full-duplex operation that concurrently supports positioning and energy transmission functions. Considering the constrained channel resources in metasurface systems, a positioning method similar to RSSI can be adopted. The features of the target at different positions can be collected, and further through Convolutional Neural Network (CNN) data classification to realize positioning. To enhance the saliency of the target at different positions, Stacked Two-stage Convolution (STC) technology can be integrated. The generated multi-order harmonics during the STC modulation can function as feature information, thereby improving the classification accuracy of CNN. This positioning method does not require occupying too much of the aperture of the metasurface, and can effectively reduce the computational complexity.
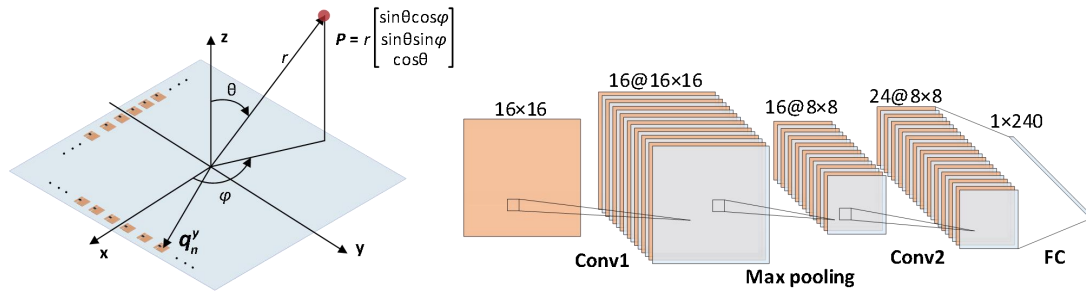
Fig. 6.8 Near-field target localization based on CNN [340].

Furthermore, the users may locate in the near field of the RIS in the XL-RIS-assisted THz localization systems. Since different RIS elements no longer share the same AoA according to the spherical wavefront of near-field channel model, the modeling and estimation of near-field channels become a more challenging task. Consequently, traditional channel estimation and localization methods will suffer severe degradation when applied in near-field scenarios.

Recently, the authors of [41] have proposed an algorithm of RIS-aided near field joint channel estimation and localization (NF-JCEL) in THz systems. As shown in Fig. 6.9, the authors considered the near-field channel model based on the spherical wavefront, and estimated the AoAs and distances

from the central reflecting element to UEs as well as the cascaded channel gains to locate the UEs by utilizing the geometric relationship. Based on the second-order Fresnel distance approximation, the researchers designed a RIS phase-shift training method to increase the rank of the channel matrix and avoid the noise amplification caused by LS estimation. Then, by utilizing the near-field channel characteristics, the researchers designed a sampling Toeplitz covariance matrix to decouple the distances and angles, and estimated the horizontal and vertical AoAs of the UEs respectively. Finally, they estimated the distances of the UEs with one-dimensional searching and obtained the estimated position by utilizing the estimated parameters and geometric relationship.
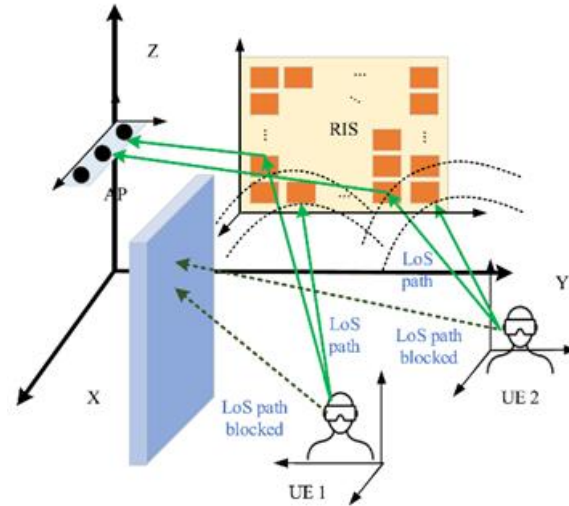
Fig. 6.9 RIS-assisted THz multi-user positioning systems.

As depicted in Fig. 6.10, the proposed algorithm prevails over the traditional far-field methods in the root mean square error (RMSE) of UE locations by utilizing the near-field AoA information. In addition, the RMSE will decrease with more RIS elements as well as more AoA information. Therefore, it is promising to deploy XL-RIS with more elements to enhance the localization accuracy.
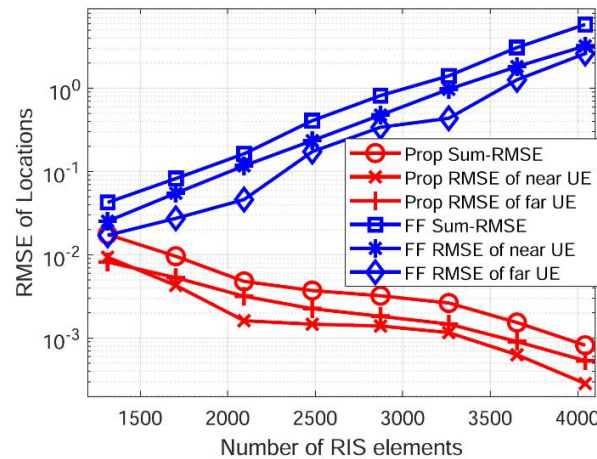
Fig. 6.10 RMSE versus the number of RIS elements.

In the following, another example of RIS-aided localization is introduced. First, the system model employed for three-dimensional (3D) localization using the RIS is presented. Furthermore, we introduce the near-field channel and a realistic amplitude-dependent phase RIS model to assess the performance metrics including positioning error bound (PEB), RMSE for localization, and achievable

data rate for communication. We examine a wireless setup comprising of a single user transmitting from position $p = [x, y, z]^T$, and an N-element RIS lens positioned in the XY plane with reference point $[0,0,0]^T$. The RIS is placed near a single antenna equipped with a corresponding RF chain for reception, located at $p_{ant} \in \mathbb{R}^3$ as per Fig. 6.11. The figure illustrates the 3D coordinate system that shows the positional and angular information of the user and RIS. The spacing between the horizontal and vertical elements is set to $\lambda/2$ where λ is the wavelength at the carrier frequency. The n-th element of the RIS is located at $\zeta_n = [x_n, y_n, 0]^T = l_n[\cos \Psi_n, \sin \Psi_n, 0]^T \in \mathbb{R}^3$ where l_n refer to the element's distance from the RIS origin to the element and Ψ_n is the n-th element azimuth angle.
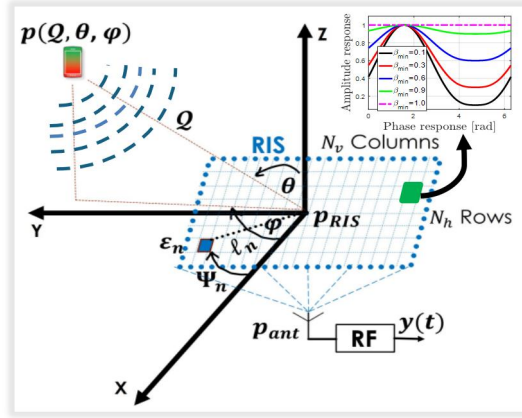
Fig. 6.11 Localization system coordinate.

The RIS is composed of N =2500 elements arranged in a $N_v \times N_h$ grid, where $N_v = N_h = 50$, at a frequency of 28 GHz with $\lambda^2/4$ element area. A single receive antenna is positioned behind it at coordinates $[0,0, -\lambda]^T$. The transmit power is 1 mW, the noise power spectral density is -174 dBm/Hz, and the reception noise figure is set to 8 dB. We choose the number of time instances to be T = 200 and the bandwidth to be 1 MHz. In our analysis, we focus on a user who possesses a wavevector k oriented in the direction $[1,1,1]^T$. The channel gains to and from the RIS are set in the near-field regime [341]. The prior knowledge about the user's location is represented by a (pdf) denoted as $p(p) = N(p; m_p, c_p)$, where $c_p = \sigma^2 I_3$. This prior information is solely employed for designing the directional beams of the RIS, and it is not utilized during the localization process or in the calculation of the (PEB). The standard deviation in each dimension (XYZ) of the prior covariance of the user position is set to $\sigma \in \{0.1,1\}$ m to evaluate the localization performance in the random, directional, and positional phase profiles.
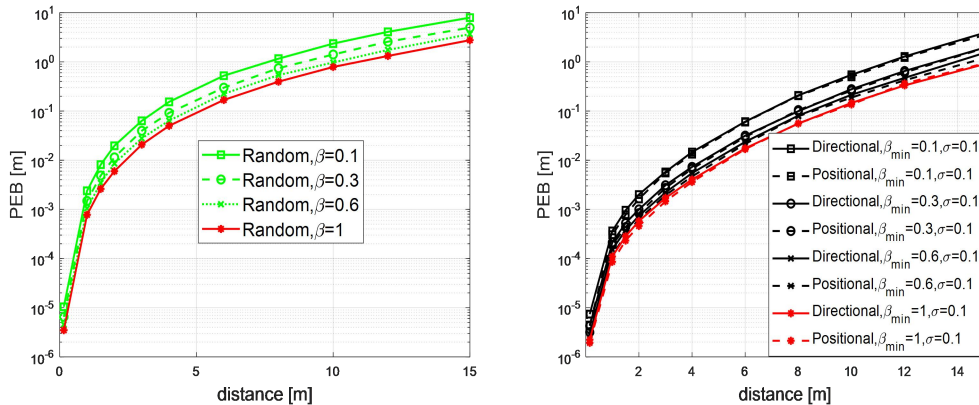
Fig. 6.12 PEB as a function of distance to the RIS using random, directional and positional RIS phase profiles.

In Fig. 6.12 we notice that by using a basic random phase configuration, we can achieve relatively low PEB, specifically below 1 meter, for user positions within a 10-meter distance from the RIS and at different values of β_{min}. By employing directional or positional phase profiles ($\sigma = 1$ and $\beta_{min} \in [0,1]$), it is possible to significantly decrease the Position Error Bound (PEB). The positional phase profile exhibits slightly superior performance compared to the directional phase profile, although the disparity between the two is negligible. Similarly, we observe that employing directional or positional phase profile allows us to achieve relatively enhanced (PEB), specifically below 1 meter, for user positioned within a 10-meter range from the RIS, regardless of the value of β_{min}.
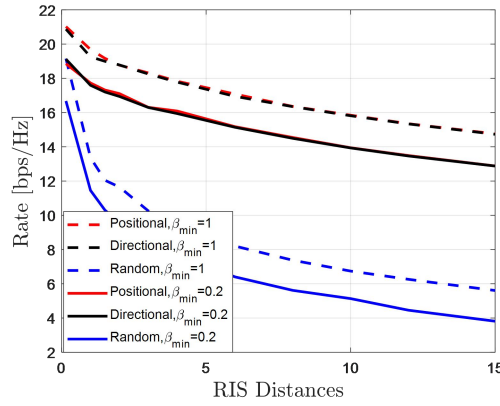
Fig. 6.13 Data Rate versus RIS distance

Fig. 6.13 shows the data rate against the distance to the RIS. Generally, the data rate is inversely proportional with the distance, and this is due the decrease in (SNR) in the reflected path, which is inversely proportional to the distance from the RIS. The realistic RIS phase shift model is adopted, and the data rate performance gap is evident when β_{min} is changed from the ideal case which is $\beta_{min} = 1$ to the actual case which is $\beta_{min} = 0.2$.

6.1.3 Near-field Localization Based on Controllable Beam Squint

For wideband massive MIMO systems using OFDM modulation, beamforming based on phase shifter (PS) structure will lead to beam squint effect. Far-field beam squint effect causes the beams of subcarriers with different frequencies to focus into different angular directions [342][343], while near-field beam squint effect causes the beams of subcarriers with different frequencies to focus at different positions. Fig. 6.14 shows an example of near-field beam squint, where a total of M+1 subcarriers are enabled. As the frequency of subcarriers increases, the beamforming of different subcarriers will focus at different positions and can be connected into a trajectory. The starting point of the trajectory is determined by the 0-th subcarrier, while the ending point of the trajectory is determined by the M-th subcarrier. In Fig. 6.15, the lowest frequency of subcarrier is 30 GHz, and its near-field beamforming is focused at position $(10\text{m}, 60°)$. The highest frequency is 36 GHz, and its near-field beamforming squints to position $(22.99\text{m}, 46.19°)$. It can be seen that near-field beam squint phenomenon cannot be ignored in wideband systems.
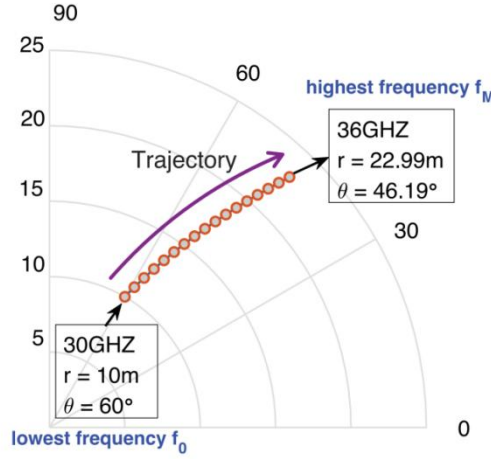
Fig. 6.14 Schematic diagram of near-field beam squint.
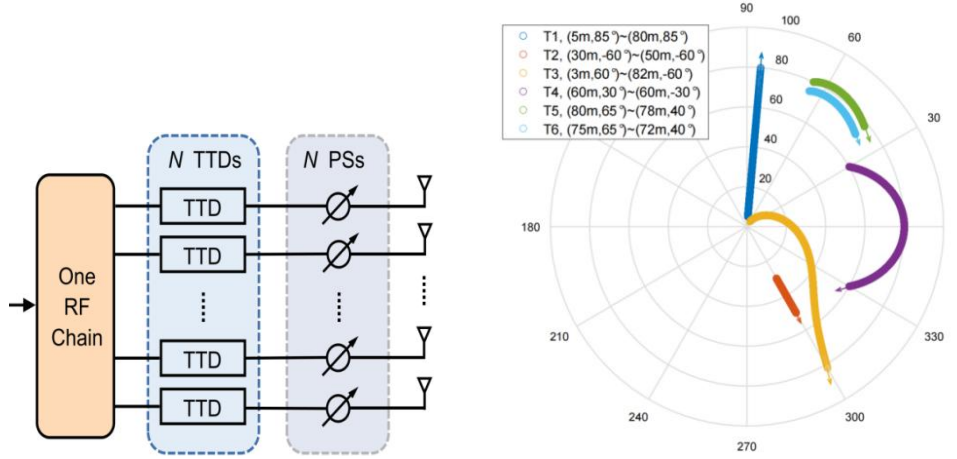
Fig. 6.15 Schematic diagram of near-field controllable beam squint.

As shown in Fig. 6.15, it is considered to cascade a true time delay (TTD) line for each PS in the BS. By carefully setting the values of PSs and TTDs, the starting point and ending point of the near-field beam squint trajectory can be reversely controlled, which is beneficial for BS to realize user localization with low pilot overhead. Specifically, Fig. 6.15 shows examples of several near-field controllable beam squint trajectories, where a total of 2048 subcarriers are enabled. Trajectories T1 and T2 are two radial straight lines. If the angle of user or target has already been obtained, using radial trajectories like T1 and T2 can quickly sense the distance of the user or target. Trajectory T3 spans the entire range of angle and distance, providing full area sensing. Trajectory T4 exhibits a symmetrical trend in angle, which is more conducive to obtaining the angle of user or target. Trajectories T5 and T6 are squinting in a smaller area, which facilitates beam scanning in a known and narrow area, such as a bus stop [356].

To realize fast near-field user localization, BS uses the beamforming scheme based on TTDs assisted near-field controllable beam squint for sensing pilot signal transmission. A low-complexity near-field user localization method is proposed, which includes the first angle sensing stage and the second distance sensing stage.

In first angle sensing stage, it is planned to use one time beam sweeping to obtain the angle estimates for all near-field users. Let the beamforming of subcarrier f_0 point to the starting point

$(r_{mid1}, \theta_{start})$ by adjusting PSs, and let the beamforming of subcarrier f_M point to the ending point (r_{mid2}, θ_{end}) by adjusting TTDs, where r_{mid1} and r_{mid2} are two appropriate values between r_{min} and r_{max}, r_{min} and r_{max} are the minimum and maximum distances required for the near-field sensing range, θ_{start} and θ_{end} are the maximum and minimum angles of the near-field sensing range. Then BS uses near-field controllable beam squint strategy to transmit pilot signals, and the beamforming focusing angles of all subcarriers gradually squints from θ_{start} to θ_{end}, covering the entire angle sensing space. The beamforming focusing distance gradually squints from r_{mid1} to r_{mid2}, and the near-field beam squint trajectory of subcarriers is similar to trajectory T4 in Fig. 6.15. All near-field users receive all subcarriers and feedback the frequencies of the maximum power subcarriers to BS. The BS can calculate the angle of each user using the frequency of these maximum power subcarriers and the formula for near-field controllable beam squint angle.

After obtaining the angle sensing result, we can enter the second distance sensing stage. Assuming there are some near-field user in the angle direction of $\hat{\theta}_{u^{near}}$, the users' distances will be sensed in the q-th beam sweeping of distance sensing. Let the beamforming of subcarrier f_0 point to the starting point $(r_{min}, \hat{\theta}_{u^{near}})$ by adjusting PSs, and let the beamforming at subcarrier f_M point to the ending point $(r_{max}, \hat{\theta}_{u^{near}})$ by adjusting TTDs. Then BS uses near-field controllable beam squint strategy to transmit pilot signals. The beamforming focusing angle of all subcarriers is always $\hat{\theta}_{u^{near}}$, and the beamforming focusing distance gradually squints from r_{min} to r_{max}. The near-field beam squint trajectory of the subcarriers is similar to trajectory T1 in Fig. 6.15. The near-field users receive subcarriers and feedback the frequencies of the maximum power subcarriers to BS. The BS uses the frequency of the maximum power subcarrier and the formula for near-field controllable beam squint distance to calculate the distance estimates of the user, thereby achieving near-field localization.

The proposed near-field localization method based on controllable beam squint cleverly utilizes the frequency-domain beam sweeping of beam squint instead of the traditional time-domain beam sweeping, greatly reducing the time overhead compared to traditional near-field localization algorithms.
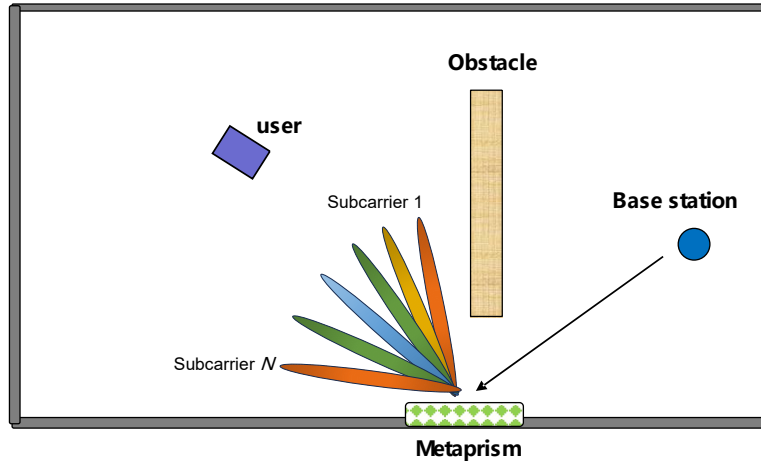
Fig. 6.16 Localization in NLOS by exploiting a metaprism (each color represents a different subcarrier).

Frequency selectivity can be successfully exploited also to provide localization in NLOS conditions by using particular metasurfaces called *metaprism*, recently introduced to enhance communication and subsequently localization at low cost [357][358]. A metaprism is a static

metasurface (i.e., not reconfigurable) that exhibits a controlled frequency selectivity within the bandwidth of interest. In particular, one possibility is to design the phase profile of the metasurface such that it depends linearly with the frequency, i.e.,

$$\varphi_n(f) = \alpha_n \cdot (f - f_0) \tag{6.2}$$

where $\varphi_n(f)$ is the reflection phase shift of the n-th cell of the metasurface, f_0 is the carrier frequency, and α_n is a cell-dependent coefficient to be properly designed according to the desired reflection behaviour (beamsteering in the far field, focusing in the near field) [357].

For example, in Fig. 6.16 each subcarrier of the OFDM signal emitted by the BS is reflected by the metaprism toward a specific direction thanks to its frequency selectivity property, thus mapping different AoD to different subcarriers. Therefore, by analyzing at which subcarrier the signal is received it is possible to infer the angle of view of the target user. In [358] it has been shown that while in the far field only angle information can be obtained with an accuracy in the order of 1 degree or less at millimeter waves, in the near field it is possible to obtain also distance information (and hence position information) through the introduction of fingerprinting-like positioning algorithms. The metaprism represents an appealing solution with several advantages compared to RIS such as: i) it is fully passive so no power supply, no dedicated signaling, and no CSI estimation schemes are needed; ii) it is transparent to the wireless communication protocol; iii) it allows parallel links pointing to different directions, then lower latency in the presence of dense users; iv) it enables simple and really low-cost positioning in NLOS conditions.

6.1.4 NLoS UE Localization with near-field effects
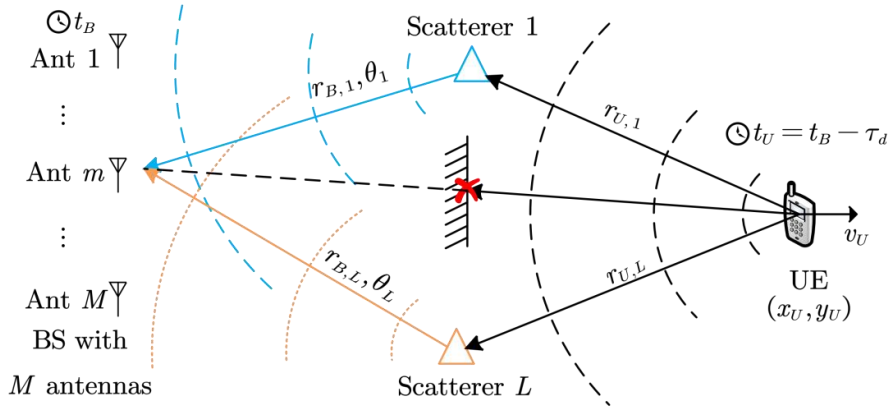
Fig. 6.17 A single BS localization system with clock asynchronism and without LoS path.

While localization in LoS scenarios has reached a level of maturity, the localization of UE in the absence of a LoS path, as shown in Fig. 6.17, has always been a challenge. It has been theoretically shown that in far-field scenarios, NLoS signals do not contribute to the equivalent Fisher information matrix for the UE's position and thus cannot improve localization accuracy if no prior information about the scatterers is available [344]. As a result, without a LoS path nor any prior information of the scatterers, accurate UE localization is impossible in far-field scenarios. From a mathematical perspective, the process of localizing UE as illustrated in Fig. 6.1 involves solving the following system of equations,

$$\begin{cases} \left(r_{B,l}cos\theta_l - x_u\right)^2 + \left(r_{B,l}sin\theta_l - y_u\right)^2 = r_{U,l}^2 \\ r_{U,l} + r_{B,l} = c\tau_l \end{cases} \forall l, ..., L. \# \tag{6.3}$$

In far-field scenarios with traditional smaller-scale arrays, assuming perfect synchronization of clocks, i.e., $\tau_d = 0$, the variables $\{\theta_l\}_{l=1}^{L}$ and $\{\tau_l\}_{l=1}^{L}$ can be estimated using array and radar signal processing. However, other variables remain unknown, resulting in an under-determined system with $2L + 2$ unknown variables and only $2L$ equations. On the other hand, it is noteworthy that different from the LoS case, in NLoS scenarios, the distance calculated from the CoA of the spherical wavefront is different from the distance obtained through the ToA. The former is the distance of the scatterer while the latter is the length of the propagation path. Leveraging on this property, in near-field scenarios with large-scale antenna array, since the array response vector is dependent on both the AoA and the distance of the scatterers, estimation of scatterer locations using one single BS becomes possible using array signal processing. Provided that $L \geq 3$, the additional estimation of $\{r_{B,l}\}_{l=1}^{L}$ through array signal processing leads to an over-determined system, enabling the estimation of UE's location. Note that when clock asynchronism between the BS and UE is considered, i.e., $\tau_d \neq 0$, $L \geq 4$ near-field scatterers are required for UE localization, and the clock difference τ_d can also be estimated.

In [345], a tensor-based method is proposed to isolate each path from the space-time-frequency three-dimensional channel tensor obtained with OFDM reference signals, enabling the estimation of the corresponding delay, Doppler shift, and scatterer position. These estimated parameters are then used to solve for the UE position. It's worth noting the tensor-based method proposed in [346] requires each path's parameters, i.e., delay, Doppler shift and scatterer position to be different for the canonical polyadic decomposition uniqueness conditions to hold. If any of the parameters are too close, e.g., two paths have close delays, Doppler shifts or two scatterers are physically close, thus having similar array response vectors, the paths may not be properly resolved due to rank deficiencies.

Literature [346] proposes a single-BS simultaneous environment sensing and NLoS UE localization scheme. This approach exploits the channel spatial sparsity and high spatial resolution of XL-arrays to estimate the locations of each near-field scatterer, which then serves as virtual anchors for UE localization. Specifically, first, successive Zero-Forcing (ZF) two-dimensional MUSIC (2D-MUSIC) is used for scatterer localization. Then, the signal from each path is isolated and the corresponding propagation delay is estimated. Finally, the above over-determined equations are solved to obtain the UE location. Compared to the tensor-based method, this method demonstrates superior robustness to closely spaced scatterers thanks to the super-resolution capability provided by 2D-MUSIC.

6.1.5 Near-field positioning technology based on the division of subarray

Due to the influence of near-field characteristics, targets are no longer absolutely located in the far-field region where signals propagate with the uniform plane wavefront model. It is possible that they may locate in the near-field region. In this case, the signal propagation model transitions to a spherical wavefront model, with angle and distance information strongly coupled [347]. On one hand, the near-field characteristics introduce new DoFs to the localization problem, allowing for the simultaneous estimation of the target's direction of arrival (DoA) and distance. On the other hand, due to the change in propagation models, traditional far-field localization algorithms will experience significant inaccuracies in near-field scenarios. To achieve high-resolution near-field localization capabilities, there is an urgent need to consider super-resolution algorithms tailored for near-field

scenarios. A straightforward approach is to extend traditional one-dimensional (1D) super-resolution algorithms, such as the MUSIC algorithm and the ESPRIT algorithm, into a 2D angle-distance domain for exhaustive search [348]. However, exhaustive search within the 2D angle-distance grid presents issues with excessive computational complexity. Thus, it's important to develop new near-field algorithms for low-complexity target localization.
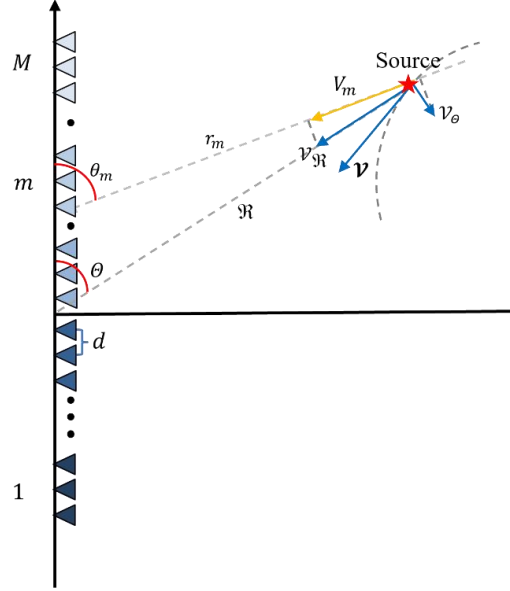
Fig. 6.18 A single BS near-field sensing system with the division of sub-array.

As shown in Fig. 6.18, consider partitioning the BS's ULA into multiple non-overlapping subarrays. Thus, we can utilize the angle and distance information perceived by the subarrays to jointly estimate the target's position, namely (R, θ). By appropriately partitioning the number of antennas in each subarray, near-field targets can be located in the far-field region of each subarray. Consequently, it is possible to leverage the time delay and Doppler information obtained by each subarray to estimate the DoA and distance information, namely (r_m, θ_m). Since the target is located within the far-field region of each subarray, classical far-field sensing methods, such as the periodogram algorithm or 1D-MUSIC algorithm, can be employed for parameter estimation within each subarray. Furthermore, by utilizing the geometric relationship between the estimation results of subarrays and the BS, the distance and DoA of the target relative to the BS ULA can be jointly estimated, thereby achieving precise estimation of the target's DoA and distance.

6.1.6 FFT-enhanced low-complexity near-field super-resolution localization

Traditional far-field super-resolution localization algorithms, such as MUSIC and ESPRIT, often exhibit high computational complexity when extended to near-field conditions[347]. While algorithms like RD-MUSIC and RR-MUSIC aim to reduce computational complexity, they face incompatibility issues with existing communication architectures[351][352]. To address the challenges of reducing computational complexity in near-field localization and meeting deployment requirements of current communication architectures, a novel low-complexity super-resolution algorithm based on FFT is proposed. By leveraging the FFT algorithm and 1D far-field beamforming, the proposed method significantly narrows the angular-distance search range for 2D spectral peak research. This enables effective complexity reduction while maintaining compatibility with existing communication architectures.
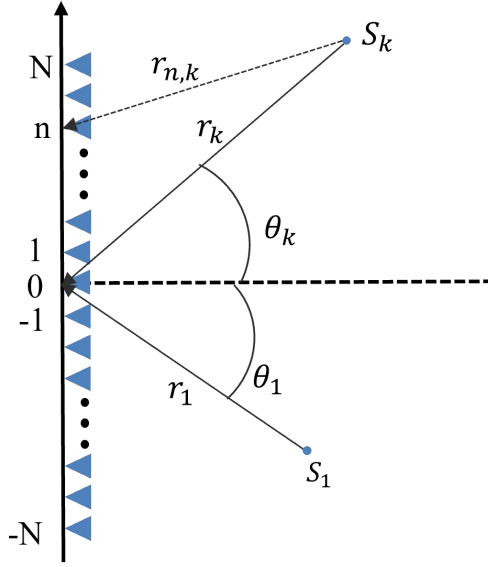
Fig. 6.19 A near-field XL-MIMO system for target localization.

As illustrated in Fig. 6.19, the BS employs an XL-MIMO array with M=2N+1 antennas to estimate K targets. The algorithm operates in three stages. In the first stage, an FFT-based spectral peak search is performed in the angular domain. Due to near-field spreading effects, the initial search yields $\widehat{K} > K$ peaks. These peaks are clustered into n angular clusters, each containing $\widetilde{K}_n$ peaks. Clusters with $\widetilde{K}_n=1$ correspond to far-field targets, whose angles θ_j can be directly determined. Clusters with $\widetilde{K}_n>1$ may contain mixed near-field and far-field targets, which requires further refinement. In the second stage, for ambiguous angular clusters, far-field beamforming is applied to partition the distance domain into $\widehat{n}$ ($\widehat{n} \leq n$) distance clusters, further reducing the search space. In the third stage, a reduced-range 2D-MUSIC search is executed within the narrowed angular-distance regions to achieve precise localization. Notably, the algorithm avoids Taylor approximations in angle and distance estimation, eliminating the requirement for antenna spacing to less than a quarter-wavelength.
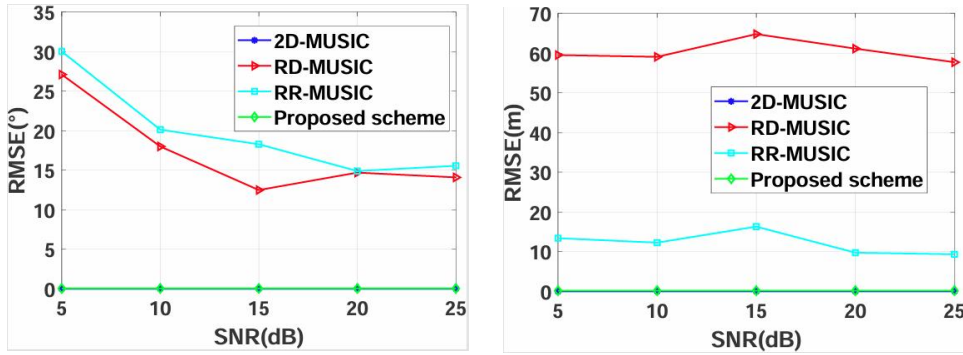
(a) RMSE of angle versus SNR (b) RMSE of distance versus SNR
Fig. 6.20 Comparison of localization accuracy of different near-field localization algorithms.

By leveraging FFT and beamforming to reduce the 2D-MUSIC search scope, the proposed algorithm achieves substantial computational efficiency improvements while maintaining the comparable localization performance of conventional 2D-MUSIC. As shown in Fig. 6.20, when antenna spacing is set to half-wavelength, RR-MUSIC and RD-MUSIC exhibit severe estimation errors, whereas the proposed algorithm maintains comparable performance with 2D-MUSIC. These results

demonstrate that the proposed method enables high-precision near-field localization while significantly reducing complexity and compatible with existing communication architectures.

6.1.7 Near-field localization based on coprime array[355]

Wireless/radar sensing has found a wide range of applications in practice, such as high-precision positioning and tracking, high-resolution imaging, and simultaneous localization and mapping. Moreover, with the technology trends evolving towards higher frequency band and larger transmitter array aperture, the Rayleigh distance, which specifies the boundary between the near-field and far-field, is greatly expanded, thus rendering environmental targets more likely to be located in the near-field region of the large-aperture array. However, existing works mainly considered dense arrays with a large number of sensors/array elements, which practically incur high power and hardware cost, as well as demanding signal processing complexity. To tackle this issue, sparse arrays have been proposed as an alternative array configuration to achieve large array aperture with a small number of sensors only, hence greatly reducing the power consumption. The main challenges of target localization for sparse arrays are two-fold. Firstly, the angle estimation algorithms based on the virtual array in the far-field cannot be directly extended to the near-field case, due to the nonlinear phase delays across the array elements. Secondly, most existing near-field localization methods are designed for uniform linear arrays. Although we can extend the subarray-based localization method to the coprime array by decomposing the coprime array into two ULAs, this approach suffers from degraded sensing DoFs due to the lack of inter-subarray mutual information. Motivated by the above, we study in this paper a new and efficient near-field localization method for large-aperture coprime array.

To resolve these challenges, we first leverage the symmetry property of coprime array to construct an effective covariance matrix, which allows to fully exploit all elements of covariance matrix and decouple the angle-and-range estimation. Then, a customized two-phase MUSIC algorithm for coprime arrays is proposed, which first detects all possible targets' angles (including the true and cross angles) by using an angular domain MUSIC algorithm, followed by the second phase to resolve the true targets' angles and ranges by devising a range domain MUSIC algorithm. The key idea is to utilize the fact that cross angles do not exhibit obvious spectrum peaks in the range domain, hence allowing for the detection of true targets. It should be noted that the performance of range estimation is affected by the accuracy of angle estimation.
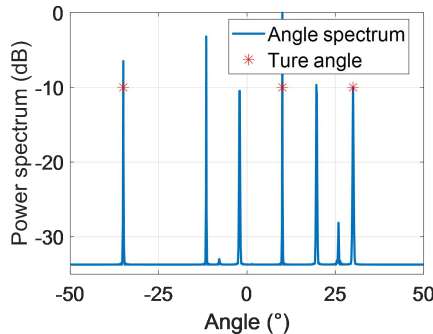
Fig. 6.21 Angle spectrum.
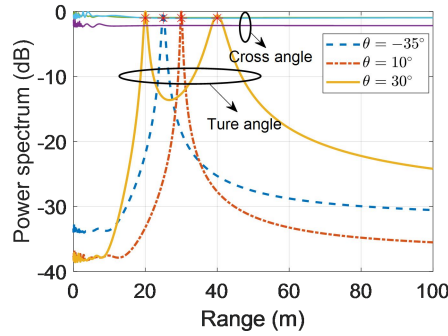
Fig. 6.22 Range spectrum.

Finally, we theoretically and numerically show that the results of spectral peak search in the angular domain and range domain by using the coprime array, where the true targets locations are marked by red stars. Furthermore, one can observe that even when two targets are positioned at the same angle, they can still be distinguished in the range domain.

6.1.8 Near-Field Localization based on Power Sensors

In XL-MIMO communication systems, traditional subspace-based methods such as MUSIC and ESPRIT face several challenges, including the high computational complexity that increases polynomially with the number of antennas, as well as the loss of orthogonality among near-field steering vectors, which can significantly degrade the performance of localization algorithms in near-field scenarios. Against this background, back projection method that has been widely adopted in microwave imaging can be considered as a practical alternative. In particular, it records the interference pattern of the incident EM wave and then emulates the reverse propagation to reconstruct the near-field wireless radio map, as demonstrated in Fig. 6.23.
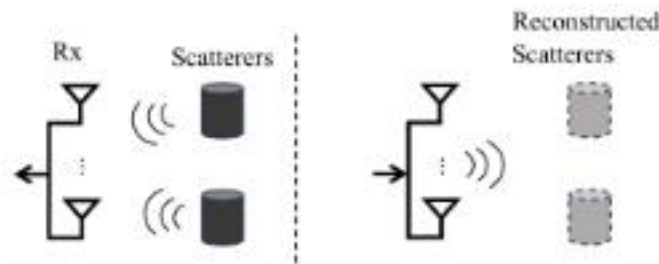
Fig. 6.23 The recording and reconstructing procedure of back projection method.

To fully leverage the large aperture while maintaining minimal complexity, the transceiver architecture can be realized using off-the-shelf power sensors to measure the power pattern of the incident electromagnetic (EM) wave. Although phase information is neglected in this approach, two key observations can still be made. First, the reconstructed radio map exhibits peaks exclusively at the positions of users or scatterers, with the peak values determined solely by the distance and the source power. Second, the fluctuations in the reconstructed map at other locations asymptotically approach zero as the number of antennas and the carrier frequency increase. Typical reconstruction results are illustrated in Fig. 6.24.
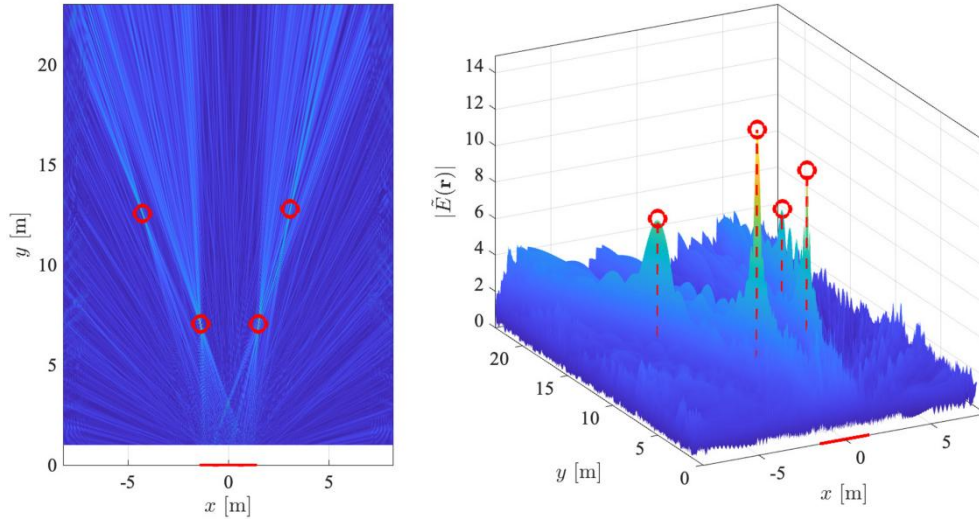
Fig. 6.24 Typical reconstruction results of back projection method.

Notably, the EM wave transmission model based on uniform arrays can be expressed in a convolutional form, which allows for implementation using fast Fourier transform (FFT). This significantly reduces the computational complexity of the back projection algorithm and eliminates the need for additional application-specific processors [353]. However, it is also observed that the traditional ULA and UPA architecture are not well-matched to the near-field spherical wave model. As the angle between the incident EM wave and the array normal direction increases, the effective aperture of the ULAs and UPAs decrease sharply at the edges. This results in non-uniform service performance for users at different near-field positions, with the best performance only achieved for users directly in front of the array.
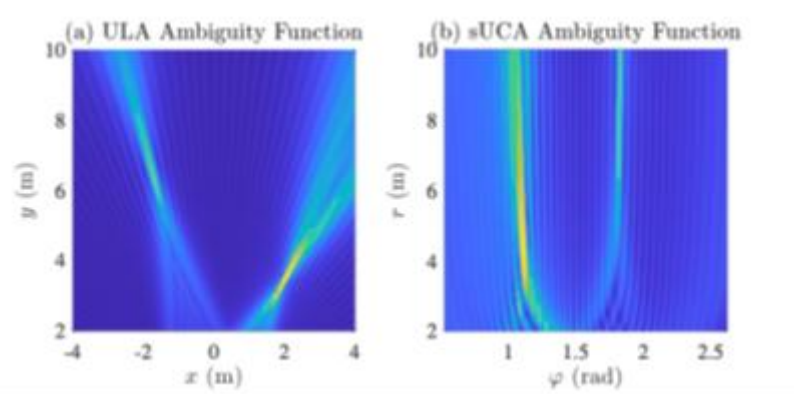
Fig. 6.25 The reconstruction results of (a) ULA and (b) sectored UCA with two targets in the near field

On the contrary, UCAs not only adapt well to the near-field model under polar coordinate system, but also exhibit angular isotropy, effectively resolving the issue of performance imbalance. The radio map reconstruction results under the UCA configuration are shown in Fig. 6.25. Compared to the reconstruction results in Fig. 6.24, this approach enables rapid localization through simple summation and a one-dimensional grid search, with resolution unaffected by the user's angular position [354].

6.2 Integrated Sensing and Communication in Near Field

6.2.1 From Far-field Sensing to Near-field Sensing

The angle, distance and velocity of the sensing target relative to the sensing node are three important metrics in wireless sensing. In traditional far-field sensing, the sensing performance of these three metrics depends on the size of the antenna array, the bandwidth of the sensed signal, and the sensing duration, respectively. However, when the sensing target is located in the near-field, the spherical wave propagation of the signal brings revolutionary changes to the sensing of these three metrics, as follows.

● **Joint angle and distance sensing in the spatial domain**

In far-field sensing systems, angle and distance sensing usually need to be processed in the spatial and frequency domains, respectively. This implies that far-field sensing systems usually require a larger bandwidth or the collaborative support of multiple sensing nodes to achieve precise target localization. However, in near-field sensing systems, the employment of large aperture antenna arrays is able to capture both angle and distance information, which makes accurate target localization possible only through spatial domain signal processing techniques [359], no longer requiring large bandwidth or the support of multiple sensing nodes, which greatly reduces the cost and complexity of the system. Additionally, the performance limits in near-field sensing scenarios are different from the traditional uniform planar wave model. In [360], a closed-form expression for the received SNR in near-field sensing is derived. Different from the conventional UPW model where the SNR scales linearly and unboundedly with the number of antennas, the SNR increases with diminishing returns in near-field sensing. Furthermore, in [361], considering XL-MIMO radar and XL-phased array radar, closed-form expressions for the Cramér-Rao bounds on angle and distance parameters are derived for monostatic and bistatic sensing systems, respectively.
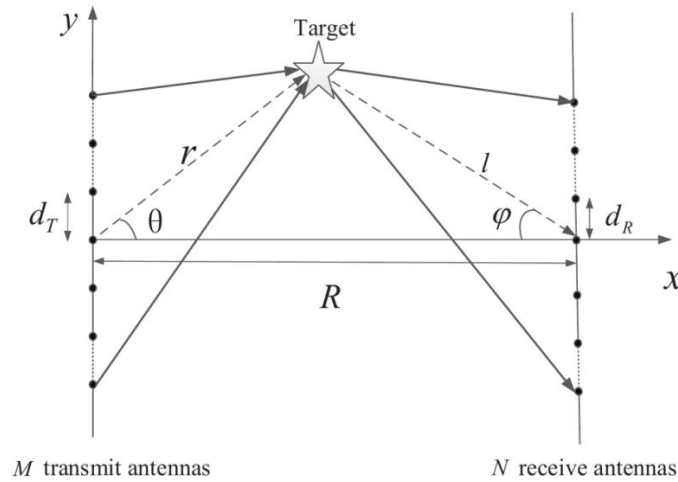
Fig. 6.26 Near-field radar sensing with XL-MIMO.

Specifically, the near-field radar sensing system with XL-MIMO is shown in Fig. 6.26. Let M and N denote the number of transmit and receive antenna elements, respectively, with inter-element spacing denoted by d_T and d_R. The distance between the transmit and receive ULAs is R. In the single-target scenario, the angles and distances from the target to the centers of the transmit and receive antenna arrays are denoted as (θ, r, φ, l). When R is known, the receiver side range and angle

parameters can be expressed in terms of the transmitter side parameters to reduce the number of parameters to be estimated, i.e.,

$$l(r,\theta) = \sqrt{R^2 + r^2 - 2Rr\cos\theta},$$
$$\varphi(r,\theta) = \arcsin\left\{\frac{r\sin\theta}{\sqrt{R^2 + r^2 - 2Rr\cos\theta}}\right\}.$$

<div align="right">(6.4)</div>

The FIM can be expressed as

$$\mathbf{F} = \frac{2}{N_0}\Re\left\{\left(\frac{\partial\mathbf{w}}{\partial\mathbf{z}}\right)\left(\frac{\partial\mathbf{w}}{\partial\mathbf{z}}\right)^H\right\},$$

<div align="right">(6.5)</div>

where $\mathbf{w}$ is the output of matched filter, $\mathbf{z}$ is the parameters to be estimated, and N_0 is the power spectral density of noise. Therefore, the CRB of angle and range can be expressed as $\mathbf{F}_{1,1}^{-1}$ and $\mathbf{F}_{2,2}^{-1}$.

It can be shown that the CRBs of angle and range in near-field sensing decrease with diminishing return and approach to certain limits as the number of antennas increases [361]

$$\lim_{\frac{D_T}{r\cos\theta}\to\infty} CRB_\theta = \frac{1}{2\gamma L}\frac{\lambda^2 d_T \sin^2\theta}{8\pi^3 r^3 \cos\theta},$$
$$\lim_{\frac{D_T}{r\cos\theta}\to\infty} CRB_r = \frac{1}{2\gamma L}\frac{\lambda^2 d_T \cos\theta}{8\pi^3 r},$$

<div align="right">(6.6)</div>

where γ is the receive SNR, d_T is the element-spacing of transmit antenna, λ is the signal wavelength. As a comparison, the CRB for angle with the conventional far-field UPW model can be derived based on [362].

$$C_\theta = \frac{1}{2\gamma L}\frac{3\lambda^2}{2\pi^2 d_T^2 M(M^2-1)\cos^2\theta},$$

<div align="right">(6.7)</div>

Fig. 6.27 shows the CRB of angle for monostatic XL-MIMO and XL-phased array radar, which that with the increasing of antenna number, using inappropriate far-field model to analyze near-field sensing with XL-arrays may cause severe errors. Besides, the CRBs for angle of phased array radar mode is smaller than that of MIMO radar mode, since the former usually benefits from an additional transmit beamforming gain. Fig. 6.28 shows bistatic near-field sensing CRBs, and compared with near-field 2-D MUSIC algorithm and Capon algorithm.
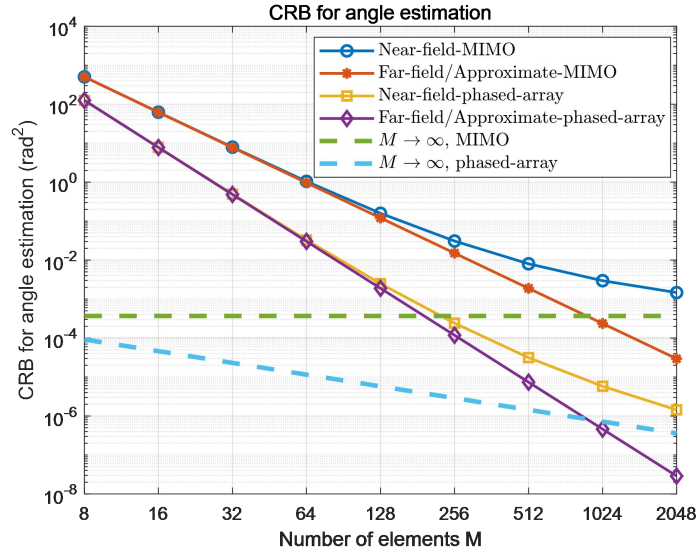
Fig. 6.27 CRB of angle for monostatic sensing.
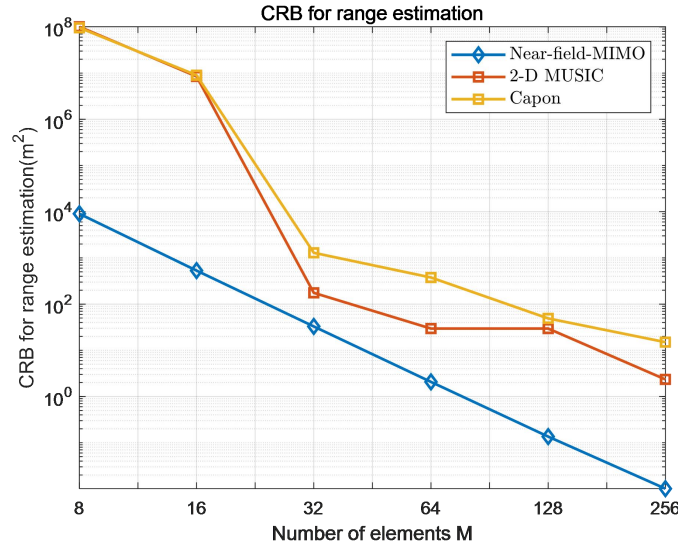
Fig. 6.28 CRB of range for bistatic sensing.

● **Multi-dimensional velocity sensing [313]**

As shown in Fig. 6.29, in a far-field sensing system, all antennas in an antenna array "see" the sensing target at almost the same angle. Consequently, the Doppler shift in the sensing signal arises solely due to the target's velocity projected in one direction, denoted as the radial velocity. As a result, far-field sensing systems cannot fully capture the complete motion of the sensing target. However, in near-field sensing, different antennas "see" the sensing target from different angles, which enables the capture of the projected component of the target velocity at different directions, as shown in Fig. 6.30. Therefore, near-field sensing is able to simultaneously sense the radial and transverse velocities of the target, obtaining complete motion state information. This complete motion state information makes it possible to accurately predict the target position at the next time interval. In communication systems, this approach can be used to design beamforming for the next communication period in advance, significantly reducing the need for channel estimation and beam training. [313] presents a near-field velocity sensing algorithm based on the maximum likelihood method. By solving a convex

optimization problem, the algorithm accurately estimates the target's radial and transverse velocities. However, when extended to multi-target scenarios, the complexity of maximum likelihood optimization increases dramatically. Therefore, there is a need to find new low-complexity near-field velocity sensing algorithms. Following the concept of subarray partitioning, as shown in Fig. 6.30, it is assumed that the extremely large scale ULA is evenly divided into M non-overlapping subarrays, ensuring that the target is within the far-field region of each subarray. This allows for the perception of the target's Doppler information in each subarray, thereby obtaining the user's radial velocity perceived by each subarray. Due to the near-field effect, the radial velocities perceived by each subarray makes a little difference. Since there is a geometric relationship between V_m and radial and transverse velocities (V_R, V_θ) relative to the BS, we can combine these M geometric relationship to obtain an overdetermined system of equations. By solving such an overdetermined problem, the target's radial and transverse velocities (V_R, V_θ) can be obtained, thus getting the target's overall motion state.
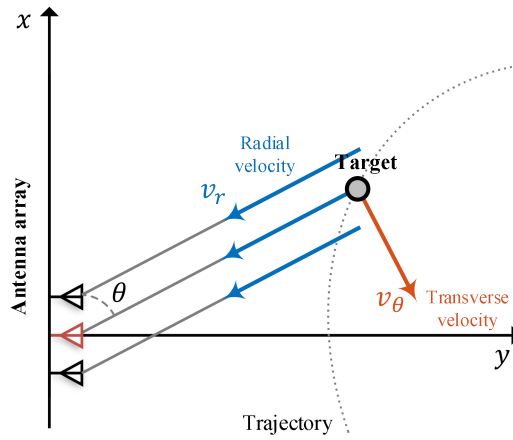
Fig. 6.29 Far-field Velocity Sensing.
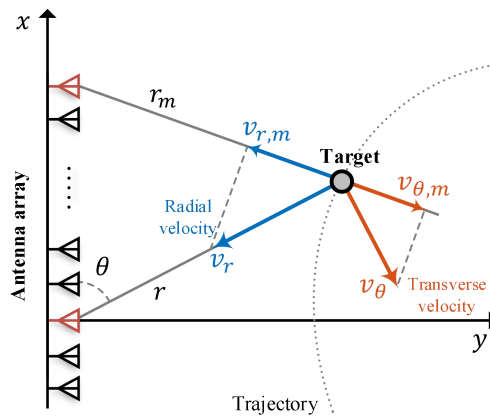
Fig. 6.30 Near-field Velocity Sensing.

6.2.2 Near-Field Integrated Sensing and Communications

ISAC represents a revolution at the intersection of sensing technology and wireless communication[363]. The core of ISAC is to optimize resource allocation and create harmonious synergies between communication and sensing (C&S) by sharing the same spectrum and hardware facilities. With the XL-array deployed in future wireless systems, wireless communication and sensing are expected to operate in the radiative near-field region, shifting from the traditional far-field channel

modeling to near-field channel modeling [313][365]. This region needs to be considered characterized by spherical waves rather than planar waves, a new channel property that will reshape near-field communication and sensing.

In terms of wireless communications, unlike the far-field beamforming steering the beam energy along a specific direction, near-field beamforming based on spherical wavefronts achieves a new function of beam-focusing, which concentrates the beam energy in a given region. This not only enhances the received signal power at the desired user, but also eliminates interference to undesired users. Furthermore, in the far field, users in the same or similar angle cannot be distinguished, and interference between these users is inevitable. In the near field, the BS can focus the beams at different distances, thus reducing interference between users. This effectively improves the DoF of the channel and further increases the system capacity.

In terms of wireless/radar sensing, the spherical wavefront at the XL-array aperture can be utilized to estimate both the target angle and range, thereby reducing the need for distributed arrays and their synchronization. Besides, the enlarged array aperture provides finer-grained spatial resolution in both the angular and range domains. In addition, the near field beam-focusing effect can be exploited to enhance the sensing SNR of echo signals for achieving more accurate estimation. While for other near-field sensing applications such as human-activity recognition, the spherical wavefront provides additional features in the range domain, hence potentially improving the recognition accuracy.

We will introduce the new opportunities and challenges brought by near-field ISAC from three perspectives: sensing-assisted near-field communication, communication-assisted near-field sensing, and joint near-field communication and sensing (JC&S) [315][366].

6.2.2.1. Sensing-assisted Near-field Communication

For near-field communication, beam training is an efficient approach in practice to acquire necessary CSI for establishing initial high-SNR links. However, they generally require much higher training overhead than in the far-field region, due to the required two-dimensional (2D) beam search over both the angular and range domains. For example, one promising approach is to exploit environmental sensing information to reduce the near-field beam search space [315]. Specifically, one can deploy a number of environment sensors in the user zone or along the user trajectory, whose position information is known a priori at the BS and thus can be used as reference location information, as shown in Fig. 6.31. As such, at the beginning of near-field beam training, the sensors around the user notify the BS that the user is present within their sensing range. Then, the BS performs low-cost beam training in a small space to obtain the optimal beamforming. Especially in high mobility scenarios, fully utilizing sensing information to assist near-field beam tracking can effectively reduce communication overhead and improve communication reliability. Then, wireless sensing can also assist in the effective allocation of wireless resources, designing resource allocation based on the sensing of vehicle motion status, and geometric relationships, while considering both communication and sensing performance, so as to provide high-quality services with almost no handover overheads [322].

Compared with the far-field case, the near-field sensing-assisted beam tracking is more challenging, since it tends to cause faster phase variations change over the XL-array. Furthermore, robust radar sensing-assisted beam tracking needs to be designed for near-field scenarios, since

near-field beams achieved by XL-arrays have very narrow beamwidths and are susceptible to beam misalignment.
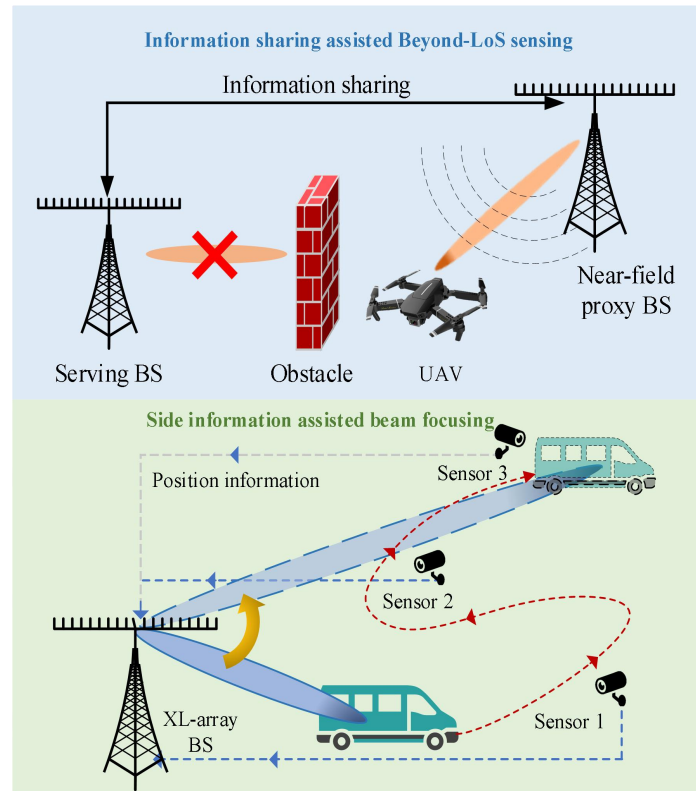
Fig. 6.31 Communication-assisted near-field sensing and sensing-assisted near-field communication.

In mmWave or THz communication systems, where LoS links become the dominant means of signal propagation, one can directly generate the near-field beam aimed at the user by utilizing location information of user (see Fig. 6.32)[320]. This approach bypasses the need for complex beam training processes, leading to reduced signaling overhead and latency. One major challenge in location-based near-field beam focusing is that due to the extremely narrow beamwidth of near-field beams, the beam focusing gain is highly sensitive to positioning accuracy, necessitating ultra-precise positioning techniques. However, conventional 5G positioning techniques relying on time and angle-based measurements typically offer only meter-level positioning accuracy. To address this issue, one can employ visual sensing technologies. Recently, visual sensing technologies, together with computer vision (CV) techniques to analyze visual sensing data, have made significant advancements in performing object classification, detection, and tracking from raw images with the aid of DL. By leveraging visual sensing data acquired from RGB cameras and depth sensors along with radio measurements, the BS can acquire accurate user position with centimeter-level accuracy, using which the near-field beams directed toward the user are efficiently generated.

The fusion of visual sensing technologies and near-field communications extends beyond just near-field beam focusing. Visual sensing data provides not only user position information but also comprehensive contextual information about the surrounding environment such as obstacles, dynamic mobility patterns, and reflective or absorptive surfaces which can significantly impact signal propagation. This integration will facilitate environment awareness, enabling adaptive and real-time services in near-field communications. For instance, by analyzing user trajectories using map data and

predicting the corresponding signal changes, the BS can accurately anticipate future near-field channel conditions. Furthermore, with these predicted near-field channel information, the BS can proactively adjust the near-field beam pattern and reallocate wireless resources to mitigate interference, track near-field beams, and manage mobility. Such proactive network management will prevent sudden radio link failures (RLF) arising from signal obstructions, thereby enhancing reliability and reducing latency in mmWave and THz communication systems.
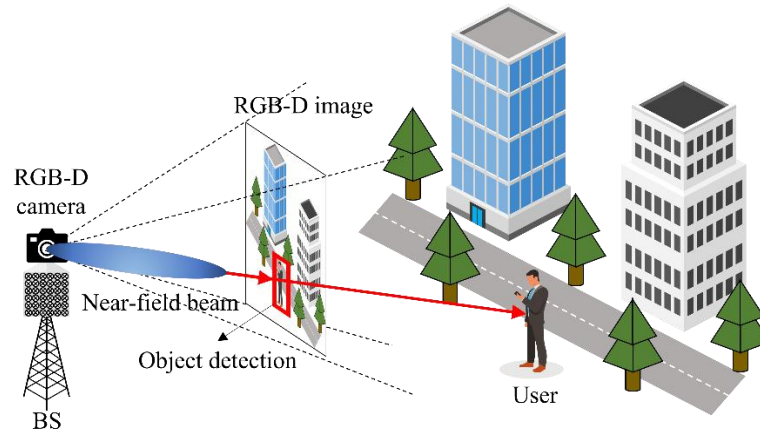
Fig. 6.32 Vision-aided positioning and location-based near-field beam focusing.

6.2.2.2. Communication-assisted Near-field Sensing

Besides sensing-assisted near-field communication, communication functionalities in cellular networks can also be used to assist near-field sensing to improve the sensing range, resolution, accuracy, and reliability. Near-field radar sensing typically relies on the LoS channels between the XL-array and targets, which, however, may not always exist due to random obstacles and environmental scatterers. To tackle this issue, a promising approach is leveraging wireless network architectures to achieve near-field networked sensing through information fusion [323]. First, consider a challenging scenario where the XL-array BS needs to sense a target located beyond its LoS due to obstacles in between, as shown in Fig. 6.31. An effective solution is to delegate the sensing task to a proxy XL-array BS, which is capable of establishing an LoS link to the target in its near-field. By exploiting spherical wavefront propagation, the proxy BS can efficiently estimate the target range and angle without the need of additional anchors as in the far-field case. Then, the proxy BS sends its estimated information to the serving BS, which then can estimate the target location based on the relative positions. In addition, in the near-field sensing system, the fusion of single sensing data collected by multiple BSs can achieve better sensing performance than single-node sensing. The 6G communication architecture is expected to provide a reconfigurable framework to support the need for the transfer of large amounts of sensing data from multiple units to converged centers with powerful computing capabilities.

Next, to further improve the radar sensing performance, an effective approach is to use widely deployed BSs to achieve mixed-field networked sensing for which the target may be located in the far-field or near-field of different BSs. In this scenario BSs can share their obtained angle and range information with each other for jointly estimating the locations and velocities of targets. Among others, an important design issue is how to effectively fuse all information to achieve accurate and

high-resolution localization by taking into account various factors such as sensing SNR, number of XL-array antennas, spatial correlation of proxy BSs.

In mixed-field network sensing, the spatial correlation of proxy BS is a critical issue. Accurately determining the near-field or far-field relationship between a signal source and a BS is essential for channel modeling, beamforming, interference mitigation, and localization. This is particularly important in scenarios where near-field BSs, such as mmWave small cells, coexist with far-field BSs, such as macro BSs. It is crucial to effectively integrate the available information based on the nature of the BS. Fig. 6.33 illustrates a scenario where both a near-field BS and a far-field BS are jointly localizing an UAV.
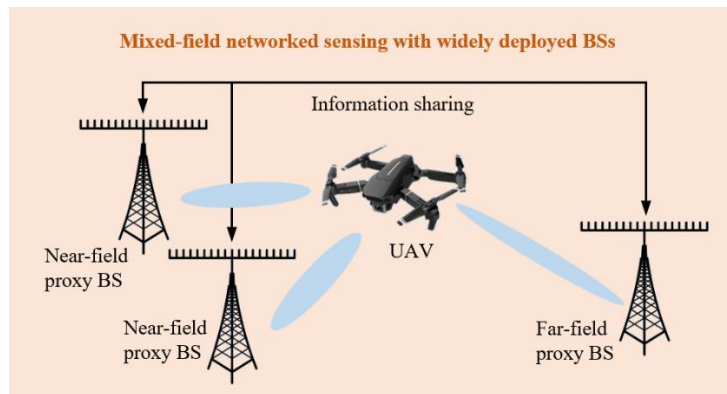
Fig. 6.33 Mixed-field networked sensing with widely deployed BSs.

Distinguishing between the near-field and far-field relationships of target signal sources and BS is crucial for improving localization accuracy. Firstly, it enables the optimization of distance estimation methods—Time of Arrival (ToA) and Time Difference of Arrival (TDoA) are effective in far-field conditions, while wavefront curvature and phase information can be leveraged for more precise distance estimation in the near field. Additionally, the near-field and far-field characteristics significantly impact AoA measurement accuracy. Traditional direction estimation algorithms are suitable for far-field scenarios, whereas near-field conditions require spherical wave modeling to obtain more accurate angular information. By integrating these insights, appropriate localization algorithms can be selected, such as triangulation for far-field environments and beam focusing or polar coordinate methods for near-field positioning[367]. Furthermore, by fusing measurement data from multiple BSs, system robustness can be significantly enhanced.

6.2.2.3.   Joint Near-field Communication and Sensing

For near-field ISAC, one design paradigm is to jointly optimize both C&S performance in a shared system architecture and hardware platform. Therefore, several new near-field effects have to be considered in balancing C&S performance trade-off for both narrow-band and wide-band systems[368]. Consider a narrow-band near-field wireless system, where an ISAC BS equipped with an XL-array simultaneously serves multiple communication users and senses surrounding targets in its near-field region[369]. For JC&S, efficient beamforming designs need to be devised to compensate for severe path-loss in high-frequency bands. Specifically, to enhance near-field communication performance, communication beams should be tuned towards the communication users at fixed locations by exploiting the near-field beam-focusing effect. On the other hand, the beam control for near-field radar sensing generally depends on its estimation aim. For target parameter estimation such as angle and

distance, the sensing beams should dynamically scan the region of interest in both the angular and range domains. To balance the C&S performance, one simple yet effective method is to apply the multi-beam design based on array-partition, which divides the entire XL-array into multiple sub-arrays, each responsible for controlling a sub-beam. However, this method reduces the number of antennas allocated per sub-array; thus, communication users/sensing targets may be located in the far-field of the sub-array, thereby reducing the beam-focusing effect. Therefore, it is necessary to properly determine the number of sub-arrays for C&S services, as well as optimize the antenna allocation for these sub-arrays to strike the C&S performance trade-off.

The spherical wave channel model assumption in the near-field can enhance the measurement accuracy of positioning and sensing. In far-field scenarios, classical positioning depends on the estimation of the RSS based positioning schemes, time of arrival (ToA) and time difference of arrival (TDoA) based positioning estimation methods, and AoA based positioning estimation. Positioning estimation methods based on RSS and ToA are not limited by the transmission and reception beams, and thus, these methods cannot leverage the hardware advantages of massive MIMO in the near-field scenarios. The positioning and sensing techniques based on the AoA are more suitable for the near-field communication systems, where the spherical wave channel model is assumed between the transmitter and receiver. According to the near-field spherical wave channel model, the AoAs of the reflected electromagnetic waves of the sensing target or the positioning signals of the target are different for each antenna. The nonlinear phase characteristics introduced by the spherical wave model are used to obtain the positioning and sensing results. Moreover, the positioning and sensing in the near-field scenarios reduce the requirement for signal bandwidth. References [370] and [371] validate the feasibility of sensing and positioning techniques in near-field scenarios. The experimental results further reveal that the weak correlation between different signal bandwidths and near-field positioning accuracy (ref. Fig. 6.34). Reference [370] further validate the impact of increasing the antenna scale on the sensing accuracy.
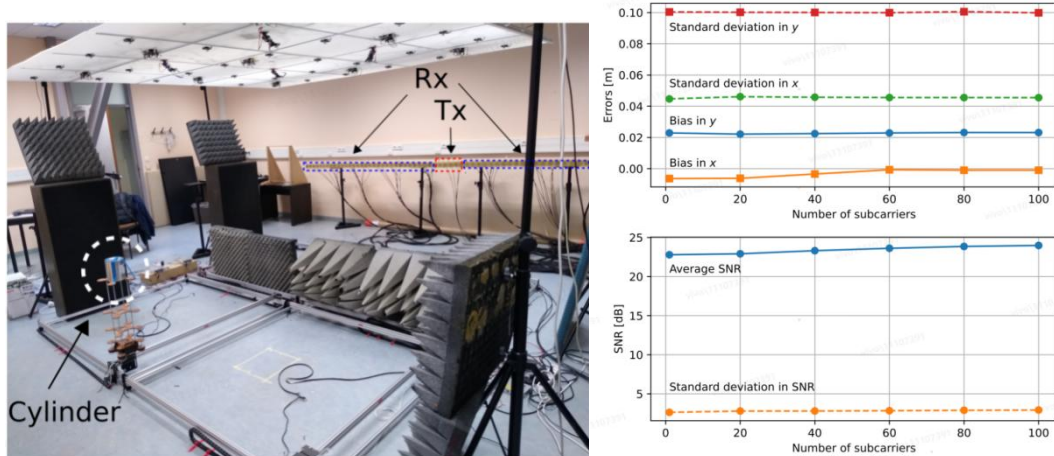
Fig. 6.34 Experimental environment for near-field sensing, and measurement results for sensing accuracy in terms of signal bandwidth [370].

6.3 Wireless Power Transfer in Near Field

WPT technology, capable of wirelessly charging low-power devices, holds significant promise in the 6G era of the IoT. Existing WPT technologies primarily focus on far-field scenarios, leading to lower energy transfer efficiency. In 6G near-field scenarios, the use of near-field spherical wave

propagation characteristics enables beam focusing techniques to concentrate the energy of radio frequency signals around the energy receiver, thereby significantly enhancing the efficiency of energy transfer [372]. Meanwhile, beam focusing technology can effectively reduce electromagnetic pollution and limit human exposure to radiated energy. This capability opens up broader prospects for the future development of wireless energy transfer technology for 6G IoT applications.

6.3.1 Electromagnetic Radiation-Based WPT

With the rapid development of the 5G/6G information age, more and more wireless smart devices (such as mobile phones, laptops, and smart sensors, etc.) bring convenience to people's lives, and these devices are widely distributed in different scenarios, so their energy supply is full of challenges. WPT technology provides a new solution to the charging problem of these mobile devices, as it can avoid complex wires while ensuring efficient and sustainable operation, so that has obvious advantages in security and flexibility, which is an indispensable technology for the future society. The existing near-field WPT mainly adopts electromagnetic induction, electromagnetic resonance, electromagnetic radiation, and other forms [373], among which electromagnetic radiation form can flexibly modulate electromagnetic waves, and carry out the ability of beamforming for different functions, so that is suitable for long transmission distance, multiple targets and different application scenarios. In the WPT system, the receiver of the electromagnetic radiation system can be designed with a smaller aperture, so that it can be fully integrated with different devices and scenarios. As electromagnetic waves can carry both information and energy, WPT technology can be combined with mobile communications and construct the SWIPT system to greatly improve the utilization of electromagnetic waves [374].

6.3.1.1.   Transmitter Design

The electromagnetic radiation-based WPT can generally reach the transmission distance of a meter level, among which the microwave power transfer (MPT) is not affected by weather conditions so that it can work all the time. The transmitter of the system can be the antenna and its array, such as parabolic antenna and microstrip array [375] to improve system performance through advantages such as high gain and low profile. Electromagnetic meta-surface, as a two-dimensional planar structure of electromagnetic metamaterials, is composed of sub-wavelength units, exhibiting electromagnetic characteristics that natural materials do not possess, to achieve flexible modulation of electromagnetic wave's amplitude, phase, polarization, and other dimensions [376], which can be achieved by reflective, transmissive, holographic and other types. By loading the diode or other active adjustable devices on the meta-surface unit, the function of the meta-surface unit can be reconstructed by adjusting the state of the active adjustable device, and the digitally encoded reconfigurable meta-surface can be formed to realize the real-time modulation according to the requirements of specific scenes. To meet the demand for high power levels in the WPT scenario, amplifiers can also be loaded on the meta-surface unit to realize different power level applications. Fig. 6.35 shows the schematic diagram of the adaptive intelligent near-field charging system using a programmable meta-surface [377].
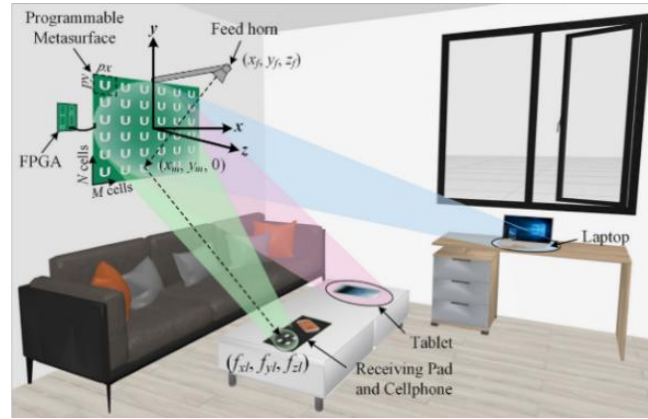
Fig. 6.35 Adaptive intelligent near-field charging system based on programmable metasurface [377].

6.3.1.2. Design of the Energy Transmission Beams

The beamforming technology can be used to distribute the electromagnetic energy at a specific region where the targets are located in the near-field range. Compared with the beams suitable for far-field range such as directional high-gain beams, the focused beam can concentrate the energy into the focal spot, which will significantly improve the receiving efficiency and reduce the aperture of the receiver. If it is necessary to charge multiple targets at the same time, multiple focused beams can be carried out and algorithm optimization can be used to improve beam performance [378]. In addition, the non-diffraction beams can be used to obtain a larger WPT range and a richer beam trajectory than the focused beam based on suppressing divergence. As shown in Fig. 6.36, since the Bessel beam has both non-diffraction and self-reconstruction characteristics, multiple targets can be charged at the same time in the beam's propagation path, thus expanding the multi-target WPT from the 2D range to the 3D range [379]. In addition, Airy beam, Pearcy beam, and other special beams with self-bending characteristics can also be included by non-diffraction beams, they have further self-bending characteristics, reflecting the ability to avoid obstacles to achieve WPT with higher performance [380].
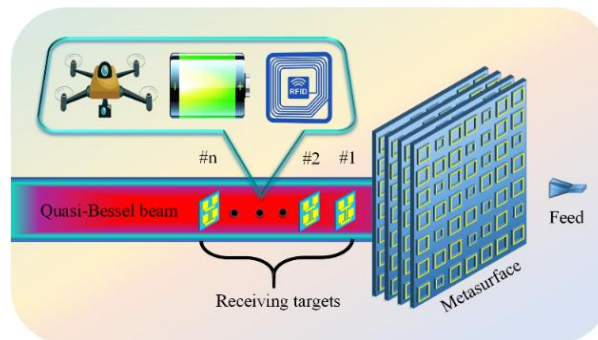
Fig. 6.36 Schematic diagram of multi-target WPT system based on quasi-Bessel beams [379].

6.3.1.3. Adaptive Wireless-Powered Network

The integration of radiative WPT technology shows promising potential to enable mobile terminal tracking and dynamic energy delivery. This necessitates the establishment of position-aware adaptive wireless power supply networks, requiring breakthroughs in two critical technological domains: precise near-field localization and real-time focused beam steering. Metasurface platforms emerge as a viable hardware solution due to their exceptional electromagnetic manipulation capabilities and inherent wireless sensing functionalities. As illustrated in Fig. 6.39, a dual-band information metasurface system

employs frequency-division cooperative operation to achieve simultaneous target localization and energy beam focusing [340]. To enhance positioning efficiency, the STC techniques and CNN-based signal processing are adopted, effectively reducing computational complexity and hardware implementation costs. This synergistic approach enables the metasurface to perform continuous terminal tracking while dynamically redirecting energy beams to maintain optimal power transfer efficiency during target movement. Thereby realize the wireless-power perception, processing and communications. The adaptive wireless-powered network has potentials to addresses the critical power sustainability challenge in ubiquitous connectivity scenarios, effectively bridging the gap between energy availability and mobility requirements in 6G ecosystems.
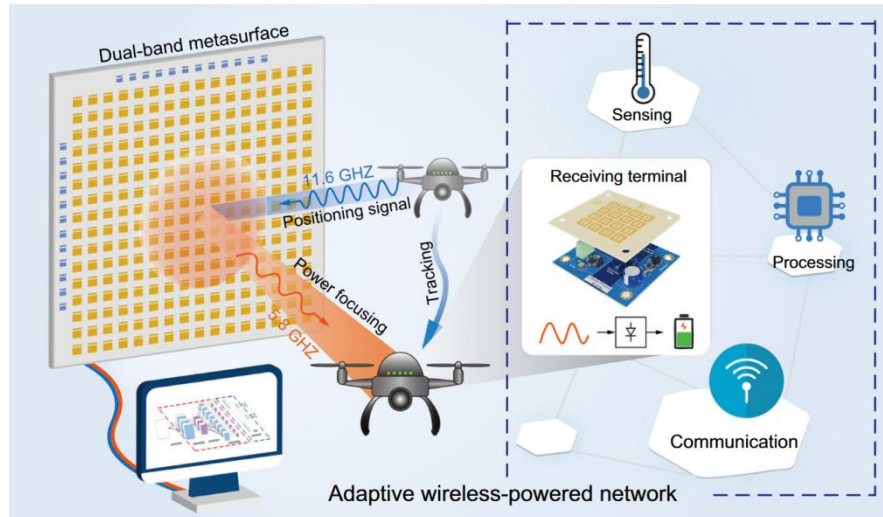
Fig. 6.37 Schematic diagram of adaptive wireless-powered network [340].

6.3.1.4. Receiver Design

The receiver of the WPT system needs to use the antenna and its array or the meta-surface to receive the transmitted electromagnetic energy [381], which is similar to the transmitter. In addition to the installation of a specific power transmitter at the transmitting end, wireless energy harvesting (WEH) can also be performed on energy in the natural environment. With the continuous implementation of concepts such as the Internet of Everything (IoE) [382], the construction of smart cities has increased the electromagnetic energy in the environment, and WEH technology has attracted wide attention because it can avoid the battery replacement of electrical devices such as sensors. After receiving the electromagnetic energy, it also needs to be converted into direct current (DC) energy by a rectifier circuit, and then the energy is stored or supplied to electrical devices. The block diagram of the whole system is shown in Fig. 6.38. Considering that there are also a large number of natural energy sources such as solar, wind, and heat in the natural environment, mixing electromagnetic energy with other forms for energy harvesting will also provide more possibilities for WEH.
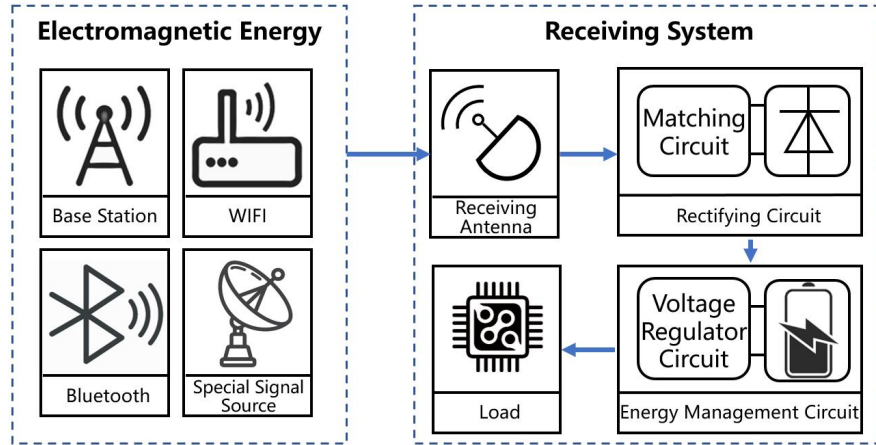
Fig. 6.38 Block diagram of wireless energy harvesting system.

To obtain more abundant electromagnetic energy, the receiving antenna should work in multi-band or wide-band and can receive or transform electromagnetic waves with different polarization. When the subwavelength unit of the electromagnetic meta-surface is used, the stability of the incoming wave's incidence angle and polarization insensitivity characteristic can be further expanded, to comprehensively harvest electromagnetic energy of different frequencies, polarizations, and directions [383]. The corresponding rectifier circuit also needs to be designed in multi-band and should have high efficiency over a large input power range [384][385]. Combining the receiving meta-surface with the rectifying circuit can further form the rectifying meta-surface. As shown in Fig. 6.39, the rectifying meta-surface achieves miniaturization, dual frequency bands, wide incidence angle, polarization insensitivity, and high rectifying efficiency, showing high performance based on removing complex circuit design [386].
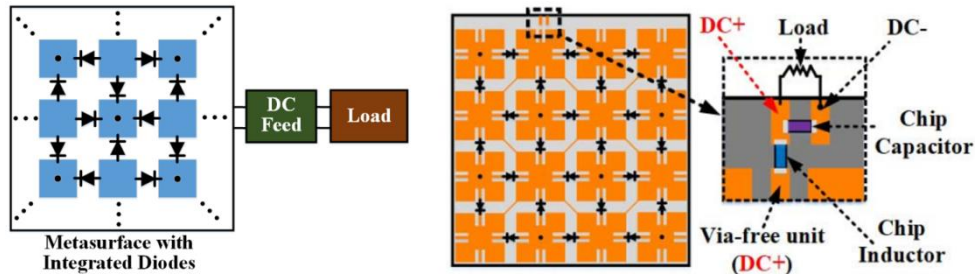
Fig. 6.39 Schematic diagram of the rectifying metasurface.

6.3.1.5. Function Expansion - SWIPT

In addition to carrying energy, electromagnetic waves can also load information, and the combination of the above two functions can form a SWIPT system, which is of great significance for the future scenario of the IoE. In the applications of SWIPT, energy, and information transmission are required to achieve their functions and do not interfere with each other, which has high requirements for the transmitter design, receiver design, and system framework. For this reason, there are systems such as SWIPT systems, wireless-powered communication networks (WPCN), wireless-powered backscatter communication (WPBC) systems [385], and other forms, which divide electromagnetic energy through different dimensions such as time, space, frequency, polarization, etc., to achieve energy transmission and communication functions respectively. Fig. 6.40 shows the SWIPT system based on frequency diversity [387] and polarization diversity [388] respectively. Through the

modulation of the energy ratio of different functions, the application of different beams, and the design of holographic meta-surface and amplifying programmable meta-surface, the energy allocation of energy transfer and information transfer can be balanced to optimize the overall performance of the system.
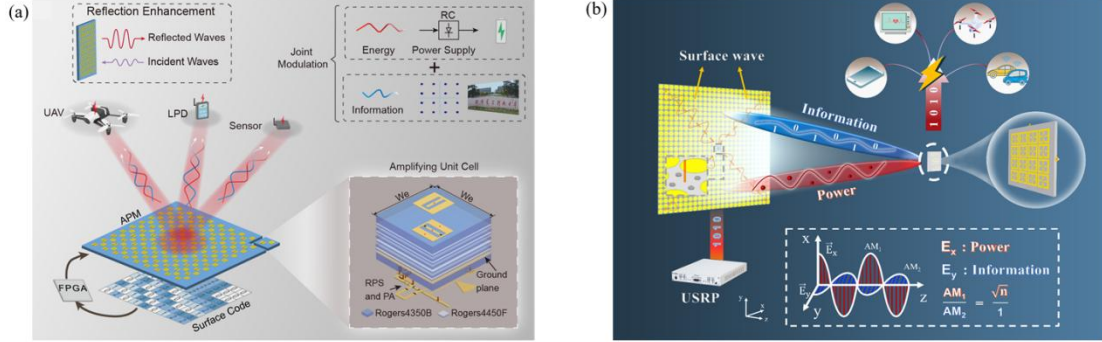
Fig. 6.40 SWIPT systems based on (a) frequency diversity and (b) polarization diversity

6.3.2 Wireless Power Transfer through Power Amplifier

In advanced transmitter systems, the PA has become an increasingly important part of sending data to faraway places by amplifying the RF signal. The PA is a crucial component in the WPT system for 6G communication because it provides outstanding power transfer. The drain efficiency (DE), power added efficiency (PAE), and output power (Pout) of the PA could have a tremendous impact on the efficacy of WPT systems.

In the WPT system, it is challenging to transmit the power efficiently from one end to the other end. While transmitting the power wirelessly from one antenna (at the transmitting end) to the other antenna (at the receiving end), there is a leakage of power. This leakage power generally depends on the input power fed to the transmitting antenna through PA and the received power received at the receiving antenna, as given in (6.7).

$$Leakage power = P_{input} - P_{Received} \tag{6.8}$$

The leakage power can also be formulated as given in (6.8)

$$Leakage power = (1 - \Gamma^2) * P_{input} \tag{6.9}$$

where the reflection coefficient (Γ) is expressed as

$$\Gamma = \left(\frac{Z_{in} - Z_o}{Z_{in} + Z_o}\right) \tag{6.10}$$

by putting the values from (6.8) and (6.9) in (6.7), we get

$$\left(1 - \left(\frac{Z_{in} - Z_o}{Z_{in} + Z_o}\right)^2\right) * P_{input} = P_{input} - P_{Received} \tag{6.11}$$

So, it is essential to find the amount of power transmitted from the transmitting side to the receiving side after the impact of leakage power. To formulate the expression for power transmitted to the receiver, we need to define the equation of other factors on which the WPT depends [390]. These factors are propagation loss (PLoss), absorption loss (ALoss), reflection loss (RLoss), transmission loss

(TrLoss), mismatch loss (MisLoss), transmitter loss (TLoss), medium loss (MLoss), and receiver loss (ReLoss). In the above equations, the values of the transmission coefficient (Tcoefficient), medium attenuation (Mattenuation), and receiver attenuation (Rattenuation) can be preassigned by the user. Then the power received by the receiving antenna can be obtained[391].

- Need of PA for WPT

WPT can be classified as either near-field (operating range Hz to MHz) or far-field (operating range MHz to THz) transmission. In general, near-field power transmission methods are more efficient than their far-field counterparts.

In [391], A switched-capacitor-based stimulator integrated circuit that enables efficient harvesting of RF power for applications involving neuro-stimulation is given. A radiating near-field (RNF) RF harvester containing a rectenna and source/transmitter with a 47.7\% efficiency at 2.4 GHz was developed and produced [392]. A class E amplifier is developed for systems that utilize capacitive coupled wireless power transfer (CCWPT) in the MHz band [393]. Also, Casanova suggested the design and optimization of a Class E PA that utilizes inductive coupling for wireless power technology [394]]. In [395], gallium nitride (GaN) -based class F PA designed at 3 GHz for wireless applications is discussed. A hybrid class E/F3 PA is analyzed and discussed in [396]. On reviewing some of the articles, it is suggested that there is a need for an efficient, high-power PA to perform WPT from the transmitter to the receiver associated with a bio-implant device.
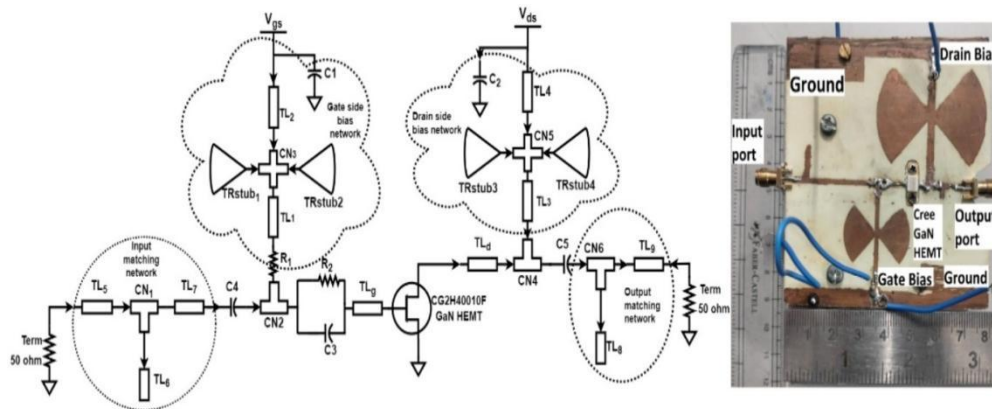
Fig. 6.41 Representation of schematic with the fabricated view of the developed PA.

A Class F^{-1} PA is designed by keeping load impedance with the even harmonics as open-circuited and odd harmonics as short-circuited [397]. Following the optimization of the transmission lines (TL) dimensions, a 10-W Cree CG2H40010F [398] GaN-based class F^{-1} PA is designed at 4.6 GHz with the operating point (Vgs = -2.7 V and Vds = 28 V). The schematic of GaN-based class F^{-1} PA with the utilization of optimized values of design parameters of microstrip TLs is shown in Fig. 6.41. The harmonic balance simulation is performed to check the small and large signal parameters of the proposed PA. The transient response of current-voltage (I-V) waveforms of the developed class F^{-1} PA is represented in Fig. 6.39, having voltage as half sinusoidal and current as a square waveform in nature.
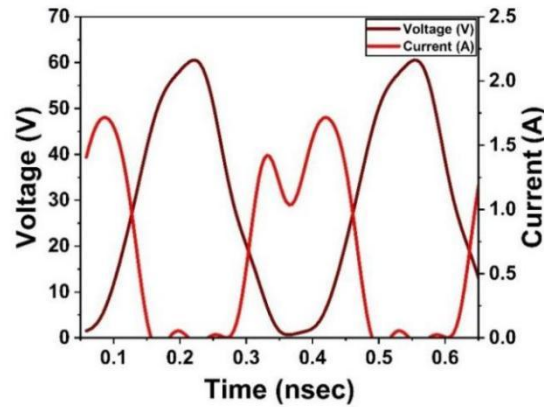
Fig. 6.42 Simulated IV curve of 10-W PA at 28 dBm input power.

The actual area of the whole PA is 88 mm × 80 mm. We have utilized a driver amplifier [397] of 17 dB gain, a signal generator (N5172B), a spectrum analyzer (N9020A), an attenuator (BW-S40W20+) from mini-circuits, a 3 dB coupler, a power sensor, and a DC power source. The measured results of the suggested PA show that both DE and Pout have an effective value (in Fig. 6.40 (a) and Fig. 6.40 (b). All other parameters are compatible with the requirements of such a type of PA for WPT. Also, this proposed PA follows the safety and regulatory guidelines required for performing WPT for 6G communications.
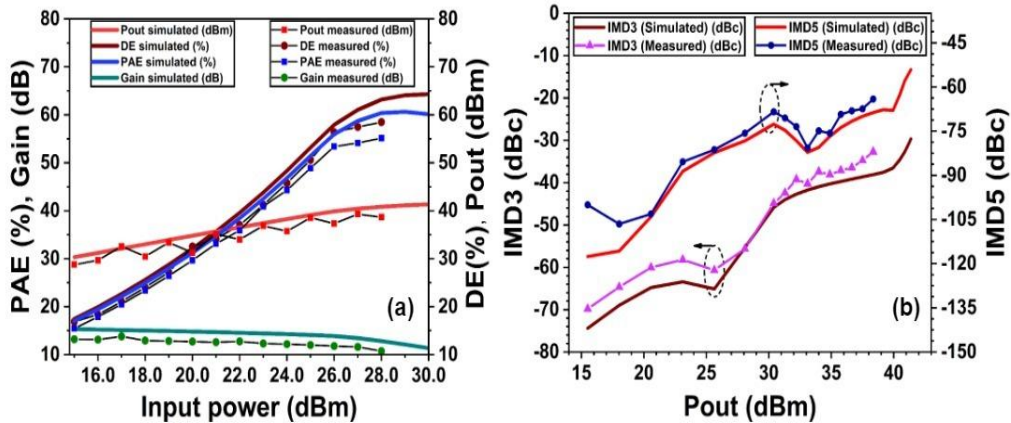
Fig. 6.43 Obtained results of (a) PAE, Pout, DE, and Gain (b) IMD3 and IMD5 w.r.t Pout of PA

6.3.3 Far/Near-Field SWIPT

Apart from serving as information carriers, wireless signals can also facilitate energy WPT employs microwave signals for energy transmission which enables the capability to charge low-power devices. WPT has found extensive application as a cable-free alternative for charging devices in diverse environments, including mobile edge computing, rapid data aggregation, mobile crowd sensing, and ISAC. As shown in Fig. 6.44, near-field SWIPT emerges as a promising technology capable of wirelessly transmitting both data and power simultaneously. In this scenario, the reception of both information and power can be carried out through either time switching or power allocation [401]. The integration of information and energy transmission eliminates the requirement for separate power or wired connections, enhancing the flexibility, mobility, and convenience of devices. Thus, SWIPT has the potential to bring about a revolutionary impact on various industries and applications.

Although most of the existing work considers either near-field or far-field communication, it is probable that a hybrid communication model will arise, incorporating both near-field and far-field users within the system [402]. This indicates that in typical communication scenarios, users may be located in near-field and far-field regions at a distance from the BS, leading to more complex interference problems. Specifically, in [402], due to the energy diffusion effect, the authors reveal a noteworthy phenomenon that when the spatial angle of the far-field beam based on the DFT is in the vicinity of the far-field user's angle, the near-field user may suffer from strong interference from the far-field beam. On the other hand, this power leakage phenomenon can also be used to benefit the near-field users, leading to new application scenarios for SWIPT with mixed fields.

In [401], a new practical scenario i.e., hybrid near-field and far-field SWIPT is considered, where the energy harvesting (EH) and information decoding (ID) receivers are located in the near-field and far-field regions of the BS that is equipped with an ultra-large-scale array, respectively. Specifically, a weighted sum power harvesting maximization problem subject to ID sum rate and BS transmit power was formulated by jointly designing the BS beamforming scheduling and power allocation. To efficiently solve this non-convex optimization problem, binary variable elimination and successive convex approximation methods were proposed to obtain a suboptimal solution.

In THz-based SWIPT system or RIS-assisted SWIPT system supported by multi-BS/multi-RIS fitted with ultra-large scale antenna arrays, the introduction of distinct channel models and beam splitting gives rise to the presence of mixed near/far fields. In this case, it is necessary to collaborative scheduling of beamforming along all BSs during the power allocation design [403]. Most studies on THz-based or RIS-aided SWIPT systems have primarily concentrated on optimizing the beam design of either the BS or RIS to fulfill the system's performance requirements. With the application of ultra-large scale array antennas, the THz channel model and beam splitting characteristics will change, resulting in traditional beam design/transmission schemes no longer being practical. Therefore, under the hybrid near/far field model, it is necessary to design a low-power and high-performance SWIPT system, in terms of transceiver structure/RIS structure, power allocation method and energy/information transfer protocol design.
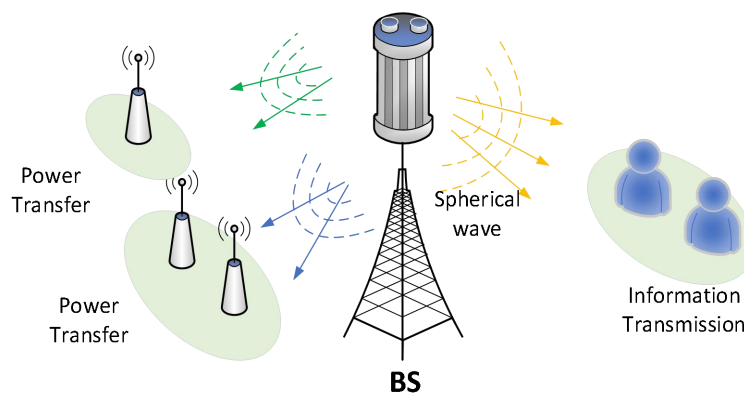
Fig. 6.44 Near-Field SWIPT.

6.3.4 Holographic SWIPT

6.3.4.1. Continuous-Aperture SWIPT System

With the development of metamaterials, reconfigurable holographic surface (RHS) with subwavelength spacing antenna elements can achieve nearly continuous antenna apertures and thus have powerful electromagnetic manipulation capabilities [404]. Imagine a SWIPT system that makes full use of the propagation characteristics of electromagnetic channels to achieve maximum energy aggregation for energy users and maximum interference cancellation for information users, so as to infinitely approach the performance limit of SWIPT. This is the concept of holographic SWIPT [405].

For near-field communication scenarios, the information user is still in a position relatively far from the transmitter, and its distance to the BS is usually considered to be much larger than the aperture of the antenna array. Based on the Fresnel approximation, the near-field channel model is usually simplified by using the Taylor series expansion of the first or second order

$$\sqrt{1+x} = 1 + x/2 - x^2/8 + 0\left(x^2\right)$$

[406]. However, for SWIPT, the energy user has a high probability of being located in the area very close to the transmitter, and the error of the near-field channel based on the Taylor series expansion will degrade the performance of SWIPT. Therefore, it is necessary to adopt a more accurate electromagnetic channel model [407]:

$$\mathbf{G(r,s)} = \frac{i\kappa Z_0}{4\pi} \frac{e^{i\kappa\|\mathbf{p}\|}}{\|\mathbf{p}\|} \left[\left(\mathbf{I}_3 - \hat{\mathbf{p}}\hat{\mathbf{p}}^H\right) + \frac{i}{\kappa\|\mathbf{p}\|}\left(\mathbf{I}_3 - 3\hat{\mathbf{p}}\hat{\mathbf{p}}^H\right) + \frac{1}{(\kappa\|\mathbf{p}\|)^2}\left(\mathbf{I}_3 - 3\hat{\mathbf{p}}\hat{\mathbf{p}}^H\right) \right].$$

(6.12)

where $\mathbf{r}$、$\mathbf{s}$ are the position coordinates of the points in the transmitting region and receiving region, respectively. $\mathbf{p} = \mathbf{r} - \mathbf{s}$. The latter two terms correspond to evanescent waves that propagate only over the metamaterial surface and become negligible at distances of a few wavelengths. The former term corresponds to the radiation field, and the well-known Fresnel zone is further divided in the first term based on the Fresnel approximation.
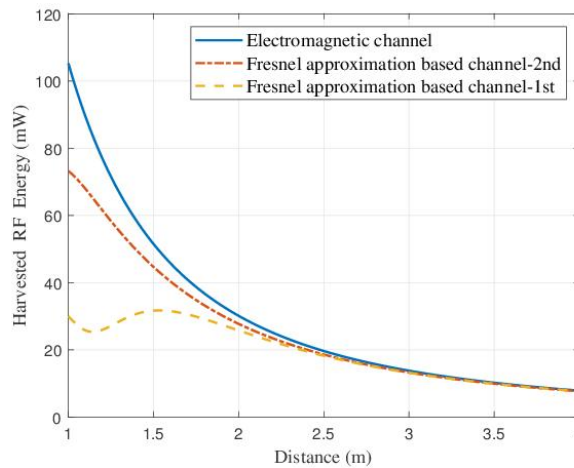
Fig. 6.45 Continuous-aperture RHS-based WPT performance [405]

A holographic metasurface with a length of 1.5m and a width of 0.5m is considered in reference [405], and the single-energy user is located on the central axis of the continuous-aperture RHS. It can be seen from Fig. 6.45 that the energy user can harvest more energy under the electromagnetic channel model. As the distance from the transmitter increases, the error of the near-field channel model under

the Fresnel approximation decreases gradually, so as to obtain the same WPT performance as the electromagnetic channel.
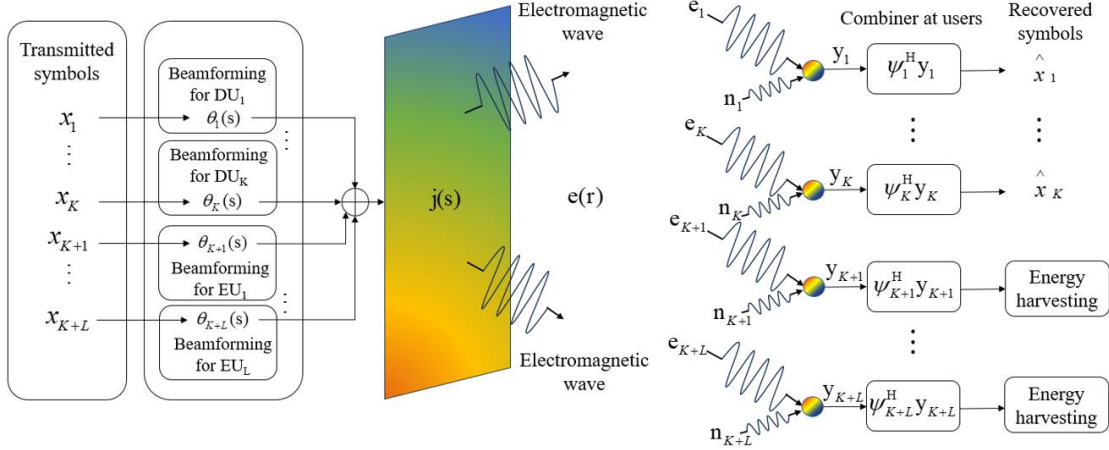
Fig. 6.46 Continuous-aperture RHS-based SWIPT transceiver [405]

For the multiuser SWIPT scenario, a careful design of the current on the continuous-aperture RHS is required to implement holographic SWIPT, including the amplitude, phase, and polarization direction of the current. In order to meet the trade-off between communication and WPT, the electromagnetic waves carrying information of different users are focused at the energy user and orthogonal at the information user as much as possible. A holographic SWIPT system is considered in [405], where the transmitter and multiple information users and energy users are equipped with holographic metasurfaces. Specifically, an optimization problem is designed to maximize the sum-rate of the information users while satisfying the energy harvesting requirements of the energy users. To solve this non-convex optimization problem, continuous-aperture RHS beamforming schemes are proposed based on block coordinate descent and successive convex approximation.

6.3.4.2. Discrete-Aperture SWIPT System

Continuous-aperture holographic metasurface offers the theoretical limit for SWIPT. However, as an idealized model, continuous-aperture metasurface is challenging to fabricate in practice. To address the practical limitations, the discrete-aperture RHS are employed to approximate the performance of their continuous-aperture RHS, achieving superior beam focusing in the near-field scenarios. As shown in Fig. 6.47, the RHS is composed of numerous dynamically tunable metamaterial elements [408]. The current signal output from the RF chain is first converted into electromagnetic waves through the feeds, becoming the reference wave. Then, the reference wave propagates along the waveguide. At each slot, it transforms into leaky waves and radiates into the free space. By controlling the radiation amplitude or phase of each element through diodes or liquid crystals, the holographic beamforming can be designed following the optical holography principles, enabling adjustable beamforming. The discrete-aperture RHS-based SWIPT transmitter is shown in Fig. 6.48. At the BS, the digital beamforming is first performed. Then, the digital signals are converted to analog signals through the RF chains and are driven by the nonlinear power amplifiers. As a result, the current signals are input into the discrete-aperture RHS for transmission. The discrete-aperture RHS leverages the propagation distance differences from the feeds to each element to generate phase shifts and employs tunable circuits to create holographic beamforming. This approach eliminates the need for numerous phase shifters, significantly reducing the fabrication cost of transceiver arrays.
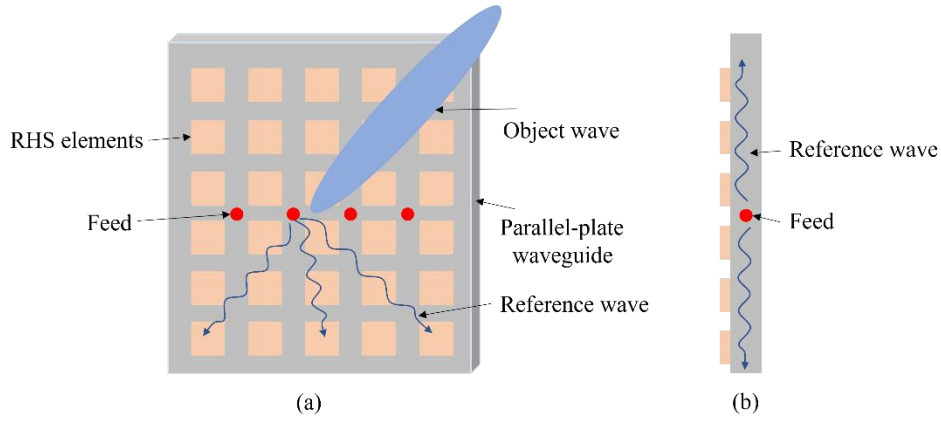
Fig. 6.47 (a)The front view of discrete-aperture RHS；(b)The right view of discrete-aperture RHS.
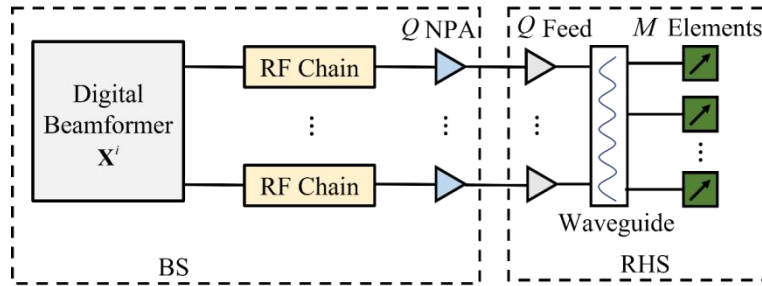
Fig. 6.48 Discrete-aperture RHS-based SWIPT transmitter.

In a pure near-field SWIPT scenario, considering an ultra large-scale discrete-aperture RHS with sufficiently large antenna aperture, the data users and energy users are situated within the near-field region. Therefore, the dedicated near-field beamforming needs to be designed for improving the SWIPT performance. The discrete-aperture RHS offers three beam control schemes [409]: 1) **Discrete amplitude control:** By controlling the on-off state of each element, the holographic beamforming design is achieved; 2) **Continuous amplitude control**: By adjusting the radiation amplitude of each element on the discrete-aperture RHS, the holographic beamforming design is implemented; 3) **Lorentz-constrained phase control**: By manipulating the phase shift of each element, the holographic beamforming design is realized. Through the precise design of the amplitude or phase of the discrete-aperture RHS elements, the optimal near-field beam focusing can be achieved, which leads to the optimal SWIPT performance. The SWIPT performance of three types of discrete-aperture RHS, i.e., continuous amplitude control-based discrete-aperture RHS, discrete amplitude control-based RHS and Lorentz-constrained phase control-based discrete-aperture RHS, are compared in Fig. 6.49, where the Lorentz-constrained phase control scheme achieves the optimal SWIPT performance. It can be observed that the continuous and discrete amplitude control schemes exhibit nearly identical SWIPT performance. This indicates that when the number of elements is very large, these two types of discrete-aperture RHS have the same beam control capability. Therefore, using the lower-cost discrete amplitude control-based discrete-aperture RHS can achieve the same SWIPT performance as the continuous amplitude control-based discrete-aperture RHS.
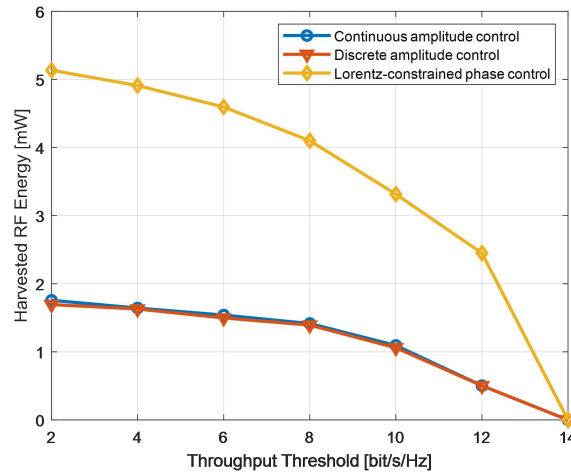
Fig. 6.49 The trade-off between the WIT and WPT performance of the discrete-aperture RHS-based transceiver.

Considering that the number of elements in the discrete-aperture RHS is extremely large, the scale of the holographic beamforming optimization problem is significantly larger, which is difficult to be solved efficiently. By considering the sparsity of wireless channels[410], the spatial orthogonality of near-field channels can be leveraged to design analog beamforming, which simplifies the holographic beamforming optimization problem and enables practical deployment. The RHS provides a cost-effective and energy-efficient solution for near-field SWIPT.

6.4 Physical Layer Security in Near-Field

6.4.1 Design of Near-Field Physical Layer Security

The broadcast nature of wireless channels exposes wireless signals to free space and makes them susceptible to eavesdropping by malicious eavesdroppers. To solve this problem, researchers have proposed the concept of physical layer security (PLS). PLS is able to utilize the physical characteristics of the wireless channel (e.g., interference, fading, noise, directionality, and discreteness) to enhance the security of the communication, thus avoiding the complexity of the generation and management of the secret key and compensating for the shortcomings of cryptography.

In order to meet the demand for dramatically increasing data rates in 6G networks and beyond, emerging technologies such as mmWave, THz, and ultra-massive multiple-input-multiple-output (UM-MIMO) are being researched incessantly. The realization of most of these techniques relies on extremely large-scale antenna arrays and tremendously high frequencies. However, deploying extensive antenna arrays and utilizing very small wavelengths substantially extends the Rayleigh distance. This extension leads to a noteworthy expansion of the near-field range, highlighting the imminent need for research in the near-field region of wireless communications.

The Rayleigh distance functions as a vital metric for distinguishing between far-field and near-field transmissions, generally, transmissions ranges beyond the Rayleigh distance are assumed to be conventional far-field plane waves. When the wireless transmission occurs within the Rayleigh distance, the conventional assumption of far-field plane waves becomes obsolete, instead, near-field effects come into play, prompting a shift in the transmission model towards a more accurate representation using spherical waves. Conventional far-field wireless communication scenarios

typically use plane-wave channel propagation models [415], which limit the security gains offered by spatial beamforming for near-field communication. As shown in Fig. 6.50, in near-field communication scenarios, when the eavesdropper is located between the BS and the legitimate user, its channel is highly correlated with the legitimate channel in terms of angle and is difficult to distinguish. Therefore, in near-field secure communication, the crucial factor is the substantial difference in distance between the legitimate user and any potential eavesdropper. The EM propagation in near-field communication is explained by the spherical wave channel model [416]. In contrast to the plane wave model, this model incorporates both direction and distance information of the receiver. This feature enables the antenna array to concentrate its beam on a specific point in free space, a phenomenon known as beam focusing. Therefore, near-field communication can leverage the additional dimension of distance to achieve more precise signal enhancement and effective interference management in wireless networks.
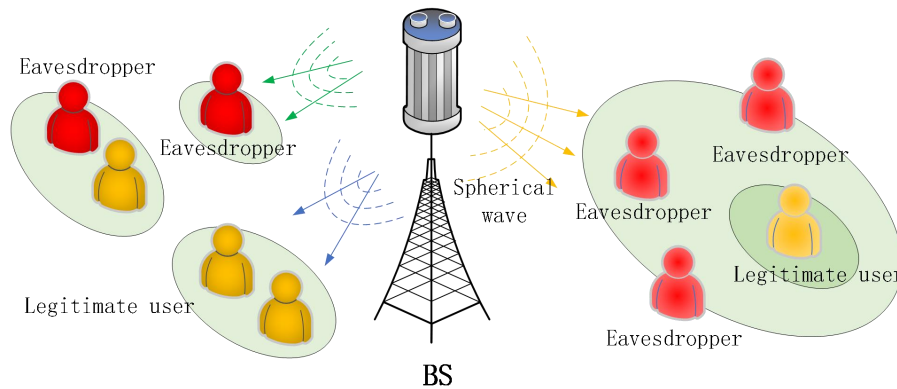
Fig. 6.50 Near-Field PLS.

Currently, studies have initiated to utilize the distance dimension in the spherical wave channel model to enhance communication security [417], however there is still a lack of research on secure beam focusing schemes for MIMO networks. In addition, the large-scale antenna arrays and full-digital beamforming structures commonly used in near-field MIMO communications result in a substantial hardware cost, so exploring cost-effective beam-focusing schemes for secrecy MIMO networks has become a current research priority. In this background, a novel near-field secure transmission framework can be used to securely transmit information to a user via a BS in response to the presence of a potential eavesdropper. When the eavesdropper is located between the user and the BS, a secure beam focusing technique based on a hybrid beamforming architecture can be used to effectively reduce the RF link overhead. It has been shown that the security rate can be further improved even the eavesdropping user is closer to the BS compared to legitimate user in near-field communication [418]. Therefore, in near-field PLS communication, its secure communication performance mainly depends on the distance between the eavesdropping user and the legitimate user, rather than the distance between the eavesdropping user and the BS.

6.4.2 Near-field secure wireless communication with delay alignment modulation

Motivated by the super spatial resolution of XL-MIMO and the multi-path sparsity of mmWave/THz channels, a novel transmission technology termed delay alignment modulation (DAM) was recently proposed to address the ISI issue in [419]. The key idea of DAM is path delay pre-/post-compensation and path-based beamforming. In particular, the unprecedented spatial

resolution of XL-MIMO and ISAC endow the transmitter/receiver with the capability of extracting the features of each multi-path, e.g., AoA/AoD, propagation delay, and Doppler frequency [420]. In this context, by judiciously performing delay pre-/post-compensation matching the respective multi-paths, and in conjunction with path-based beamforming, DAM enables all multi-path signal components to reach the receiver concurrently and constructively. As a result, the original time-dispersive channel can be transformed into the simple AWGN channel, yet free from the sophisticated channel equalization or multi-carrier transmissions. Besides the perfect DAM targeting for zero delay spread, the generic DAM technique was further developed in [420] for manipulating the channel delay spread to a certain value, which enables a flexible framework for efficient single- or multi-carrier transmissions. Furthermore, to address the Doppler shift and ISI issues in the more general time-variant frequency-selective channels, DAM can be extended to delay-Doppler alignment modulation (DDAM) to achieve the Doppler-ISI dual mitigation [421][422], where the time-variant frequency-selective channels can also be transformed into time-invariant ISI-free channels.

In addition to the ISI issue caused by the multipath propagation, the open and broadcast nature of wireless environment renders legitimate communications susceptible to malicious eavesdropping and attacks. In particular, DAM achieves ISI elimination at the desired receiver, while for other locations with different spatial signature from the receiver, it inherently causes ISI. Such an ISI may play the same role as the AN to degrade the eavesdropping link without sacrificing the transmit power, rendering DAM quite promising for secure transmissions [423]. Specifically, as shown in Fig. 6.51 a near-field secure wireless communication with the transmitter-side DAM is considered, where the transmitted signal of Alice is [423]

$$\mathbf{x}[n] = \sum_{l=1}^{L_{\mathrm{B}}} \mathbf{f}_l s[n - \kappa_l],$$

(6.13)

where L_{B} denotes the number of multi-paths between Alice and Bob, $\mathbf{f}_l$ denotes the path-based beamforming, and $\kappa_l \geq 0$ is the deliberately introduced delay for the symbol sequence, with $\kappa_l \neq \kappa_{l'}, \forall l \neq l'$, as illustrated in Fig. 6.51 .
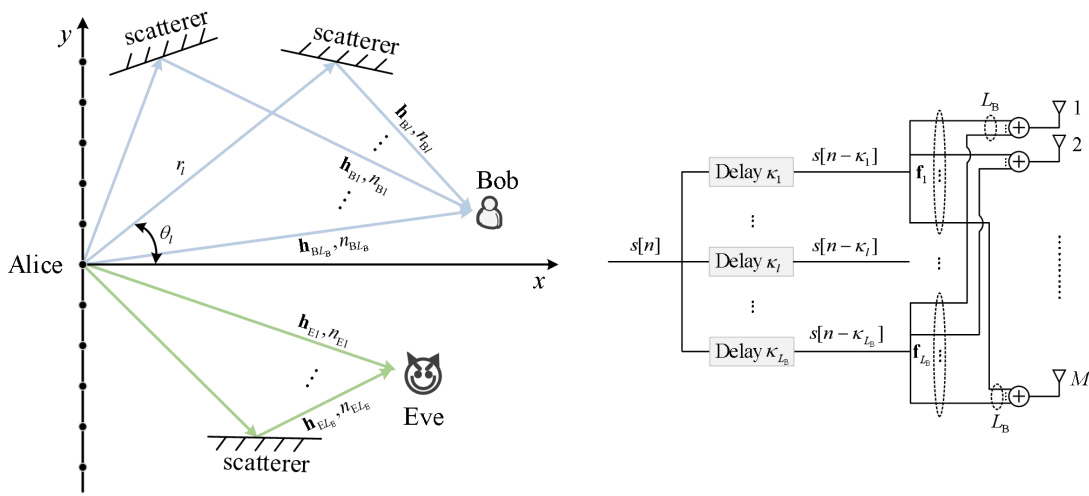
(a) A near-field secure communication system   (b) Transmitter architecture for DAM
Fig. 6.51 Near-field secure wireless communication with DAM.

For the asymptotic case, when the antenna number of Alice is much larger than the number of multi-paths for Bob and Eve, the near-field channel vectors tend to be asymptotically orthogonal, as shown in Fig. 6.52. This eases the requirement for different channel vectors with distinct AoDs in the far-field region, thanks to the super-spatial resolution brought by XL-ULA. Thus, without relying on the CSI of Eve, DAM is able to achieve an "ISI- and information leakage-free communication" with delay pre-compensation and low-complexity path-based Maximum Ratio Transmission (MRT) beamforming.
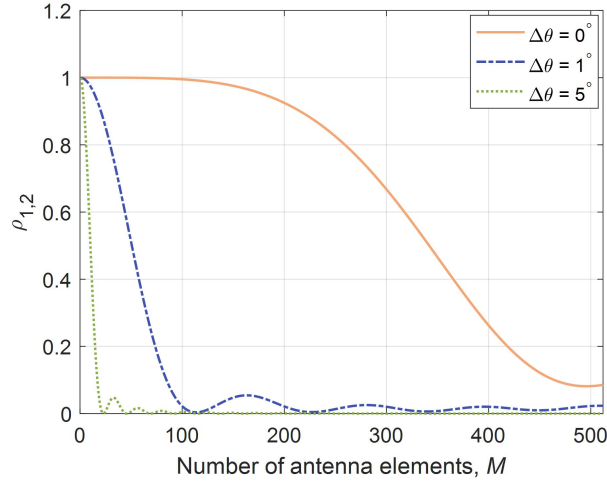
Fig. 6.52 The absolute square of the normalized inner product for two near-field channel vectors, where $(r_1, \theta_1) = (30 \text{ m}, 0°)$ and $(r_2, \theta_2) = (45 \text{ m}, \theta_1 + \Delta\theta)$.

Fig. 6.53 shows the secrecy rate versus the number of antenna elements M for the DAM transmission and AN-based OFDM schemes. It is observed that compared to the AN-based OFDM scheme, the two DAM beamforming schemes achieve considerable gain, which is due to the following two reasons. On the one hand, compared to the OFDM scheme that inserts a CP at each OFDM symbol, DAM is able to significantly reduce the guard interval overhead. On the other hand, DAM secure transmission inherently introduces the ISI to Eve, which saves the power allocating to the AN. This can be reflected by the observation that the DAM secure transmission is still superior to AN-based OFDM when the impact of CP overhead is excluded.
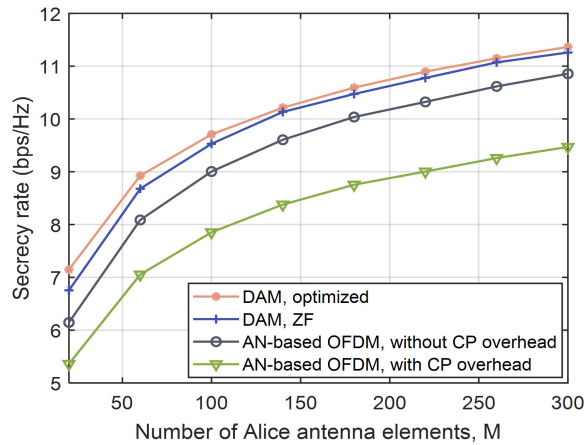
Fig. 6.53 Secrecy rate versus the number of antenna elements at Alice.

6.4.3 RIS Empowered Near-field Physical Layer Security Transmission Design

Due to the characteristics of the double-fading effect in reflective cascaded channels and high path loss in the high-frequency band, the performance improvement of traditional RIS-assisted wireless communication is limited. Considering that the RIS array gain is proportional to the square of the number of reflection elements, increasing the number of RIS elements can effectively compensate for the severe double-fading effect in cascaded channels. Therefore, traditional RIS is evolving towards extremely XL-RIS. XL-RIS-assisted communication systems are more likely to establish near-field communication, where the distance between the transmitter and XL-RIS, or XL-RIS and the receiver, is less than the Rayleigh distance, allowing XL-RIS-assisted wireless communication systems to operate in the near-field region [35].

In far-field covert communication systems, positive covert communication rates cannot be achieved when the warden and the legitimate receiver are at the same direction and the warden is closer to the XL-RIS. Near-field communication systems have DoFs in both angle and distance, whereas distance freedom allows covert communication systems to achieve positive covert rates in the above scenario. The authors in [424] studied an XL-RIS-assisted near-field covert communication system. In this study, the achievable covert rate is maximized by optimizing the BS's hybrid precoding and the reflection coefficient matrix of the XL-RIS. A beam diffraction pattern is also revealed in this study, i.e., a transitional state between beam steering and beam focusing. Fig. 6.54 shows the normalized heatmap of beam diffraction, with XL-RIS located at coordinates (0,0). It can be observed that the beam first splits and creates a null region at the warden and then converges at the legitimate receiver, Bob. The beam diffraction phenomenon can be extended to XL-RIS-assisted multi-user systems, NOMA systems, and enhance near-field physical layer security.
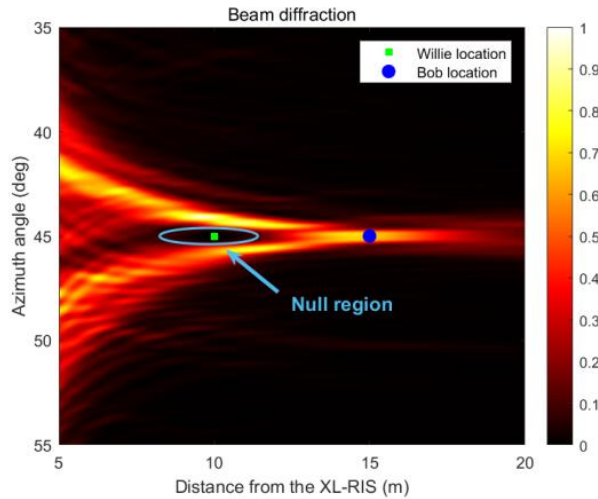
Fig. 6.54 Beam diffraction in near-field.

6.4.4 Near-field Physical Layer Secure with Beam Focusing Effect
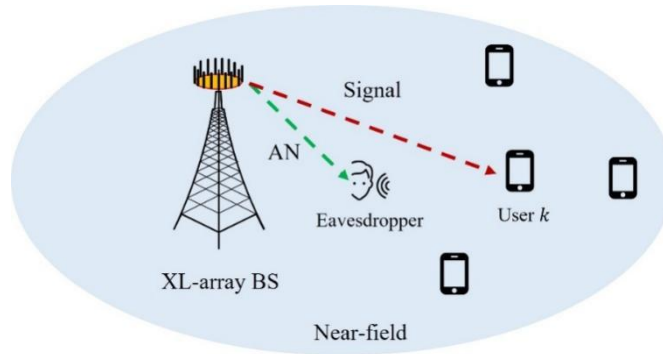
Fig. 6.55 A near-field PLS system.

This beam focusing effect can also be leveraged to reduce the information leakage from both the angular and distance domains, thereby effectively safeguarding the legitimate information transmission. However, most of the existing works either numerically demonstrated the performance improvement by exploiting the beam focusing effect or directly applied conventional far-field designs to near-field secure transmission. This thus fails to fully unveil the potential of near-field PLS, highlighting the need for more in-depth research on the sophisticated secure transmission design. For example, AN has been extensively utilized in conventional far-field secure communications for PLS enhancement, which is designed deliberately to impair the channel of the eavesdropper while at the same time having a limited effect on the signal-to-interference-plus-noise ratio (SINR) at the legitimate users. However, it still remains unknown whether AN is advantageous to the near-field beam focusing-based PLS, and the analytical secrecy performance characterizations of near-field PLS remain lacking. More specifically, the following aspects are worthy of investigation: 1) whether the AN can utilize the beam focusing property embedded in near-field spherical wavefront; 2) under what conditions is AN most beneficial. To answer these questions, the authors of [425] studied the security provisioning for a near-field communication system, where the BS equipped with an XL-array transmits confidential information to multiple near-field legitimate users in the presence of one near-field eavesdropper. Several insightful observations are provided for the case with one legitimate user and one eavesdropper involved. In particular, it is shown that incorporating AN into the beam focusing-based PLS can bring two prominent benefits. On the one hand, AN is essential to security provisioning, being capable of transforming an insecure system into a secure one. On the other hand, we reveal an interesting fact that allocating only a small proportion of power to AN can lead to significant security gain enhancement compared to the case without AN taken into account.

6.5 Near-Field Based OAM

Wireless communication technology carries information through the frequency, amplitude, phase, polarization, and other dimensions of electromagnetic waves, but the linear momentum and its combined application are limited by the existing dimensions, and it is difficult to achieve significant efficiency improvement. As a new technology for next-generation mobile communication, orbital angular momentum (OAM) has the property different from that of electromagnetic wave radiative linear momentum and is expected to be used to expand the communication dimension, which can be

used to transmit data or as a new DoF to control beam, to increase communication capacity and improve system performance.

6.5.1 OAM and Vortex Waves

OAM is an inherent physical quantity of electromagnetic wave belonging to angular momentum, and electromagnetic wave carrying OAM can be called electromagnetic vortex wave (also known as vortex wave or vortex beam) [426]. Compared with conventional plane waves, vortex waves have helically distributed phase wavefronts and can be distinguished by the periodicity of the helical phase, which is also embodied as their intrinsic modes. In theory, the OAM carried by vortex waves has an infinite variety of mutually orthogonal modes, which can be used as a new physical dimension independent of time, frequency, polarization, and other DoFs. As spectrum resources are increasingly scarce and the communication rate is close to the limit of Shannon's theorem, OAM shows important research and application value in wireless communication, imaging, detection, and other fields.

OAM differentiates the space resources in the same direction, provides a new dimension, and realizes the high DoF spatial multiplexing transmission under LOS channel without multipath, so that can solve the problem of limited multiplexing layer number of single users in high-frequency LOS channel. OAM greatly improves channel capacity and spectral efficiency by expanding new dimensions, its mode orthogonality can be used for interference elimination (such as inter-cell interference, upstream and downstream interference, full-duplex self-interference, etc.), and can be used to enhance communication security and avoid eavesdropping.

The technology based on OAM has a wider application prospect in the future of wireless communication. The characteristics of OAM apply to microwave wireless backhaul links, achieving more efficient and high-speed wireless self-backhaul, effectively reducing the construction cost and laying difficulty of optical fiber, and improving the flexibility of network deployment. OAM has high spectral efficiency, realizes high-speed data interaction, and can support 6G new scenarios such as digital twin domain and intelligent interaction. In addition, OAM can be used for point-to-point high-speed communication and short-distance single-user ultra-high-rate data transmission. OAM technology in near-field transmission can make full use of the high DoF of the LOS channel and reduce OAM mode crosstalk caused by multipath. The application of OAM is more suitable for high-frequency communication, as the probability of near-field transmission is significantly increased at this time, the combination with high-frequency architecture is a development trend of OAM technology in the future.

The generation, modulation, reception, and detection of vortex waves are the basis of its practical application. To realize the phase factor of $e^{jl\Phi}$ corresponding to the spiral phase of vortex waves (where j is the imaginary unit, l is the OAM mode of the vortex wave, and Φ is the spatial azimuth angle), the UCA or a reasonably optimized UCA model should be formed using generation devices. The existing methods can be used in the form of spiral phase plates, antenna arrays, single antenna, electromagnetic meta-surface, etc. At the receiving end, the beam can be received by the receiving device corresponding to the transmitting end. If the OAM mode needs to be detected, the Fourier transform relationship between the spatial azimuth domain and the OAM mode domain can be used to analyze the OAM mode spectrum of the vortex wave based on the Fourier transform principle and sampling theorem.

6.5.2 Near-Field Modulation of Vortex Beams

The propagation environment is usually uncontrollable, and the reflection, scattering, and refraction caused by obstacles will affect the LOS channel and destroy the orthogonality of modes. The multipath effect is significantly reduced in near-field transmission, which better guarantees the orthogonality between OAM modes, reduces beam diffusion, realizes the expansion from SU to MU, and supports the simultaneous transmission of multiple users.

The traditional vortex beam has obvious divergence characteristics, so the application of long distance is often limited, and it is easier to make use of its advantages in the modulation of vortex beams in the near field region. The modulation for vortex beams in the near-field has also become a key technology in the research and application of OAM. In particular, the non-diffraction beam can be combined with the vortex beam by using the diffractive suppression characteristic embodied in transmission, to realize the non-diffraction vortex beam within a certain propagation distance. Because the modulation of the non-diffraction beam and vortex beam is very complicated, it is often necessary to use the array with many elements such as antenna array or meta-surface.

Typical non-diffraction beams include the Bessel Beam, Airy Beam, Mathieu Beam, etc., of which the high-order Bessel beam itself has vortex characteristics, and other non-diffraction beams can often form non-diffraction vortex beams by combining the non-diffraction beam with the spiral phase. Fig. 6.56 shows the design of a transmissive electromagnetic meta-surface to generate a quasi-Bessel vortex beam through simultaneous modulation of amplitude and phase [427]. It can be seen that combining the non-diffraction beam with the traditional OAM beam can effectively suppress the divergence in the near field region, to achieve better application. Another approach is to combine OAM with focusing functions as proposed in [428], where the impact of different solutions is investigated in terms of achievable communication modes. While focusing functions allow a better performance, they make the receiver design dependent on the actual distance between the transmitter and the receiver.
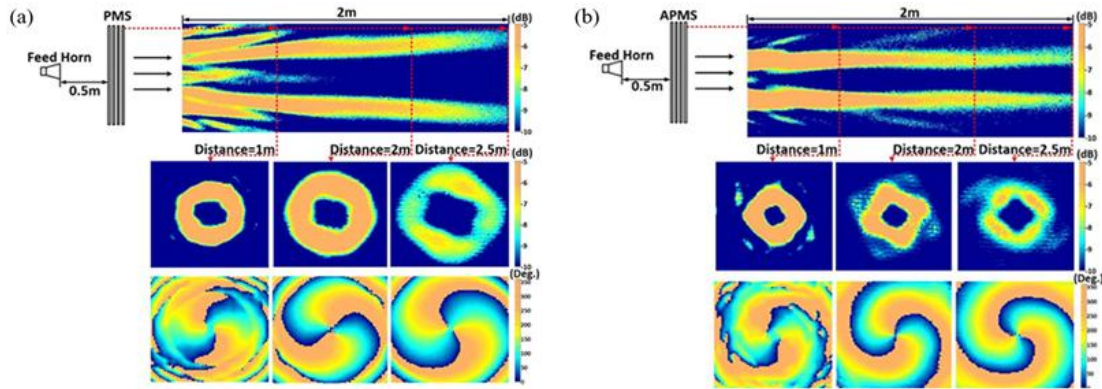
Fig. 6.56 Comparison of the electric field between (a) conventional OAM beam and (b) non-diffraction Bessel vortex beam [427].

6.5.3 The Reception of Vortex Beam and the Detection of OAM

Effective reception and OAM detection of vortex beams are important topics in theory and application research. Typical reception methods of vortex beam are aperture sampling, which can be divided into full aperture sampling and partial aperture sampling according to the type of sampling aperture, as shown in Fig. 6.57. The full aperture sampling and receiving method can effectively ensure

the orthogonality between different OAM modes, while the OAM modes that can be received by partial aperture need to differ by a certain multiple. In addition, the receiving and demodulation of OAM can be realized under the condition of minimal sampling receiving aperture based on the analysis of the sampling matrix [430]. This method abstracts the receiving of OAM mode as a matrix equation-solving problem, so that the relevant matrix equation-solving methods (such as singular value decomposition, least square method), or some signal processing methods can be used, which greatly expands the research idea and realization means of OAM reception and detection. Other coherent and partially-coherent demodulation schemes have been recently proposed in [428].
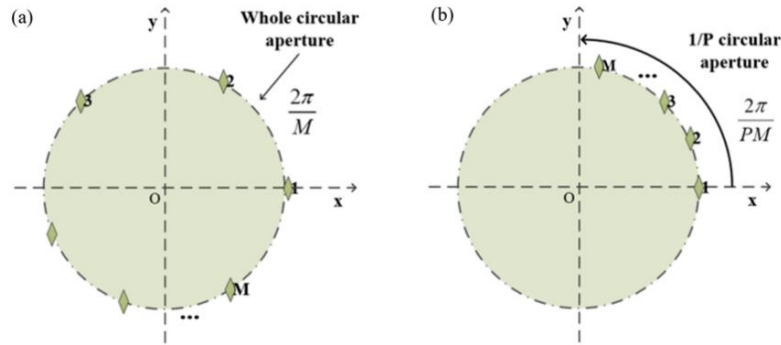
Fig. 6.57 Schematic diagram of (a) full aperture sampling and receiving method and (b) partial aperture sampling and receiving method [429].

6.6 Near-Field Based Intelligent Communications

6.6.1 Near-Field Based Semantic Communication System

In order to further improve the transmission efficiency of wireless communication and make full use of the computation power of the device, the original data is first subjected to feature extraction to obtain relevant semantic information, and then the lightweight semantic information is transmitted through the near field communication architecture to achieve high efficiency transmission. The difference from traditional communication is that the semantic communication architecture based on near-field communication needs to take the near-field channel into account in the joint training of semantic proposing at the joint transmitter and semantic recovery at the receiver, as shown in Fig. 6.58.
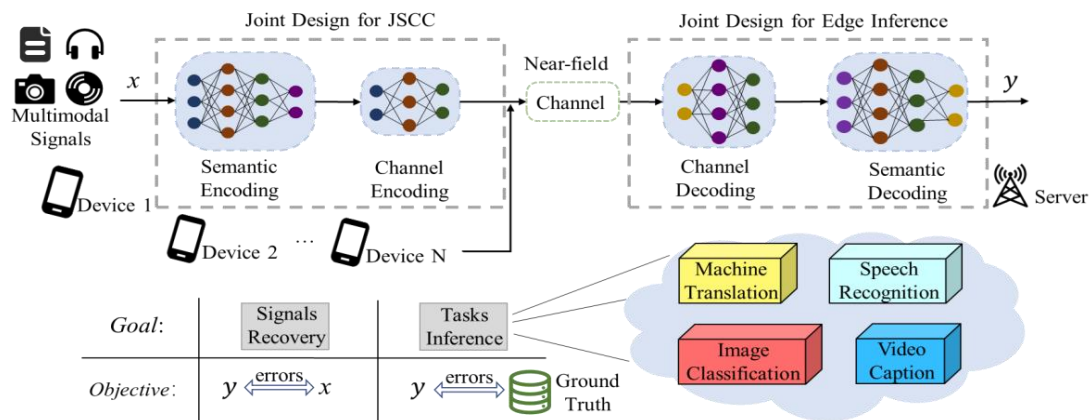
Fig. 6.58 An illustration of the near-field based semantic communication system.

6.6.2 Near-Field Based Federated Learning Framework

Consider a federated learning system over the wireless communication network. In order to protect the privacy of user data, each user will transmit the calculated local federated learning model through the wireless channel and retain local privacy data. The BS will collect the local federated learning model to further perform model aggregation. Considering that the channel between the user and the BS is a near-field channel, it is necessary to re-derive the convergence model of the federated learning system based on near-field channels to establish the energy and delay model of the federated learning system based on near-field communication. Jointly optimizing communication and learning parameters in the near-field communication obtains the optimal resource allocation.
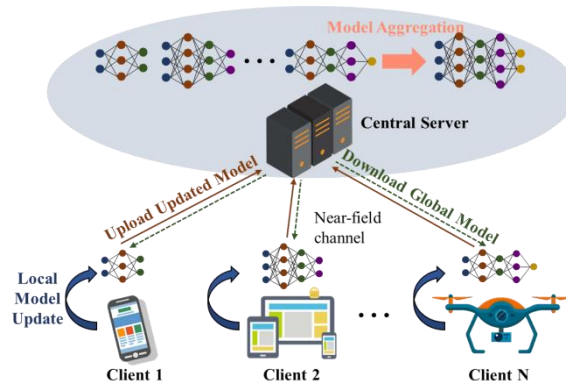
Fig. 6.59 An illustration of the near-field based federated learning framework.

6.6.3 AI-based Near-field Wideband Beamforming Design

The 6G system exhibits significant trends in the development of extremely large-scale antenna arrays and tremendously high frequencies, thus is more likely to operate in the near-field region. In wideband communication, traditional phase shifter-based analog beamforming methods experience beam splitting phenomenon, resulting in a reduction in beamforming gain. To enhance near-field beam focusing and alleviate wideband beam splitting, a hybrid beamforming architecture based on true-time delay is designed at the transmitter. The true-time delay can apply different phase shifts to different frequency components, thereby achieves beam focusing in wideband large-scale antenna communication systems. For the design of true-time delay-based hybrid beamforming, traditional approaches employ fully digital approximate optimization to jointly solve the digital beamforming matrix, analog beamforming matrix, and delay matrix. For instance, one can utilize the weighted minimum mean square error (WMMSE) method to find the optimal fully digital beamformer, then use block coordinate descent to approximate the delay-based hybrid beamforming to the fully-digital beamformer. However, the near-field wideband beamforming design based on fully-digital approximate optimization methods faces challenges such as high computational complexity and susceptibility to changes in channel environments. In this regard, the near-field wideband intelligent beamforming, as illustrated in Fig. 6.60 (left), is proposed. For example, deep reinforcement learning (DRL) algorithms can interact with the environment in real-time to obtain channel capacity information as rewards for updating the network, addressing issues associated with traditional optimization methods. As shown in Fig. 6.60 (right), DRL methods can significantly reduce optimization iteration time and achieve 90% performance compared to the WMMSE-based optimization method [431].
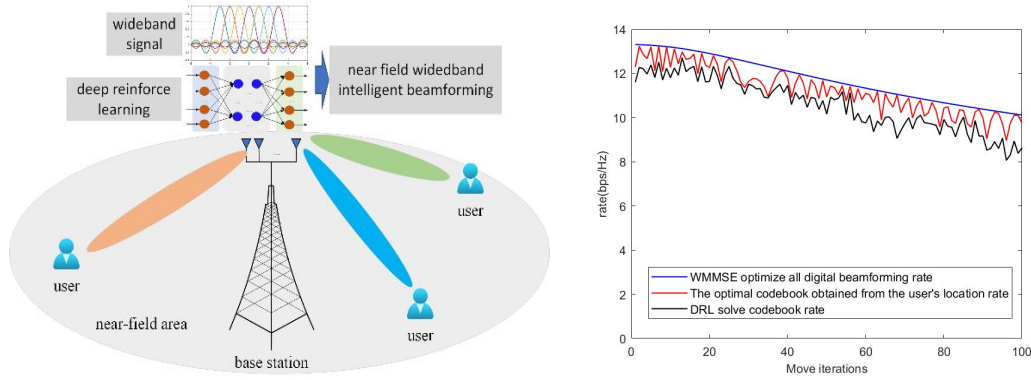
Fig. 6.60 Near-field intelligent beamforming (left) and performance comparison (right).

6.7 Near-field On-chip Wireless Communications

6.7.1 On-chip Wireless Communication Based on On-chip Antenna

With the continuous development of the field of mobile communication, the demand for miniaturization of communication systems has become increasingly urgent. On-chip antennas refer to the antenna structures integrated within the chip. It has the characteristics of miniaturization, low cost, collaborative design with the circuit, high integration and suitability for large-scale mass production. They serve as a feasible alternative within chips to wired signal interconnection. For the future 6G communication systems operating in the THz frequency range (100 GHz to 10 THz), the physical size of antennas is significantly reduced. This provides feasibility for utilizing on-chip antennas to achieve high-frequency interconnectivity with chips, enabling the realization of fully integrated on-chip wireless communication systems. Compared to traditional communication systems, this not only significantly improves data transmission rates but also greatly enhances system integration. Therefore, on-chip antenna technology emerges as a highly attractive research direction in the field of 6G communication.

On-chip communication typically adopts the system architecture illustrated in Fig. 6.61[432]. At the transmitter, the modulated signal is amplified by a power amplifier (PA) and then transmitted by the on-chip antenna. The on-chip antenna at the receiver transmits the received signal to the low noise amplifier (LNA) for low noise amplification, enhancing the sensitivity of the entire receiver. The signal is filtered, frequency-shifted, amplified, and then demodulated to extract the baseband signal. The distance between the transceivers in on-chip communication systems is small, and the required output power is low. The most commonly used on-chip antennas for on-chip communication are monopole and dipole antennas.
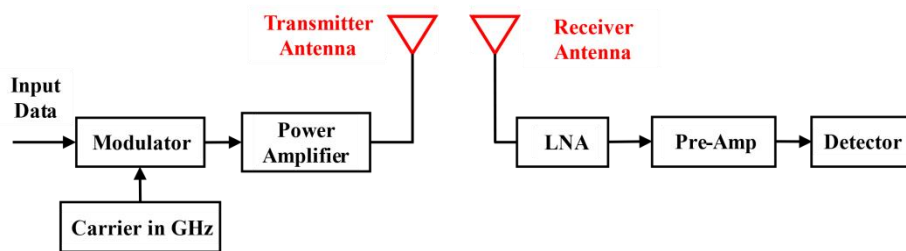
Fig. 6.61 Commonly used on-chip communication system block diagram[432]

In reference [433], researchers developed two planar on-chip antenna topologies on a SiPh platform, as illustrated in Fig. 6.62, for intra-chip RF transmission and network-on-chip (NOC)

communication. Furthermore, by suppressing electromagnetic radiation, Electromagnetic bandgap (EBG) structures have been used to package open microstrip line baluns to enhance the overall wireless inter-chip link budget [434]. Previous research has integrated Substrate Integrated Waveguide with Metamaterials technologies and present a THz planar on-chip antenna for intra-chip wireless communications. This antenna operates in a single thin substrate layer, resulting in significantly reduced losses introduced by the antenna substrate[435].
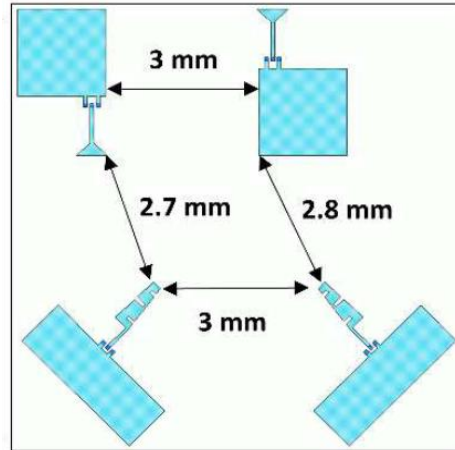
Fig. 6.62 Layout representation for the intra-chip communication arrangement[433].
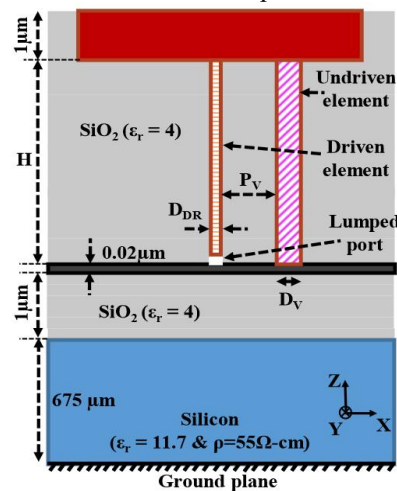
Fig. 6.63 Cross-section of the on-chip top-hat antenna [437].

The majority of on-chip antennas currently available for wireless communication systems are based on silicon technology[436]. In standard silicon-based processes, the silicon substrate has a high relative dielectric constant and a substantial substrate thickness, leading to a significant increase in antenna radiation losses. To address the above issue, researchers have proposed several methods to enhance the radiation efficiency of on-chip antennas. For instance, a novel interconnection device utilizing an on-chip vertical top-hat monopole antennas instead of horizontally placed antennas, as shown in Fig. 6.63, is used in 225 GHz on-chip wireless communication. This approach mitigates the challenges associated with the low transmittance in the plane of the chip and the limited radiation resistance of the silicon substrate when the radiation orthogonal to the plane of the chip[437]. Researchers have also proposed manufacturing THz on-chip antennas on SiC substrates based on GaN technology, as illustrated in Fig. 6.64. This approach enables on-chip full integration with GaN

monolithic microwave integrated circuit (MMIC) chips, further enhancing the radiation efficiency and gain of the antennas[438].
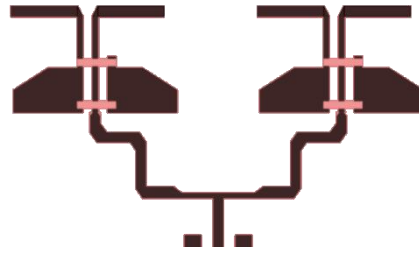
Fig. 6.64 On-chip antenna based on GaN technology [438].

On-chip antennas can be utilized as implantable devices for military, medical and commercial applications. For example, implanted antennas for biomedical therapy and diagnostics, have been designed to monitor various physiological parameters. Furthermore, in conjunction with various kinds of sensors, on-chip antennas can be implanted as part of a biomedical telemetry system, facilitating wireless communication between implantable devices and external instruments. The integration of on-chip antenna technology within wireless transmission systems holds the potential to provide an array of possibilities for the advancement of wireless communication in the 6G era.

6.7.2 On-chip Wireless Communication Based on 3D Stacking Chips

The development of integrated circuits has driven the emergence of system-on-chip (SoC) technology, enabling more functions to be implemented on the same chip. However, the design and manufacturing of SoCs still face challenges, such as increased size due to complex functionalities and difficulties in integrating heterogeneous functional modules with existing process technologies. To address these challenges and meet the demands of 6G communication, researchers have proposed three-dimensional (3D) stacking chips technology, which involves stacking different chips together to form a 3D structure, thereby further enhancing system integration.

However, 3D stacking technology needs to address the interconnection issues between stacked chips, which are crucial for the overall performance of the system[439]. Currently, interconnection technologies used in 3D stacking chips can be classified into two main categories: wired and wireless. Wired interconnection technologies include multi-chip packaging (MCP) and through silicon via (TSV)[440]. MCP involves vertically stacking several chips, with the signals and power pads of each chip connected to a Printed Circuit Board (PCB) through solder joints for communication. TSV technology utilizes vertical silicon vias to achieve interconnection between chips. While these two communication methods can solve interconnection and packaging issues between stacked chips, they also have drawbacks. For example, MCP technology suffers from issues like long solder wires and different resonant frequencies, while TSV technology faces problems like high development costs and low yield rates. At the same time, both of these technologies need to introduce additional electrostatic protection devices. Wireless interconnection technologies applied to 3D stacking chips eliminate the need for wires and silicon vias for communication between chips, effectively overcoming the aforementioned issues. This represents an important direction for future chip design and system integration technologies. Wireless interconnection technologies for chip-to-chip communication in 3D

stacking chips mainly include coupled wireless interconnection technologies and on-chip antenna interconnection technologies as mentioned in section 6.7.1.

Utilizing coupling wireless interconnection technologies: In chip-to-chip near-field communication within stacked chips, coupled interconnection technologies are commonly employed in the mid to low-frequency bands of 6G communication, primarily achieved through capacitive coupling or inductive coupling. Capacitive coupling requires the two plates of the capacitive structure to be placed as close as possible, necessitating face-to-face stacking of chips. As a result, capacitive coupling is not only limited by the number of communicating chips (applicable only to 2-chip configurations) but also constrained by communication distances. Furthermore, capacitive coupling has a larger area and is susceptible to interference from other channels. In contrast, inductive coupling has more advantages than capacitive coupling. Inductively coupled interconnect is not only an efficient and low-cost way of interconnecting chips, but also can reduce power consumption and parasitic effects of complex circuits. Fig. 6.65(a) illustrates the traditional inductive coil array structure used for wireless chip-to-chip communication[441]. By inserting a shielding structure between adjacent coils, as shown in Fig. 6.65(b), crosstalk can be reduced. Additionally, to address crosstalk issues and minimize chip area, researchers have further proposed a zigzag structure, depicted in Fig. 6.65(c).

(a)

(b)

(c)
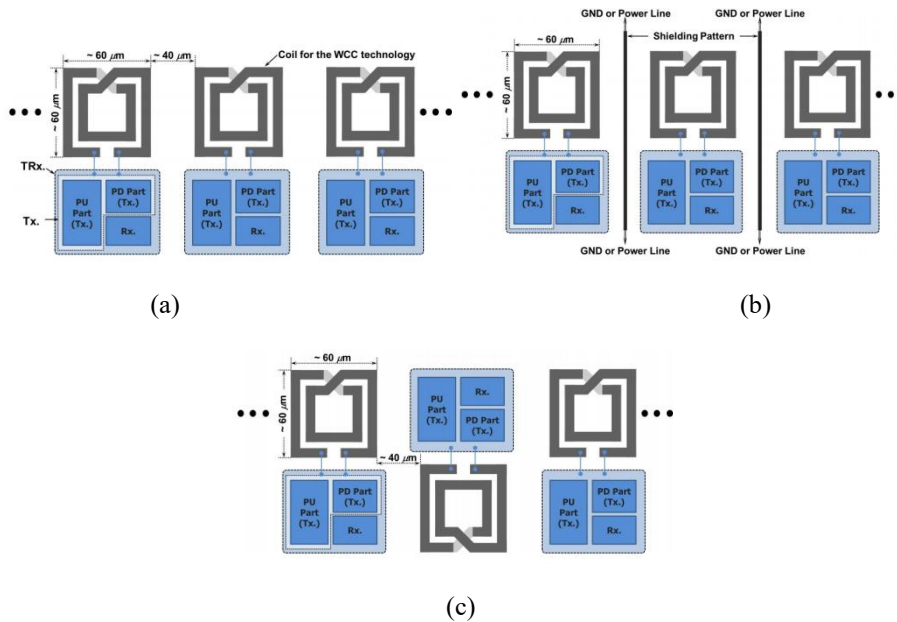
Fig. 6.65 (a)Typical coil array structure, (b)Coil array structure with a shielding pattern, (c)Proposed zigzag-shaped coil array for wireless chip-to-chip communication.

On-chip antenna wireless interconnection technology: In chip-to-chip near-field communication within stacked chips, on-chip antenna technology is predominantly employed in the mid to high-frequency bands of 6G communication. While 3D integrated circuits boast high integration density, the flexibility of communication between these circuits is constrained by internal and external links. Wireless data communication between on-chip antennas can alleviate issues such as high latency, low flexibility, and poor scalability associated with wired communication. It can also address the challenge of lower signal frequencies when transmitting wireless communication through coupling. Wireless interconnection systems consist of transmitters and receivers integrated with on-chip antennas. The most commonly used on-chip antennas for chip-to-chip communication in 3D stacking chips are

monopole and dipole antennas, zigzag antennas, linear antennas, curved antennas and through glass via (TGV)-integrated antennas[442].
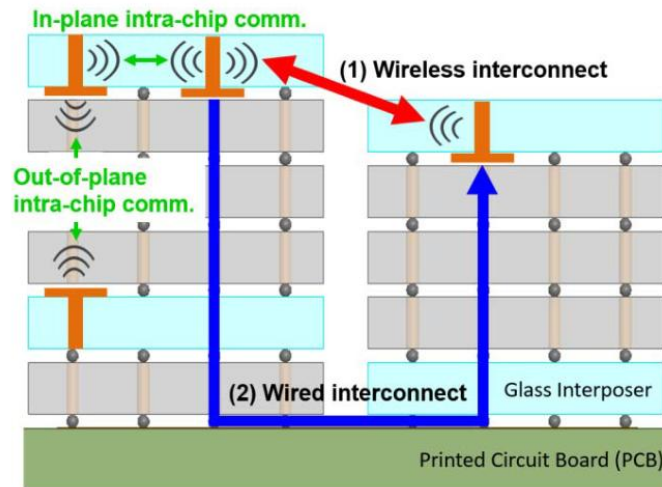
Fig. 6.66 Illustration of wireless in-plane/out-of-plane intra-/interchip communications utilizing TGV-integrated antennas in 3D System-in-Packaging (SiP).

With the advancement of 6G wireless communication, there is a growing demand for higher circuit integration density to exponentially increase the number of transistors per unit area. To meet this current requirement, researchers have proposed three-dimensional stacking chips technology. Traditional wired interconnections such as MCP and TSV face numerous challenges in integration and packaging, including increased power consumption, significant delays, high crosstalk, and complex manufacturing processes associated with wiring across multiple in-plane and out-of-plane dimensions. In comparison to wired methods, wireless interconnection can reduce signal delays, increase communication distances, and decrease chip size. The utilization of wireless interconnection technology employing inductive/capacitive coupling and on-chip antennas provides a solution for on-chip communication and chip interconnection.

6.8 Near-field and Material Sensing

Material sensing technology is playing an increasingly important role in intelligent manufacturing, environmental monitoring and other fields. Traditional material perception technology mainly relies on visual image analysis, which has many limitations in low light, line-of-sight occlusion, bad weather and other scenes. Recent studies have shown that BS massive MIMO arrays have the potential to estimate the electromagnetic coefficient of near-field objects by using OFDM communication signals, and then realize near-field-based object material perception[443]. The near-field material perception problem belongs to one of electromagnetic inverse scattering problems, so the electromagnetic inverse scattering model should be established first.
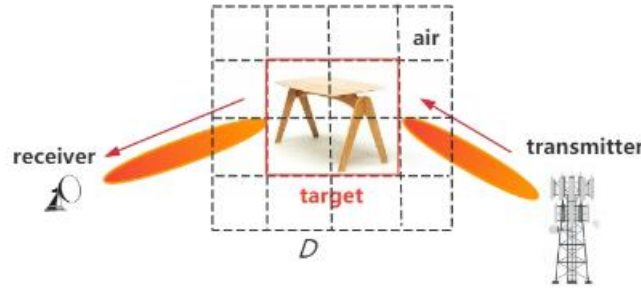
Fig. 6.67 Sensing scenario.

As shown in Fig. 6.67, consider a system model consisting of a multi-antenna transmitter, a target, and a multi-antenna receiver. For the system shown in Fig. 6.67, the forward scattering channel model is built using the Lippman-Schwinger equation. Because OFDM signal contains many sub-carrier signals of different frequencies, it is necessary to establish a forward channel at each frequency. Due to the fact that objects occupy only a small part of the sensing domain, the electromagnetic coefficient vector to be sensed can be estimated by combining the compressed sensing method. In particular, it can be solved by using the optimization method of mixed norm minimization. Because permittivity contrast and conductivity contrast have the same support set, a model based on generalized multiple measurement vectors (GMMV), the key is to use the joint sparsity structure to improve perception.

Suppose that the known object is made of one of several possible materials whose permittivity and conductivity have been accurately measured in advance. It should be noted that only materials with significant differences in dielectric constant or conductivity can be distinguished. The material identification method consists of two steps: first, clustering, and then classification.

In order to determine the material of the target, we first need to distinguish between the part of D occupied by air and the part occupied by the target. To achieve this, we use the K-means clustering algorithm to divide the sampling points in D into two categories. K-means is an unsupervised algorithm with strong generalization ability for clusters of different shapes and sizes, and convergence is guaranteed regardless of the target. Since the relative permittivity and conductivity have different dimensions, we use dimensionless and scale-invariant Mahalanobis distances in the K-means clustering algorithm. The number of clusters is predetermined at 2, representing air and target respectively. The cluster centroid of air, representing the average permittivity and conductivity values of air, is expected to approach the point (1,0). On the other hand, the centroid of the target cluster, which represents its average permittivity and conductivity, is expected to be significantly farther away from the (1,0) point.

After the clustering is complete, the next step is to determine the material category of the target. This is done by calculating the Mahalanobis distance between the cluster centroid of the target material and the true values of the permittivity and conductivity of each possible material. The target is then classified into the material category with the shortest Mahalanobis distance, which indicates the closest match between the measured electromagnetic properties of the target and the known properties of the material.

7 Engineering Practice and Standardization

7.1 Engineering Implementation

In addition to technical research of near-field technology introduced in above section, the practical application of near-field technology in engineering implementation also requires attention with several challenges present that must be addressed[1][2].

● Constructing Near-field Propagation Environments

The traditional research on near-field communication mainly focuses on the BS equipped with large scale centralized antenna array, and the near-field propagation effect can be clearly observed with such configuration. However, the lack of flexibility in antenna placement and the high cost associated with the installation and maintenance of large antenna systems hinder the widespread and flexible implementation of near-field technology. To overcome these challenges, alternative and flexible configurations shall be explored, such as deploying smaller, distributed antenna systems that can realize the performance of large antennas. Additionally, the potential key technologies for the 6G, such as RIS, show promise in artificially creating controllable near-field propagation environments [316].

● Network deployment

In traditional cellular network deployment based on far-field propagation assumptions, the main focus of deployment optimization is to ensure that each cell in the network can effectively communicate with mobile devices within its coverage area. However, in near-field-assumption-based network deployment, the optimization objective must consider not only signal strength distribution but also the changes in spatial freedom caused by near-field propagation characteristics [316]. Therefore, optimizing near-field network deployment requires consideration of factors, including:

- Near-Field Distance Conditions: The distance of devices to the antenna array is related the signal's transmission behavior compared to far-field scenarios. The signals transmission in near-field distance exhibit more complex spatial patterns, requiring a detailed understanding of near-field propagation characteristics.

- Aperture Size: Physical dimensions of antenna arrays play an important role in determining the radiation patterns of signals. Larger apertures may offer advantages in terms of directivity and beamforming capabilities but also introduce challenges in terms of device size and deployment feasibility.

- Deployment Density: In dense urban environments, where multiple antennas are closely spaced together, near-field effects may become more pronounced, which may need further consideration when deploying the antenna arrays.

● Spectrum

Compared to conventional mobile communication systems, 6G will operate in higher-frequency bands, which not only presents new opportunities for enhanced communication capabilities but also introduces unique challenges in network deployment and operation. The transition to higher frequency bands enabling 6G networks to achieve greater near-field propagation distances since the near-field distance increases with frequency for a given antenna aperture size. For example, at present, the frequency bands below 6 GHz are either fully utilized or rapidly being occupied by existing 4G and 5G commercial networks. For the foreseeable future, several newly allocated frequency bands above 6

GHz are anticipated to become the primary carriers for 6G communications, e.g., upper 6 GHz bands, mmWave bands, and even sub-THz bands (ref Fig. 7.1).
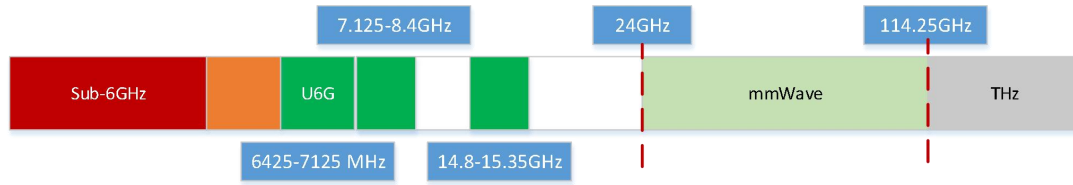
Fig. 7.1 6G Potential Spectrum

7.2 Potential Standardization Impacts

From the perspective of standardization, the impact of near-field communication standards is reflected primarily in the following aspects. On the one hand, traditional standards, such as the 5G channel model standard TR38.901, are based on far-field assumptions. Their parameters and models exhibit biases in the near-field region, necessitating corresponding improvements and extensions. In December 2023, the 3GPP approved a project to enhance the 7-24GHz channel model at the RAN#102 plenary session [444]. This project will be based on the channel model standard in TR38.901, adding modeling for new frequency bands, near-field propagation, and spatial non-stationary characteristics to compensate for the limitations of existing 5G channel model standards, in order to cover existing and potential near-field application evaluation needs in the future. On the other hand, signal propagation in near-field environments, characterized by spherical wavefront, requires redesigning and adjusting technical solutions to optimize system performance across multiple dimensions, such as angle and distance. With the development of key 6G technologies such as RIS, ELAA, ISAC, and WPT, near-field effects directly influence protocol design and system implementation for these technologies. Standardization efforts urgently need to provide systemic solutions from a holistic perspective.

7.2.1 Near-Field Channel Modeling

Near-field channel modeling, as the primary task of standardization, faces challenges in accurately characterizing propagation characteristics due to the inadequacy of far-field models. Traditional 5G channel models, like TR38.901[445], assume electromagnetic waves propagate in the form of plane waves. However, in the actual near-field region, the prominent presence of spherical wavefront effects results in significant differences in channel characteristics, including the number of paths, path strength, cluster structure, and spatial non-stationarity, compared to far-field scenarios[446]. Consequently, the establishment of near-field channel models requires improvements and extensions in the following areas:

● Modeling Methodologies

When constructing near-field channel models, different methodologies have their advantages and disadvantages. Common methods include the Geometry-Based Stochastic Channel Model (GBSM), the Map-Based Hybrid Channel Model (MHCM), and deterministic models, such as ray-tracing.

GBSM is relatively simple in structure, easy to implement, and computationally efficient, making it widely used in preliminary channel modeling. It generates channel parameters through geometric modeling and stochastic distribution rules, and is suitable for large-scale simulations and parameter adjustments. However, its accuracy is limited, particularly in describing detailed phenomena and local propagation effects, such as spherical wavefront.

MHCM combines deterministic environmental information with stochastic statistical characteristics. By utilizing geographic and environmental map data, it can more accurately simulate the real effects of obstacles, reflections, and scattering on signals in the near field, while maintaining statistical sampling capabilities. This method performs better in terms of accuracy but is more complex compared to GBSM.

Deterministic methods, which describe details such as the transmission environment, antenna positions, and reflectors, can simulate each propagation path with high precision, providing the most detailed results. However, they are computationally intensive and are typically used to validate other models or conduct in-depth analyses of specific scenarios.

In the actual standardization process, it is necessary to balance the accuracy and complexity of different models based on application scenarios and computational resources. Standardization should aim to build a channel model system that reflects near-field characteristics while meeting practical application needs, providing theoretical support and technical foundations for subsequent standardization efforts.

● Parameter Adjustment and Model Extension

In near-field communication environments, channel models based on far-field assumptions struggle to accurately describe propagation phenomena under spherical wavefronts. To reflect the actual characteristics of channels in the near field, it is necessary to modify and extend the channel parameter generation modules in existing standards (e.g., TR38.901).

Traditional parameter generation modules assume all antenna elements on the same antenna panel are co-located, thereby generating a unified set of channel parameters. In near-field scenarios, however, significant physical position differences between antenna elements cause variations in channel parameters (e.g., delay, phase, Doppler shift) for each antenna element, typically following certain patterns. Therefore, when modifying parameter generation modules, the impact of positional differences between antenna elements on channel parameters must be considered. For delay parameters, the influence of delay resolution needs to be factored in, while for phase parameters, the relative positions of antenna elements and clusters must be accounted for.

To generate channel parameters with near-field characteristics, the physical location information of clusters can be incorporated. Using statistical models to aid modeling can better capture the variations of LoS and NLOS paths in the near field, dynamically adjusting the channel parameter generation modules. This method balances the deterministic information of local details and the overall statistical features of near-field propagation, providing a more precise and extensible technical basis.

The near-field channel model established through parameter adjustment and model extension can accommodate various dynamic propagation phenomena in the near field and provide a solid data generation foundation for more complex modeling methods in the future.

● Continuity Issues

In practical channel modeling and simulation, far-field and near-field channels often coexist in the same scenario. However, due to fundamental differences in propagation mechanisms and parameter generation methods, treating far-field and near-field separately with different models or algorithms may lead to discontinuities between them. Such discontinuities not only affect the overall consistency of system models but also make simulation results unreliable, potentially misleading subsequent system design and performance evaluations. For example, in scenarios where far-field and near-field channels

coexist, discontinuities can cause abrupt changes in channel parameters, leading to transmission anomalies or distorted simulation data that fail to reflect the real-world signal propagation accurately.

One solution to ensure continuity is to adopt the same implementation framework for both far-field and near-field modeling. This approach guarantees continuity, ensuring that key parameters (e.g., delay, phase, and power attenuation) evolve gradually and continuously during the transition from far-field to near-field, rather than undergoing abrupt changes.

● Spatial Non-Stationarity

In near-field communication, the spatial non-stationarity of channels is more pronounced, especially in scenarios involving large-scale antenna arrays or complex obstacles. Accurately describing and simulating the correlation variations of channel parameters in space has become a significant challenge in current standardization efforts. Common methods include physical blocker-based approach and stochastic based approach[447].

Spatial non-stationarity is largely influenced by surrounding obstacles. Physical blocker-based approach can more accurately describe the attenuation effects of obstacles of different sizes and positions on signal propagation, demonstrating superior accuracy and flexibility.

Compared to Physical blocker-based approach, stochastic based approach generate visible ranges and obstruction losses based on statistical characteristics. These methods are computationally less intensive and suitable for large-scale simulations. However, they often lack flexibility, failing to capture subtle local variations and accurately distinguish between different obstacles.

By conducting in-depth research and standardizing spatial non-stationarity, future communication systems will be better equipped to adapt to dynamic environments, improve the accuracy of channel parameter estimation, and enhance the reliability of simulation results, thereby providing a robust technical foundation for near-field communication and 6G networks.

7.2.2 Standardization of Near-Field Technology

Far-field protocols typically assume wireless propagation as plane waves, focusing on angle-domain techniques such as channel estimation, beamforming, codebook design, and beam training. In near-field environments, however, signals exhibit spherical wave characteristics, requiring technical solutions to consider spatial distance effects in addition to angle precision. This necessitates upgrades to existing standard designs.

Existing pilot signals and channel estimation principles are affected by spherical wavefronts in near-field environments, reducing the accuracy of traditional methods. To adapt to the high spatial correlation of near-field channels, new pilot design methods based on spherical wavefront must be explored, along with sparse channel estimation algorithms tailored to near-field scenarios. These ensure the accurate capture of channel information in both the distance and angle domains.

In far-field environments, beamforming is mostly limited to angle-domain optimization. In near-field environments, spherical wave focal effects can be exploited to design beams in both angle and distance domains using polar coordinate systems. New beamforming standards will enable dynamic beam adjustment, precisely focusing energy to enhance signal strength, reduce interference, and improve system coverage quality.

Traditional codebook designs rely on plane wave assumptions and may fail to capture near-field-specific channel variations. Codebook designs based on spherical wavefronts need to incorporate dynamic adjustment mechanisms to adapt to multidimensional variations. Beam training

should expand the search space and use hierarchical searches or machine learning techniques to achieve low-complexity, fast optimization, ensuring efficient beam configuration selection in dynamic near-field environments.

The improvement and redesign of standards not only ensure foresight and flexibility but also provide unified design principles and technical foundations for the integration of various key technologies (e.g., RIS and ELAA) in future 6G networks.

In March 2025, the 3GPP held a 6G workshop in Incheon, Korea, where various companies presented their research and proposals on 6G technologies[2], including advancements in near-field communication. Multiple companies, including ZTE, DOCOMO, InterDigital, CEWiT, and Xiaomi, highlighted the significance of near-field technology and the challenges it may present [448]-[460]. The discussions covered key aspects of channel characteristics, beam management, CSI enhancement, codebook design, and MIMO improvements to optimize near-field communication. Companies explored techniques to overcome the challenges posed by large-scale antenna arrays and the transition from far-field to near-field communication.

7.2.3 Standardization of Enabling Technologies

The 6G era will introduce new key technologies, such as RIS, ELAA, ISAC, and WPT. These technologies must also be optimized under the influence of near-field effects, requiring corresponding updates to related standards.

RIS can alter the wireless propagation environment by controlling reflection and refraction phases. In near-field regions, where spherical wavefront effects are significant, RIS systems require redesigned beamforming, channel estimation, and codebook protocols. For example, standards for RIS links based on spherical wavefront models can be developed to design high-precision reflection coefficient control algorithms and customized signal processing schemes, ensuring beam focusing and adaptability in two- or three-dimensional spaces.

In ISAC systems, near-field effects influence not only communication links but also the accuracy of sensing information. Innovative signal processing and interference cancellation techniques can help achieve seamless integration of communication and sensing on the same hardware platform. Under near-field conditions, the interplay between communication and sensing, as well as energy allocation, must be regulated through new standard designs to maximize both functionalities.

For ELAA systems, near-field beamforming design must consider the propagation characteristics of electromagnetic waves in large antenna arrays, using spherical wavefront analysis to achieve precise energy control and target positioning.

WPT technologies must focus on energy focusing and safe transmission in near-field environments, incorporating power control and beam focusing techniques in the distance domain to enhance energy transfer efficiency and system safety.

In designing 6G standard protocols, unified and scalable standards must be established to support both traditional far-field designs and seamless transitions to emerging near-field scenarios, ultimately realizing high-precision, high-efficiency, and wide-coverage wireless networks.

---

[2]3GPP workshop on 6G, Incheon, Korea, 10th – 11th March, 2025.
https://www.3gpp.org/component/content/article/6gworkshop-2025?catid=67&Itemid=101

7.2.4 Standardization Activities

Recently, several organizations have undertaken activities to promote the standardization of near-field technology, advancing research in this area significantly (ref Fig. 7.2).

(1) In December 2023, 3GPP Rel-19 approved the 7–24GHz channel measurement and modeling research project, with a key focus on near-field characteristics (Note: Work item Rapporteur(s): Lee, Daewon, Intel, Zhang, Nan, ZTE).

(2) On March 15, 2024, ZTE led the successful establishment of the "Near Field Model and Mechanism Project" in ETSI ISG RIS.

(3) On April 25, 2024, ZTE Corporation, in collaboration with China's three major telecom operators, initiated a near-field technology research project under the CCSA TC5WG6.[3]

(4) On April 18, 2024, the "New Technologies and Materials" sub-forum of the 6G Conference released the "6G Near-Field Technology White Paper."[4]

(5) On April 27, 2024, the initiative "Jointly Promote 6G Near-Field Technologies Research and Standardization" was released at the first "Near Field Communication Theory and Application" forum hosted by the Institute of Electronics.[5]

(6) On February 25, 2025, organizations including ZTE Corporation, Tsinghua University, Beijing University of Posts and Telecommunications, Zhejiang University, China Unicom, etc., jointly led the establishment of the "Near-Field Communication Task Group" within the China IMT-2030 (6G) Promotion Group.

Fig. 7.2 Activities to promote the standardization of the near-field technology

7.3 Technical Experiment and Prototype Test

7.3.1 Measurement on Terahertz Near-Field Channel

7.3.1.1. Terahertz Near-Field Channel Measurement System

The THz MISO channel measurement system is composed of three parts, as shown in Fig. 7.3, including the computer (PC) as the control platform, the Ceyear 3672C VNA, the displacement platform carrying the THz Tx module, and the rotator carrying the THz Rx module [461][443].

---

[3]https://www.ccsa.org.cn/
[4]https://www.c114.com.cn/wireless/2935/a1261616.html
[5]https://mp.weixin.qq.com/s/0Hpjf-ETKwvGPH_K-SyQIQ
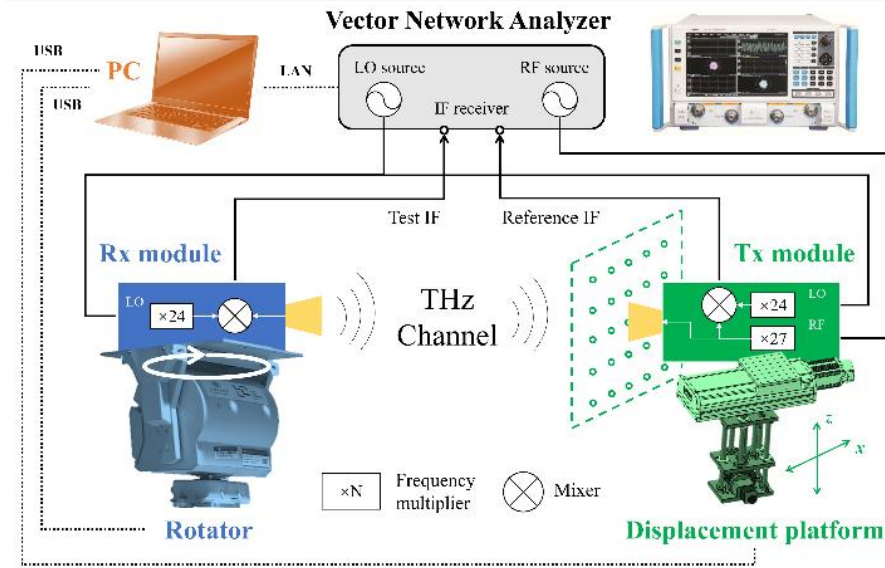
Fig. 7.3 The diagram of the measuring system.

The measuring part consists of Tx and Rx modules and the VNA. The VNA generates radio frequency (RF) and local oscillator (LO) sources. The 9.6296 GHz-11.8518 GHz RF signal is multiplied by 27 to reach the carrier frequencies. The 10.8336 GHz-13.3336 GHz LO signal is multiplied by 24. As designed, the mixed intermediate frequency (IF) signal has a frequency of 7.6 MHz. Two IF signals at Tx and Rx modules, i.e., the reference IF signal and the test IF signal, are sent back to the VNA, and the transfer function of the device under test (DUT) is calculated as the ratio of the two frequency responses. The DUT contains not only the wireless channel, but also the device, cables, and waveguides. To eliminate their influence, the system calibration procedure is conducted, which is described in detail in our previous works [462][463].

The mechanical part is composed of the displacement platform and the rotator. The displacement platform carries the Tx module to move linearly in the x-axis (horizontally) and the z-axis (vertically). The rotator carries the Rx module to scan the horizontal plane to receive angular-resolved multi-path components (MPCs). In the static environment, virtual antenna array measurement is free of mutual coupling and represents the ideal case of the actual antenna array.

The PC alternately controls the movement of Tx through the displacement platform, the movement of Rx through the rotator, and the measuring process through the VNA. The measurement starts from the virtual antenna element in Tx at the left bottom corner, and all elements in the uniform planar arrays (UPAs) are scanned first horizontally (in the x-axis) and then vertically (in the z-axis). At each element in Tx, the Rx scans horizontally and measures the THz channel once per angle.

7.3.1.2. Channel Measurement Deployment

In measurements, we investigate the THz frequency band ranging from 260 GHz to 320 GHz, which covers a substantially large bandwidth of 60 GHz. As a result, the time and space resolution are 16.7 ps and 5 mm, respectively. Key parameters of the measurements are summarized in Table 7.1.

Table 7.1 Summary of measurement parameters.

Parameter	LoS measurement	Measurement 1	Measurement 2	
Frequency band	260-320 GHz			
Bandwidth	60 GHz			
Time resolution	16.7 ps			
Space resolution	5 mm			
Sweeping interval	60 MHz	30 MHz	10 MHz	
Sweeping points	1001	2001	6001	
Max excess delay	16.7 ns	33.3 ns	100 ns	
Max path length	5 m	10 m	30 m	
Notation	LoS measurement	Tx1-Rx1	Tx2-Rx2	Tx3-Rx3
Tx/Rx height	/		1.05 m	
Tx gain / HPBW	7 dBi / 60°	25 dBi / 8°	7 dBi / 60°	
Rx gain / HPBW	7 dBi / 60°		25 dBi / 8°	
Rx angular scan	/	0°:2°:90°	0°:2°:358°	
Tx array size	32 mm × 32 mm	56 mm × 56 mm	48 mm × 48 mm	
Rayleigh distance	3.9690 m	12.1259 m	8.9088 m	

First, we investigate the near-field LoS propagation [464]. The propagation channel is confined in a 0.69 m (length) × 0.61 m (width) × 1.00 m (depth) anechoic chamber. The inside surfaces of the chamber are wrapped by absorbing materials to restrain the multi-path effect. Tx and Rx are placed at two ends of the artificial channel. The Tx is installed on a displacement platform, which supports horizontal and vertical movements in the xz-plane perpendicular to the Tx-Rx line-of-sight. The displacement precision is 0.02 mm for both axes. The Rx is static, and the center of the Tx array is aligned with the Rx, with a distance of 0.86 m. The PC alternately controls the movement of Tx through the displacement platform and the measuring process through the VNA. Key parameters of the measurement are summarized in Table 7.1.

In the measurement, as shown in Fig. 7.4, four sides of the channel are all wrapped by absorbing materials. Three cases are measured, i.e., the virtual UPA at Tx consisting of 16×16, 32×32, and 64×64 elements, with element spacing of 0.5 mm, as summarized in Table 7.2. All cases share the same center of UPA, and the Rx is perpendicularly pointing to this center. In terms of the Rayleigh distance, arrays in Case 1, 2, and 3 belong to the far-field region, far-near-field boundary, and the near-field region, respectively. The measurement starts from the element at the left bottom corner, and all elements in the UPA are scanned first horizontally (in the x-axis) and then vertically (in the z-axis). The measuring time for each position is about 2.3 s. However, the measuring time is subject to the motion driven by the displacement platform, which takes about 4 hours to traverse a 64×64 UPA.
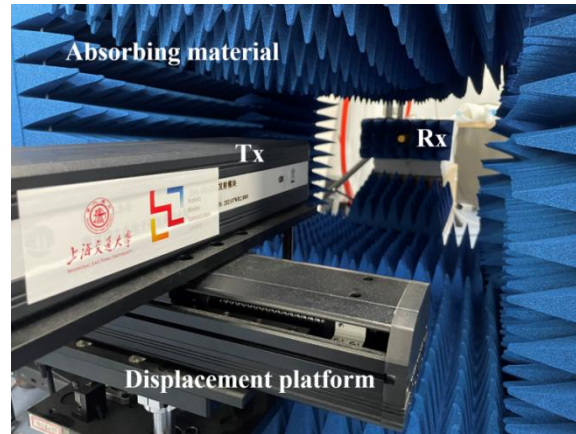
Fig. 7.4 Overview of the LoS measurement.

Then, a small-scale measurement, from Tx1 to Rx1, is carried out [461]. The goal of the measurement is to investigate the cluster parameter from scatterers (the wall, in this deployment) in the NF region. A virtual UPA that spans 56 mm × 56 mm is considered. In this case, the Rayleigh distance is 12.1259 m. For the center carrier frequency of 290 GHz, the half-wavelength spacing is 0.517 mm, which means the antenna array of this size consists of over 3000 antenna elements. To save the measuring time, channels at 64 uniform element positions are measured at Tx, as illustrated in Fig. 7.5(a).

The scale of the scenario is 2.5 m × 3 m, which guarantees that the reflection happens in the NF region. Furthermore, the small scale of the scenario enables the reduction of the maximum detectable path length to 10 m, corresponding to the frequency sweeping interval of 30 MHz and sweeping points of 2001 for each channel measurement. To increase the angular resolution, the Rx rotator scans from 0° to 90° with the step of 2°. Furthermore, high-directive antennas are integrated at both Tx and Rx modules, with gains of around 25 dBi.
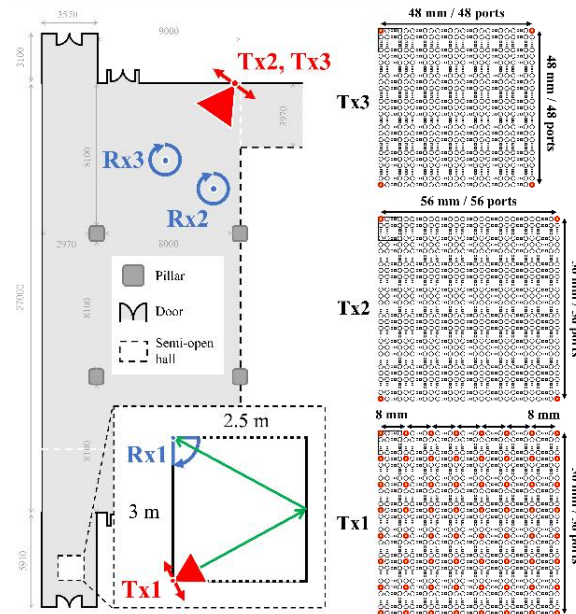
(a) Measurement deployment.
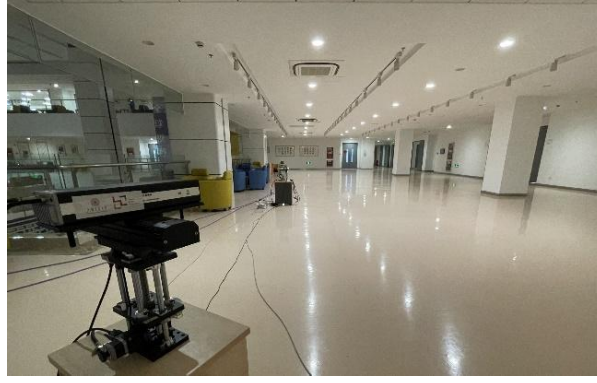
(b) The photo of the measurement.

Fig. 7.5 Overview of the measurement.
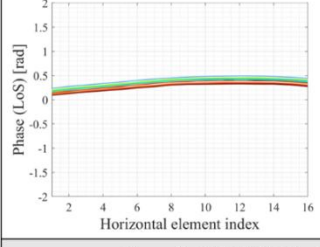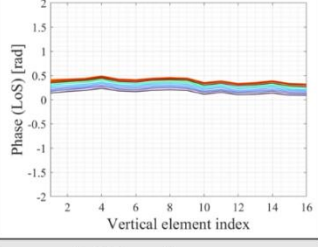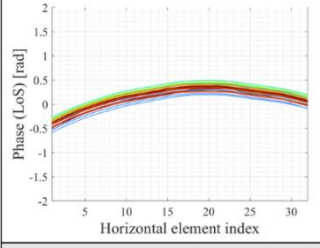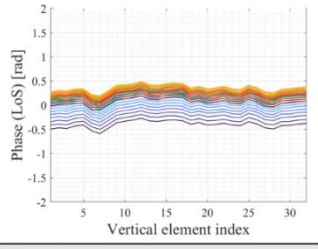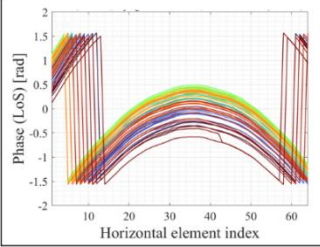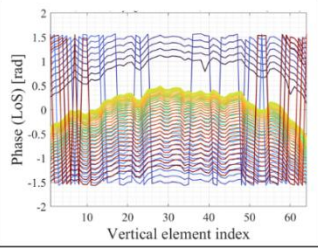
After that, another measurement is carried out in a larger-scale scenario [461], as shown by Tx2-Rx2 and Tx3-Rx3 in Fig. 7.5(b). The UPAs span 56 mm × 56 mm and 48 mm × 48 mm as comparison. Different from the setup in the first measurement, the maximum detectable path length is increased to 30 m, corresponding to the frequency sweeping interval of 10 MHz and sweeping points of 6001 for each channel measurement. Besides, the scan range of arrival angles covers 0° to 360°. Under this circumstance, the measuring time at each antenna element is multiplied by 12. Therefore, to balance the measuring time, we measure the channels at four vertexes of the antenna array, where the variation of parameters can be best observed. Moreover, another antenna with a larger HPBW, 60°, is equipped at the Tx. The height of Tx and Rx is 1.05 m, and the distance between Tx and Rx is 5.9 m.

7.3.1.3. Measurement Result

(1) LoS Measurement

Table 7.2 summarizes the phase change along horizontal (x-axis) and vertical (z-axis) positions. Colored lines indicate phase change among horizontal/vertical elements at different vertical/horizontal positions. In the FF case, the maximum phase difference across each column and each row are both smaller than $\pi/8$, which accords with the definition of Rayleigh distance and can be regarded as a linear phase change. When the UPA expands to 32×32 in Case 2 and 64×64 in Case 3, the phase difference gradually exceeds $\pi/8$, and a non-linear phase change can be clearly observed. In particular, the phase change among vertical elements is less smoother, since the measurement scans the UPA first in the x-axis and then in the z-axis. In other words, the measurement at vertical elements is not continuous and is affected by the positional accuracy of the displacement platform.

Table 7.2 Phase of the LoS ray across the UPA.

Phase change Δφ among horizontal elements	Phase change Δφ among vertical elements
Case 1: 16×16 UPA, Far-field	
Δφ ≤ 0.2840 < π/8	Δφ ≤ 0.1713 < π/8
Case 2: 32×32 UPA, Far-near-field boundary	
π/8 < 0.7476 ≤ Δφ ≤ 0.7875	Δφ ≤ 0.3166 < π/8
Case 3: 64×64 UPA, Near-field	
Δφ > π	Δφ > π

(2) Measurement 1

Fig. 7.6 illustrates the variation of cluster parameters, i.e., delay and azimuth arrival angle, across different positions in the UPA, respectively. The cluster contains the wall-reflected ray and surrounding scattering rays. The cluster delay is the mean of delays inside the cluster, while the cluster angle is determined by the azimuth angle of the strongest ray inside the cluster.
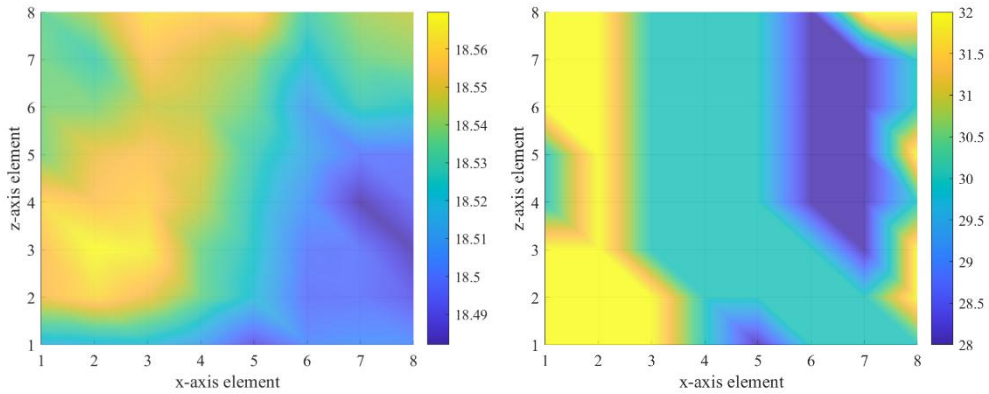
(a) Delay.   (b) Azimuth angle of arrival.
Fig. 7.6 Properties of cluster parameters.

First, as shown in Fig. 7.6(a), the variation in cluster delay is 0.0878 ns, corresponding to the variation in distance of 26.34 mm. Due to symmetry of the scenario, the distance from each element at Tx to the scatterer is half of the total path length. Hence, the deviation of the distance from elements at Tx to the scatterer exceeds is 13.17 mm, larger than 1/16 of the wavelength, 0.065 mm. Second, the theoretical variation in the departure angle is about 1.5° across 64 elements at Tx. Due to the reflection, scattering, and influence of antenna radiation patterns, the variation in the arrival angle reaches 4°, as shown in Fig. 7.6(b). Despite the inevitable superposition of power inside the received beam in the practical measurement, in the simulation of cross-field channels, the departure/arrival angle of the MPC should still be carefully modeled when scatterers are in the near-field region, as the antenna gain differs in the antenna radiation pattern at different angles.

(3) Measurement 2

In the measurement in a larger indoor scenario, as shown in Fig. 7.7, power-delay-angle profiles (PDAPs) are similar at four Tx antenna elements for Tx2-Rx2 and Tx3-Rx3 channels, respectively. According to the multi-path component distance (MCD) based Density-Based Spatial Clustering of Applications with Noise (DBSCAN) clustering algorithm [465], 8-14 clusters are observed from Tx2 to Rx2, and 9-13 clusters are observed from Tx3 to Rx3, while the difference in the number of clusters comes from the difference in received power and the classification method which distinguishes MPCs and noise samples by thresholding [462]. At Tx2-Rx2, the delay spread varies from 9.4651 ns to 17.4153 ns between different antenna elements at Rx, and the azimuth angular spread varies from 16.6728° to 26.7276°. At Tx3-Rx3, the delay spread varies from 3.3929 ns to 4.3441 ns between different antenna elements at Rx, and the azimuth angular spread varies from 11.0671° to 12.8708°. According to the PDAP results, more scatterers are located in the NF region for Tx2-Rx2 channel than for Tx3-Rx3 channel. Therefore, the variation in large-scale parameters is more significant between antenna elements at Tx2.
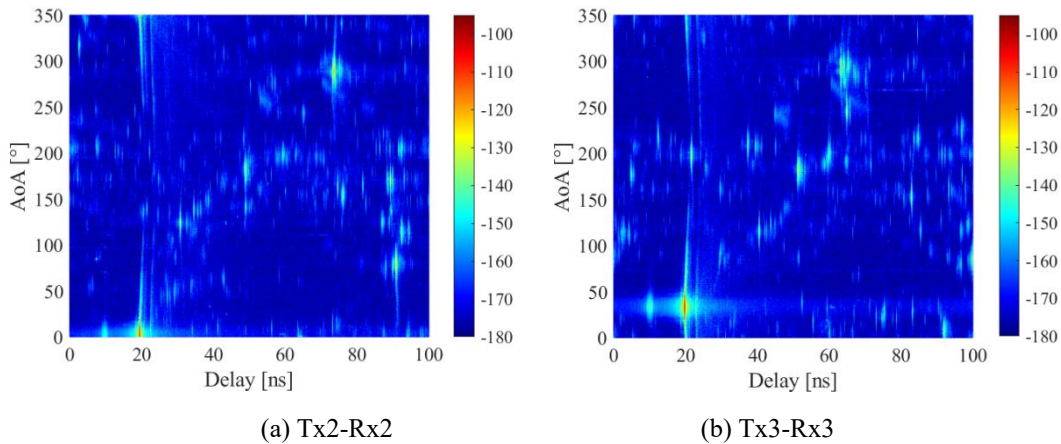
(a) Tx2-Rx2   (b) Tx3-Rx3

Fig. 7.7 Power-delay-angle profile of channels for (a) Tx2-Rx2, (b) Tx3-Rx3.

The channel from the s-th antenna element at the Tx to the Rx ($s = 1,2,\ldots,4$) is represented by complex gains $\boldsymbol{h_s} \in \mathbb{C}^{6001 \times 1}$. We denote $\mathbf{H} = [\boldsymbol{h_1}, \boldsymbol{h_1}, \ldots, \boldsymbol{h_s}]$, and calculate the transmitter spatial correlation matrix as

$$\mathbf{R}_{(T)} = \frac{\mathbf{HH}^*}{\|\mathbf{H}\|\|\mathbf{H}\|^{\mathbf{T}}} \tag{7.1}$$

where $*$ is the complex conjugate transpose of the matrix. $\|\mathbf{H}\| = [\|\boldsymbol{h_1}\|_F, \|\boldsymbol{h_2}\|_F, \dots, \|\boldsymbol{h_s}\|_F]^{\mathbf{T}}$ where $\|\boldsymbol{h_s}\|_F^2 = tr(\boldsymbol{h_s}^{\mathbf{T}}\boldsymbol{h_s})$ is the Frobenius norm.

For the MISO channel, we assess the distinction between channels from different Tx antenna elements to the single Rx antenna. In specific, the impact of transmitter correlation can be evaluated by a real number [466], the EDoFs constrained by the transmitter spatial correlation matrix, as

$$\mathrm{EDoF}_{(T)} = \left(\frac{tr(\mathbf{R}_{(T)})}{\|\mathbf{R}_{(T)}\|_F}\right)^2 \tag{7.2}$$

The value of $EDoF_{(T)}$ varies from 1 to the number of Tx antenna elements N_t. When $EDoF_{(T)}$ is closer to N_t, it represents that channels from different Tx antenna elements to the single Rx antenna are distinctive, and can support beamforming or diversity. Moreover, it indicates that channels in the cross-field have the potential for multiplexing if there are adequate antennas at the receiver. On the contrary, when $EDoF_{(T)}$ is close to 1, these channels are correlated so that they barely offer diversity or multiplexing gain.}

The assessment of the measurement result is elaborated as follows. In the measurement, $N_t = 4$. The EDoF constrained by the Tx antenna array is 3.3460 for Tx2, and the counterpart is 3.3031 for Tx3, which are both close to N_t. These values indicate the distinction between antenna elements at the Tx for near-field and cross-field channels, and the necessity of element-level modeling of channels with scatterers in the cross-field, even though the physical array size is small. Besides, the Rayleigh distance is 12.1 m for the antenna array at Tx2, and the counterpart is 8.9 m for the antenna array at Tx3. Therefore, more scatterers are located in the NF region for the Tx2-Rx2 channel than for the Tx3-Rx3 channel. The comparison between Tx2-Rx2 and Tx3-Rx3 channels indicates that the MIMO channel with more scatterers in the near-field has larger potential for diversity or multiplexing.

Furthermore, we simulate the MISO channel in indoor and UMa-cellular scenarios at 290 GHz. In the indoor scenario, the height of Tx and Rx is 1.05 m. In the UMa scenario, the height of Tx and Rx is 25 m and 1.5 m, respectively. The 2D Tx-Rx distance varies from 1 m to 150 m for the indoor scenario and 10 m to 5 km for the UMa scenario. We simulate each antenna element as a custom antenna with 3-dB beamwidth of 360° horizontally and 60° vertically. We evaluate the system capacities by using near-field, far-field, and the proposed cross-field models at 290 GHz, in both indoor and outdoor scenarios at different distances between BS and UE. The system is composed of two distributed ELAAs at BS and UE, respectively. $N_t = 64$ and $N_r = 64$ antenna elements, planar-shaped with the antenna spacing of 1 m are equipped in each ELAA. The transmit power is 10 dBm, and the power allocation scheme over parallel element-to-element channels is based on water-filling. The simulation result is illustrated in Fig. 7.8. It is observed that the capacity of the proposed cross-field model lies between the counterparts of near-field and far-field models. In specific, for communications between ELAAs at short BS-UE distances, the capacity of the cross-field model reaches 80% that of the near-field model, while the far-field model leads over 50% reduction in capacity caused by miscalculation of distance, path loss and phase.

(a) Indoor channel, 290 GHz, $N_t = N_r = 64$ (b) Indoor channel, 290 GHz, $N_t = N_r = 64$

Fig. 7.8 Channel capacity at various BS-UE distances.
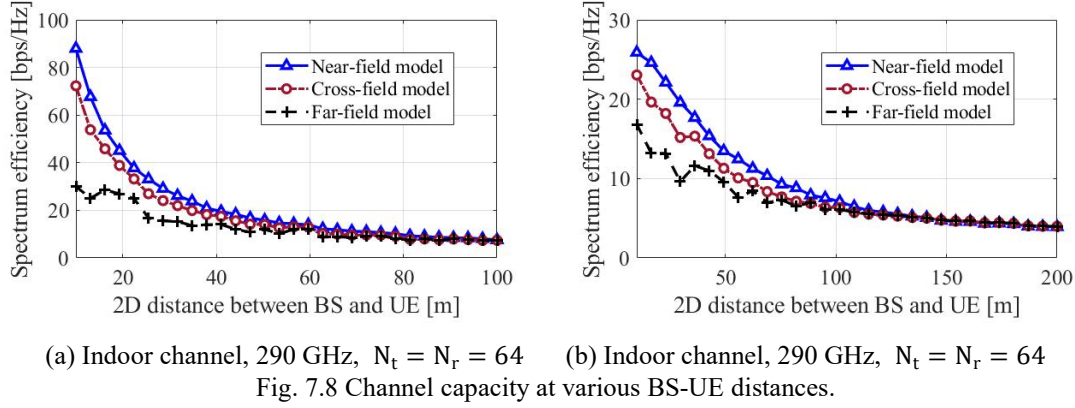
7.4 RIS-assisted Near-Field for Wireless Hot-Spot Applications

Channel measurement with holographic RISs presents a significant challenge due to the time and resources required, and the variability in RIS designs complicates achieving consistent results. Factors such as transmitter-receiver distance, aperture size, near-field and far-field effects, and antenna radiation patterns influence free-space path loss in RIS-assisted wireless communications.

To evaluate performance in both near-field and far-field conditions, channel sounding measurements are essential. A study in [467] presented an indoor channel measurement campaign using a holographic RIS to create virtual LoS hot-spot scenarios in both near-field and far-field environments. The study used a Keysight M8195A arbitrary waveform generator and a standard gain horn antenna for signal transmission, and a Keysight Infiniium series UXR0334B real-time oscilloscope for analyzing the received signal as shown in Fig. 7.9. Measurements were conducted in a controlled environment, ensuring no human presence or moving objects to maintain time-invariance. The center frequency of the radio signal was set to 3.5 GHz, utilizing a varactor diode voltage-controlled 2-bit holographic RIS with 1,850 unit cell elements.
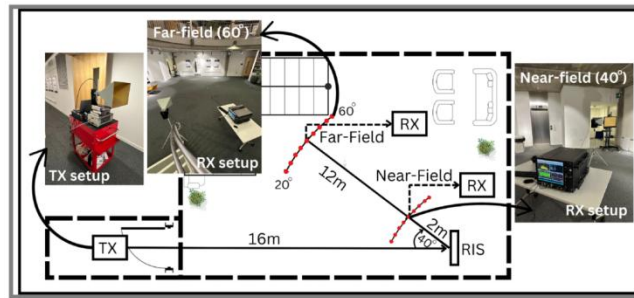
Fig. 7.9 Indoor channel sounding measurement campaign with a 3.5 GHz RIS.

The study focused on evaluating the performance of the RIS in both active and inactive states and examining the effects on the timing of multipath signal arrivals and associated performance enhancements using Power Delay Profiles (PDPs). Key findings of this study include:

• Activating the RIS enhances gain in the direction of the virtual LoS, with improvements of up to 13 dB at a 2m distance in the near-field and 4-5 dB in at a 12m distance in the far-field, compared to when the RIS is off or configured with a random pattern

• The RIS increases the delay spread when active, indicating that the beamforming capabilities introduce additional multipath components directed toward the receiver

• The RIS's improvement on PDP sharply drops when the UE is moved a few tens of centimeters when configured at a specific angle with the near field radiation pattern i.e. its beamwidth is very

narrow

- When the RIS is wrongly configured with a far-field pattern for a near-field UE position, its PDP peak is 8 dB lower, indicating a strong dependency on the distance-based codebook design as shown in Fig. 7.10 and Fig. 7.11.
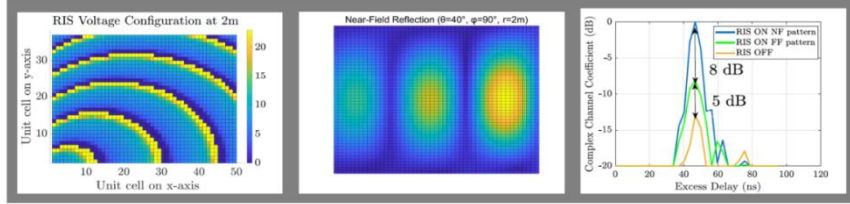
Fig. 7.10 RIS near-field beam pattern for the reflection angle θ = 40∘, ϕ = 0∘ at 2 m distance (r), and the corresponding peak of the PDP in the near-field for both RIS on and RIS off cases.
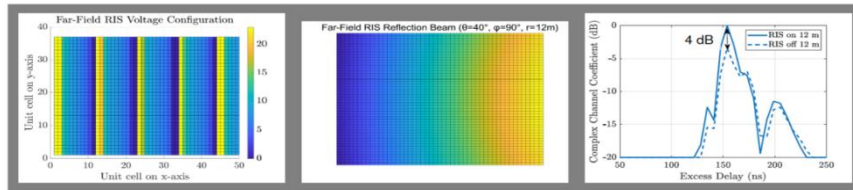
Fig. 7.11 RIS linear phase gradient far-field response pattern for the reflection angle θ = 40∘, ϕ = 0∘, and the corresponding peak of the PDP in the far-field at 12 m separation distance between RIS and RX for both RIS on and RIS off cases.

The study also explored the feasibility of using first-order reflections within the virtual LoS to enhance performance in targeted hot-spot regions. The findings can be used to validate simulation results of commercial network planning software that considers holographic metasurfaces for equalizing channel response and integrating RIS into ray-tracing software can optimize the RIS's radiation pattern for selected environments, as shown in Fig. 7.12 where a typical office room is modelled in a commercial raytracing software and the EM field distribution for a fixed TX position is calculated. Secondly, a RIS is introduced into the room based on a measured radiation pattern, and the EM field distribution for the room is calculated that validates the PDP improvement with the RIS presented earlier. This method provides an accurate result of the total received power at the RX from the TX through various multipaths and the channel impulse response. The resulting software is able to extract the power from each path (each ray) and can estimate the key parameters of the channel such as the strongest path and delay between different paths. These findings validate the potential of utilizing RIS in hot-spot scenarios, where precise control of first-order reflections is essential for optimal performance.
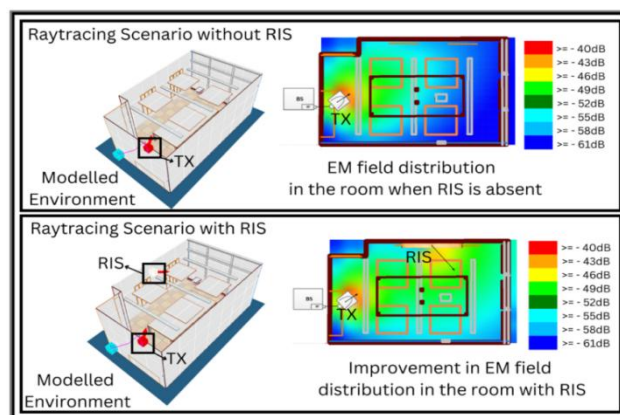
Fig. 7.12 Raytracing simulations in the near field with and without RIS.

8 Summarization and Prospects

In conclusion, the exploration of near-field propagation characteristics has garnered significant attention and achieved substantial progress. This article represents a pioneering industry effort as the first comprehensive and systematic white paper on the subject. It meticulously compiles and summarizes research findings across various aspects of near-field technology, including application scenarios, foundational theories, channel measurement and modeling, transmission technologies, and cross-domain technological integration. Special emphasis is placed on advancements in both engineering implementation and standardization processes, addressing primary 6G spectrum allocation, enabling technologies for near-field propagation, and network deployment strategies. This compilation aims to establish a robust theoretical foundation and provide actionable guidelines for future research directions in near-field technology.

Challenges persist, however, in advancing near-field technology research and its practical engineering applications. These multifaceted hurdles include:

(1) The need for deeper theoretical exploration to develop more rigorous frameworks;

(2) Significant gaps in measurement data for near-field channels, highlighting the necessity for methodological refinements in channel modeling;

(3) Persistent oversimplifications in assumptions about transmission technology assumptions, necessitating investigations into complex, real-world scenarios and solutions.

(4) Further efforts are needed to strengthen the engineering and standardization of near-field technology.

The synergy between near-field technology and other domains emerges as a novel research frontier. Further study is warranted to unravel the unique attributes of near-field propagation and develop optimal harnessing strategies. Critical to practical implementation is standardization—the 3GPP's initiation of standardization research on near-field channel models marks a constructive first step. Balancing academic rigor with proactive engineering and standardization efforts will be pivotal to enabling effective near-field technology deployment in emerging 6G networks.

Looking forward, near-field technology promises to unlock new electromagnetic spatial dimensions for future wireless communication systems. It is increasingly recognized as a cornerstone technology for achieving ultra-high data rates, precise sensing capabilities, and efficient WPT in 6G frameworks. Its potential to serve as a key enabling technology for the 6G wireless air interface is particularly compelling. Anticipation remains high for groundbreaking research outcomes, with expectations for near-field technology to play an augmented role in shaping the next-generation wireless network landscape.

Reference

[1] Y. Zhao, L. Dai, and R. Zhang, et al., "Near-field Communications: Characteristics, Technologies, and Engineering," Frontiers of Information Technology & Electronic Engineering, vol. 25, pp. 1580-1626, February 2025.

[2] Y. Zhao, L. Dai, and J. Zhang, et al., "Near-field Communications: Theories and Applications," Frontiers of Information Technology & Electronic Engineering, vol. 25, pp. 1575-1579, February 2025.

[3] T. Cui, S. Jin, and J. Zhang, et al., "Research Report on Intelligent Metasurface Technology," IMT-2030 (6G) Promotion Group, 2021.

[4] RIS TECH Alliance, "Reconfigurable Intelligent Surface White Paper (2023)," March 2023, Hangzhou, China. Available: http://www.risalliance.com/en/riswp2023.html

[5] IMT-2030 (6G) Promotion Group, "White Paper on Typical Scenarios and Key Capabilities of 6G", July 2022.

[6] L. Zhu, W. Ma, and R. Zhang, "Movable Antennas for Wireless Communication: Opportunities and Challenges," IEEE Communications Magazine, vol. 62, no. 6, pp. 114-120, June 2024.

[7] J. Zhang, J. Xiang, and B. Ai, "6G Multi Antennas and Reconfigurable Intelligent Surface", Electronic Industry Press, 2023.

[8] Z. Zhou, X. Gao, J. Fang and Z. Chen, "Spherical Wave Channel and Analysis for Large Linear Array in LoS Conditions," 2015 IEEE Globecom Workshops (GC Wkshps), San Diego, CA, USA, 2015, pp. 1-6.

[9] W. Guo, Y. Zhao, and C. Li, "Special Topic on Near-Field Communication and Sensing Towards Field Communication and Sensing Towards 6G," ZTE COMMUNICATIONS, vol 22, no.1, March 2024.

[10] ITU-R WP 5D, "M.2160-0 (11/2023), "Framework and overall objectives of the future development of IMT for 2030 and beyond," November 2023, Available: https://www.itu.int/rec/R-REC-M.2160/en

[11] R. Liu, H. Lin, and H. Lee, "Beginning of the Journey Toward 6G: Vision and Framework," IEEE Communications Magazine, vol. 61, no. 10, pp. 8-9, October 2023.

[12] R. Liu, L. Zhang, and R. Y., "The ITU Vision and Framework for 6G: Scenarios, Capabilities, and Enablers," IEEE Vehicular Technology Magazine, pp.2-10, February 2025.

[13] R. Liu et al., "6G Enabled Advanced Transportation Systems," IEEE Transactions on Intelligent Transportation Systems, vol. 25, no. 9, pp. 10564-10580, September. 2024.

[14] H. Zhang, N. Shlezinger, and F. Guidi, et al., "6G Wireless Communications: From Far-Field Beam Steering to Near-Field Beam Focusing," IEEE Communications Magazine, vol. 61, no. 4, pp. 72-77, April 2023.

[15] "Regulations on the Allocation of Radio Frequencies in the People's Republic of China," Order No. 62 of the Ministry of Industry and Information Technology of the People's

Republic   of   China,   May   2023.   Available:
https://www.gov.cn/govweb/gongbao/2023/issue_10646/202308/content_6898890.html.

[16] "WRC-23 Booklet: Agenda and Relevant Resolutions," ITU, December. 2023. Available:
https://www.itu.int/wrc-23/booklet-wrc-23/

[17] 3GPP. RP-234018, "Channel Modelling Enhancements for 7-24 GHz," 3GPP TSG RAN
Meeting #102, Edinburgh, UK, 2023.

[18] "Next   G   Alliance   Report: 6G   Technologies,"   June.   2022.   Available:
https://www.nextgalliance.org/wp-content/uploads/dlm_uploads/2022/07/TWG-report-6G-te
chnologies.pdf

[19] M. Jian and R. Liu, "Baseband Signal Processing for Terahertz: Waveform Design,
Modulation and Coding," 2021 International Wireless Communications and Mobile
Computing (IWCMC), Harbin City, China, 2021, pp. 1710-1715.

[20] H. Sarieddeen, M. -S. Alouini and T. Y. Al-Naffouri, "An Overview of Signal Processing
Techniques for Terahertz Communications," Proceedings of the IEEE, vol. 109, no. 10, pp.
1628-1665, Oct. 2021

[21] I. F. Akyildiz, C. Han, and Z. Hu, et al., "Terahertz Band Communication: An Old Problem
Revisited and Research Directions for the Next Decade," IEEE Transactions on
Communications, vol. 70, no. 6, pp. 4250-4285, June 2022.

[22] H. Zhang, N. Shlezinger, and F. Guidi, et al., "Beam Focusing for Near-Field Multiuser
MIMO Communications," IEEE Transactions on Wireless Communications, vol. 21, no. 9,
pp. 7476-7490, September. 2022.

[23] H. Zhang, N. Shlezinger, and F. Guidi, et al., "Beam Focusing for Near-Field Multiuser
MIMO Communications," IEEE Transactions on Wireless Communications, vol. 21, no. 9,
pp. 7476-7490, September. 2022.

[24] A. Singh, A. J. Alqaraghuli and J. M. Jornet, "Wavefront Engineering at Terahertz
Frequencies Through Intelligent Reflecting Surfaces," 2022 IEEE 23rd International
Workshop on Signal Processing Advances in Wireless Communication (SPAWC), Oulu,
Finland, 2022, pp. 1-5.

[25] A. Singh, I. V. A. K. Reddy, D. Bodet, and J. M. Jornet, "Bessel Beams for 6G - A
Performance Analysis," 2022 56th Asilomar Conference on Signals, Systems, and
Computers, Pacific Grove, CA, USA, 2022, pp. 658-664.

[26] A. Singh, V. Petrov, and J. M. Jornet, "Utilization of Bessel Beams in Wideband Sub
Terahertz Communication Systems to Mitigate Beamsplit Effects in the Near-field,"
ICASSP 2023 - 2023 IEEE International Conference on Acoustics, Speech and Signal
Processing (ICASSP), Rhodes Island, Greece, 2023, pp. 1-5.

[27] I. V. Reddy, D. Bodet, et al., "Ultrabroadband terahertz-band communications with
self-healing bessel beams," Communications Engineering, vol 2, October 2023.

[28] K. D. Paschaloudis, R. C. M. Pimenta, and G. Soriano, et al., "Near-Field Links with
Obstructed Line of Sight via Bessel Beams," 2023 17th European Conference on Antennas

and Propagation (EuCAP), Florence, Italy, 2023, pp. 1-3.

[29]   H. Guerboukha, et al. "Curving THz wireless data links around obstacles," Communications Engineering, vol.3, pp.1-8, May 2024.

[30]   A. Singh, A. J. Alqaraghuli and J. M. Jornet, "Wavefront Engineering at Terahertz Frequencies Through Intelligent Reflecting Surfaces," 2022 IEEE 23rd International Workshop on Signal Processing Advances in Wireless Communication (SPAWC), Oulu, Finland, 2022, pp. 1-5.

[31]   A. Singh, M. Andrello, N. Thawdar and J. M. Jornet, "Design and Operation of a Graphene-Based Plasmonic Nano-Antenna Array for Communication in the Terahertz Band," IEEE Journal on Selected Areas in Communications, vol. 38, no. 9, pp. 2104-2117, Sept. 2020.

[32]   F. Akyildiz, and J. M. Jornet, "Realizing Ultra-Massive MIMO (1024×1024) Communication in the (0.06-10) Terahertz Band," Nano Communication Networks, vol. 8, pp. 46-54, 2020.

[33]   V. Petrov, D. Bodet, and A. Singh, "Mobile Near-Field Terahertz Communications for 6G and 7G Networks: Research Challenges," Frontiers in Communications and Networks, vol. 4, March 2023.

[34]   D. Bodet and J. M. Jornet, "Joint Waveform & Wavefront Engineering for Terahertz Communications in 6G," *2023 IEEE International Conference on Acoustics, Speech, and Signal Processing Workshops (ICASSPW)*, Rhodes Island, Greece, 2023, pp. 1-5.

[35]   M. Cui, Z. Wu, Y. Lu, et al., "Near-Field MIMO Communications for 6G: Fundamentals, Challenges, Potentials, and Future Directions," IEEE Communications Magazine, vol. 61, no. 1, pp. 40-46, January 2023.

[36]   R. Liu, Q. Wu, M. Di Renzo, et al., "A Path to Smart Radio Environments: An Industrial Viewpoint on Reconfigurable Intelligent Surfaces," IEEE Wireless Communications, vol. 29, no. 1, pp. 202-208, February 2022.

[37]   R. Liu, J. Dou, P. Li, et al., "Simulation and Field Trial Results of Reconfigurable Intelligent Surfaces in 5G Networks," IEEE Access, vol. 10, pp. 122786-122795, 2022.

[38]   Z. Tang, Y. Chen, Y. Wang, et al., "Near-Field Sparse Channel Estimation for Extremely Large-Scale RIS-Aided Wireless Communications," IEEE Globecom Workshops Proceedings, Kuala Lumpur, Malaysia, 2023.

[39]   S. Lv, Y. Liu, X. Xu, et al., "RIS-Aided Near-Field MIMO Communications: Codebook and Beam Training Design," *IEEE Transactions on Wireless Communications*, vol. 23, no. 9, pp. 12531-12546, September. 2024.

[40]   Z. Wang, X. Mu and Y. Liu, "Near-Field Integrated Sensing and Communications," *IEEE Communications Letters*, vol. 27, no. 8, pp. 2048-2052, August 2023.

[41]   Y. Pan, C. Pan, S. Jin, et al., "RIS-Aided Near-Field Localization and Channel Estimation for the Terahertz System," *IEEE Journal of Selected Topics in Signal Processing*, vol. 17, no. 4, pp. 878-892, July 2023.

[42] H. Lu, Y. Zeng, C. You, et al., "A Tutorial on Near-Field XL-MIMO Communications Toward 6G," *IEEE Communications Surveys & Tutorials*, vol. 26, no. 4, pp. 2213-2257, Fourthquarter 2024.

[43] X. Li, H. Lu, Y. Zeng, et al., "Near-Field Modeling and Performance Analysis of Modular Extremely Large-Scale Array Communications," *IEEE Communications Letters*, vol. 26, no. 7, pp. 1529-1533, July 2022.

[44] X. Li, H. Lu, Y. Zeng, et al., "Modular extremely large-scale array communication: Near-field modelling and performance analysis," *China Communications*, vol. 20, no. 4, pp. 132-152, April 2023.

[45] H. Wang and Y. Zeng, "Can Sparse Arrays Outperform Collocated Arrays for Future Wireless Communications?," *2023 IEEE Globecom Workshops (GC Wkshps)*, Kuala Lumpur, Malaysia, 2023, pp. 667-672.

[46] B. Ning, S. Yang, Y. Wu, et al., "Movable Antenna-Enhanced Wireless Communications: General Architectures and Implementation Methods," arXiv preprint arXiv:2407.15448, 2024.

[47] L. Zhu, W. Ma, and R. Zhang, "Modeling and Performance Analysis for Movable Antenna Enabled Wireless Communications," IEEE Transactions on Wireless Communications, vol. 23, no. 6, pp. 6234-6250, June 2024.

[48] W. Mei, X. Wei, B. Ning, et al., "Movable Antenna Position Optimization: A Graph-Based Approach," IEEE Wireless Communications Letters, vol. 13, no. 7, pp. 1853-1857, April 2024.

[49] L. Zhu, W. Ma, Z. Xiao, et al., "Performance Analysis and Optimization for Movable Antenna Aided Wideband Communications," IEEE Transactions on Wireless Communications, vol. 23, no. 12, pp. 18653-18668, Decmber 2024.

[50] W. Ma, L. Zhu, and R. Zhang, "MIMO Capacity Characterization for Movable Antenna Systems," IEEE Transactions on Wireless Communications, vol. 23, no. 4, pp. 3392-3407, April 2024.

[51] L. Zhu, W. Ma, B. Ning, et al., "Movable-Antenna Enhanced Multiuser Communication via Antenna Position Optimization," IEEE Transactions on Wireless Communications, vol. 23, no. 7, pp. 7214-7229, July 2024.

[52] L. Zhu, W. Ma, and R. Zhang, "Movable-Antenna Array Enhanced Beamforming: Achieving Full Array Gain with Null Steering," IEEE Communications Letters, vol. 27, no. 12, pp. 3340-3344, December 2023.

[53] W. Ma, L. Zhu, and R. Zhang, "Multi-Beam Forming with Movable-Antenna Array," IEEE Communications Letters, vol. 28, no. 3, pp. 697-701, March 2024.

[54] X. Shao, Q. Jiang, and R. Zhang, "6D Movable Antenna Based on User Distribution: Modeling and Optimization," IEEE Transactions on Wireless Communications, vol. 24, no. 1, pp. 355-370, January 2025.

[55] X. Shao, R. Zhang, Q. Jiang, et al., "6D Movable Antenna Enhanced Wireless Network via

Discrete Position and Rotation Optimization," IEEE Journal on Selected Areas in Communications, vol. 43, no. 3, pp. 674-687, March 2025.

[56] X. Shao and R. Zhang, "6DMA Enhanced Wireless Network with Flexible Antenna Position and Rotation: Opportunities and Challenges," *IEEE Communications Magazine*, vol. 63, no. 4, pp. 121-128, April 2025.

[57] J. Ding, L. Zhu, Z. Zhou, et al., "Near-Field Multiuser Communications Aided by Movable Antennas," IEEE Wireless Communications Letters, vol. 14, no. 1, pp. 138-142, January 2025.

[58] Y. Chen, M. Chen, H. Xu, et al., "Joint Beamforming and Antenna Design for Near-Field Fluid Antenna System," IEEE Wireless Communications Letters, vol. 14, no. 2, pp. 415-419, February 2025.

[59] L. Zhu, W. Ma, Z. Xiao, et al., "Movable Antenna Enabled Near-Field Communications: Channel Modeling and Performance Optimization," IEEE Transactions on Communications, early access, 2025.

[60] R. Liu, M. Jian, D. Chen, et al., "Integrated Sensing and Communication Based Outdoor Multi-Target Detection, Tracking, and Localization in Practical 5G Networks," Intelligent and Converged Networks, vol. 4, no. 3, pp. 261-272, September 2023.

[61] T. Mao, J. Chen, Q. Wang, C. Han, Z. Wang and G. K. Karagiannidis, "Waveform Design for Joint Sensing and Communications in Millimeter-Wave and Low Terahertz Bands," IEEE Transactions on Communications, vol. 70, no. 10, pp. 7023-7039, Oct. 2022.

[62] F. Zhang, T. Mao, R. Liu, Z. Han, S. Chen, and Z. Wang, "Cross-Domain Waveform Design for 6G Integrated Sensing and Communication," arXiv preprint arXiv:2311.04483, 2024.

[63] A. Sakhnini, S. De Bast, M. Guenach, A. Bourdoux, H. Sahli, and S. Pollin, "Near-Field Coherent Radar Sensing Using a Massive MIMO Communication Testbed," IEEE Trans. Wireless Communication, vol. 21, no. 8, pp. 6256–6270, Aug. 2022.

[64] H. Chen et al., "6G Localization and Sensing in the Near Field: Features, Opportunities, and Challenges," IEEE Wireless Communications, vol. 31, no. 4, pp. 260-267, August 2024.

[65] R. Liu, C. Zhang and J. Song, "Line of Sight Component Identification and Positioning in Single Frequency Networks Under Multipath Propagation," IEEE Transactions on Broadcasting, vol. 65, no. 2, pp. 220-233, June 2019.

[66] M. Lipka, S. Brückner, E. Sippel and M. Vossiek, "On the Needlessness of Signal Bandwidth for Precise Holographic Wireless Localization," 2020 17th European Radar Conference (EuRAD), Utrecht, Netherlands, 2021, pp. 202-205.

[67] H. Chen, M. F. Keskin, A. Sakhnini, N. Decarli, S. Pollin, D. Dardari, and H. Wymeersch, "6G Localization and Sensing in the Near Field: Fundamentals, Opportunities, and Challenges," arXiv preprint arXiv:2308.15799, 2023.

[68] Y. Zhang, C. Liu, "5G Ultra-dense Network Fingerprint Positioning Method Based on matrix completion," China Communication,2023, 20 (3) , pp.105-118.

[69] D. Zou, W. Meng, S. Han, K. He and Z. Zhang, "Toward Ubiquitous LBS: Multi-Radio

Localization and Seamless Positioning," IEEE Wireless Communications, vol. 23, no. 6, pp. 107-113, December 2016.

[70] Z, W. Meng, S. Han. "Euclidean Distance Based Handoff Algorithm for Fingerprint Positioning of WLAN System," IEEE Wireless Communications and Networking Conference(WCNC), 2013, pp.1564-1568.

[71] D. Zou and L. He, "Fusion Handover Algorithm Based on Accuracy Estimation," 2022 2nd International Conference on Frontiers of Electronics, Information and Computation Technologies (ICFEICT), Wuhan, China, 2022, pp. 282-286.

[72] D. Zou, W. Meng and S. Han, "An Accuracy Estimation Algorithm for Fingerprint Positioning System," 2014 Fourth International Conference on Instrumentation and Measurement, Computer, Communication and Control, Harbin, China, 2014, pp. 573-577.

[73] L. Chen, P. Wen, D. Zou, F. Li and L. He, "An Innovative Accuracy Estimation Algorithm of Fingerprint Positioning," 2022 International Wireless Communications and Mobile Computing (IWCMC), Dubrovnik, Croatia, 2022, pp. 201-204..

[74] L. He, D. Zou. "Fusion Localization Based on Accuracy Estimation," 2022 5th International Conference on Advanced Electronic Materials, Computers and Software Engineering (AEMCSE 2022), 2022, pp. 12-18.

[75] S. Hu, F. Rusek and O. Edfors, "Beyond Massive MIMO: The Potential of Positioning With Large Intelligent Surfaces," IEEE Transactions on Signal Processing, vol. 66, no. 7, pp. 1761-1774, 1 April1, 2018.

[76] S. Hassouna, et al. "A survey on reconfigurable intelligent surfaces: Wireless communication perspective," IET Commun. 17, 497–537 (2023).

[77] Q. Wu, S. Zhang, B. Zheng, C. You and R. Zhang, "Intelligent Reflecting Surface-Aided Wireless Communications: A Tutorial," IEEE Transactions on Communications, vol. 69, no. 5, pp. 3313-3351, May 2021.

[78] A. Elzanaty, A. Guerra, F. Guidi and M. -S. Alouini, "Reconfigurable Intelligent Surfaces for Localization: Position and Orientation Error Bounds," IEEE Transactions on Signal Processing, vol. 69, pp. 5386-5402, 2021.

[79] T. S. Rappaport et al., "Wireless Communications and Applications Above 100 GHz: Opportunities and Challenges for 6G and Beyond," IEEE Access, vol. 7, pp. 78729-78757, 2019.

[80] G. Gradoni and M. Di Renzo, "End-to-End Mutual Coupling Aware Communication Model for Reconfigurable Intelligent Surfaces: An Electromagnetic-Compliant Approach Based on Mutual Impedances," IEEE Wireless Communications Letters, vol. 10, no. 5, pp. 938-942, May 2021.

[81] E. Bjoernson, "Optimizing a Binary Intelligent Reflecting Surface for OFDM Communications under Mutual Coupling," WSA 2021; 25th International ITG Workshop on Smart Antennas, French Riviera, France, 2021, pp. 1-6.

[82] P. Xu, G. Chen, Z. Yang and M. D. Renzo, "Reconfigurable Intelligent Surfaces-Assisted

Communications With Discrete Phase Shifts: How Many Quantization Levels Are Required to Achieve Full Diversity?," IEEE Wireless Communications Letters, vol. 10, no. 2, pp. 358-362, Feb. 2021.

[83] C. Pan et al., "Reconfigurable Intelligent Surfaces for 6G Systems: Principles, Applications, and Research Directions," IEEE Communications Magazine, vol. 59, no. 6, pp. 14-20, June 2021.

[84] C. Ozturk, M. F. Keskin, H. Wymeersch and S. Gezici, "RIS-Aided Near-Field Localization Under Phase-Dependent Amplitude Variations," IEEE Transactions on Wireless Communications, vol. 22, no. 8, pp. 5550-5566, Aug. 2023.

[85] Z. Abu-Shaban, K. Keykhosravi, M. F. Keskin, G. C. Alexandropoulos, G. Seco-Granados and H. Wymeersch, "Near-field Localization with a Reconfigurable Intelligent Surface Acting as Lens," ICC 2021 - IEEE International Conference on Communications, Montreal, QC, Canada, 2021, pp. 1-6.

[86] J. He, H. Wymeersch, L. Kong, O. Silvén and M. Juntti, "Large Intelligent Surface for Positioning in Millimeter Wave MIMO Systems," 2020 IEEE 91st Vehicular Technology Conference (VTC2020-Spring), Antwerp, Belgium, 2020, pp. 1-5.

[87] S. Hassouna, M. A. Jamshed, M. Ur-Rehman, et al., "RIS-assisted Near-field Localization Using Practical Phase Shift Model," Sci Rep14, 4350 (2024). https://doi.org/10.1038/s41598-024-54859-3.

[88] Y. Zhang et al., "An Efficient Caching and Offloading Resource Allocation Strategy in Vehicular Social Networks," IEEE Transactions on Vehicular Technology, vol. 73, no. 4, pp. 5690-5703, April 2024.

[89] Y Yang, Y Zhang and Z Zhuo. "Adaptive Time Slot Resource Allocation in SWIPT IoT Networks," Computer Modeling in Engineering and Sciences,2023,vol.136, no. 3, pp:2787-2813.

[90] Z. Zhang, Y. Liu, Z. Wang, X. Mu and J. Chen, "Physical Layer Security in Near-Field Communications," IEEE Transactions on Vehicular Technology, vol. 73, no. 7, pp. 10761-10766, July 2024.

[91] F. Rusek, D. Persson, and B. K. Lau ,et al., "Scaling Up MIMO: Opportunities and Challenges with Very Large Arrays," IEEE Signal Processing Magazine, vol. 30, no. 1, pp. 40-60, January 2013.

[92] J. M. Jornet, and A. Sangwan. "Nanonetworking in the Terahertz Band and Beyond." IEEE Nanotechnology Magazine (2023).

[93] S. Abadal, and C. Han, et al., "Wave Propagation and Channel Modeling in Chip-scale Wireless Communications: A Survey From Millimeter-wave to Terahertz and Optics." IEEE access 8 (2019): 278-293.

[94] A. Sindgi and U. B. Mahadevaswamy, "Wavelet-Powered mm-Wave OFDM for Efficient Wireless Network-on-Chip Communication," 2023 International Conference on Network, Multimedia and Information Technology (NMITCON), Bengaluru, India, 2023, pp. 1-8.

[95] R. Medina, J. Kein, and Y. Qureshi, et al., "Full System Exploration of On-Chip Wireless Communication on Many-Core Architectures," 2022 IEEE 13th Latin America Symposium on Circuits and System (LASCAS), Puerto Varas, Chile, 2022, pp. 1-4.

[96] H. -i. Kim, R. Bowrothu and Y. -K. Yoon, "Tri-axis Polarized Loop Antenna for mmWave Wireless Inter/intra Chip Communications," 2020 IEEE 70th Electronic Components and Technology Conference (ECTC), Orlando, FL, USA, 2020, pp. 1875-1880.

[97] V. Petrov ,et al., "Terahertz Band Intra-Chip Communications: Can Wireless Links Scale Modern x86 CPUs?," IEEE Access, vol. 5, pp. 6095-6109, July 2017.

[98] A. Yaghjian, "An Overview of Near-Field Antenna Measurements," IEEE Transactions on Antennas and Propagation., vol. 34, no. 1, pp. 30–45, January 1986.

[99] K. T. Selvan and R. Janaswamy, "Fraunhofer and Fresnel Distances: Unified Derivation for Aperture Antennas," IEEE Antennas and Propagation Magazine., vol. 59, no. 4, pp. 12–15, August 2017.

[100] M. Cui and L. Dai, "Near-Field Wideband Beamforming for Extremely Large Antenna Arrays," IEEE Transactions on Wireless Communications, vol. 23, no. 10, pp. 13110-13124, October 2024.

[101] H. Lu and Y. Zeng, "How Does Performance Scale with Antenna Number for Extremely Large-Scale MIMO?," 2021 IEEE International Conference on Communications(ICC), Montreal, QC, Canada, 2021, pp. 1-6.

[102] H. Lu and Y. Zeng, "Communicating With Extremely Large-Scale Array/Surface: Unified Modeling and Performance Analysis," IEEE Transactions on Wireless Communications, vol. 21, no. 6, pp. 4039-4053, June 2022.

[103] R. Li, S. Sun, and M. Tao, "Applicable Regions of Spherical and Plane Wave Models for Extremely Large-Scale Array Communications," China Communications, 2023. Available: https://arxiv.org/pdf/2301.06036.pdf.

[104] J.-S. Jiang and M. Ingram, "Spherical-Wave Model for Short-Range MIMO," IEEE Transactions on Communications, vol. 53, no. 9, pp. 1534–1541, September 2005.

[105] F. Bohagen, P. Orten, and G. E. Oien, "On Spherical vs. Plane Wave Modeling of Line-of-Sight MIMO Channels," IEEE Transactions on Communications, vol. 57, no. 3, pp. 841–849, March 2009.

[106] P. Wang, Y. Li and B. Vucetic ,et al., "Tens of Gigabits Wireless Communications Over E-Band LoS MIMO Channels With Uniform Linear Antenna Arrays," IEEE Transactions on Wireless Communications, vol. 13, no. 7, pp. 3791-3805, July 2014.

[107] S. Sun, R. Li and C. Han ,et al., "How to Differentiate between Near Field and Far Field: Revisiting the Rayleigh Distance." arXiv preprint arXiv:2309.13238,2023.

[108] H. Chen, A. Elzanaty , and R. Ghazalian ,et al., "Channel Model Mismatch Analysis for XL-MIMO Systems from a Localization Perspective," GLOBECOM 2022 - 2022 IEEE Global Communications Conference, Rio de Janeiro, Brazil, 2022, pp. 1588-1593.

[109] C. Feng and Y. Zeng, "When Does UPW Model Become Invalid for XL-MIMO With

Directional Array Elements?," IEEE Communications Letters, vol. 28, no. 2, pp. 422-426, February 2024.

[110] S. Zeng, B. Di and H. Zhang ,et al., "Near-Far Field Boundary Analysis and Transmit Covariance Optimization for Dual-Polarized XL-MIMO Communications, " IEEE Wireless Communications and Networking Conference (WCNC), Milan, IT, March 2025.

[111] S. Zeng, B. Di, and H. Zhang ,et al., "Revisiting Near-Far Field Boundary in Dual-Polarized XL-MIMO Systems, " Available: https://arxiv.org/abs/2502.14694

[112] A. Pizzo, L. Sanguinetti and T. L. Marzetta, "Spatial Characterization of Electromagnetic Random Channels," IEEE Open Journal of the Communications Society, vol. 3, pp. 847-866, 2022.

[113] W. C. Chew, "Waves and Fields in Inhomogenous Media, "Hoboken, NJ, USA: Wiley, 1995.

[114] L. Wei ,et al., "Tri-Polarized Holographic MIMO Surfaces for Near-Field Communications: Channel Modeling and Precoding Design," IEEE Transactions on Wireless Communications, vol. 22, no. 12, pp. 8828-8842, December 2023.

[115] M. Cui, L. Dai, and R. Schober ,et al., "Near-field wideband beamforming for extremely large antenna array," arXiv preprint arXiv:2109.10054, September 2021.

[116] P. Ramezani, A. Kosasih, and A. Irshad ,et al., "Exploiting the Depth and Angular Domains for Massive Near-Field Spatial Multiplexing," IEEE BITS the Information Theory Magazine, vol. 3, no. 1, pp. 14-26, March 2023.

[117] Z. Wu and L. Dai, "Multiple Access for Near-Field Communications: SDMA or LDMA?,"IEEE Journal on Selected Areas in Communications, vol. 41, no. 6, pp. 1918-1935, June 2023.

[118] Z. Wu, M. Cui and L. Dai, "Enabling More Users to Benefit From Near-Field Communications: From Linear to Circular Array," IEEE Transactions on Wireless Communications, vol. 23, no. 4, pp. 3735-3748, April 2024.

[119] K. Chen, C. Qi, and J. Huang ,et al., "Near-Field Communications for Extremely Large-Scale MIMO: A Beamspace Perspective, " IEEE Communications Magazine, early access, 2025.

[120] D. Dardari, "Communicating With Large Intelligent Surfaces: Fundamental Limits and Models," IEEE Journal on Selected Areas in Communications, vol. 38, no. 11, pp. 2526-2537, November 2020.

[121] D. Dardari and N. Decarli, "Holographic Communication Using Intelligent Surfaces," IEEE Communications Magazine, vol. 59, no. 6, pp. 35-41, June 2021.

[122] N. Decarli and D. Dardari, "Communication Modes With Large Intelligent Surfaces in the Near Field," IEEE Access, vol. 9, pp. 165648-165666, 2021.

[123] R. Ji ,et al., "Extra DoF of Near-Field Holographic MIMO Communications Leveraging Evanescent Waves," IEEE Wireless Communications Letters, vol. 12, no. 4, pp. 580-584, April 2023.

[124] A. Pizzo, A. Torres, and L. Sanguinetti ,et al., "Nyquist Sampling and Degrees of Freedom of Electromagnetic Fields," IEEE Transactions on Signal Processing, vol. 70, pp. 3935-3947, 2022.

[125] C. Ouyang ,et al., "Near-field Communications: A Degree-of-freedom Perspective," arXiv preprint arXiv:2308.00362, 2023.

[126] Z. Xie, Y. Liu and J. Xu ,et al., "Performance Analysis for Near-Field MIMO: Discrete and Continuous Aperture Antennas," IEEE Wireless Communications Letters, vol. 12, no. 12, pp. 2258-2262, Dec. 2023.

[127] S. Verdu, "Spectral Efficiency in the Wideband Regime," IEEE Transactions on Information Theory, vol. 48, no. 6, pp. 1319-1343, June 2002.

[128] D. Miller, "Communicating with Waves Between Volumes: Evaluating Orthogonal Spatial Channels and Limits on Coupling Strengths." Appl Opt. 2000 Apr 10;39(11):1681-99.

[129] Z. Dong and Y. Zeng, "Near-Field Spatial Correlation for Extremely Large-Scale Array Communications," IEEE Communications Letters, vol. 26, no. 7, pp. 1534-1538, July 2022.

[130] H. Lu ,et al., "A Tutorial on Near-Field XL-MIMO Communications Toward 6G," IEEE Communications Surveys & Tutorials, vol. 26, no. 4, pp. 2213-2257, Fourthquarter 2024.

[131] B. Zhuo, J. Gu and W. Duan ,et al., "Extremely Large-Scale Array System: Cooperative NFC or FFC?," IEEE Wireless Communications Letters, vol. 13, no. 5, pp. 1250-1254, May 2024.

[132] B. Zheng, T. Ma and X. Yi ,et al., "Intelligent Reflecting Surface-Aided Transmit Diversity and Performance Analysis," ICC 2023 - IEEE International Conference on Communications, Rome, Italy, 2023, pp. 2822-2827.

[133] B. Zheng and R. Zhang, "Simultaneous Transmit Diversity and Passive Beamforming With Large-Scale Intelligent Reflecting Surface," IEEE Transactions on Wireless Communications, vol. 22, no. 2, pp. 920-933, Feb. 2023.

[134] H. Lu and Y. Zeng, "How Does Performance Scale with Antenna Number for Extremely Large-Scale MIMO?," ICC 2021 - IEEE International Conference on Communications, Montreal, QC, Canada, 2021, pp. 1-6.

[135] H. Wang and Y. Zeng, "Can Sparse Arrays Outperform Collocated Arrays for Future Wireless Communications?," 2023 IEEE Globecom Workshops (GC Wkshps), Kuala Lumpur, Malaysia, 2023, pp. 667-672.

[136] X. Li, H. Lu and Y. Zeng ,et al., "Near-Field Modeling and Performance Analysis of Modular Extremely Large-Scale Array Communications," IEEE Communications Letters, vol. 26, no. 7, pp. 1529-1533, July 2022.

[137] X. Li, H. Lu and Y. Zeng ,et al., "Modular Extremely Large-scale Array Communication: Near-field Modelling and Performance Analysis," China Communications, vol. 20, no. 4, pp. 132-152, April 2023.

[138] X. Li, Z. Dong and Y. Zeng ,et al. "Near-Field Beam Focusing Pattern and Grating Lobe Characterization for Modular XL-Array," GLOBECOM 2023 - 2023 IEEE Global

Communications Conference, Kuala Lumpur, Malaysia, 2023, pp. 4068-4073.

[139] X. Li, Z. Dong and Y. Zeng ,et al. "Multi-User Modular XL-MIMO Communications: Near-Field Beam Focusing Pattern and User Grouping," IEEE Transactions on Wireless Communications, vol. 23, no. 10, pp. 13766-13781, Oct. 2024.

[140] Q. Wu and R. Zhang, "Intelligent Reflecting Surface Enhanced Wireless Network via Joint Active and Passive Beamforming," IEEE Transactions on Wireless Communications, vol. 18, no. 11, pp. 5394-5409, Nov. 2019.

[141] C. Feng , H. Lu and Y. Zeng ,et al. "Near-Field Modeling and Performance Analysis for Extremely Large-Scale IRS Communications," IEEE Transactions on Wireless Communications, vol. 23, no. 5, pp. 4976-4989, May 2024.

[142] C. Feng, H. Lu and Y. Zeng ,et al. "Wireless Communication with Extremely Large-Scale Intelligent Reflecting Surface," 2021 IEEE/CIC International Conference on Communications in China (ICCC Workshops), Xiamen, China, 2021, pp. 165-170.

[143] Z. Dong and Y. Zeng "Near-Field Spatial Correlation for Extremely Large-Scale Array Communications," IEEE Communications Letters, vol. 26, no. 7, pp. 1534-1538, July 2022.

[144] H. Lu, Y. Zeng, C. You, et al."A tutorial on near-field XL-MIMO communications towards 6G," arXiv preprint arXiv:2310.11044, 2023.

[145] G. Bartoli, A. Abrardo and N. Decarli, et al. "Spatial Multiplexing in Near Field MIMO Channels with Reconfigurable Intelligent Surfaces," IET Signal Processing, vol. 17, no. 3, p. e12195, 2023.

[146] S. Shen, B. Clerckx and R. Murch, et al. "Modeling and Architecture Design of Reconfigurable Intelligent Surfaces Using Scattering Parameter Network Analysis," IEEE Transactions on Wireless Communications, vol. 21, no. 2, pp. 1229-1243, Feb. 2022.

[147] H. Wang and Y. Zeng "SNR Scaling Laws for Radio Sensing with Extremely Large-Scale MIMO," 2022 IEEE International Conference on Communications Workshops (ICC Workshops), Seoul, Korea, Republic of, 2022, pp. 121-126.

[148] H. Wang, Z. Xiao and Y. Zeng, et al. "Cramér-Rao Bounds for Near-Field Sensing With Extremely Large-Scale MIMO," IEEE Transactions on Signal Processing, vol. 72, pp. 701-717, 2024.

[149] X. Gan, C. Huang and Z. Yang, et al. "Near-Field Localization for Holographic RIS Assisted mmWave Systems," IEEE Communications Letters, vol. 27, no. 1, pp. 140-144, Jan. 2023.

[150] A. Pizzo, T. L. Marzetta and L. Sanguinetti, et al. "Spatially-Stationary Model for Holographic MIMO Small-Scale Fading," IEEE Journal on Selected Areas in Communications, vol. 38, no. 9, pp. 1964-1979, Sept. 2020.

[151] A. Pizzo, T. Marzetta and L. Sanguinetti, "Holographic MIMO Communications Under Spatially-Stationary Scattering," 2020 54th Asilomar Conference on Signals, Systems, and Computers, Pacific Grove, CA, USA, November 2020, pp. 702-706.

[152] A. Pizzo, L. Sanguinetti and T. L. Marzetta, "Fourier Plane-Wave Series Expansion for Holographic MIMO Communications," IEEE Transactions on Wireless Communications,

vol. 21, no. 9, pp. 6890-6905, September 2022.

[153] H. Zhang, C. You, and C. Zhou. "Near-Field Beam Focusing Under Discrete Phase Shifters," arXiv preprint arXiv:2409.14685, 2024.

[154] K. Zhi, C. Pan, H, Ren, et al., "Performance Analysis and Low-Complexity Design for XL-MIMO With Near-Field Spatial Non-Stationarities," IEEE Journal on Selected Areas in Communications, vol. 42, no. 6, pp. 1656-1672, June 2024.

[155] T. Gong, P. Gavriilidis, and R Ji, et al., "Holographic MIMO Communications: Theoretical Foundations, Enabling Technologies, and Future Directions," IEEE Communications Surveys & Tutorials, vol. 26, no. 1, pp. 196-257, Firstquarter 2024.

[156] S. S. A. Yuan, L. Wei, X. Chen, C. Huang and W. E. I. Sha, "Electromagnetic Normalization of Channel Matrix for Holographic MIMO Communications," IEEE Transactions on Wireless Communications.

[157] G. T. Ruck, D. E. Barrick, and W. D. Stuart, et al., "Radar Cross Section Handbook," Peninsula Publishing, New York, 1970.

[158] E. F. Knott, J. F. Shaeffer, and M. T. Tuley, "Radar Cross Section," Institution of Engineering and Technology, 2004.

[159] "IEEE Recommended Practice for Radar Cross-Section Test Procedures," IEEE Std 1502-2020 (Revision of IEEE Std 1502-2007) , vol., no., pp.1-78, 29 December 2020.

[160] J. Melin, "Measuring Radar Cross Section at Short Distance," IEEE Transactions on Antennas and Propagation, vol. 35, no. 8, pp. 991-996, August 1987.

[161] X. Sheng, W. Song, "Essentials of Computational Electromagnetics", John Wiley and Sons Singapore Pte. Ltd, 2012.

[162] I. J. LaHaie, E. I. LeBaron and J. W. Burns, "Far field Radar Cross-Section (RCS) Predictions from Planar Near Field Measurements," IEEE Antennas and Propagation Society International Symposium 1992 Digest, Chicago, IL, USA, 1992, pp. 1542-1545 vol.3.

[163] I. J. LaHaie, "Overview of An Image-Based Technique for Predicting Far-Field Radar Cross Section from Near-Field Measurements," IEEE Antennas and Propagation Magazine, vol. 45, no. 6, pp. 159-169, December 2003.

[164] I. J. LaHaie, and S. A. Rice, "Antenna-Pattern Correction for Near-Field-To-Far Field RCS Transformation of 1D Linear SAR Measurements," IEEE Antennas and Propagation Magazine, vol. 46, no. 4, pp. 177-183, Aug. 2004.

[165] C. Coleman, I. Lahaie, and S. Rice, "Antenna Pattern Correction for The Circular Near Field-To-Far Field Transformation (CNFFFT)," Antenna Measurement Techniques Association,27th Annual Meeting & Symposium 2005.

[166] I. J. Lahaie, C. M. Coleman, and A. Scott. Rice, "An Improved Version of The Circular Near Field-To-Far Field Transformation (CNFFFT) ," 27th Annual Meeting of the Antenna Measurement Techniques Association (AMTA'05), Newport, RI, F, 2005.

[167] S. A. Rice, I. J. Lahaie, "A Partial Rotation Formulation of The Circular

Near-Field-To-Far-Field Transformation (CNFFFT) ,” IEEE Antennas Propagation Magazine, 2007, 49(3): 209-14.

[168] J. Zhang, Z. Zheng, and Y. Zhang, et al., “3D MIMO for 5G NR: Several Observations from 32 to Massive 256 Antennas Based on Channel Measurement,” IEEE Communications Magazine, vol. 56, no. 3, pp. 62-70, Mar. 2018.

[169] J. Zhang, H. Miao, and P. Tang, et al., “New Mid-Band for 6G: Several Considerations from Channel Propagation Characteristics Perspective,” IEEE Communications Magazine, Accepted, 2024.

[170] P. Tang, J. Zhang, and H. Xu, et al., “Preliminary Perspectives on 3GPP Standardization of The Propagation Channel Model for FR3 Bands for NR,” Science China Information Sciences, 2025, 68(3):1-2.

[171] M. Li, Z. Yuan,and Y. Lyu, “Gigantic MIMO Channel Characterization: Challenges and Enabling Solutions,” IEEE Communications Magazine, vol. 61, no. 10, pp. 140-146, October 2023.

[172] E. Bjornson, L. Sanguinetti, and H. Wymeersch, et al., “Massive MIMO Is A Reality-What Is Next? Five Promising Research Directions for Antenna Arrays,” Digital Signal Process., vol. 94, pp. 320, Nov. 2019.

[173] P. Tang, J. Zhang, and H. Miao, et al., “XL-MIMO Channel Measurement, Characterization, and Modeling for 6G: A Survey,” Frontiers of Information Technology & Electronic Engineering. Available: https://jzus.zju.edu.cn/iparticle.php, August 2024.

[174] H. Miao, P. Tang, and L. Tian, et al., “Analysis of Near-Field Effects, Spatial Non-Stationary Characteristics Based on 11-15 GHz Channel Measurement in Indoor Scenario,” IEEE 25th International Workshop on Signal Processing Advances in Wireless Communications, 2024, pp. 231-235.

[175] J. Zhang, Y. Zhang, and Y. Yu, et al., “3-D MIMO: How Much Does It Meet Our Expectations Observed From Channel Measurements?,” IEEE Journal on Selected Areas in Communications, vol. 35, no. 8, pp. 1887-1903, Aug. 2017.

[176] X. Li, E. Leitinger, and M. Oskarsson, et al., “Massive MIMO-Based Localization and Mapping Exploiting Phase Information of Multipath Components,” IEEE Transactions on Wireless Communications, vol. 18, no. 9, pp. 4254-4267, Sept. 2019.

[177] Y. Zheng,C. Wang, and R. Yang, et al., “Ultra-Massive MIMO Channel Measurements at 5.3 GHz and a General 6G Channel Model,” IEEE Transactions on Vehicular Technology, vol. 72, no. 1, pp. 20-34, Jan. 2023.

[178] Y. Lyu, Z. Yuan, and M. Li, et al., “Enabling Long-Range Large-Scale Channel Sounding at Sub-THz Bands: Virtual Array and Radio-Over-Fiber Concepts,” IEEE Communications Magazine, vol. 62, no. 2, pp. 16-22, February 2024.

[179] J. Medbo, H. Asplund and J. -E. Berg, “60 GHz Channel Directional Characterization Using Extreme Size Virtual Antenna Array,” 2015 IEEE 26th Annual International Symposium on Personal, Indoor, and Mobile Radio Communications (PIMRC), Hong Kong, China, 2015,

pp. 176-180.

[180] X. Gao, F. Tufvesson, and O. Edfors, et al., "Measured Propagation Characteristics for Very-Large MIMO at 2.6 GHz," 2012 Conference Record of the Forty Sixth Asilomar Conference on Signals, Systems and Computers (ASILOMAR), 2012, pp. 295-299.

[181] J. Li, Y. Zhao, "Channel Characterization and Modeling for Large-scale Antenna Systems," 2014 14th International Symposium on Communications and Information Technologies (ISCIT), Incheon, Korea (South), 2014, pp. 559-563.

[182] B. Ai, K. Guang, and R. He, et al., "On Indoor Millimeter Wave Massive MIMO Channels: Measurement and Simulation," IEEE Journal on Selected Areas in Communications, vol. 35, no. 7, pp. 1678-1690, July. 2017.

[183] C. Wang, J. Zhang, and L. Tian, et al., "The Spatial Evolution of Clusters in Massive MIMO Mobile Measurement at 3.5 GHz," Proc. IEEE VTC, 2017, pp. 1-6.

[184] Q. Wei，P. Tang, and H. Miao, et al., "Measurement-Based Analysis of XL-MIMO Channel Characteristics in a Corridor Scenario," 2024 IEEE 99th Vehicular Technology Conference (VTC2024-Spring), Singapore, Singapore, 2024, pp. 1-6,

[185] "METIS channel models," document Deliverable/ICT-317669/D1.4 V3,Tech. Rep., Mar.2017.

[186] J. Zhang, J. Lin ,and P. Tang, et al., "Deterministic Ray Tracing: A Promising Approach to THz Channel Modeling in 6G Deployment Scenarios", IEEE Communication Magazine, vol. 62, no. 2, pp. 48-54, February 2024.

[187] L. Liu, C. Oestges, and J. Poutanen, et al., "The COST 2100 MIMO Channel Model," IEEE Wireless Communication, vol. 19, no. 6, pp. 92-99, December 2012.

[188] X. Gao, F. Tufvesson, and O. Edfors, "Massive MlMO channels - Measurements and models," 2013 AsilomarConference on Signals, Systems and Computers, Pacific Grove, CA, USA, 2013, pp. 280-284.

[189] E. T. Michailidis, N. Nomikos, and P. Trakadas et al., "Three-dimensional Modeling of mmwave Doubly Massive MIMO Aerial Fading Channels," IEEE Transactions on Vehicular Technology , vol. 69, no. 2, pp. Feb. 1190-1202, February.2020.

[190] W. Zuo, P. Tang, and H. Miao et al., "Analysis of Spatial Non-Stationary Characteristics for 6G XL-MIMO Communication, " 2024 Vehicular Technology Conference (VTC2024-Spring), Singapore, Singapore, 2024, pp. 1-6.

[191] Z. Yuan, J. Zhang, and V. Degli-Esposti, et al., "Efficient Ray-tracing Simulation for Near-field Spatial Non-stationary mmWave Massive MIMO Channel and Its Experimental Validation, " IEEE Transactions on Wireless Communications, vol. 23, no. 8, pp. 8910-8923, August. 2024.

[192] Z. Yuan, J. Zhang, and Y. Ji, et al., "Spatial Non-Stationary Near-Field Channel Modeling and Validation for Massive MIMO Systems, " IEEE Transactions on Antennas and Propagation, vol. 71, no. 1, pp. 921-933, January. 2023.

[193] T. Gao, P. Tang, and L. Tian, et al., "A 3GPP-Like Channel Simulation Framework

Considering Near-field Spatial Non-stationary Characteristics of Massive MIMO," 2023 IEEE Globecom Workshops(GCWkshps)., Kuala Lumpur, Malaysia, 2023, pp. 1493-1498

[194] E. D. Carvalho, A. Ali, A. Amiri, M. Angjelichinoski and R. W. Heath, "Non-Stationarities in Extra-Large-Scale Massive MIMO," IEEE Wireless Communications, vol. 27, no. 4, pp. 74-80, August 2020,.

[195] E. Björnson, L. Sanguinetti, H. Wymeersch, et al., "Massive MIMO is a reality—What is next?: Five promising research directions for antenna arrays," Digital Signal Processing, vol. 94, no. 1, pp. 3-20, November. 2019.

[196] A. Amiri, M. Angjelichinoski, and R. W. Heath, "Extremely Large Aperture Massive MIMO: Low Complexity Receiver Architectures,". 2018 IEEE Globecom Workshops (GC Wkshps), Abu Dhabi, United Arab Emirates, 2018, pp. 1-6.

[197] A. Ali, E. D. Carvalho and R. W. Heath, "Linear Receivers in Non-Stationary Massive MIMO Channels With Visibility Regions,". IEEE Wireless Communications Letters, vol. 8, no. 3, pp. 885-888, June 2019..

[198] X. Li, S. Zhou, and J. Wang, "Capacity Analysis for Spatially Non-Wide Sense Stationary Uplink Massive MIMO Systems," IEEE Transactions on Wireless Communications, vol. 14, no. 12, pp. 7044-7056, December 2015.

[199] A. Amiri, S. Rezaie, C. N. Manchón and E. de Carvalho, "Distributed Receiver Processing for Extra-Large MIMO Arrays: A Message Passing Approach," IEEE Transactions on Wireless Communications, vol. 21, no. 4, pp. 2654-2667, April 2022.

[200] Y. Zhu, H. Guo and V. K. N. Lau, "Bayesian Channel Estimation in Multi-User Massive MIMO with Extremely Large Antenna Array," IEEE Transactions on Signal Processing, vol. 69, pp. 5463-5478, September 2021.

[201] Y. Han, S. Jin, C. -K. Wen and X. Ma, "Channel Estimation for Extremely Large-Scale Massive MIMO Systems," IEEE Wireless Communication Letters, vol. 9, no. 5, pp. 633-637, May 2020.

[202] Z. Dong, X. Li, and Y. Zeng, et al, "Near-Field Spatial Correlation for Multi-Path XL-Array Communications with Partial Visibility," 2023 IEEE Global Commun. Conf. (GLOBECOM), Kuala Lumpur, Malaysia, 2023, pp. 1525-1530.

[203] Y. Liu, Z. Wang, and J. Xu, et al., "Near-Field Communications: A Tutorial Review," IEEE Open Journal of the Communications Society., vol. 4, pp. 1999-2049, August. 2023.

[204] Y. Liu, J. Xu, and Z. Wang, et al., "Near-field Communications: What Will Be Different?" IEEE Wireless Communications, vol. 32, no. 2, pp. 262-270, April 2025.

[205] L. Wei, C. Huang, and Z.Zhang, et al., "Multi-User Holographic MIMO Surfaces: Channel Modeling and Spectral Efficiency Analysis," IEEE Journal of Selected Topics in Signal Processing, vol. 16, no. 5, pp. 1112-1124, August. 2022.

[206] L. Wei, C. Huang, and Z.Yang, et al., "Tri-Polarized Holographic MIMO Surfaces for Near-Field Communications: Channel Modeling and Precoding Design," IEEE Transactions on Wireless Communications, vol. 22, no. 12, pp. 8828-8842, December. 2023.

[207] H. Jiang, W. Shi, and Z. Zhang, et al., "Large-Scale RIS Enabled Air-Ground Channels: Near-Field Modeling and Analysis," IEEE Trans. Wireless Commun, vol. 24, no. 2, pp. 1074-1088, February. 2025.

[208] H. Jiang, B. Xiong, and H. Zhang, et al., "Physics-Based 3D End-to-End Modeling for Double-RIS Assisted Non-Stationary UAV-to-Ground Communication Channels," IEEE Trans. Commun., vol. 71, no. 7, pp. 4247-4261, July 2023.

[209] B. Xiong, Z. Zhang, and H. Jiang, et al., "A 3D non-stationary MIMO channel model for reconfigurable intelligent surface auxiliary UAV-to-ground mmWave communications," IEEE Trans. Wireless Commun., vol. 21, no. 7, pp. 5658-5672, July 2022.

[210] B. Xiong, Z. Zhang and H. Jiang, et al., "A statistical MIMO channel model for reconfigurable intelligent surface assisted wireless communications," IEEE Trans. Commun., vol. 70, no. 2, pp. 1360-1375, February. 2022.

[211] H. Jiang et al., "Hybrid Far- and Near-Field Modeling For Reconfigurable Intelligent Surface Assisted V2VChannels: A sub-array Partition Based Approach," IEEE Trans. Wireless Commun., vol. 22, no. 11, pp. 8290-8303, November. 2023.

[212] H. Jiang et al., "A General Wideband Non-Stationary StochasticChannel Model For Intelligent Reflecting Surface-Assisted MIMO Communications," IEEE Trans. Wireless Commun., vol. 20, no. 8, pp. 5314-5328, August. 2021.

[213] H. Jiang et al., "Three-Dimensional Geometry-Based Stochastic Channel Modeling for Intelligent Reflecting Surface-Assisted UAV MIMO Communications," IEEE Wireless Commun. Lett., vol. 10, no. 12, pp. 2727-2731, December. 2021.

[214] B. Xiong et al., "Reconfigurable Intelligent Surface Auxiliary mmWave Communication: What if LoS path exists?" IEEE Wireless Commun. Lett., vol. 12, no. 2, pp. 247-251, Feb. 2023.

[215] H. Xing, Y. Zhang, J. Zhang, H. Xu, G. Liu ,and Q. Wang, "An Approximate Wave-Number Domain Expression for Near-Field XL-Array Channel," IEEE Trans. Veh. Technol.

[216] A. Pizzo, T. L. Marzetta and L. Sanguinetti, "Spatially-Stationary Model for Holographic MIMO Small-scale Fading," IEEE J. Sel. Areas Commun., vol. 38, no. 9, pp. 1964-1979, September. 2020.

[217] N. Agrawal, E. Tohidi, R. L. G. Cavalcante, and S. Stanczak, "Towards Bridging the Gap between Near and Far-Field Characterizations of the Wireless Channel", IEEE International Conference on Communications (ICC), Denver, USA, June 2024.

[218] M. Cui, and L. Dai, "Channel Estimation for Extremely Large-Scale MIMO: Far-Field or Near-field". IEEE Transactions on Communications, 2022, 70(4): 2663-2677.

[219] S. Liu, X. Yu, Z. Gao, and D. W. K. Ng, "DPSS-Based Codebook Design for Near-Field XL-MIMO Channel Estimation," ICC 2024 - IEEE International Conference on Communications, Denver, CO, USA, 2024, pp. 3864-3870.

[220] X. Zhang, H Zhang, Y C. Eldar, "Near-Field Sparse Channel Representation and Estimation in 6G Wireless Communications," IEEE Transactions on Communications, 2023.

[221] X. Zhang, Z. Yang, H. Zhang, et al., "Near-Field Channel Estimation for Extremely Large-Scale Array Communications: A Model-Based Deep Learning Approach ," IEEE Communications Letters, 2023, 27(4):1155-1159.

[222] W. Li, H. Yin, Z. Qin, et al., "Wavefront Transformation-Based Near-Field Channel Prediction for Extremely Large Antenna Array with Mobility," arXiv preprint arXiv:2312.02175, 2023.

[223] S. Yue, S. Zeng, L. Liu, and B. Di, "Channel Estimation For Holographic Communications in Hybrid Near-Far Field," 2023 IEEE Global Communications Conference (GLOBECOM). Kuala Lumpur, Malaysia: IEEE, 2023: 1-6.

[224] L. Lu, K. Ma, and Z. Wang, "Block-Dominant Compressed Sensing for Near-Field Communications: Fundamentals, Solutions and Future Directions," arXiv preprint arXiv: 2403.12369, 2024.

[225] H. Wu, L. Lu, and Z. Wang, "Near-Field Channel Estimation in Dual-Band XL-MIMO with Side Information-Assisted Compressed Sensing," arXiv preprint arXiv: 2403.12620, 2024.

[226] X, Guo, Y. Chen, Y. Wang, "Compressed Channel Estimation for Near-Field XL-MIMO Using Triple Parametric Decomposition," IEEE Transactions on Vehicular Technology, 2023, 72(11): 15040-15045.

[227] Y. Chen, Y. Wang, Z. Wang, et al, "Angular-Distance Based Channel Estimation for Holographic MIMO[J]," arXiv preprint arXiv:2311.15158, 2023

[228] H. Lei, J. Zhang, H. Xiao, et al., "Channel Estimation for XL-MIMO Systems with Polar-Domain Multi-Scale Residual Dense Network, "IEEE Transactions on Vehicular Technology, 2023.

[229] X. Shi, X. Wang, J. Tan, and J. Wang, "Sparse Estimation for XL-MIMO with Unified LoS/NLoS Representation," 2024 IEEE International Conference of Communication (ICC). Denver, USA: IEEE, 2024.

[230] Y. Jin, J. Zhang, C. Huang, et al., "Multiple Residual Dense Networks for Reconfigurable Intelligent Surfaces Cascaded Channel Estimation", IEEE Transactions on Vehicular Technology, 2021, 71(2): 2134-2139.

[231] W. Yu, Y. Shen, H. He, S. Song, J. Zhang, B Letaief K., "An Adaptive and Robust Deep Learning Framework for THz Ultra-Massive MIMO Channel Estimation", IEEE Journal of Selected Topics in Signal Processing, 2023, 71(4): 761-776.

[232] W. Yu, Y. Shen, H. He, S. Song, J. Zhang, Murch R, B Letaief K, "Bayes-Optimal Unsupervised Learning for Channel Estimation in Near-Field Holographic MIMO", IEEE Journal of Selected Topics in Signal Processing, 2024, 18(4): 714-729.

[233] W. Yu, H. He, X. Yu, S. Song, J. Zhang, B Letaief K, "Blind Performance Prediction for Deep Learning Based Ultra-Massive MIMO Channel Estimation", 2023 IEEE International Conference on Communications (ICC), Rome, Italy: IEEE, 2023: 2613-2618.

[234] W. Yu, Y. Ma, H. He, S. Song, J. Zhang, B Letaief K, "Deep Learning for Near-Field XL-MIMO Transceiver Design: Principles and Techniques," IEEE Communications

Magazine, 2025, 63(1): 52-58.

[235] W. Yu, Y. Ma, H. He, S. Song, J. Zhang, B Letaief K, " Deep Learning for Near-Field XL-MIMO Transceiver Design: Principles and Techniques," IEEE Communications Magazine, 2025, 63(1): 52-58.

[236] C. You, Y. Cai, Y. Liu, M. Di Renzo, T. M. Duman, A. Yener, and A. L. Swindlehurst, "Next Generation Advanced Transceiver Technologies for 6G and beyond," arXiv preprint arXiv:2403.16458, 2024.

[237] C. Zhou, C. You, S. Gong, B Lyu, B. Zheng, Y. Gong, "Channel Estimation for XL-IRS Assisted Wireless Systems with Double-Sided Visibility Regions," arXiv preprint arXiv:2408.17014, 2024.

[238] H. Miao, F. Zhang, and R. Tao, "Fractional Fourier Analysis Using the Möbius Inversion Formula," IEEE Transactions on Signal Processing, 2019, 67(12): 3181-3196.

[239] M. Jian, A. Tang, Y. Chen and Y. Zhao, "Fractional Fourier Transformation Based XL-MIMO Near-Field Channel Analysis," 2024 IEEE 25th International Workshop on Signal Processing Advances in Wireless Communications (SPAWC), Lucca, Italy, 2024, pp. 221-225.

[240] P. -Z. Xu, W. Xiang and Q. -Y. Yu, "DFrFT-Based Near-Field Channel Estimation for Extremely Large-Scale MIMO Systems," IEEE Communications Letters, vol. 28, no. 8, pp. 1914-1918, August. 2024.

[241] H. Miao, and M. Peng, "Near-field High-speed User Sensing in Wideband mmWave Communications: Algorithms and Bounds," IEEE Transactions on Signal Processing, vol. 73, pp. 919-935, 2025.

[242] Y. Xi, F. Zhu, B. Zhou, et al., "Gridless Hybrid-Field Channel Estimation for Extra-Large Aperture Array Massive MIMO Systems," IEEE Wireless Communications Letters, vol. 13, no. 2, pp. 496-500, February 2024.

[243] B. Xu,J. Zhang, H. Du, et al., "Resource Allocation for Near-field Communications: Fundamentals, Tools, and Outlooks," arXiv preprint arXiv:2310.17868, 2023.

[244] J. Zhang, J. Zhang, Y. Han, et al., "Average Spectral Efficiency for TDD-based Non-stationary XL-MIMO with VR Estimation," 2022 14th International Conference on Wireless Communications and Signal Processing (WCSP). Nanjing, China: IEEE, 2022: 973-977.

[245] J. Tian, Y. Han, S. Jin, et al., "Low-overhead Localization and VR Identification for Subarray-based ELAA Systems," IEEE Wireless Communications Letters, vol. 12, no. 5, pp. 784-788, May 2023.

[246] Y. Chen, and L. Dai, "Non-stationary Channel Estimation for Extremely Large-scale MIMO," IEEE Transactions on Wireless Communications, vol. 23, no. 7, pp. 7683-7697, July 2024.

[247] Y. Han, S. Jin, C. Wen, et al., "Localization and Channel Reconstruction for Extra Large RIS-assisted Massive MIMO Systems," IEEE Journal of Selected Topics in Signal

Processing, vol. 16, no. 5, pp. 1011-1025, August 2022.

[248] Y. Chen, M. Jian, and L. Dai, "Channel Estimation for RIS Assisted Wireless Communications: Stationary or Non-stationary?," IEEE Transactions on Signal Processing, vol. 72, pp. 3776-3791, 2024.

[249] D. Liu, J. Wang, Y. Li, et al., "Location-based Visible Region Recognition in Extra-large Massive MIMO Systems," IEEE Transactions on Vehicular Technology, vol. 72, no. 6, pp. 8186-8191, June 2023.

[250] M. Najafi, V. Jamali, R. Schober, et al., "Physics-based Modeling and Scalable Optimization of Large Intelligent Reflecting Surfaces," IEEE Transactions on Communications, vol. 69, no. 4, pp. 2673-2691, April 2021.

[251] Z. Zhang, et al., "Active RIS vs. Passive RIS: Which Will Prevail in 6G?," IEEE Transactions on Communications, vol. 71, no. 3, pp. 1707-1725, March 2023.

[252] E. Basar, and H. V. Poor, "Present and Future of Reconfigurable Intelligent Surface-empowered Communications," IEEE Signal Processing Magazine, vol. 38, no. 6, pp. 146-152, November 2021.

[253] A. L. Swindlehurst, G. Zhou, R. Liu, et al., "Channel Estimation with Reconfigurable Intelligent Surfaces—a General Framework," Proceedings of the IEEE, vol. 110, no. 9, pp. 1312-1338, September 2022.

[254] Y. Zhu, Y. Liu, Q. Wu, et al., "Channel Estimation by Transmitting Pilots from Reconfigurable Intelligent Surface," IEEE Transactions on Wireless Communications, vol. 23, no. 4, pp. 3328-3343, April 2024.

[255] X. Wei, and L. Dai, "Channel Estimation for Extremely Large-Scale Massive MIMO: Far-Field, Near-Field, or Hybrid-Field?," IEEE Communications Letters, vol. 26, no. 1, pp. 177-181, January 2022.

[256] H. Zhang, N Shlezinger, F. Guidi, et al., "Beam Focusing for Near-field Multi-user MIMO Communications," IEEE Transactions on Wireless Communications, vol. 21, no. 9, pp. 7476-7490, September 2022.

[257] H. Zhang, N. Shlezinger, F. Guidi, et al., "6G Wireless Communications: From Far-field Beam-steering to Near-field Beam-focusing," IEEE Communications Magazine, vol. 61, no. 4, pp. 72-77, April 2023.

[258] P. Ramezani, A. Kosasih, A. Irshad, et al., "Exploiting the Depth and Angular Domains for Massive Near-field Spatial Multiplexing." IEEE BITS the Information Theory Magazine, vol. 3, no. 1, pp. 14-26, March 2023.

[259] J. Wang, X. Zhang, X. Shi, et al., "Higher Spectral Efficiency for mmWave MIMO: Enabling Techniques and Precoder Designs," IEEE Communications Magazine, vol. 59, no. 4, pp. 116-122, April 2021.

[260] F. Gao, B. Wang, C. Xing, et al., "Wideband Beamforming for Hybrid Massive MIMO Non-terrestrial Communications," 2023 IEEE 98th Vehicular Technology Conference (VTC2023-Fall), Hong Kong, Hong Kong, 2023, pp. 1-5.

[261] L. Dai, J. Tan, Z. Chen, et al., "Delay-phase Precoding for Wideband THz Massive MIMO," IEEE Transactions on Wireless Communications, vol. 21, no. 9, pp. 7271-7286, September 2022.

[262] Z. Wang, X. Mu, and Y. Liu. "Beamfocusing Optimization for Near-field Wideband Multi-user Communications," IEEE Transactions on Communications, vol. 73, no. 1, pp. 555-572, January 2025.

[263] X. Zheng, W. Cheng, J. Wang, et al., "Location-Driven Beamforming for RIS-Assisted Near-Field Communications," IEEE Communications Magazine, vol. 63, no. 1, pp. 44-50, January 2025.

[264] X. Zheng, W. Cheng, and J. Wang, "Huygens-Fresnel Model Based Position-Aided Phase Configuration for 1-bit RIS Assisted Wireless Communication," IEEE Transactions on Communications, vol. 72, no. 8, pp. 5102-5116, August 2024.

[265] Z. Wang, X. Mu, Y. Liu, et al., "TTD Configurations for Near-field Beamforming: Parallel, Serial, or Hybrid?," IEEE Transactions on Communications, vol. 72, no. 6, pp. 3783-3799, June 2024.

[266] H. Zhang, C. You, and C. Zhou. "Near-field Beam Focusing Under Discrete Phase Shifters." arXiv preprint arXiv:2409.14685, 2024.

[267] C. Zhou, C. You, H. Zhang, et al., "Sparse Array Enabled Near-field Communications: Beam Pattern Analysis and Hybrid Beamforming Design," arXiv preprint axXiv:2401.05690, 2024.

[268] H. Zhang, C. You, and C. Zhou. "Near-field Beam Focusing Under Discrete Phase Shifters." arXiv preprint arXiv:2409.14685, 2024.

[269] B. Xu, J. Zhang, J. Li, et al., "Jac-PCG Based Low-complexity Precoding for Extremely Large-scale MIMO Systems," IEEE Transactions on Vehicular Technology, vol. 72, no. 12, pp. 16811-16816, December 2023.

[270] X. Li, X. Wang, X. Hou, et al., "RIS-aided Mega MIMO: Achieving Orthonormal Spatial Multiplexing with Adaptive Aperture," 2022 IEEE Globecom Workshops (GC Wkshps), Rio de Janeiro, Brazil, 2022, pp. 692-698.

[271] X. Tian, N. Gonzalez-Prelcic, and R. W. Heath, "Variable Beamwidth Near Field Codebook Design for Communications Aided by A Large Scale RIS," in Proc. IEEE GLOBECOM, Kuala Lumpur, Malaysia, Dec. 2023.

[272] V. Jamali, G. C. Alexandropoulos, and R. Schober, et al., "Low-to-zero-overhead IRS Reconfiguration: Decoupling Illumination and Channel Estimation," IEEE Commun. Letters, vol. 26, no. 4, pp. 932-936, 2022.

[273] K. Chen, C. Qi, and Y. Li, et al., Near-field Multiuser Communications Based on Sparse Arrays[J]. IEEE Journal of Selected Topics in Signal Processing, 2024.

[274] F. Zheng, H. Yu, and C. Wang, et al., Extremely Large-scale Array Systems: Near-filed Codebook Design and Performance analysis[J]. arXiv preprint arXiv:2306.01458, 2023.

[275] X. Li, X. Wang, and X. Hou, et al., "Two-Step Beamforming Scheme for Large-Dimension

Reconfigurable Intelligent Surface," 2022 IEEE 95th Vehicular Technology Conference: (VTC2022-Spring), Helsinki, Finland, 2022, pp. 1-5.

[276] F. Wang, X. Wang, and X Li, et al., "Ring-type Codebook Design for Reconfigurable Intelligent Surface Near-field Beamforming," 2022 IEEE 33rd Annual International Symposium on Personal, Indoor and Mobile Radio Communications (PIMRC), Kyoto, Japan, 2022, pp. 391-396.

[277] F. Wang, X. Hou, and X. Li, et al., "Flexible Coverage Control of Reconfigurable Intelligent Surface with Ring-Type Codebook," 2024 IEEE Wireless Communications and Networking Conference (WCNC), Dubai, United Arab Emirates, 2024, pp. 1-6.

[278] Y. Zhang, B. Di, and H. Zhang, et al., "Codebook Design for Large Reconfigurable Refractive Surface Enabled Holographic MIMO Systems," GLOBECOM 2022 - 2022 IEEE Global Communications Conference, Rio de Janeiro, Brazil, 2022, pp. 639-644.

[279] Y. Zhang, B. Di, and H. Zhang, et al., Near-far Field Beamforming for Holographic Multiple-input Multiple-output. Journal of Communications and Information Networks, 2023, 8(2): 99-110.

[280] S. Zhang, Y. Zhang, and B. Di, "Near-Far Field Codebook Design for IOS-Aided Multi-User Communications," GLOBECOM 2023 - 2023 IEEE Global Communications Conference, Kuala Lumpur, Malaysia, 2023, pp. 2888-2893.

[281] Y. Zhang, X. Wu, and C. You, "Fast Near-Field Beam Training for Extremely Large-Scale Array," IEEE Wireless Communications Letters, vol. 11, no. 12, pp. 2625-2629, Dec. 2022.

[282] X. Wu, C. You, and J. Li, et al., "Near-Field Beam Training: Joint Angle and Range Estimation With DFT Codebook," IEEE Transactions on Wireless Communications, vol. 23, no. 9, pp. 11890-11903, Sept. 2024.

[283] K. Chen, C. Qi, and C. Wang, et al., "Beam Training and Tracking for Extremely Large-Scale MIMO Communications," IEEE Transactions on Wireless Communications, vol. 23, no. 5, pp. 5048-5062, May 2024.

[284] K. Chen, C. Qi, and O. A. Dobre, et al., "Triple-Refined Hybrid-Field Beam Training for mmWave Extremely Large-Scale MIMO," IEEE Transactions on Wireless Communications, vol. 23, no. 8, pp. 8556-8570, Aug. 2024.

[285] C. Wu, C. You, and Y. Liu, et al., "Two-Stage Hierarchical Beam Training for Near-Field Communications," IEEE Transactions on Vehicular Technology, vol. 73, no. 2, pp. 2032-2044, Feb. 2024.

[286] Y. Lu, Z. Zhang, and L. Dai, "Hierarchical Beam Training for Extremely Large-Scale MIMO: From Far-Field to Near-Field," IEEE Transactions on Communications, vol. 72, no. 4, pp. 2247-2259, April 2024.

[287] X. Shi, J. Wang, and Z.Sun, et al., "Spatial-chirp Codebook-based Hierarchical Beam Training for Extremely Large-scale Massive MIMO". IEEE Transactions on Wireless Communications, 2023.

[288] M. Cui, L. Dai,and Z. Wang, et al., "Near-Field Rainbow: Wideband Beam Training for

XL-MIMO," IEEE Transactions on Wireless Communications, vol. 22, no. 6, pp. 3899-3912, June 2023.

[289] W. Liu, H. Ren, and C. Pan, et al., "Deep Learning Based Beam Training for Extremely Large-Scale Massive MIMO in Near-Field Domain," IEEE Communications Letters, vol. 27, no. 1, pp. 170-174, Jan. 2023.

[290] W. Liu, C. Pan, and H. Ren, et al., "Low-Overhead Beam Training Scheme for Extremely Large-Scale RIS in Near Field," IEEE Transactions on Communications, vol. 71, no. 8, pp. 4924-4940, Aug. 2023.

[291] G. Jiang and C. Qi, "Near-Field Beam Training Based on Deep Learning for Extremely Large-Scale MIMO," IEEE Communications Letters, vol. 27, no. 8, pp. 2063-2067, Aug. 2023.

[292] X. Li, Z. Dong, and Y. Zeng, et al., "Codebook Design and Beam Training for Multi-user Modular XL-MIMO Communications: From far-field to near-field," submitted to IEEE Trans. Commun., 2024.

[293] C. Zhou, C. You, Z. Huang, S. Shi., Y. Gong, C.-B. Chae and K. Huang, "Multi-beam Training for Near-field Communications in High-frequency Bands," arXiv preprint axXiv: 2406.14931, 2024.

[294] C. Zhou, C. Wu, C. You, J. Zhou and S. Shi, "Near-field Beam training with Sparse DFT Codebook," arXiv preprint axXiv: 2409.14685, 2024.

[295] E. T. Michailidis, N. Nomikos, and P. Trakadas, et al., "Three-Dimensional Modeling of mmWave Doubly Massive MIMO Aerial Fading Channels," IEEE Transactions on Vehicular Technology, vol. 69, no. 2, pp. 1190-1202, Feb. 2020.

[296] W. Yi, J. Zhang, and Z. Wang, et al.,"Mobility-Aware Predictive Beam Training of Extremely Large-scale MIMO-OFDM Systems for High-Speed Railway", submitted to IEEE Transactions on Intelligent Transportation Systems, 2024.

[297] Z. Wang, J. Zhang, and H. Duet, et al., "A Tutorial on Extremely Large-Scale MIMO for 6G: Fundamentals, Signal Processing, and Applications," IEEE Communications Surveys & Tutorials, vol. 26, no. 3, pp. 1560-1605, thirdquarter 2024.

[298] Y. Zhang, X. Wu, and C. You, "Fast Near-Field Beam Training for Extremely Large-Scale Array," IEEE Wireless Communications Letters, vol. 11, no. 12, pp. 2625-2629, Dec. 2022.

[299] M. Cui, L. Dai, Z. Wang, S. Zhou and N. Ge, "Near-Field Rainbow: Wideband Beam Training for XL-MIMO," IEEE Transactions on Wireless Communications, vol. 22, no. 6, pp. 3899-3912, June 2023.

[300] Y. Chen and L. Dai, "Near-field Wideband Beam training for ELAA with Uniform Circular Array," Sci. China Inf. Sci., vol. 67, no. 6, pp. 162303, May 2024.

[301] Z. Wu, L. Dai, "Multiple Access for Near-Field Communications: SDMA or LDMA?," IEEE Journal on Selected Areas in Communications, vol. 41, no. 6, pp. 1918-1935, June 2023.

[302] N. Agrawal, E. Tohidi, R. L. G. Cavalcante, et al., "Towards Bridging the Gap Between

Near and Far-Field Characterizations of the Wireless Channel," ICC 2024 - IEEE International Conference on Communications, Denver, CO, USA, 2024, pp. 4464-4469.

[303] Z. Ding, "Resolution of Near-Field Beamforming and its Impact on NOMA," arXiv preprint arXiv:2308.08159, 2023.

[304] J. Zuo, X. Mu, and Y. Liu, "Non-Orthogonal Multiple Access for Near-Field Communications," arXiv preprint arXiv:2308.08159, 2023.

[305] Z. Ding, R. Schober and H. V. Poor, "NOMA-Based Coexistence of Near-Field and Far-Field Massive MIMO Communications," IEEE Wireless Communications Letters, vol. 12, no. 8, pp. 1429-1433, August 2023.

[306] Y. Polyanskiy, "A perspective on massive random-access," 2017 IEEE International Symposium on Information Theory (ISIT), Aachen, Germany, 2017, pp. 2523-2527.

[307] J. Gao, Y. Wu, T. Li, et al., "Energy Efficiency of MIMO Massive Unsourced Random Access With Finite Blocklength," IEEE Wireless Communications Letters, vol. 12, no. 4, pp. 743-747, April 2023.

[308] X. Xie, Y. Wu, J. An, et al., "Massive Unsourced Random Access: Exploiting Angular Domain Sparsity," IEEE Transactions on Communications, vol. 70, no. 4, pp. 2480-2498, April 2022.

[309] V. M. Baeza, "Multiuser non coherent massive mimo schemes based on dpsk for future communication systems," Tesis doct., Universidad Carlos III de Madrid, 2019.

[310] A. Schenk and R. F. H. Fischer, "Noncoherent Detection in Massive MIMO Systems," WSA 2013; 17th International ITG Workshop on Smart Antennas, Stuttgart, Germany, 2013, pp. 1-8.

[311] V. M. Baeza, A. G. Armada, "Performance and Complexity Tradeoffs of Several Constellations for Non Coherent Massive MIMO," 2019 22nd International Symposium on Wireless Personal Multimedia Communications (WPMC), Lisbon, Portugal, 2019, pp. 1-6.

[312] C. You, B. Zheng, W. Mei, et al., "How to Deploy Intelligent Reflecting Surfaces in Wireless Network: BS-Side, User-Side, or Both Sides?," Journal of Communications and Information Networks, vol. 7, no. 1, pp. 1-10, March 2022.

[313] B. Zheng and R. Zhang, "IRS Meets Relaying: Joint Resource Allocation and Passive Beamforming Optimization," IEEE Wireless Communications Letters, vol. 10, no. 9, pp. 2080-2084, September 2021.

[314] J. Feng, B. Zheng, C. You, et al., "Joint Passive Beamforming and Deployment Design for Dual Distributed-IRS Aided Communication," IEEE Transactions on Vehicular Technology, vol. 72, no. 10, pp. 13758-13763, October 2023.

[315] B. Zheng, C. You and R. Zhang, "Double-IRS Assisted Multi-User MIMO: Cooperative Passive Beamforming Design," IEEE Transactions on Wireless Communications, vol. 20, no. 7, pp. 4513-4526, July 2021.

[316] Y. Zhao, "RIS Constructing 6G Near-Field Networks: Opportunities and Challenges," arXiv:2403.15390, 2024.

[317] A. Guerra, F. Guidi, D. Dardari, et al., "Near-Field Tracking With Large Antenna Arrays: Fundamental Limits and Practical Algorithms," IEEE Transactions on Signal Processing, vol. 69, pp. 5723-5738, 2021.

[318] 3GPP(2020),Study on Channel Model for Frequencies from 0.5 to 100 GHz", V16.1.0.Tech. Rep. 38.901.

[319] 3GPP. RP-234018, Channel Modelling Enhancements for 7-24 GHz. 3GPP TSG RAN Meeting #102, Edinburgh, UK, 11th – 15th December, 2023.

[320] S. Kim, J. Moon, J. Wu, et al., "Vision-Aided Positioning and Beam Focusing for 6G Terahertz Communications," IEEE Journal on Selected Areas in Communications, vol. 42, no. 9, pp. 2503-2519, September 2024.

[321] A. Elzanaty, J. Liu, A. Guerra, et al., "Near and Far Field Model Mismatch: Implications on 6G Communications, Localization, and Sensing." ArXiv abs/2310.06604, 2023.

[322] A. Chen, L. Chen, et al., "Near-Field Positioning and Attitude Sensing Based on Electromagnetic Propagation Modeling," ArXiv, vol. abs/2310.17327, 2023.

[323] A. Chen, L. Chen, Y. Chen, et al., "Cramér-Rao Bounds of Near-Field Positioning Based on Electromagnetic Propagation Model," IEEE Transactions on Vehicular Technology, vol. 72, no. 11, pp. 13808-13825, November 2023.

[324] A. Elzanaty, A. Guerra, F. Guidi, et al., "Toward 6G Holographic Localization: Enabling Technologies and Perspectives," IEEE Internet of Things Magazine, vol. 6, no. 3, pp. 138-143, September 2023.

[325] Q. Yang, A. Guerra, F. Guidi, et al., "Near-field Localization with Dynamic Metasurface Antennas," IEEE International Conference on Acoustics, Speech and Signal Processing (ICASSP). Rhodes Island, Greece: IEEE, 2023: 1-5.

[326] F. Guidi, D. Dardari, "Radio positioning with EM processing of the spherical wavefront," IEEE Transactions on Wireless Communications, vol. 20, no. 6, pp. 3571-3586, June 2021.

[327] A. Guerra, F. Guidi, and D. Dardari, "Single-Anchor Localization and Orientation Performance Limits Using Massive Arrays: MIMO vs. Beamforming," IEEE Transactions on Wireless Communications, vol. 17, no. 8, pp. 5241-5255, Augest 2018.

[328] A. Elzanaty, A. Guerra, F. Guidi, et al., "Toward 6G holographic localization: Enabling technologies and perspectives," IEEE Internet of Things Magazine, vol. 6, no. 3, pp. 138-143, September 2023.

[329] H. Wymeersch, B. Denis, "Beyond 5G wireless localization with reconfigurable intelligent surfaces," in ICC 2020 - 2020 IEEE International Conference on Communications (ICC), June 2020.

[330] D. Dardari, N. Decarli, A. Guerra, et al., "LOS/NLOS near-field localization with a large reconfigurable intelligent surface," IEEE Transactions on Wireless Communications, vol. 21, no. 6, pp. 4282-4294, June 2022.

[331] S. Palmucci, A. Guerra, A. Abrardo, et al., "Two-timescale Joint Precoding Design and RIS Optimization for User Tracking in Near-field MIMO Systems," IEEE Transactions on Signal

Processing, vol. 22, no. 12, pp. 8587-8602, Dec 2023.

[332] G. Torcolacci, A. Guerra, H. Zhang et al., "Holographic Imaging With XL-MIMO and RIS: Illumination and Reflection Design," IEEE Journal on Selected Topics in Signal Processing, vol. 18, no. 4, pp. 587–602, 2024.

[333] Z. Abu-Shaban, K. Keykhosravi, M. F. Keskin, et al., "Near-field Localization with a Reconfigurable Intelligent Surface Acting as Lens," ICC 2021 - IEEE International Conference on Communications, Montreal, QC, Canada, 2021, pp. 1-6.

[334] A. Elzanaty, A. Guerra, F. Guidi, et al., "Reconfigurable Intelligent Surfaces for Localization: Position and Orientation Error Bounds," IEEE Transactions on Signal Processing, vol. 69, pp. 5386-5402, 2021.

[335] D. Xia, X. Wang, J. Han, et al., "Accurate 2-D DoA Estimation Based on Active Metasurface With Nonuniformly Periodic Time Modulation," IEEE Transactions on Microwave Theory and Techniques, vol. 71, no. 8, pp. 3424-3435, 2023.

[336] Z. Zhang, W. Chen, W. Zheng, et al., "Localization of Near-Field Sources: A Reduced-Dimension MUSIC Algorithm," IEEE Communications Letters, vol. 22, no. 7, pp. 1422-1425, 2018.

[337] O. Rinchi, A. Elzanaty and M. -S. Alouini, "Compressive Near-Field Localization for Multipath RIS-Aided Environments," IEEE Communications Letters, vol. 26, no. 6, pp. 1268-1272, 2022.

[338] X. Gan, C. Huang, Z. Yang, et al., "Near-Field Localization for Holographic RIS Assisted mmWave Systems," IEEE Communications Letters, vol. 27, no. 1, pp. 140-144, 2023.

[339] A. Elzanaty, A. Guerra, F. Guidi, et al, "Toward 6G Holographic Localization: Enabling Technologies and Perspectives," IEEE Internet of Things Magazine, vol. 6, no. 3, pp. 138-143, 2023.

[340] D. Xia, J. Han, Y. Mu, et al. "Adaptive Wireless-powered Network Based on CNN Near-field Positioning by a Dual-band Metasurface," Nature Communications, vol. 15, no. 1, pp. 10358, 2024.

[341] Z. Abu-Shaban, K. Keykhosravi, M. F. Keskin, et al., "Near-field Localization with a Reconfigurable Intelligent Surface Acting as Lens," ICC 2021 - IEEE International Conference on Communications, Montreal, QC, Canada, 2021, pp. 1-6.

[342] B. Wang, F. Gao, S. Jin, et al., "Spatial- and Frequency-Wideband Effects in Millimeter-Wave Massive MIMO Systems," IEEE Transactions on Signal Processing, vol. 66, no. 13, pp. 3393-3406, 2018.

[343] H. Luo, F. Gao, H. Lin, et al., "YOLO: An Efficient Terahertz Band Integrated Sensing and Communications Scheme with Beam Squint," IEEE Transactions on Wireless Communications, vol. 23, no. 8, pp. 9389-9403, 2024.

[344] Y. Shen and M. Z. Win, "Fundamental Limits of Wideband Localization— Part I: A General Framework," IEEE Transactions on Information Theory, vol. 56, no. 10, pp. 4956-4980, 2010.

[345] I. Podkurkov, G. Seidl, L. Khamidullina, et al., "Tensor-Based Near-Field Localization Using Massive Antenna Arrays," IEEE Transactions on Signal Processing, vol. 69, pp. 5830-5845, 2021.

[346] H. Lu, Y. Zeng, C. You, et al., "A Tutorial on Near-Field XL-MIMO Communications Toward 6G," IEEE Communications Surveys & Tutorials, vol. 26, no. 4, pp. 2213-2257, 2024.

[347] Y. . -D. Huang and M. Barkat, "Near-field multiple source localization by passive sensor array," IEEE Transactions on Antennas and Propagation, vol. 39, no. 7, pp. 968-975, July 1991.

[348] Z. Zhou, Z. Xiao and Y. Zeng, "Single-BS Simultaneous Environment Sensing and UE Localization Without LoS Path by Exploiting Near-Field Scatterers," IEEE Communications Letters, vol. 28, no. 9, pp. 2071-2075, 2024.

[349] H. Lu and Y. Zeng, "Delay alignment modulation: Enabling equalization-free single-carrier communication," IEEE Wireless Commun. Lett., vol. 11, no. 9, pp. 1785–1789, Sep. 2022.

[350] H. Lu and Y. Zeng, "Delay Alignment Modulation: Enabling Equalization-Free Single-Carrier Communication," IEEE Wireless Communications Letters, vol. 11, no. 9, pp. 1785-1789, 2022.

[351] J. Xie, H. Tao, X. Rao, et al,. "Passive localization of noncircular sources in the near-field," 2015 16th International Radar Symposium (IRS), Dresden, Germany, 2015, pp. 493-498.

[352] X. Zhang, W. Chen, W. Zheng, et al., "Localization of Near-Field Sources: A Reduced-Dimension MUSIC Algorithm," IEEE Communications Letters, vol. 22, no. 7, pp. 1422-1425, 2018.

[353] S. Liu, X. Yu, Z. Gao, et al., "Sensing-Enhanced Channel Estimation for Near-Field XL-MIMO Systems," IEEE Journal on Selected Areas in Communications, vol. 43, no. 3, pp. 628-643, March 2025.

[354] S. Liu and X. Yu, "Low-Complexity Near-Field Localization with XL-MIMO Sectored Uniform Circular Arrays," GLOBECOM 2024 - 2024 IEEE Global Communications Conference, Cape Town, South Africa, 2024, pp. 4756-4761.

[355] H. Cheng, C. You, and C. Zhou, "Near-Field Localization with Coprime Array," arXiv preprint arXiv:2411.01529, 2024.

[356] H. Luo, F. Gao, W. Yuan, et al., "Beam Squint Assisted User Localization in Near-Field Integrated Sensing and Communications Systems," IEEE Transactions on Wireless Communications, vol. 23, no. 5, pp. 4504-4517, 2024.

[357] D. Dardari and D. Massari, "Using MetaPrisms for Performance Improvement in Wireless Communications," IEEE Transactions on Wireless Communications, vol. 20, no. 5, pp. 3295-3307, 2021.

[358] M. Lotti, G. Calesini and D. Dardari, "NLOS Localization Exploiting Frequency-selective Metasurfaces," 2024 IEEE International Conference on Communications Workshops (ICC Workshops), Denver, CO, USA, 2024, pp. 1012-1016.

[359] Z. Wang, X. Mu and Y. Liu, "Near-Field Integrated Sensing and Communications," IEEE Communications Letters, vol. 27, no. 8, pp. 2048-2052, 2023.

[360] H. Wang and Y. Zeng, "SNR Scaling Laws for Radio Sensing with Extremely Large-Scale MIMO," 2022 IEEE International Conference on Communications Workshops (ICC Workshops), Seoul, Korea, Republic of, 2022, pp. 121-126.

[361] H. Wang, Z. Xiao and Y. Zeng, "Cramér-Rao Bounds for Near-Field Sensing With Extremely Large-Scale MIMO," IEEE Transactions on Signal Processing, vol. 72, pp. 701-717, 2024.

[362] R. Boyer, "Performance Bounds and Angular Resolution Limit for the Moving Colocated MIMO Radar," IEEE Transactions on Signal Processing, vol. 59, no. 4, pp. 1539-1552, April 2011

[363] F. Liu et al., "Integrated Sensing and Communications: Toward Dual-Functional Wireless Networks for 6G and Beyond," IEEE Journal on Selected Areas in Communications, vol. 40, no. 6, pp. 1728-1767, June 2022.

[364] Z. Wang, X. Mu and Y. Liu, "Near-Field Velocity Sensing and Predictive Beamforming,"arXiv preprint arXiv:2311.09888, 2023.

[365] J. Feng et al., "Joint Passive Beamforming and Deployment Design for Dual Distributed-IRS Aided Communication," IEEE Transactions on Vehicular Technology, vol. 72, no. 10, pp. 13758-13763, Oct. 2023.

[366] H. Chen et al., "6G Localization and Sensing in the Near Field: Features, Opportunities, and Challenges," IEEE Wireless Communications, vol. 31, no. 4, pp. 260-267, August 2024.

[367] Z. Chen, L. Huang, H. C. So, et al., "Deep Reinforcement Learning Over RIS-Assisted Integrated Sensing and Communication: Challenges and Opportunities," IEEE Vehicular Technology Magazine.

[368] J. Cong, C. You, J. Li, et al. "Near-field Integrated Sensing and Communication: Opportunities and Challenges," arXiv preprint arXiv:2310.01342, 2023.

[369] C. You, Y. Zhang, C. Wu, et al. "Near-field Beam Management for Extremely Large-scale Array Communications, " arXiv preprint arXiv:2306.16206, 2023.

[370] A. Sakhnini, S. De Bast, M. Guenach, et al., "Near-Field Coherent Radar Sensing Using a Massive MIMO Communication Testbed," IEEE Transactions on Wireless Communications, vol. 21, no. 8, pp. 6256-6270, Aug. 2022.

[371] M. Lipka, S. Brückner, E. Sippel, et al., "On the Needlessness of Signal Bandwidth for Precise Holographic Wireless Localization," 2020 17th European Radar Conference (EuRAD), 2021, pp. 202–205.

[372] H. Zhang, N. Shlezinger, F. Guidi, et al., "Near-Field Wireless Power Transfer for 6G Internet of Everything Mobile Networks: Opportunities and Challenges," IEEE Communications Magazine, vol. 60, no. 3, pp. 12-18, March 2022.

[373] Z. Zhang, H. Pang, A. Georgiadis, et al., "Wireless Power Transfer—An Overview," IEEE Transactions on Industrial Electronics, vol. 66, no. 2, pp. 1044-1058, Feb. 2019.

[374] R. Zhang and C. K. Ho, "MIMO Broadcasting for Simultaneous Wireless Information and Power Transfer," IEEE Transactions on Wireless Communications, vol. 12, no. 5, pp. 1989-2001, May 2013.

[375] K. Huang, X. Chen, C. Liu, "The Principle and Technology of Microwave Wireless Energy Transmission," Beijing: Science Press, 2021.

[376] L. LI, P. ZHANG, J. HAN, et al., "Key Technologies of Microwave Wireless Power Transfer and Energy Harvesting Based on Electromagnetic Metamaterials," (Invited). Acta Photonica Sinica,2021, vol.50, no.10，pp:1-16.

[377] J. Han, L. Li, T. Cui, et al., "Adaptively Smart Wireless Power Transfer Using 2-Bit Programmable Metasurface," IEEE Transactions on Industrial Electronics, vol. 69, no. 8, pp. 8524-8534, Aug. 2022.

[378] X. Wu et al., "Multitarget Wireless Power Transfer System Strategy Based on Metasurface-Holography Multifocal Beams," IEEE Transactions on Microwave Theory and Techniques, vol. 71, no. 8, pp. 3479-3489, Aug. 2023.

[379] H. Xue et al., "Multitarget Wireless Power Transfer System Using Metasurface for Quasi-Bessel Beams With Large Half Power Beam Length," IEEE Transactions on Microwave Theory and Techniques, vol. 70, no. 10, pp. 4449-4462, Oct. 2022.

[380] S. Zhang, H. Xue, S. Zhao, et al., "Generation and Modulation of A Two-dimensional Airy Beam Based on A Holographic Tensor Metasurface". Phys. Rev. Appl. 2022, vol.18,no.6, pp: 6-40.

[381] J. Zhou, P. Zhang, J. Han, et al., "Metamaterials and Metasurfaces for Wireless Power Transfer and Energy Harvesting," in Proceedings of the IEEE, vol. 110, no. 1, pp. 31-55, Jan. 2022.

[382] Atzori, Luigi, A. Iera, et al., "The internet of things: A survey ". Computer networks 2010, vol.54, no.15, pp: 2787-2805.

[383] X. Zhang, H. Liu, and L. Long, "Tri-band Miniaturized Wide-angle and Polarization-insensitive Metasurface for Ambient Energy Harvesting". Applied physics letters, 2017,vol.111, no.7.

[384] Z. Du and X. Zhang, "High-Efficiency Single- and Dual-Band Rectifiers Using a Complex Impedance Compression Network for Wireless Power Transfer," IEEE Transactions on Industrial Electronics, vol. 65, no. 6, pp. 5012-5022, June 2018.

[385] M. Chang, X. Ma, J. Han, et al., "Metamaterial Adaptive Frequency Switch Rectifier Circuit for Wireless Power Transfer System," IEEE Transactions on Industrial Electronics, vol. 70, no. 10, pp. 10710-10719, Oct. 2023.

[386] L. Li, X. Zhang, C. Song, et al., "Compact Dual-Band, Wide-Angle, Polarization- Angle -Independent Rectifying Metasurface for Ambient Energy Harvesting and Wireless Power Transfer," IEEE Transactions on Microwave Theory and Techniques, vol. 69, no. 3, pp. 1518-1528, March 2021.

[387] X. Wang, J. Han, G. Li, et al., " High-performance Cost Efficient Simultaneous Wireless

Information and Power Transfers Deploying Jointly Modulated Amplifying Programmable Metasurface". Nat. Commun. 2023, vol.14, pp:6002.

[388] H. Liu, Y. Li, F. Cheng, et al., "Holographic Tensor Metasurface for Simultaneous Wireless Powers and Information Transmissions Using Polarization Diversity". Advance Functional Materials, 2023, 2307806.

[389] T. Rappaport, "Wireless Communications: Principles and Practice", 2/E. Pearson Education India, 2010.

[390] A. Goldsmith, "Wireless Communications". Cambridge university press, 2005.

[391] L. A. M, L. H. Truong, and T. V. Quyen, "Wireless Power Transfer Near-field Technologies for Unmanned Aerial Vehicles (UAVs): A Review," EAI Endorsed Transactions on Industrial Networks and Intelligent Systems 7, no. 22 (2020): e5-e5.

[392] H. Lyu, J. Wang, and A. Babakhani, "An Energy-efficient Wirelessly Powered Millimeter-scale Neurostimulator Implant Based on Systematic Codesign of an Inductive Loop Antenna and a Custom Rectifier," IEEE transactions on biomedical circuits and systems, vol. 12, no. 5, pp. 1131–1143, 2018.

[393] B. J. DeLong, A. Kiourti, and J. L. Volakis, "A Radiating Near-field Patch Rectenna for Wireless Power Transfer to Medical Implants at 2.4 GHz," IEEE Journal of Electromagnetics, RF and Microwaves in Medicine and Biology, vol. 2, no. 1, pp. 64–69, 2018.

[394] R. Narayanamoorthi, A. Vimala Juliet, and Z. M. Leonowicz, " Class E Power Amplifier Design and Optimization for the Capacitive Coupled Wireless Power Transfer System in Biomedical Implants," Energies, vol. 10, no. 9, pp. 1–20, 2017.

[395] J. J. Casanova, Z. N. Low, and J. Lin, "Design and Optimization of a Class-E Amplifier for a Loosely Coupled Planar Wireless Power System," IEEE Transactions on Circuits and Systems II: Express Briefs, vol. 56, no. 11, pp. 830-834, November 2009.

[396] G. Bhargava, P. K. Rath, and S. Majumdar, "GaN-based Class-F Power Amplifier for 5G Applications," 2022 IEEE Microwaves, Antennas, and Propagation Conference (MAPCON), Bangalore, India, 2022, pp. 1444-1449.

[397] G. Bhargava, and S. Majumdar, "Highly Linearized GaN HEMT Based Class E/F3 Power Amplifier," 2021 Devices for Integrated Circuit (DevIC), Kalyani, India, 2021, pp. 564-568.

[398] S. Cripps, "RF Power Amplifiers for Wireless Communications, " Second Edition. Artech house Norwood, MA, 2006, vol. 250.

[399] Cree GaN-HEMT Datasheet, "Cree CG2H40010F Packaged Discrete Transistor,"April 2022, Available: https://assets.wolfspeed.com/uploads/2020/12/CG2H40010.pdf.

[400] G. Bhargava, S. Majumdar, and F. Medjdoub, " Importing Experimental Results via S2D Model in ADS Tool for Power Amplifier Design, " IETE Journal of Research, pp.1-8,2024.

[401] Y. Zhang , C. You, and W. Yuan, "Joint Beam Scheduling and Power Allocation for SWIPT in Mixed Near-and Far-Field Channels," arXiv preprint arXiv:2304.07945, 2023.

[402] Y. Zhang, C. You, and B. Zheng, "Mixed Near- and Far-Field Communications for

Extremely Large-Scale Array: An Interference Perspective," IEEE Communications Letters, vol. 27, no. 9, pp. 2496-2500, Sept 2023.

[403] Y. Zhang, and C. You, "SWIPT in Mixed Near- and Far-Field Channels: Joint Beam Scheduling and Power Allocation," arXiv preprint arXiv:2310.20186,2023.

[404] C. Huang et al., "Holographic MIMO Surfaces for 6G Wireless Networks: Opportunities, Challenges, and Trends," IEEE Wireless Communications, vol. 27, no. 5, pp. 118-125, October 2020.

[405] Q. Huang, J. Hu, and K. Yang, "Holographic Integrated Data and Energy Transfer," IEEE Transactions on Wireless Communications, vol. 23, no. 12, pp. 18987-19002, December. 2024.

[406] J. Sherman, "Properties of Focused Apertures in the Fresnel Region," IRE Transactions on Antennas and Propagation, vol. 10, no. 4, pp. 399-408, July 1962.

[407] A. Poon, R. Brodersen, and D. Tse, "Degrees of Freedom in Multiple-antenna Channels: A Signal Space Approach," IEEE Transactions on Information Theory, vol. 51, no. 2, pp. 523-536, February. 2005.

[408] H. Zhang et al., "Holographic Integrated Sensing and Communication," IEEE Journal on Selected Areas in Communications, vol. 40, no. 7, pp. 2114-2130, July 2022.

[409] J. Xu, and L. You, "Near-Field Wideband Extremely Large-Scale MIMO Transmissions with Holographic Metasurface-Based Antenna Arrays," IEEE Transactions on Wireless Communications, vol. 23, no. 9, pp. 12054-12067, September 2024.

[410] M. Cui, and L. Dai , "Channel Estimation for Extremely Large-Scale MIMO: Far-Field or Near-Field?," IEEE Transactions on Communications, vol. 70, no. 4, pp. 2663-2677, April 2022.

[411] C. Huang et al., "Holographic MIMO Surfaces for 6G Wireless Networks: Opportunities, Challenges, and Trends," IEEE Wireless Communications, vol. 27, no. 5, pp. 118-125, October 2020.

[412] Q. Huang, J. Hu, Y. Zhao, et al., "Holographic Integrated Data and Energy Transfer," IEEE Transactions on Wireless Communications, vol. 23, no. 12, pp. 18987-19002, December 2024.

[413] J. Sherman, "Properties of Focused Apertures in the Fresnel Region," IRE Transactions on Antennas and Propagation, vol. 10, no. 4, pp. 399-408, July 1962.

[414] A. Poon, R. Brodersen, and D. Tse,"Degrees of Freedom in Multiple-antenna Channels: A Signal Space Approach," IEEE Transactions on Information Theory, vol. 51, no. 2, pp. 523-536, February 2005.

[415] Z. Zhang, J. Chen, and Y. Liu, "On the Secrecy Design of STAR-RIS Assisted Uplink NOMA Networks," IEEE Transactions on Wireless Communications, vol. 21, no. 12, pp. 11207-11221, December 2022.

[416] H. Zhang, N. Shlezinger, and F. Guidi, "Beam Focusing for Near-Field Multiuser MIMO Communications," IEEE Transactions on Wireless Communications, vol. 21, no. 9, pp.

7476-7490, September 2022.

[417] G. Anaya-López, J. P. González-Coma, and F. J. López-Martínez, "Spatial Degrees of Freedom for Physical Layer Security in XL-MIMO," 2022 IEEE 95th Vehicular Technology Conference: (VTC2022-Spring), Helsinki, Finland, 2022, pp. 1-5.

[418] Z. Zhang, et al., "Physical Layer Security in Near-field Communications," arXiv preprint arXiv: 2302.04189, 2023.

[419] H. Lu, and Y. Zeng, "Delay Alignment Modulation: Enabling Equalization-Free Single-Carrier Communication," IEEE Wireless Communications Letters, vol. 11, no. 9, pp. 1785-1789, September 2022.

[420] H. Lu, and Y. Zheng, "Delay Alignment Modulation: Manipulating Channel Delay Spread for Efficient Single- and Multi-Carrier Communication," IEEE Transactions on Communications, vol. 71, no. 11, pp. 6316-6331, November 2023.

[421] H. Lu and Y. Zeng, "Delay-Doppler Alignment Modulation for Spatially Sparse Massive MIMO Communication," IEEE Transactions on Wireless Communications, vol. 23, no. 6, pp. 6000–6014, Jun 2024.

[422] Z. Xiao, X. Liu, and Y. Zeng, et al., "Rethinking Waveform for 6G: Harnessing Delay-Doppler Alignment Modulation," IEEE Communications Magazine, 2024.

[423] H. Lu and Y. Zeng, "Near-field Secure Wireless Communication with Delay Alignment Modulation," Frontiers of Information Technology & Electronic Engineering, early access, 2024.

[424] J. Liu, G. Yang, and Y. Liu, et al., "RIS Empowered Near-field Covert Communications," arXiv preprint arXiv:2401.13564, 2024, https://arxiv.org/abs/2401.13564.

[425] Y. Zhang, Y. Fang, and X. Yu, et al., "Performance Analysis and Low-complexity Beamforming Design for Near-field Physical Layer Security," arXiv preprint arXiv:2407.13491, 2024.

[426] L. Li, H. Xue, and Q. Feng, "Research Progresses in Theory and Applications of Vortex Electromagnetic Waves," Journal of Microwave Science, 2018.

[427] N. Kou, S. Yu, and L. Li, "Generation of high-order Bessel vortex beam carrying orbital angular momentum using multilayer amplitude phase modulated surfaces in radiofrequency domain," Applied Physics Express, 2017.

[428] G. Torcolacci, N. Decarli and D. Dardari, "Holographic MIMO Communications Exploiting the Orbital Angular Momentum," IEEE Open Journal of the Communications Society, vol. 4, pp. 1452-1469, 2023.

[429] Y. Hu, S. Zheng, and X. Jin, et al., "Simulation of Orbital Angular Momentum Radio Communication Systems Based on Partial Aperture Sampling Receiving Scheme," IET Microwaves, Antennas & Propagation, 2016.

[430] Y. Shi, T. Hu, and Z. Meng, et al., "Demodulation Method of Orbital Angular Momentum Vortex Wave by Few Fields Sampled on An Extremely Small Partial Aperture in Radiation Region," Applied Physics Reviews, 2023.

[431] W. Ding, G. Yang, and J. Liu, et al., "Near-field Wide-band Intelligent Beamforming Based on Deep Reinforcement Learning," submitted to IEEE Transactions on Communications, Jan 2024.

[432] N. P. Deepa and K. L. Sudha, "Investigation of Inter and Intra Chip Wireless Channel Modelling," 2017 International Conference on Computing Methodologies and Communication (ICCMC), Erode, India, pp. 657-662, 2017.

[433] A. S. Dhillon, F. Melanson and O. Liboiron-Ladouceur, "Intra-Chip Wireless Communication using RF On-Chip Antennas in Silicon Photonics," 2023 Photonics North (PN), Montreal, QC, Canada, pp. 1-2, 2023.

[434] Y. Al-Alem, A. A. Kishk and R. M. Shubair, "Employing EBG in Wireless Inter-Chip Communication Links: Design and Performance," 2020 IEEE International Symposium on Antennas and Propagation and North American Radio Science Meeting, Montreal, QC, Canada, pp. 1303-1304, 2020.

[435] B. Paudel and X. J. Li, "A Terahertz On-Chip Antenna for Intra-Chip Wireless Communications," 2022 IEEE Conference on Antenna Measurements and Applications (CAMA), Guangzhou, China, pp. 1-3, 2022.

[436] H. M. Cheema and A. Shamim, "The Last Barrier: On-Chip Antennas," IEEE Microwave Magazine, vol. 14, no. 1, pp. 79-91, Jan-Feb 2013.

[437] R. S. Narde, J. Venkataraman and A. Ganguly, "Disc-Loaded, Vertical Top-Hat Monopole Antenna at 225 GHz for On-Chip Wireless Communications," 2019 IEEE International Symposium on Antennas and Propagation and USNC-URSI Radio Science Meeting, Atlanta, GA, USA, pp. 1883-1884, 2019.

[438] W. Liu, C. Yi, and X. Liu, et al., "On Chip Antennas for 6G Wireless Communication Based on GaN Technology," Chinese Electronics Society. Compilation of papers at the National Microwave and Millimeter Wave Conference in 2023 (II). Xi'an University of Electronic Science and Technology, 2023.

[439] A. Fazzi et al., "3D Capacitive Interconnections with Mono- and Bi-Directional Capabilities," 2007 IEEE International Solid-State Circuits Conference. Digest of Technical Papers, San Francisco, CA, USA, pp. 356-608, 2007.

[440] C. Lee, J. Park, and J. Y oo, et al, "Study of The Coil Structure for Wireless Chip-to-Chip Communication Applications," Progress In Electromagnetics Research Letters, vol. 38, pp. 127–136, Mar 2013.

[441] C. Lee, J. Park and C. Park, "Zigzag-Shaped Coil Array Structure for Wireless Chip-to-Chip Communication Applications," IEEE Transactions on Electron Devices, vol. 61, no. 9, pp. 3245-3251, Sept 2014.

[442] S. Hwangbo, Y. -K. Yoon and A. B. Shorey, "Millimeter-Wave Wireless Chip-to-Chip (C2C) Communications in 3D System-in-Packaging (SiP) Using Compact Through Glass Via (TGV)-Integrated Antennas," 2018 IEEE 68th Electronic Components and Technology Conference (ECTC), San Diego, CA, USA, pp. 2074-2079, 2018.

[443] Y. Jiang, F. Gao, and S. Jin, "Electromagnetic Property Sensing: A New Paradigm of Integrated Sensing and Communication," arXiv e-prints, p. arXiv:2312.16428, December 2023.

[444] 3GPP. RP-234018, Channel Modelling Enhancements for 7-24 GHz. 3GPP TSG RAN Meeting #102, Edinburgh, UK, 11th – 15th December, 2023.

[445] ETSI, 2020. ETSI TR 138 901 V16.1.0 (2020-11), Study on Channel Model for Frequencies from 0.5 to 100 GHz. V16.1.0. Technical Report 38.901 (3GPP TR 38.901 version 16.1.0 Release16). https://www.etsi.org/deliver/etsi_tr/138900_138999/138901/16.01.00_60/tr_138901v160100p.pdf

[446] 3GPP. R1-2402621, Discussion on the channel model adaptation and extension. 3GPP TSG RAN WG1 Meeting #116-bis, Changsha, Hunan Province, China, 15th – 19th April , 2024.

[447] 3GPP. R1-2406129, Discussion on channel model adaptation and extension. 3GPP TSG RAN WG1 Meeting #118, Maastricht, NL, 19th – 23rd August , 2024.

[448] ZTE Corporation, Sanechips. 6GWS-250008, 6G Motivation and Day1 Functions – RAN Aspects, 3GPP workshop on 6G, Incheon, Korea, 10th – 11th March ,2025.

[449] vivo. 6GWS-250049, vivo view on 6G RAN technology, 3GPP workshop on 6G, Incheon, Korea, 10th – 11th March ,2025.

[450] NTT DOCOMO, INC.. 6GWS-250052. Vision & priorities for 6G radio technology, 3GPP workshop on 6G, Incheon, Korea, 10th – 11th March ,2025.

[451] Spreadtrum, UNISOC. "Spreadtrum Vision & Priorities for 6G Radio Technology," 3GPP workshop on 6G(6GWS-250063), Incheon, Korea, 10th - 11th March, 2025.

[452] Sharp. "Sharp's Views on Vision and Priorities for Next Generation Radio Technology," 3GPP workshop on 6G(6GWS-250093), Incheon, Korea, 10th - 11th March, 2025.

[453] Xiaomi. "Xiaomi's Views on 6G RAN," 3GPP workshop on 6G(6GWS-250096), Incheon, Korea, 10th - 11th March, 2025.

[454] CAICT. "Views on 6G – RAN," 3GPP workshop on 6G(6GWS-250118), Incheon, Korea, 10th - 11th March, 2025.

[455] ETRI, Ewha Womans University, Kookmin University, et al. "Vision and Priorities for 6G RAN," 3GPP workshop on 6G(6GWS-250121), Incheon, Korea, 10th - 11th March, 2025.

[456] CEWiT. "Views on 6G Technology," 3GPP workshop on 6G(6GWS-250125), Incheon, Korea, 10th - 11th March, 2025.

[457] Fainity Innovation. "FAI's Perspective on 6G," 3GPP workshop on 6G(6GWS-250141), Incheon, Korea, 10th - 11th March, 2025.

[458] InterDigital. "Vision and Priorities for Next Generation Radio Technology," 3GPP workshop on 6G(6GWS-250163), Incheon, Korea, 10th - 11th March, 2025.

[459] Indian Institute of Tech (M), IIT Kanpur. "Vision and Priorities for 6G," 3GPP workshop on 6G(6GWS-250165), Incheon, Korea, 10th - 11th March, 2025.

[460] Indian Institute of Tech (M), IIT Kanpur. "IIT Kanpur's Vision & Priorities for 6G Radio Technology," 3GPP workshop on 6G(6GWS-250175), Incheon, Korea, 10th - 11th March, 2025.

[461] Y. Wang, C. Han, S. Sun, et al, "Cross Far- and Near-Field Channel Measurement and Modeling in Extremely Large-scale Movable Antenna Array Systems," arXiv preprint arXiv:2405.16893, 2024.

[462] Y. Wang, Y. Li, Y. Chen, Z. Yu, and C. Han, "0.3 THz Channel Measurement and Analysis in an L-shaped Indoor Hallway," 2022 IEEE International Conference on Communications (ICC 2022), Seoul, Korea, 2022, pp. 2870-2875.

[463] Y. Li, Y. Wang, Y. Chen, et al, "Channel Measurement and Analysis in an Indoor Corridor Scenario at 300 GHz," 2022 IEEE International Conference on Communications (ICC 2022), Seoul, Korea, 2022, pp. 2888-2893.

[464] Y. Wang, S. Sun, and C. Han, "Far- and Near-Field Channel Measurements and Characterization in the Terahertz Band Using a Virtual Antenna Array," IEEE Communications Letters, vol. 28, no. 5, pp. 1186-1190, May 2024.

[465] Y. Chen, Y. Li, C. Han, et al, "Channel Measurement and Ray-Tracing-Statistical Hybrid Modeling for Low-Terahertz Indoor Communications," IEEE Transactions on Wireless Communications, vol. 20, no. 12, pp. 8163-8176, December. 2021.

[466] T. Muharemovic, A. Sabharwal, and B. Aazhang, "Antenna Packing in Low-Power Systems: Communication Limits and Array Design," IEEE Transactions on Information Theory, vol. 54, no. 1, pp. 429-440, January. 2008.

[467] D. Serghiou, A.T. Joy, A. Tishchenko, et al. "Holographic RIS-assisted Indoor Channel Characterization for Wireless Hot-Spot Applications," 2025.

List of Terms and Abbreviations

3GPP	3rd Generation Partnership Project
AN	Artificial Noise
AoA	Angle of Arrival
AoD	Angle of Departure
ASPP	Atrous spatial pyramid pooling
ASPP-RDN	Atrous spatial pyramid pooling-based residual dense network
BS	Base Stations
C&S	Communication and Sensing
CAP-MIMO	Continuous-aperture-MIMO
CCWPT	Capacitively Coupled Wireless Power Transfer
CE	Channel Estimation
CIR	Channel Impulse Response
CNFFFT	Spherical near-field to Far-Field Transformation
CNN	Convolutional Neural Network
CoA	Curvature of Arrival
CRB	Cramer-Rao Bound
CRLB	Cramér-Rao lower bound
CS	Compressive Sensing
CSI	Channel State Information
CV	Computer vision
DBSCAN	Density-Based Spatial Clustering of Applications with Noise
DC	Direct Current
DFO	Doppler frequency offset
DFT	Discrete Fourier Transform
D-MIMO	Distributed MIMO
DoA	Direction of Arrival
DoF	Degree of Freedom
DPSS	Discrete Prolate Spheroidal Sequence
DPSK	Differential Phase Shift Keying
DRL	Deep Reinforcement Learning
DUT	Device Under Test
EBG	Electromagnetic Bandgap
ECA	Extended Coprime Array
EDoFs	Effective DoFs
EH	Energy Harvesting
ELAA	Extremely Large-scale Antenna Array
EM	Electromagnetic
ESPRIT	Estimation of Signal Parameters via Rotational Invariance Technique

FFC	Far-Field Communications
FFT	Fast Fourier Transform
FIM	Fisher information matrix
FRFT	Fractional Fourier Transform
FRFT	Fractional Fourier Transform
FSE	Fourier Series Expansion
FSK	Frequency-Shift Keying
GaN	Gallium Nitride
GBSM	Geometry-based Stochastic Channel Model
GMMV	Generalized Multiple Measurement Vectors
GS	GerchbergSaxton
HMIMO	Holographic MIMO
HSR	High-Speed Railway
ID	Information Decoding
IF	Intermediate Frequency
IoE	Internet of Everything
IoT	Internet of Things
ISAC	Integrated Sensing and Communication
ISI	Inter-Symbol Interference
ITU	International Telecommunication Union
ITU-R WP5D	International Telecommunication Union's 5D Working Group on Wireless Communications
IUI	Inter-User Interference
L1-RSRP	Layer 1 Reference Signal Receiving Power
LDMA	Location Division Multiple Access,
LNA	Low Noise Amplifier
LoS	Line-of-Sight
LSA	Linear Sparse Array
MA	Movable Antenna
Massive IoT	Massive Internet of things
MCD	Multi-path Component Distance
MCP	Multi-Chip Packaging
MEMS	Microelectromechanical System
METIS	Mobile and wireless communications Enablers for the Twenty-twenty Information Society
MHCM	Map-based Hybrid Channel Model
MIIT	Ministry of Industry and Information Technology
MIMO	Multiple-Input-Multiple-Output
MISO	Multiple-Input-Single-Output
MMIC	Monolithic Microwave Integrated Circuit
mMTC	Massive Machine-Type Communications

mmWave	Millimeter Wave
MNBT	Mobility-oriented Near-field Beam Training
MPC	Multi-Path Component
MPT	Microwave Power Transfer
MRC	Maximum Ratio Combining
MRT	Maximum Ratio Transmission
MUSIC	Multiple Signal Classification
NFC	Near-field Communications
NF-JCEL	Near Field Joint Channel Estimation and Localization
NLoS	Non-Line-of-Sight
NMSE	Normalized Mean-Square Error
NOC	Network-on-Chip
NOMA	Non-Orthogonal Multiple Access
NUSW	Non-Uniform Spherical Wave
OAM	Orbital Angular Momentum
OFDM	Orthogonal Frequency Division Multiplexing
OMA	Orthogonal Multiple Access
OMP	Orthogonal Matching Pursuit
OTFS	Orthogonal Time Frequency Space
PA	Power Amplifier
PAA	Phased Array Antenna
PAS	Power Angular Spectrum
PCB	Printed Circuit Board
PD-OMP	Power-Diffusion-Aware Orthogonal Matching Pursuit
PDAP	Power-Delay-Angle Profile
PEB	Positioning Error Bound
PEC	Perfect Electric Conductor
PLS	Physical Layer Security
PMI	Precoding Matrix Indicator
P-MRDN	Polar-domain Multiple Residual Dense Network
P-MSRDN	Polar-domain Multi-Scale Residual Dense Network
P-OMP	Polar-domain Orthogonal Matching Pursuit
PS	Phase Shifter
PT	Polar-domain Transform
RB	Resource Block
RCS	Radar Cross Section
RD-MUSIC	Reduced-Dimensional Multiple Signal Classification
RDN	Residual Dense Network
RF	Radio Frequency
RHS	Reconfigurable Holographic Surface
RIS	Reconfigurable Intelligent Surface

rKA	randomized Kaczmarz
RLF	Radio Link Failure
RMSE	Root Mean Square Error
RNF	radiating near-field
RSS	Received Signal Strength
RTC	Ring-Type Codebook
SA	Sparse Array
SDMA	Spatial Division Multiple Access,
SE	Spectral Efficiency
SIC	Successive Interference Cancellation
SIMO	Single-Input-Multiple-Output
SiP	System-in-Packaging
SIR	Signal-to-Interference Ratio
SNR	Signal to Noise Ratio
SoC	System-on-a-Chip
SPD-MIMO	Spatially Discrete MIMO
SPIM	Spatial Path Index Modulation
STC	Stacked Two-stage Convolution
SWIPT	Simultaneous Wireless Information and Power Transmission
SWSS	Spatial Wide-Sense Stationarity
TD	Time Delay
TDoA	Time Difference of Arrival
TGV	Through Glass Via
THz	Terahertz
TL	Transmission Lines
ToA	Time of Arrival
ToF	Time of Flight
TPD	Triple Parametric Decomposition
TSV	Through Silicon Via
TTD	True Time Delay
UCA	Uniform Circular Array
UCPA	Uniform Circular Planar Array
ULA	Uniform Linear Array
UM-MIMO	Ultra-Massive Multiple-Input-Multiple-Output
UMa	Urban Macro
UPA	Uniform Planar Array
UPW	Uniform Plane Wave
URA	Unsourced Random Access
USW	Uniform Spherical Wave
VNA	Vector Network Analyzer
VR	Visibility Region

WEH	Wireless Energy Harvesting
WMMSE	Weighted Minimum Mean Square Error
WPBC	Wireless-Powered Backscatter Communication
WPCN	Wireless-Powered Communication Network
WPT	Wireless Power Transfer
WRC-23	World Radiocommunication Conference 2023
XL-array	Extremely Large-Scale Array
XL-MIMO	Extremely Large-Scale MIMO
XL-RIS	Extremely Large-Scale RIS
ZF	Zero-Forcing